Characterization of hydrogeologic units in the northern Albuquerque Basin, New Mexico

Edited by

William C. Haneburg and John W. Hawley

New Mexico Bureau of Geology and Mineral Resources, New Mexico Tech
Socorro, New Mexico 87801

Open-file Report 402C

1996

Chapter 1: Hydrogeologic Framework of Basin Areas in Bernalillo and Southern Sandoval Counties, New Mexico

by

John W. Hawley
New Mexico Bureau of Mines and Mineral Resources,
2808 Central SE
Albuquerque, NM 87106

SUMMARY

The hydrogeologic framework of the Albuquerque (ABQ) Basin has three basic components (hydrostratigraphic, lithofacies, and structural) that, when properly defined and integrated, provide a comprehensive working model of the subsurface geohydrologic system on both local and regional scales. The general framework of the entire Basin Complex (Plates 1-3) between Cochiti Dam and San Acacia (Santo Domingo, Central, Belen) is described by Hawley et al in other sections of this report, and is summarized in Appendix I. The distribution and character of these hydrogeologic units in the central part of the Basin between Bernalillo and Isleta is the primary subject of this chapter (Plates 4-19). Emphasis is on basin- and valley-fill deposits that constitute the major aquifer systems in the Albuquerque-Rio Rancho Metropolitan (ABQ-Metro) Area. Previous work on development of hydrogeologic modeling concepts in Rio Grande rift (RGR) basins of New Mexico is reviewed by Hawley and Haase (1992), Hawley and Lozinsky (1992), and Hawley et al. (1995). Current information on the Cenozoic geology of the RGR structural province is presented in Keller and Cather (1994); and earlier reports by Chapin (1971, 1988), Kelley (1977, 1982), Hawley (1978), Riecker (1979), Tedford (1981, 1982), Lozinsky and Tedford (1991), Hawley and Love (1991), and Cather (1992) and should also be consulted for additional information on rift-basin development.

1. **Hydrostratigraphic units** are the major integrative components of the model and comprise mappable bodies of basin and valley fill (scales 1:24,000-1:500,000) that have definable lithologic and hydrologic characteristics and can be grouped on the basis of position in a stratigraphic sequence. Units are defined in terms of (a) stratigraphic position, (b) distinctive combinations of lithologic features (lithofacies) such as grain-size distribution, mineralogy and sedimentary structures, (c) depositional environment, and (d) general age of deposition. Genetic classes include ancestral-river, present river valley, basin-floor playa, and alluvial-fan piedmont deposits. The attributes of four major (RA, USF, MSF, LSF) and three minor (TA, VA, PA) classes into which of the area's basin and valley fills have been subdivided are defined in Appendix C and schematically illustrated in Figure 3. The Upper (USF), Middle (MSF), and Lower (LSF) Santa Fe hydrostratigraphic units roughly correspond to the (informal) upper, middle, and lower rock-stratigraphic subdivisions of Santa Fe Group described in the preceding section (OF-402B; Appendix C). The other major hydrostratigraphic unit (RA) comprises Rio Grande and Rio Puerco deposits of late Quaternary age (<15,000 yrs) that form the upper part of the regional shallow-aquifer system. Units TA, VA and PA include river-terrace deposits, fills of major arroyo valleys, and surficial piedmont-slope alluvium that are primarily in the unsaturated (vadose) zone. Distribution of hydrostratigraphic units throughout Albuquerque-Rio Rancho area of Bernalillo and Sandoval Counties is illustrated on Plates 4-19 (1:24,000 to 1:100,000 scales).

2. **Lithofacies units**, defined in Appendix D and schematically illustrated in Figure 4, are the basic building blocks of the model where site-specific subsurface information is available (e.g. borehole drilling, sample and geophysical logs). Lithofacies are mappable bodies defined primarily in terms of sediment-grain-size characteristics (gravel, sand, silt, clay, or mixtures thereof), mineral composition, degree of cementation, geometry of bodies of a given textural class, subsurface distribution patterns, and in inferred environment of deposition. They have distinctive differences in geophysical and

1–2

geochemical properties and in hydrologic behavior (Chapters 2 to 6 of this report; OF-402C, Chapters 2 and 3; Haase, 1992; Hawley and Lozinsky, 1992; Haase and Lozinsky, 1992; Mozley et al., 1992; Haneberg and Hawley, 1995). In this study, ABQ Basin deposits have been divided into twelve major lithofacies subunits (I to X, A, B) that are used in combination with the major hydrostratigraphic unit classes to provide a schematic 3-D view of subsurface conditions in the ABQ Metro Area (Plates 4 to 19). These maps, cross sections, supporting well-log interpretations compiled in Appendix F, and the "Key" to the Basin's hydrogeologic framework (Appendix I) constitute the major body of basic data and interpretative information used in preparation of this report.

Basin-fill lithofacies I, II, III, V and VI are unconsolidated. Facies I, II and III are restricted to basin floors, and facies V and VI occur respectively on distal to proximal parts of piedmont slopes. Any thin zones of induration (strong cementation) that may be present are not continuous. Clean, uncemented sand and gravel bodies are major constituents of facies I and II; and much of the coarse-clast assemblage in these fluvial deposits is derived from source areas north of the Albuquerque Basin. Clay and sandstone zones, respectively, form a significant part of lithofacies III and IV; but both units contain extensive well-connected layers of permeable sand. Subdivision IV includes thick, eolian and fluvial sand units that are partly indurated (common calcite cement). Lithofacies V and VI are, respectively, characterized by lenticular bodies of gravelly sand and sandy gravel that are bounded by poorly sorted layers of gravel, sand, silt, and clay (loamy gravels to gravelly loams). These facies form the dominant distal (V) to medial and medial to proximal (VI) components of piedmont alluvial aprons (usually formed by coalescent alluvial fans). Fans expanding out from the mouths of large upland drainage basins (e.g. Tijeras Canyon) include extensive (distributary) networks of coarse-grained, stream-channel fills (clean, gravelly sand), which form a large part of subfacies Va and VIa. On the other hand, small high-gradient fans derived from small-steep mountain-front watersheds contain a high proportion of the debris-flow and sheet-flood materials, which are dominated by the poorly sorted mixtures of fine- and coarse-grained sediments that

characterize subfacies Vb and VIb. Lithofacies VII and VIII are, respectively, partly to well-indurated equivalents of facies V and VI. Lithofacies IX and X primarily comprise thick sequences of fine-grained basin-floor sediments, with disconnected (lenticular) bodies of sand and sandstone, that include playa-lake beds and other lacustrine sediments. Facies IX is primarily non-indurated, while unit X (not recognized in basin-fill deposits mapped herein) contains large amounts of mudstone, siltstone, and shale.

Coarse-grained channel deposits of the ancestral Rio Grande system (clean sand and gravel units of lithofacies I and II) are the major components of the upper Santa Fe (USF-2,4) hydrostratigraphic units. Ancestral-river deposits form the most important aquifers and potential enhanced-recharge zones in the basin. Buried arroyo-channel deposits (facies Va and VIa) in the extensive piedmont alluvial aprons that flanked the ancestral-river plain form another major hydrogeologic unit that also has greater than average aquifer performance and recharge potential. These ancient complexes of distributary-channel fills occur in piedmont alluvial deposits of the upper Middle and Upper Santa Fe Group (MSF-1,3 and USF-1-3) that are now partly dissected by valleys of the present Embudo, Campus, Tijeras, Calabacillas, and Montoyas arroyo systems in the Central (ABQ) Basin area.

The present, deeply entrenched river-valley system, which has developed since early Pleistocene time (past million years) is partly occupied by a succession of inset fills that include a) fluvial-channel and floodplain facies (A), and b) arroyo-channel and fan facies (B). These lithofacies are the basic building blocks of hydrostratigraphic units RA, TA and VA. Subfacies A1 and A2 comprise, respectively, gravel- and sand-dominated channel deposits of the Rio Grande (RA) system that form the bulk of the shallow-aquifer system beneath modern river-valley floors. These subfacies are also major components of the river-terrace (TA) fills that flank the inner Rio Grande and Puerco Valley in many places; and they are equivalent to subfacies Iv of Hawley and Haase (1992) and Hawley and Lozinsky (1992). Silt-clay-rich subfacies A3 is locally an important component of both inner-valley (RA) and river-terrace (TA) fills, particularly beneath the modern

floodplain and channel area, in and south of "downtown" Albuquerque. Lithofacies B is an undivided complex of textural and clast-type classes associated with the high-gradient, ephemeral depositional environments of tributary arroyo (wash) systems that are graded to present (RA) and former (TA) river-valley floors. Facies B is a general correlative of subfacies Vv of Hawley and Haase (1992), and Hawley and Lozinsky (1992), and it is the product of the same alluvial, hyperconcentrated-flood-flow and mass-wasting processes that produced piedmont lithofacies V and VI.

3. **Structural and bedrock features** (Appendix I) include a) basin-bounding mountain uplifts, bedrock units beneath the basin fill, b) fault zones within and at the edges of the basin that influence sediment thickness and composition, and c) the igneous intrusive and extrusive (volcanic) rocks that locally penetrate or overlap basin-fill deposits. Regional tectonic and more-local structural controls on lithofacies distribution patterns and subbasin "segmentation" are illustrated on Plates 2 to 15 and they are described in more detail in other parts of this report (OF-402). Emphasis here is on how geologic structure relates both to internal aquifer characteristics, and to boundary conditions that enhance or restrict groundwater flow. For example, the dominantly eastward-tilted (multiple) half-graben structure of the northern and eastern subbasins between Cochiti and Belen (Cochiti-Bernalillo, Metro Area, Wind Mesa, and Lunas-Bernardo Depressions - Plate 2) has clearly controlled the position and character of ancestral Rio Grande deposits (Unit USF-2, facies I, II, III) since basin throughflow was initiated about 5 Ma ago. Three deep graben structures beneath the San Felipe-Santa Ana, Albuquerque, and Cat Hills volcanic fields have been identified in this study that also played a major role in controlling the position of ancestral Rio Grande channels as the northern part of the Basin Complex filled. Prior to late-Miocene time rapidly subsiding subbasin blocks formed extensive internally drained areas particularly in the southern part of the Basin Deltaic and lacustrine sedimentation occurred in these areas during episodes when contributing fluvial systems were unable to deliver the amounts of water and sediment needed to maintain

through-flow conditions. Dominantly fine-grained facies (III, IX and X) are major components of hydrostratigraphic unit MSF (Fig. 4) in such sites of restricted or ponded surface drainage.

Major structural features are generally delineated on Plates 2 and 3, and include the Sandia Pueblo Bench (SPB), Mountainview prong (MVp), Atrisco-Barelas trend (A-B zone), Rio Grande-fault system (RGfs), Atrisco-Rincon transfer zone (ARtz), Loma Colorada transfer zone (LCtz), and Tijeras-Gabaldon accommodation zone (TGaz). These major subsurface structures have little or no surface (geomorphic) expression, but they have a significant impact on the behavior of the shallow and intermediate aquifer systems in the ABQ-Metro Area. The A-B trend and RGfz are fold and/or fault components of major structures (with general NW-SE strike) that border and cross the Alameda-Armijo (A-A) subbasin of the Metro Area depression (Figure 1b, Plate 3). This southward ascending structural ramp is located between the Sandia Pueblo bench (and Corrales segment of Rio Grande fault system) and the A-B structural trend (Plates 2 and 13) that parallels the Tingley Beach reach of the river. Aquifer transmissivity appears to decrease by at least a factor of 4 downstream direction between the deepest (north) and shallowest (south) parts of the Alameda-Armijo. In this area, the upper Santa Fe aquifer zone (USF-2, 4; facies Ib, II, and III) thins from about 1600 ft beneath Corrales to about 400 ft at Rio Bravo Blvd. The depth to Middle Santa Fe (MSF) facies IX and III decreases southward by about the same amount beneath this reach of the Rio Grande.

The western and eastern parts of the Metro Area Depression, respectively, designated the Paradise Hills and East Heights subbasins in this report (Fig. 1b, Plate 3), are characterized by thick, Upper Santa Fe Group basin fill (Subunits USF-4 and 2). These coarse-grained sediments (facies I, II, III) were deposited by the ancestral Rio Grande system in two deep structural depressions. Block-fault (graben) subsidence in the Basin area now occupied by the Albuquerque Volcanoes formed the western subbasin; and eastward rotation of East Heights hanging-wall (half-graben) blocks along the western margin of the Sandia uplift produced the eastern subbasin (Fig. 3). The effect of these

structural features on Middle (?) and Upper Santa Fe lithofacies distribution and aquifer characteristics was only revealed after study of more than 100 borehole geophysical and drilling logs from deep wells in the Albuquerque-Rio Rancho area during the course of this investigation. The mapped (and inferred) distribution patterns of thick (highly transmissive) fluvial facies units (I-III) in the Upper Santa Fe (USF-2,4) basin-fill sequence coincide with the East and West Mesa "groundwater troughs" originally identified by Bjorklund and Maxwell (1961) and Titus (1961). The western trough continues southward in a south-southwest-trending belt in the "West Mesa" (Llano de Albuquerque) area that includes the Albuquerque and Cat Mesa volcanic fields (Plates 7-11; Fig. 4) in both the western Metro Area and central Wind Mesa structural depression.

Chapter 2

Faults as Hydrogeologic Units in the Albuquerque Basin

William C. Haneberg
New Mexico Bureau of Mines and Mineral Resources, Socorro, NM 87801

PURPOSE AND SCOPE

The primary purpose of the work described in the chapter is to investigate faults as hydrogeologic units, analogous to the stratigraphic units delineated during the course of investigations by Hawley and Haase (1992) and their colleagues, within the Albuquerque Basin. This was accomplished by:

1. Obtaining publicly available data showing groundwater levels in the vicinity of selected faults within the Albuquerque Basin, from which the effects of faults on groundwater flow fields could be inferred.

2. Reviewing published studies of fault zone hydrogeology.

3. Examining exhumed portions of the Sand Hills and Hubbell Springs faults along the margins of the Albuquerque Basins as possible analogs for inaccessible structures such as the Rio Grande, Isleta, and West Sandia faults.

4. Comparing groundwater-level profiles across selected Albuquerque Basin faults with theoretical profiles obtained from a newly developed mathematical model of steady state groundwater flow across idealized faults. This allows the influence of the faults to be isolated from the influence of the juxtaposed aquifers on either side of the faults.

Recommendations for future investigations of fault zone hydrogeology within the Albuquerque Basin are also discussed at the end of this chapter.

SUMMARY

Faults can have significant effects on groundwater flow, due either to the hydraulic properties of the fault zones or juxtaposition of aquifer units of differing transmissivity, or some combination of the two. Although their true thicknesses may be small, faults in the Albuquerque Basin are inclined and cut through thick aquifers. Thus, their presence is reflected by broad zones of hydraulic influence ranging in width from hundreds of meters to kilometers in map view. Simple analytical models of horizontal steady-state flow across vertical faults were developed in order to better understand the role of faults as hydrogeologic units. High-

transmissivity faults, low-transmissivity faults, and faults along which appreciable fluid flow occurs all produce distinct head profiles that can be used to infer the hydrogeologic nature of faults in real aquifers. For faults along which leakage is insignificant, the model suggests that low-transmissivity faults will have a much greater effect on fault-normal flow than will high-transmissivity faults. Additional complications introduced by dipping faults were investigated using a finite difference model of steady horizontal flow. Comparison of observed water level profiles with theoretical type-curves suggests that the Hubbell Springs fault is a low-transmissivity flow barrier by virtue of reduced fault-zone and hangingwall transmissivity. A lack of reliable water level data and changing interpretations on their exact location and style of displacement, however, make it impossible to analyze the hydrogeologic influence of features such as segments of the Isleta and Rio Grande fault zones beneath the City of Albuquerque.

RECOMMENDATIONS FOR FUTURE WORK

The primary impediments to a thorough understanding of the hydrogeology of faults in the Albuquerque Basin are the lack of reliable water-level data and uncertainty about the geologic framework. Therefore, future aquifer characterization work should include drilling, coring, geophysical logging, and installation of at least three multi-level piezometers on each side of the Isleta, Rio Grade, and west Sandia faults in order to better define both horizontal and vertical flow directions an hydraulic gradients. Additionally, detailed subsurface mapping will be required to better define the exact locations of major structures in three dimensions. On a broader scale, multi-level piezometer nests should also be installed in several dozen locations throughout the city in order to obtain reliable hydraulic head data. Cores should be obtained by drilling through one or more of the dipping faults in order to determine if exhumed faults along the basin margins can be studied as analogs to faults currently beneath the water table. Any new piezometers should also be adequate for collection of water quality samples as well in order to determine if the faults have any detectable effects on geochemical processes beneath the water table. Both detailed field studies of exhumed faults and numerical modeling studies should also be continued in order to better define variables such as the effective widths of faults as hydrogeologic units, the nature of fault segmentation within basin-fill deposits. variations in structural style and permeability along strike, the importance of vertical groundwater flow along major faults, and the hydraulic properties of fault zones at various scales.

Chapter 2

Faults as Hydrogeologic Units in the Albuquerque Basin

William C. Haneberg
New Mexico Bureau of Mines and Mineral Resources, Socorro

Abstract. — Faults can have significant effects on groundwater flow, due either to the hydraulic properties of the fault zones or juxtaposition of aquifer units of differing transmissivity, or some combination of the two. Although their true thicknesses may be small, faults in the Albuquerque Basin are inclined and cut through thick aquifers. Thus, their presence is reflected by broad zones of hydraulic influence ranging in width from hundreds of meters to kilometers in map view. Simple analytical models of horizontal steady-state flow across vertical faults were developed in order to better understand the role of faults as hydrogeologic units. High-transmissivity faults, low-transmissivity faults, and faults along which appreciable fluid flow occurs all produce distinct head profiles that can be used to infer the hydrogeologic nature of faults in real aquifers. For faults along which leakage is insignificant, the model suggests that low-transmissivity faults will have a much greater effect on fault-normal flow than will high-transmissivity faults. Additional complications introduced by dipping faults were investigated using a finite difference model of steady horizontal flow. Comparison of observed water level profiles with theoretical type-curves suggests that the Hubbell Springs fault is a low-transmissivity flow barrier by virtue of reduced fault-zone and hangingwall transmissivity. A lack of reliable water level data and continually changing interpretations of basin structural geology, however, make it impossible to analyze the hydrogeologic influence of features such as the Iseleta and Rio Grande faults beneath the City of Albuquerque.

INTRODUCTION

Faults can function as high-permeability zones of enhanced groundwater flow or as low-permeability barriers that impede groundwater flow, and as a consequence may exert a strong influence on hydraulic head distributions in faulted aquifers. By impeding groundwater flow and increasing up-gradient hydraulic heads, faults can also influence the location of surficial geologic features such as springs and landslides. If two or more immiscible fluids are present, which is a situation of interest in both petroleum exploration and non-aqueous phase liquid contamination problems, fine-grained fault gouge can form a capillary seal that prevents entry of the non-wetting phase and compartmentalizes sedimentary basins. Clayey fault gouge may act as a geologic membrane, inducing both chemical concentration gradients and osmotic pressure gradients (T.M. Whitworth, personal communication, 1994). Therefore, faults may have the potential to influence geochemical processes such as diagenesis and cementation as

well as hydrodynamics. A high-permeability fault that serves initially as a conduit for increased fluid flow can evolve over time into a low-permeability flow barrier due to cementation or pore collapse, or may even alternate between periods of high- and low-permeability as a consequence of deformation during earthquake cycles (Sibson, 1990). In some cases, the evolution from high- to low-permeability may be the consequence of human activity such as grouting of fault zones to control seepage in and around engineered works (e.g., Levens et al, 1994).

Purpose and Scope

The primary purpose of the work described in this chapter was to investigate faults as hydrogeologic units, analogous to the stratigraphic units delineated during the course of investigations by Hawley and Haase (1992) and their colleagues, within the Albuquerque Basin. This was accomplished by:

1) Obtaining publicly available data showing groundwater levels in the vicinity of selected faults within the Albuquerque Basin, from which the effects of faults on groundwater flow fields could be inferred.

2) Reviewing published studies of fault zone hydrogeology.

3) Examining exhumed portions of the Sand Hills and Hubbell Springs faults along the margins of the Albuquerque Basins as possible analogs for inaccessible structures such as the Rio Grande, Isleta, and West Sandia faults.

4) Comparing water level profiles across selected Albuquerque Basin faults with theoretical groundwater level profiles obtained from a newly developed mathematical model of steady state groundwater flow across idealized faults. This allows the influence of the faults to be isolated from the influence of the juxtaposed aquifers on either side of the faults.

Recommendations for future investigations of fault zone hydrogeology within the Albuquerque Basin are also discussed at the end of this chapter.

Conceptual Models of Fault Hydrogeology

The potential effects of faults on groundwater flow have long been known by hydrogeologists. For example, Tolman (1937) illustrated the changes in water level gradient that can occur when saturated sands and gravels are separated by low-permeability faults. In a passage particularly relevant to the Albuquerque Basin, he wrote (Tolman, 1937, p. 235):

"If the geology is hidden by a superficial deposit, the working out of the geologic structure would be aided by a contour map of the water table, and the faults, if impervious and therefore acting as barriers,

would be indicated by closely spaced contours of the ground-water cascades below them and by effluent seepage above them."

Tolman went on describe the effects of the Niles-Irvington fault in the San Francisco Bay region of California on topographically driven groundwater flow along a mountain front and the advance of a groundwater mound generated by increased recharge as a consequence of flooding along an overlying creek. He also described the segmentation of the Los Angeles basin into boxlike compartments by upthrown fault blocks and faults within the basin-fill alluvium.

Three decades later, Davis and DeWeist (1966) suggested the following reasons why faults in unconsolidated sediments commonly act as barriers to groundwater flow:

1) Cataclasis or granulation of wall rock material.
2) Realignment of elongated clasts to reduce fault-normal permeability and increase fault-parallel permeability.
3) Juxtaposition of water-bearing strata of differing permeability or transmissivity.
4) Cementation or mineralization of the fault zone.

Knipe (1993) recently recast these four mechanisms as three modes of porosity and permeability reduction along faults:

1) Porosity collapse seals, which would include porosity reduction by both grain crushing and grain realignment.
2) Pore-filling cement seals.
3) Juxtaposition seals.

He also emphasized that porosity and permeability along a fault, and thus structurally-controlled groundwater flow paths, can change throughout the earthquake cycle.

Smith et al (1990) were primarily interested in faults that serve as conduits for groundwater flow and heat transport in low-permeability crystalline rocks. Nonetheless, they proposed a conceptual model for the hydraulic structure of fault zones that has relevance for the hydrogeology of fault zones in weakly consolidated sediments such as those in the Albuquerque Basin. They realized that faults are typically composed of anastomosing segments that branch, rejoin, and envelope undeformed pods of protolith. Smith et al further suggested that each fault segment in a crystalline rock could be viewed as a core of low-permeability fault gouge surrounded by a heavily fractured or damaged zone characterized by enhanced permeability. Among the points raised by Smith et al is the common occurrence of higher permeability hanging wall rocks and lower permeability footwall rocks. They speculated that their model could be extended to weakly consolidated clastic rocks by imagining a three-dimensional network of low-permeability fault rock completely surrounding undeformed pods

of more permeable protolith. Examples of this model include the deformation bands or granulation seams such as those described by Aydin and Johnson (1978), Antonellini and Aydin (1994), Pittman (1981), and others.

GROUNDWATER FLOW AND FAULTS IN THE ALBUQUERQUE BASIN

The Albuquerque Basin is one of a series of fault-controlled basins along the Rio Grande Rift, a major crustal structure extending from northern Mexico through Colorado (*e.g.*, Kelley, 1977; Hawley, 1978; Keller and Cather, 1994). Hawley and Haase (1992) proposed a structural model— based largely on projection of seismic reflection profiles and interpretation of cuttings from scattered oil test wells— consisting of southern and northern sub-basins separated by the structurally complicated Tijeras fault zone. Both sub-basins were believed to consist of deep central grabens flanked by shallow structural shelves or benches such as the Hubbell Bench. Major structures such as the Isleta and Rio Grande faults were inferred to strike very nearly north-south beneath Albuquerque. Santa Fe group thickness was shown to range from zero in areas of bedrock outcrop along the basin margins to an inferred maximum of more than 6000 m (20,000 ft) in the central graben of the northern sub-basin. Recently completed geophysical log correlations, however, suggest a significantly different model (see Hawley, Chapter 1, this report).

Without citing any evidence, Thorn et al (1993) speculated that faults are barriers to groundwater flow in the Albuquerque Basin because they are highly cemented and juxtapose aquifer units of differing transmissivity. Changing structural interpretations and the lack of piezometers with which to measure hydraulic head in aquifers beneath the City of Albuquerque make it difficult to reliably analyze the influence of major faults on groundwater flow beneath the city. After assessing the quality of existing data, therefore, it was decided to concentrate on examples for which better field data were available.

A well known example of fault-controlled groundwater flow in the Albuquerque Basin occurs along the Hubbell Springs fault south of the city. Titus (1963) described head drops or groundwater cascades across the Ojuelos fault (now known as the Hubbell Springs fault). Near Comanche Springs in Valencia County, water levels are inferred to drop by as much as 155 m (510 ft) across the Hubbell Springs fault (Figure 2-1). Titus subjectively inferred an extremely abrupt water level change across the fault zone. The wells from which he obtained water levels are widely spaced, and there is no independent evidence for or against such an abrupt change. Thus, the water level profile in Figure 2-1 shows both an abrupt and a gradual change in water level across the fault, neither of which can be rejected on the basis of available data. Springs occur along the up-thrown footwall rocks adjacent to the fault where Paleozoic sedimentary

rocks are exposed at the surface in the footwall, but are generally absent in areas lacking Paleozoic outcrops. Titus believed that the water level decrease across the Hubbell Springs fault zone is a consequence of transmissivity contrast between Paleozoic sedimentary rocks in the footwall and Tertiary basin fill sediments in the hangingwall, but did not comment on the hydraulic properties of the fault itself.

Water levels in the vicinity of Hells Canyon Wash, encompassing the northern portion of Isleta Pueblo and the southern portion of Kirtland Air Force Base, also show that the Hubbell Springs fault is a groundwater barrier (W.D. White, 1994, personal communication). Water level contours. which were computer-generated without regard to the presence of a fault, show three distinct zones corresponding to basin-fill sediments and modern-day alluvium of the Rio Grande, the Hubbell Springs fault, and Paleozoic sedimentary rocks in the footwall (Figure 2-2). Unlike the Hubbell Springs fault near Comanche Springs, well spacing near Hells Canyon Wash is sufficient to demonstrate that water levels decrease gradually over a zone more than 7 km (4 mi) wide.

The Hubbell Springs fault has also been investigated as part of the Sandia National Laboratories site-wide hydrogeologic characterization, where the combined Tijeras, Sandia, and Hubbell Springs faults comprise their own hydrogeologic region (Sandia National Laboratories. 1994). Monitoring well water levels show that water level decreases by more than 230 m (750 ft) from the footwall to the hangingwall of the Hubbell Springs faults, which led Sandia hydrogeologists to speculate that the fault could be separating two distinct groundwater flow zones. The Hubbell Springs fault has also been intersected during the drilling of two wells (SFR-3T and SFR-3P) along the southern boundary of the Sandia National Laboratories/Kirtland Air Force Base complex. Lithologic logs describe the fault zone rocks as grayish green sandstone, mudstone, siltstone, and shale 23 to 43 m (75 to 140 ft) thick. The true thickness of the fault zone, which is characterized by highly contorted and fractured beds. is given as 18 m (60 ft). Subsurface data suggests a minimum of 300 m (900 ft) of pre-Santa Fe Group throw across the Hubbell Springs fault; a prominent scarp and the occurrence of numerous gravel and cobble clasts in Santa Fe age sediments adjacent to the fault imply a record of displacement through the Cenozoic.

Grant (1982) speculated that the Travertine Hills, which are composed of heavily cemented Quaternary gravels resting atop the footwall of the Hubbell Springs fault within the boundaries of Kirtland Air Force Base, represent the remains of an ancient geothermal system operating within the basin. He suggested that meteoric water infiltrated along the western edge of the basin, was heated and mineralized as it flowed to depths of 5 or 6 km, flowed upward along a highly permeable Hubbell Springs fault, and finally precipitated the calcium carbonate that

holds together the Travertine Hills. Grant went on to speculate that changes in the basin-wide hydrologic regime or cementation of the Hubbell Springs fault eventually brought an end to the hydrothermal system.

Titus (1963) also described springs, seeps, travertine, and salt deposits along the footwall of the Rio Puerco fault zone, which separates Paleozoic and Mesozoic sedimentary rocks of the Lucero Uplift from Santa Fe group basin-fill sediments along the western margin of of the Albuquerque Basin. He assumed that, in addition to spring discharge, some groundwater leaks across the fault, which he described as a groundwater dam. His water level contour map shows decreases on the order of 35 m (115 ft) between springs on the upthrown footwall and wells about 1.6 km (1 mile) away in the hangingwall.

Observations of impeded groundwate r flow or groundwater cascades across the Hubbell Springs fault and Rio Puerco fault zone suggests that they are low-permeability features. Thus, these groundwater barriers may be submerged analogs of normal faults along the margins the Albuquerque Basin, for example the Sand Hills fault along the eastern escarpment of the Rio Puerco valley, that are characterized by well-cemented zones.

In arroyos cut into the Ceja de Rio Puerco rim, near the terminus of Southern Boulevard west of Rio Rancho (stop A-3 of Hawley and Love, 1991), the Sand Hills fault offsets both the Middle Buff and Upper Red units of the Santa Fe group. Wright (1946) inferred the occurrence of episodic movement along two splays of the Sand Hills fault, based upon his observations of intermittent sediment accumulation on the downthrown (eastern) blocks. The cemented zone, which Wright originally described as a clastic dike, is on the order of 1 m thick, with rounded to sub-rounded clasts distributed throughout a finer-grained matrix, and occurs as erosionally-resistant ribs in arroyo bottoms that are difficult or impossible to trace across intervening ridge crests. Pods of stratified and undeformed sands and gravels are preserved within the fault zone in some places, as are localized shear zones resembling the deformation bands (Aydin and Johnson, 1978; Pittman, 1981; Antonellini and Aydin, 1994; Antonellini et al, 1994). Elongated concretions that may reflect paleo-groundwater flow occur in many places along the cemented zone, and appear to be capped by pebbles of a diameter nearly identical to that of the concretions. In some places, the concretions are steeply dipping whereas in other places they are nearly horizontal; moreover, spherical and elongated L-shaped concretions also occur at different places along the fault. One can speculate that basin-scale groundwater flow was topographically driven from west to east across the east-dipping Sand Hills fault, which lies along the western periphery of the basin, and consequently that the concretions represent precipitation of calcite cement in low-pressure zones down-gradient of the pebbles. Mozley and Goodwin (this volume) describe the petrography and structural fabric

2-6

of the fault zone rocks, as well as the elongated concretions, in more detail.

OTHER PUBLISHED STUDIES

Field and Laboratory Studies

Antonellini and Aydin (1994) conducted detailed air permeameter studies of sandstones and small faults occurring as deformation bands in sandstones near Moab, Utah. Permeability of intact sandstone generally ranged between 10^{-14} m^2 and 10^{-13} m^2. In comparison to intact sandstone, fault-normal permeability decreases by approximately three orders of magnitude within cataclastic deformation bands and by more than seven orders of magnitude in wall rock adjacent to large-scale slip surfaces. Fault-parallel permeability in cataclastic deformation bands was generally one to two orders of magnitude less than that of the intact sandstone. The permeability of cemented non-cataclastic dilatant deformation bands, in contrast, is typically one order of magnitude less than that of the surrounding sandstone. In one place where a zone of deformation bands is bounded by slip surfaces, fault-parallel permeability averaged over 1 m increments increased by about one order of magnitude whereas fault-normal permeability decreased by more than three orders of magnitude along the slip surfaces. Within the deformation bands bounded by the slip surfaces, however, fault normal permeability was about one order of magnitude less than that of the intact sandstone and fault parallel conductivity is about the same as that of the intact sandstone. In another location where two members of the Entrada Sandstone were juxtaposed, the average permeability between the two units differed by approximately a factor of 50, whereas the average permeability along the slip surface was about two orders of magnitude less than that of the more permeable sandstone member (Figure 2-3). Antonelleni et al (1994) concluded that deformation band formation begins with dilation and is followed by grain crushing and compaction, and that this process is developed to different levels controlled by a combination of porosity, confining pressure, clay content, and strain magnitude. Thus, it is possible that faults that formed in sandstones subjected to low confining pressures are characteristically dilatant whereas faults formed in sandstones subjected to high confining pressure are characteristically contractive, with obvious implications for pre-cementation permeability.

In their study of deformation bands as petroleum reservoir seals in the Permo-Triassic Hopeman Sandstone of Scotland, Edwards et al (1993) observed a gradual decrease in fluorite cementation with increasing distance from deformation bands in a quartz-cemented sandstone but found no granulated fluorite crystals within the bands. Additionally, they observed that pervasive fluorite cementation was restricted to the same sides of the bands as were fluorite-filled veins.They proposed a scheme in which porosity and permeability were first reduced by

cataclasis along the deformation bands and then increased by subsequent dilational fracturing, allowing the passage of fluorite-bearing fluids.

Maclay and Small (1983) described groundwater flow through fault bounded blocks of Edwards Limestone within the Balcones fault zone of Texas, and concluded that juxtaposition of cavernous limestones against low-porosity limestones resulted in partial to almost complete blockage of flow across the faults. They did not, however, address the hydraulic properties of the faults *per se*.

Kolm and Downey (1994) analyzed regional groundwater flow patterns in complexly faulted aquifers beneath the Amargosa Desert of southern Nevada and California, and concluded that fault-normal flow was reduced and fault-parallel flow enhanced. Previously, Huntoon and Lundy (1979) had described zones of enhanced transmissivity in interbedded sandstone and limestones of the Casper aquifer adjacent to fault zones and monoclines near Laramie, Wyoming. In some cases there was a hundred-fold increase in transmissivity in fracture zones extending meters to tens of meters away from faults, which resulted in preferential flow parallel to (but not necessarily within) fault zones.

Ganser (1987) investigated the hydraulic properties of a fault in crystalline rocks. He concluded that the permeability of the Ramapo fault in New Jersey was indistinguishable from the juxtaposed mylonitic gneiss and metabasalt on either side of the fault, and no higher than 10^{-16} m^2, due to the inferred presence of secondary mineralization and clayey fault gouge.

Results from laboratory studies by Morrow et al (1981, 1984) have shown that the permeability of pure clay samples, clay-rich fault gouge samples, and sandy clay fault gouge samples is dependent upon both pressure and displacement. In these two studies, the permeability typically decreased an order of magnitude or more as confining pressure was increased from 0 to 200 MPa (Figure 2-4). The initial permeability of the gouge samples ranged over three orders of magnitude, from 10^{-21} to 10^{-18} m^2. In most cases, most of the permeability reduction occurred within the first 50 to 100 MPa of confining pressure increase, and unloading curves yielded consistently lower permeability values than loading curves. Gouge rich in montmorillonite or mixed-layer clays had the lowest permeability; gouge containing illite and kaolinite had intermediate permeability; and gouge containing serpentine had the highest permeability. The low-permeability gouge samples were composed primarily of grains less than 0.045 mm in diameter, whereas the higher permeability gouge samples had grain size distributions ranging from granules to clay-size grains, with only a small percentage less than 0.045 mm in diameter. Displacement under a confining pressure of 200 MPa reduced

the permeability of coarse-grained gouge samples by an order of magnitude or more, whereas the permeability of the fine-grained gouge samples was reduced by much less than an order of magnitude (Figure 2-5). Two of the sandy clay gouges with initially low permeability dilated after 4 to 5 mm of shear, and the permeability of one of these samples increased nearly an order of magnitude during 10 mm of displacement.

Modeling Studies

Bernard et al (1989) formulated a finite element model to analyze two-dimensional groundwater flow across a vertical fault. In their model, flow was restricted to a non-deformable anisotropic aquifer broken by the fault. Although they recognized that hydraulic properties such as permeability could change significantly in and around a fault, they assumed that the magnitudes of such changes would be negligible. Their primary objectives were to quantify 1) the head loss as a consequence of constriction across the fault zone (i.e., aquifer truncation) and 2) the length of the zone adjacent to the fault in which the water level gradient differed significantly from its unperturbed value.

Barroll and Reiter (1990) analyzed groundwater flow and heat transport through Tertiary clastic basin-fill sediments of the LaJencia basin in central New Mexico using a uncoupled finite difference models for steady-state groundwater flow and advective heat transport. They had to include a low-permeability vertical fault zone to deflect groundwater flow upwards and account for a surface heat flow spike observed in their field data, implicitly raising the important possibility that low-permeability faults can deflect groundwater flow upwards and perhaps produce flow fields that are largely indistinguishable from those produced by groundwater flow channeled through a high-permeability fault zone. This has implications for qualitative arguments about the role of high- and low-permeability faults in the evolution of sedimentary basins. For example, a low-permeability Hubbell Springs fault could have served the same role as a high-permeability Hubbell Springs fault in Grant's (1982) conjectural hydrothermal model of the Albuquerque Basin.

Forster and Smith (1988) modeled coupled groundwater flow and heat transport in idealized topographically-driven flow systems, some of which included a steeply-dipping, high-permeability fracture zone that served to channel both groundwater flow and heat flow upwards. More recently, Forster and Evans (1991) conducted field, laboratory, and modeling studies of the hydrogeology of thrust faults and adjacent rocks in crystalline terranes. They investigated fault zones composed of alternating layers of low-permeability gouge (10^{-17} m^2) and high-permeability damage zones (10^{-15} m^2). Protolith permeability was on the order of

10^{-16} m^2. Although the gouge itself was isotropic with respect to permeability, the alternating gouge and damage zones produced a highly anisotropic fault zone with maximum permeability parallel to the layering. Finite element simulations of topographically-driven, coupled groundwater and heat flow through a crystalline thrust sheet resting atop horizontal sedimentary rocks were also used to investigate the hydrogeologic significant of thrust faults. They modeled the fault as a 1 m thick zone with isotropic permeability between four and eleven orders of magnitude greater than the surrounding rocks, and found that the fault served to focus groundwater flow. Results from a parametric study of fault zone hydraulic properties further illustrated that variations in permeability along the fault had a significant and far-reaching effect on both groundwater pressure and temperature within both the fault and adjacent rocks.

Most recently, Ge and Garven (1994) developed a sophisticated finite model in which wall rocks are simulated as poroelastic solids and faults are simulated as thin zones of elastic-plastic material. They also incorporated slip elements in order to allow large deformations along the fault zone, and used their model to simulate groundwater flow induced by the emplacement of a thrust sheet in the Canadian Rockies, concentrating on the destabilizing influence of high pore fluid pressure generated along low-permeability faults.

ANALYSIS OF STEADY ONE-DIMENSIONAL FLOW

As illustrated by the examples discussed above, faults can be incorporated into sophisticated two- or three-dimensional numerical models of steady and unsteady groundwater flow, heat flow, and solid mechanics The purpose of this investigation, however, is to analyze the role of faults in a real but poorly constrained hydrogeologic environment. Therefore, the highly simplified approach developed by Haneberg (in press) is followed, wherein three flow domains are identified: one aquifer unit to the left of the fault, one aquifer unit to the right of the fault, and the fault itself (Figure 2-6). Vertical flow is initially ignored, and later incorporated implicitly into the model by allowing for recharge from or discharge to the fault. The model uses vertically averaged hydraulic parameters and yields water level profiles, so that its complexity is consistent with the sparse field observations that the model is used to interpret.

No Fault Zone Recharge or Discharge

In this, the simplest case, steady-state confined flow in each of the three domains is described by

$$d^2h'/dx'^2 = 0 \qquad\qquad\qquad (2\text{-}1)$$

with the general solutions

$$h'_l = c_1 + c_2\, x' \tag{2-2a}$$

$$h'_f = c_3 + c_4\, x' \tag{2-2b}$$

$$h'_r = c_5 + c_6\, x' \tag{2-2c}$$

The r and l subscripts denote values in the right and left aquifers, respectively, and the f subscript denotes values within the fault. Hydraulic head is represented by h and the horizontal coordinate is x. Primed variables are dimensional and non-primed variables dimensionless throughout the paper. Thus, there are six constants of integration to be found for the three-domain problem. Head is fixed along each end of the flow system, giving the two boundary conditions

$$h'_l = -\Delta h'/ 2 \qquad \text{along } x' = -L'_a / 2 \tag{2-3}$$

$$h'_r = +\Delta h'/ 2 \qquad \text{along } x' = +L'_a / 2 \tag{2-4}$$

where Δh is a head differential imposed across the system. The three flow domains are linked by requiring continuity of heads and fluxes along each of the two interfaces between aquifer and fault, giving rise to the four additional boundary conditions

$$h'_l = h'_f \qquad \text{along } x' = -L'_f / 2 \tag{2-5}$$

$$h'_f = h'_r \qquad \text{along } x' = +L'_f / 2 \tag{2-6}$$

$$T'_l\,(dh'_l / dx') = T'_f\,(dh'_f / dx') \qquad \text{along } x' = -L'_f / 2 \tag{2-7}$$

$$T'_f\,(dh'_f / dx') = T'_r\,(dh'_r / dx') \qquad \text{along } x' = +L'_f / 2 \tag{2-8}$$

Transmissivity, T', is a vertically-averaged parameter that is commonly used to reduce the dimensionality of groundwater flow problems. It is defined as the product of hydraulic conductivity and the saturated thickness of flow (i.e., aquifer thickness for confined conditions) or, in terms of permeability rather than hydraulic conductivity,

$$T' = k'\rho'g'b' / \mu' \tag{2-9}$$

Here, k' is permeability, ρ' is the fluid density, g' is gravitational acceleration, μ' is fluid viscosity, and b' is the saturated thickness of flow. Boundary conditions (2-3) through (2-8) are evaluated using the general solutions (2-2), giving rise to six linear equations with six unknowns. The computer program *Mathematica* (Wolfram, 1991) was used to obtain the solutions presented in this paper. After some rearrangement to obtain the normalized variables:

$$h_l = h'_l / \Delta h' \tag{2-10}$$

$$h_f = h'_f / \Delta h' \tag{2-11}$$

$$h_r = h'_r / \Delta h' \tag{2-12}$$

$$L_f = L'_f / L'_a \tag{2-13}$$

$$T_l = T'_l / T'_f \tag{2-14}$$

$$T_r = T'_r / T'_f \tag{2-15}$$

$$x = x' / L'_a \tag{2-16}$$

the solutions for head in each of the three flow domains can be expressed as

$$h_l = [(L_f - 1) T_l + (L_f + 1) T_r - 2 T_r (L_f T_l - 2 x)] / D \tag{2-17}$$

$$h_f = [(L_f - 1) T_l - (L_f - 1) T_r + 4 T_l T_r x] / D \tag{2-18}$$

$$h_r = -[(L_f + 1) T_l + (L_f - 1) T_r - 2 T_l (L_f T_r + 2 x)] / D \tag{2-19}$$

with the common denominator

$$D = 4 L_f T_l T_r - 2 (L_f - 1) (T_l + T_r) \tag{2-20}$$

Normalized transmissivity values can then be calculated by taking the ratios of hydraulic gradients. For example,

$$T_r = (dh_f / dx) / (dh_r / dx) \tag{2-21}$$

and

$$T_l = = (dh_f / dx) / (dh_l / dx) \tag{2-22}$$

Because two of the internal boundary conditions required that flux be continuous across the

fault-aquifer interfaces but did not specify the magnitude of flux, the three hydraulic gradients form an under determined set of equations and only transmissivity ratios can be calculated. (Recall that, for example, $T_r = T'_r / T'_f$). Thus, whereas one can easily estimate transmissivity ratios using field-calculated hydraulic gradients on either side of a faulted aquifer, an independent estimate of the magnitude of one of the three transmissivities is required to calculate the magnitude of the other two values.

If aquifer transmissivity is identical on either side of the fault, the aquifer hydraulic gradients on both sides will be identical but segments of the head profile curve will be separated by a gap, the height of which is inversely proportional to the magnitude of transmissivity contrast between the fault and the aquifers (Figure 2-7). For low-transmissivity faults, that is to say those with dimensionless aquifer transmissivities greater than unity, hydraulic gradients within the aquifers are very small and the hydraulic gradient across the fault zone is very steep. For high-transmissivity faults with no recharge or discharge, in contrast, hydraulic gradients in the aquifers are steep and the hydraulic gradient across the fault zone vanishes. Compared to the unit hydraulic gradient that would exist in the absence of a fault, which is indicated by a dashed line on the head profile plots, a low-transmissivity fault has a much larger effect on head distribution than does a high-transmissivity fault. In the case of a low-transmissivity fault, groundwater flux across the fault is hindered by the fault zone transmissivity rather than by the ability of the aquifer to supply water to the fault. In the contrasting case of a high-transmissivity fault, flux is limited not by the physical properties of the fault zone, but rather by the inability of the aquifer to deliver enough groundwater to avoid a head deficit up-gradient from the fault. The effectiveness of low-transmissivity faults as barriers to groundwater flow is also proportional to fault zone thickness (Figure 2-8). For a given set of transmissivity values, the fault zone hydraulic gradient decreases and the magnitude of head drop increases with increasing fault zone width. This is in agreement with the conclusions of Deming (1994), who analyzed the ability of pressure seals, which would include the low-transmissivity faults discussed in this paper, to maintain anomalous hydraulic gradients.

A second, slightly more complicated case involves a fault separating aquifers of different transmissivity. Geologic examples of this case might include a growth fault, across which syntectonic deposition produced a thick hangingwall aquifer and a thin footwall aquifer of similar transmissivity, or a juxtaposition seal in which a fault separates two aquifers of similar thickness but different transmissivity. When the problem is formulated in terms of aquifer transmissivity there is no distinction, at least hydraulically, between these two geologic scenarios. As with the previous example, the general form of the head profile is controlled by the relative transmissivity of the fault zone. Low-transmissivity faults produce an up-gradient

2-13

head excess, whereas high-transmissivity faults produce an up-gradient head deficit. The transmissivity contrast between the left and right aquifers, however, gives rise to a hydraulic gradient ratio that is the inverse of the aquifer transmissivity ratio. A high-transmissivity left-side aquifer will draw groundwater into itself, as illustrated in Figure 2-9. For very low transmissivity faults, say on the order of $T_r = 10^3$, a more transmissive left aquifer appears to have little effect on the head profile. As the transmissivity contrast between the fault and the two aquifers decreases, however, the effect of a more transmissive left aquifer becomes apparent because the magnitude of the up-gradient head excess (relative to the unperturbed unit hydraulic gradient dashed line) is noticeably smaller than the down-gradient head deficit. For high-transmissivity faults the effect is slightly different. There is a head deficit, measured relative to the unperturbed unit hydraulic gradient, on both sides of the fault, but the magnitude of the up-gradient deficit is slightly larger than the magnitude of the down-gradient deficit. For the opposite case of a low-transmissivity left aquifer, the head profile curves are very nearly the opposite, with more pronounced up-gradient head excesses and, in the case of a highly transmissive fault, an overall head excess across the entire system (Figure 2-10).

Juxtaposition of two aquifers of differing transmissivity across an infinitely thin fault having no hydraulic properties of its own is a special case of the situation described above. In such a case, the ratio of hydraulic gradients is, as above, the inverse of the ratio of the two aquifer transmissivities. Because the idealized fault is infinitely thin and has no hydraulic properties, however, there is no gap between the left and right aquifer head profiles.

Recharge or Discharge Along the Fault

In addition to asking what effects a fault has on fault normal flow, one might also ask what effects flow parallel to the fault zone might have on head distribution in the surrounding aquifers. Fault zone recharge or discharge is incorporated into the present model by adding a source-sink term to the governing equation for flow within the fault zone, so that equation (2-1) becomes

$$d^2h'_f/dx'^2 = -R'_f/T'_f \qquad (2\text{-}23)$$

where R'_f is the recharge per unit breadth of the fault zone, with units of length/time. Positive values of R'_f indicate recharge from the fault into the aquifer, and negative values of R'_f indicate discharge from the aquifer into the fault. The general solution for head within the fault zone thus becomes

$$h_f = -1/2 \ (R'_f/T'_f) \ x'^2 + c_7 \ x' + c_8 \tag{2-24}$$

whereas the general solutions for h'_l and h'_r remain unchanged. To simplify this example, the transmissivity of both aquifers is required to be identical, so that $T'_l = T'_r = T'_a$. A similar procedure can be followed to derive solutions for which the aquifer transmissivities differ or for which source-sink terms are included for one or both of the aquifers, but the resulting solutions rapidly become unwieldy as additional complexities are added. For the case of recharge or discharge along the fault zone, it is also necessary to redefine the three normalized heads as

$$h_l = h'_l \ / \ L'_a \tag{2-25}$$
$$h_f = h'_f \ / \ L'_a \tag{2-26}$$
$$h_r = h'_r \ / \ L'_a \tag{2-27}$$

This redefinition of the three normalized heads emphasizes a fundamental difference that is introduced when fault zone recharge or discharge occurs. If fault zone recharge or discharge is not allowed, then the imposed hydraulic gradient Δh is merely a scaling factor that can be used to normalize the particular solutions. That is to say, the shape of the head profile across the fault is independent of the magnitude of Δh. If fault zone recharge or discharge is allowed, however, the magnitude of Δh controls in part the shape of the head profile because it reflects the resistance to flow from the fault and into the aquifer in the case of recharge. Conversely, the magnitude of Δh reflects the ease with which water can be delivered from the aquifer in the case of discharge to the fault zone. Thus, the magnitude of Δh affects the shape of the head profile in cases where there is fault zone recharge or discharge. Additionally, the normalized recharge and imposed hydraulic gradient are

$$R_f = R'_f \ L'_f \ / \ T'_f \tag{2-28}$$

and

$$\Delta h = \Delta h' \ / \ L'_a \tag{2-29}$$

The normalized recharge represents the ratio of flow into or out of the fault zone relative to the ability of the fault to transmit water under a unit hydraulic gradient.

Solution of equations (2-2a), (2-2c), and (2-23) for the six appropriate constants yields, after rearranging into dimensionless form,

$$h_l = [R_f T_a L_f - 2 \Delta h L_f T_a{}^2 - (L_f - 1) R_f + 2 \Delta h L_f T_a + 2 R_f T_a L_f x$$
$$- 2 R_f (L_f - 1) x + 4 \Delta h T_a x] \; / \; [4 T_a (L_f T_a - L_f + 1)] \qquad (2\text{-}30)$$

$$h_f = 1/4 (R_f / T_a) - 1/4 (R_f \; L_f / T_a) + 1/8 (R_f \; L_f) - 1/2 (R_f \; x^2) / L_f$$
$$+ (\Delta h T_a x) / (L_f T_a - L_f + 1) \qquad (2\text{-}31)$$

$$h_r = [R_f \; T_f L_f + 2 \Delta h L_f T_a{}^2 - (L_f - 1) R_f \; - 2 \Delta h L_f T_a - 2 R_f \; L_f T_a x$$
$$+ 2 R_f \; (L_f - 1) x + 4 \Delta h T_a x] \; / \; [4 T_a (L_f T_a - L_f + 1)] \qquad (2\text{-}32)$$

A set of curves illustrating these solutions for a fault with transmissivity one order of magnitude less than aquifer transmissivity is plotted in Figure 2-11. Small values of recharge or discharge, in this case within the range $-5 < R_f < 5$, appear to have little effect on the head profiles. Recharge from the fault increases heads slightly on both sides of the fault, whereas discharge to the fault decreases heads slightly on both sides of the fault. For larger values of recharge or discharge, in this case $R_f = \pm 10$, the effect is more significant. Although recharge from the fault increases head in both the left and the right aquifers, the increase is greater in the right, or up-gradient, aquifer. This is due to the effect of flow from the fault and into both aquifers combined with the barrier effect of a low-transmissivity fault. For discharge to the fault zone, head decreases in the left, or down-gradient, aquifer more than it decreases in the right aquifer. For a fault with transmissivity one order of magnitude greater than the adjacent aquifers, however, recharge from the fault produces a groundwater mound and discharge to the fault produces a groundwater trough regardless of the magnitude of R_f (Figure 2-12). For the case illustrated here, the perturbation due to fault recharge or discharge overshadows the regional hydraulic gradient. If the transmissivity contrast between the fault and the adjacent aquifers is eliminated, the mounds and troughs persist although their amplitudes are reduced by about an order of magnitude and the presence of an imposed hydraulic gradient becomes more apparent (Figure 2-13).

Non-Vertical Faults

Non-vertical or dipping faults present additional complications that cannot be explicitly analyzed using the analytical solutions developed up to this point. As illustrated in Figure 2-16

for a hypothetical listric normal fault, a dipping fault will decrease transmissivity by thinning the aquifer even if the fault itself has no hydraulic properties. The apparent width for a planar normal fault, which is what one might infer by looking for changes in gradient on a water level contour map, is given by

$$w = D/\tan \theta \qquad (2\text{-}33)$$

where w is the apparent fault width in map view, D is the vertical separation between the top of the footwall aquifer and the bottom of the hangingwall aquifer, and θ is the dip of the fault. For listric faults, acceptable results can be calculated by averaging the tangents of the dip angles at the top of the footwall aquifer and the base of the hangingwall aquifer. Although the details will differ, similar reductions in transmissivity will occur regardless of whether the fault is planar or listric, normal or reverse. The only exception that comes to mind is a thrust fault that ramps upward through and then along the top of an aquifer, in which case aquifer thickness would increase.

A finite difference solution of the one-dimensional steady flow equation

$$0 = (d/dx) [T (dh/dx)] \qquad (2\text{-}34)$$

was used to calculate head profiles that might arise as a consequence of tectonic thinning and differences in footwall and hangingwall aquifer thickness. A dimensionless grid spacing of $\Delta x = 0.025$ and a tolerance of 10^{-5} were used for the results given in this chapter. Simulation of the dimensionless head profile produced by left-to-right flow across the hypothetical fault illustrated in Figure 2-14 shows that the principal effect is an increase in head (relative to the unperturbed unit hydraulic gradient) all along the profile, with a slight increase in hydraulic gradient across the fault zone (Figure 2-15). In this example, the fault is infinitesimally thin and has no hydraulic properties of its own. Given only the finite difference simulation results and a knowledge of the analytical solutions developed previously in this chapter, one might look for changes in hydraulic gradient and correctly infer a hangingwall to footwall transmissivity ratio of $T_l/T_r = 1.4$. One might also incorrectly infer, however, the existence of a fault with a dimensionless width of $L_f = 0.05$, and normalized transmissivity values of $T_l/T_f = 1.6$ and $T_l/T_f = 1.2$. Because of the inherent non-uniqueness of head distributions, identical head profiles can be produced by any number of different transmissivity fields and, consequently, it is impossible to infer a unique transmissivity distribution from water level profiles or contour maps.

Application to the Hubbell Springs Fault

Water level gradients calculated graphically from the profiles presented previously in this chapter (Figure 2-1) can be used to estimate transmissivity ratios for rocks near the Hubbell Springs fault. Water level profiles suggest that this fault is a low-transmissivity barrier to flow. If it is assumed that the Hubbell Springs fault near Comanche Springs has an effective width of 1 m, which is on the order of the cemented thickness of the exhumed Sand Hills fault, then the hangingwall aquifer is calculated to be about 20,000 times as transmissive as the fault and the hangingwall aquifer is calculated to be about 2000 times as transmissive as the fault. If, however, the Hubbell Springs fault is assumed to be a broad zone 1800 m wide, which is the maximum value that one might infer given the spacing of data points in Figure 2-1, the hangingwall aquifer is calculated to be about 20 times as transmissive as the fault and the footwall aquifer is calculated to be about 2 times as transmissive as the fault. In either case, note that the hangingwall to footwall transmissivity ratio remains constant at 10. Along the Hells Canyon Wash profile, the hangingwall aquifer is calculated to be about 10 times as transmissive as the fault and the footwall aquifer is calculated to be about 5 times as transmissive as the fault, giving a hangingwall to footwall transmissivity ratio of about 2.

DISCUSSION

Three problems make it difficult to objectively assess the quantitative effect of Albuquerque Basin faults on groundwater flow. First, water levels within the City are typically obtained from high-volume production wells for which the influence of well hydraulics is uncertain. For example, the development of a seepage face along a well may mean that the aquifer water level is substantially higher than that measured in the well. Second, most of the water level measurement points are widely spaced relative to the width of the faults or fault zones. Thus, water levels must be interpolated across faults and the observations can become as much a product of data processing as the natural processes that they are meant to reflect. Third, changing structural interpretations make it difficult to know where to look for evidence of fault-controlled groundwater flow. If one makes the *a priori* assumption that the faults have little effect and contours the data using standard contouring methods, then the effect of faults on groundwater flow may appear to be small. If, on the other hand, one makes the *a priori* assumption that faults have a significant effect and contours data separately on each side of the fault, then in many cases the result will be the appearance of a sharp change in water levels across a very small distance. This problem can be illustrated by comparing the styles of contouring in Figures 2-1 and 2-2, both of which show changes in groundwater levels in different places across the Hubbell Springs fault. Given the spacing of data points, there is no way to tell how much of the difference between the two plots is a consequence of

hydrogeologic variability and how much is a consequence of contouring styles.

To help develop a conceptual understanding of faults as hydrogeologic units, steady-state groundwater flow across high- and low-permeability fault zones was analyzed using models of one-dimensional vertically-averaged flow, in which simple polynomial solutions are obtained for flow domains on either side of the fault as well as within the fault itself. The effects of flow along the fault zone can be implicitly incorporated into the model by the addition of a source-sink term to the equation governing flow within the fault. In the absence of fault zone recharge or discharge, low-transmissivity faults appear to have a more significant effect on groundwater flow than do high-transmissivity faults because flow across a high-transmissivity fault is limited by the ability of the up-gradient aquifer to supply a sufficient amount of water to the fault. For a low-transmissivity fault, water supply does not present a problem. Moreover, fault zone thickness has only a minor effect in this analysis and, in the limit, the hydraulic gradient across an infinitely thin and infinitely impermeable fault will approach infinity. In reality, however, faults may be composed of discontinuous or partially linked segments resulting in an imperfect flow barrier.

If the possibility of recharge or discharge along the fault is considered, then flux along a highly-transmissive fault can in theory overshadow any regional hydraulic gradients because groundwater can be removed from or added to the adjacent aquifers at a rate greater than the aquifers are able to dissipate the excess head. Thus, fault zone recharge or discharge is characterized by groundwater mounds or troughs. The solutions developed in this paper can be used to qualitatively determine the nature of a faulted aquifer system. For example, one might use head profiles across a fault to decide whether the fault is acting as a high-permeability conduit or a low-permeability flow barrier, whether recharge or discharge is occurring along the fault, or whether there is a transmissivity contrast between aquifers on either side of the fault. If information about fault zone width and one independent estimate of transmissivity is available, then the solutions can be further used to obtain quantitative transmissivity estimates.

RECOMMENDATIONS FOR FUTURE WORK

The primary impediments to a thorough understanding of the hydrogeology of faults in the Albuquerque Basin are the lack of reliable water level data and uncertainty about the geologic framework. Therefore, future aquifer characterization work should include drilling, coring, geophysical logging, and installation of at least three multi-level piezometers on each side of the Isleta, Rio Grande, and West Sandia faults in order to better define both horizontal and vertical flow directions and hydraulic gradients. Additionally, detailed subsurface mapping will be required to better define the exact locations of major structures in three dimensions. On a

broader scale, multi-level piezometer nests should also be installed in several dozen locations throughout the city in order to obtain reliable hydraulic head data. Cores should be obtained by drilling through one or more of the dipping faults in order to determine if exhumed faults along the basin margins can be studied as analogs to faults currently beneath the water table. Any new piezometers should also be adequate for the collection of water quality samples as well in order to determine if the faults have any detectable effects on geochemical processes beneath the water table. Both detailed field studies of exhumed faults and numerical modeling studies should also be continued in order to better define variables such as the effective widths of faults as hydrogeologic units, the nature of fault segmentation within basin-fill deposits, variations in structural style and permeability along strike, the importance of vertical groundwater flow along major faults, and the hydraulic properties of fault zones at various scales.

REFERENCES CITED

Antonellini, M. and Aydin, A., 1994, Effect of faulting on fluid flow in porous sandstones: Petrophysical properties: AAPG Bulletin, v. 78, p. 355-377.

Antonellini, M.A., Aydin, A., and Pollard, D.D., 1994, Microstructure of deformation bands in porous sandstones at Arches National Park, Utah: Journal of Structural Geology, v. 16, p. 941-959.

Aydin, A. and Johnson, A.M., 1978, Development of faults as zones of deformation bands and as slip surfaces in sandstone: Pure and Applied Geophysics, v. 116, p. 931-942.

Barroll, M.W. and Reiter, M., 1990, Analysis of the Socorro hydrogeothermal system, central New Mexico: Journal of Geophysical Research, v. 95, p. 21,949-21,963.

Bear, J., 1972, Dynamics of fluids in porous media: New York, American Elsevier.

Bernard, D., Danis, M., and Quintard, M., 1989, Effects of permeability anisotropy and throw on the transmissivity in the vicinity of a fault, in Beck, A.E., Garven, G., and Stegena, L., eds., Hydrogeological regimes and their subsurface thermal effects: American Geophysical Union Geophysical Monograph 47, p. 119-128.

Davis, S.N. and DeWeist, R.J.M., 1966, Hydrogeology: John Wiley & Sons, New York.

Deming, D., Factors necessary to define a pressure seal: AAPG Bulletin, v. 78, p. 1,005-1,009.

Edwards, H.E., Becker, A.D., and Howell, J.A., 1993, Compartmentalization of an eolian sandstone by structural heterogeneities: Permo-Triassic Hopeman Sandstone, Moray Firth, Scotland in North, C.P. and Prosser, J., eds., Characterization of fluvial and eolian reservoirs: Geological Society Special Publication

No. 73, p. 339-366.

Forster, C.B. and Evans, J.P., Hydrogeology of thrust faults and crystalline thrust sheets: results of combined field and modeling studies: Geophysical Research Letters, v. 18, p. 979-982, 1991.

Forster, C.B. and Smith, L., Groundwater flow systems in mountainous terrain: 2. controlling factors: Water Resources Research, v. 24, p. 1,011-1,023.

Grant, P.R., 1982, Geothermal potential in the Albuquerque area, New Mexico in Grambling, J.A. and Wells, S.G., eds., Albuquerque country II: New Mexico Geological Society, Thirty-third Annual Field Conference Guidebook, November 4-6, 1982, p. 325-331.

Ge, S. and Garven, G., 1994, A theoretical model for thrust-induced deep groundwater expulsion with application to the Canadian Rocky Mountains: Journal of Geophysical Research, v. 99, p. 13,851-13,868.

Haneberg, W.C., in press, Steady-state groundwater flow across idealized faults: Water Resources Research.

Hawley, J.W., compiler, 1978, Guidebook to the Rio Grande rift in New Mexico and Colorado: New Mexico Bureau of Mines and Mineral Resources Circular 163.

Hawley, J.W., and Haase, C.S., compilers, 1992, Hydrogeologic framework of the northern Albuquerque Basin: New Mexico Bureau of Mines and Mineral Resources Open-File Report 387.

Hawley, J.W. and Love, D.W., 1991, Quaternary and Neogene landscape evolution: a transect across the Colorado Plateau and Basin and Range Provinces in west-central New Mexico, in Julian, B. and Zidek, J., eds., Field guide to geologic excursions in New Mexico and adjacent areas of Texas and Colorado: New Mexico Bureau of Mines and Mineral Resources Bulletin 137, p. 105-148.

Huntoon, P.A. and Lundy, D.A., 1979, Fracture-controlled ground-water circulation and well siting in the vicinity of Laramie, Wyoming: Ground Water, v. 17, p. 463-469.

Keller, G.R. and Cather, S.M., eds., 1994, Basins of the Rio Grande Rift: Structure, Stratigraphy, and Tectonic Setting: Geological Society of America Special Paper 291, 304 p.

Kelley, V.C., 1977, Geology of Albuquerque Basin, New Mexico: New Mexico Bureau of Mines and Mineral Resources Memoir 33.

Knipe, R.J., 1993, The influence of fault zone processes and diagenesis on fluid flow, in Horbury, A.D. and Robinson, A.G., eds., Diagenesis and basin development: AAPG Studies in Geology #36, p. 135-148.

Kolm, K.E. and Downey, J.S., 1994, Diverse flow patterns in the aquifers of the Amargosa Desert and vicinity, southern Nevada and California: Bulletin of the Association of Engineering Geologists, v. 31, p. 33-47.

Levens, R.L., Williams, R.E., and Ralston, D.R., 1994, Hydrogeologic role of geologic structures. Part I: the paradigm: Journal of Hydrology, v. 156, p. 227-243.

Maclay, R.W. and Small, T.A., 1983, Hydrostratigraphic subdivisions and fault barriers of the Edwards aquifer, south-central Texas, U.S.A.: Journal of Hydrology, v. 61, p. 127-146.

Morrow, C., Shi, L.Q., and Byerlee, J., 1981, Permeability and strength of San Andreas fault gouge under

high pressure: Geophysical Research Letters, v. 8, p. 325-328.

Morrow, C., Shi, L.Q. , and Byerlee, J. , 1984, Permeability of fault gouge under confining pressure and shear stress: Journal of Geophysical Research, v. 89, p. 3,193-3,200.

Pittman, E.D., 1981, Effect of fault-related granulation on porosity and permeability of quartz sandstone, Simpson Group (Ordovician), Oklahoma: AAPG Bulletin, v. 65, p. 2,381-2,387.

Sandia National Laboratories, 1994, Site-wide hydrogeologic characterization project, calendar year 1993 annual report: Albuquerque, Sandia National Laboratories.

Sibson, R.H., 1990, Conditions for fault-valve behaviour, in R.J. Knipe and E.H. Rutter, editors, Deformation mechanisms, rheology and tectonics: Geological Society Special Publication No. 54, p. 15-28.

Smith, L., Forster, C., and Evans, J., 1990, Interaction of fault zones, fluid flow, and heat transfer at the basin scale, in Neuman, S.P. and Neretnieks, I., eds., Hydrogeology of low permeability environments: Verlag Heinz Heise, p. 41-67.

Thorn, C.R., McAda, D.P. , and Kernodle, J.M. , 1993, Geohydrologic framework and hydrologic conditions in the Albuquerque Basin, central New Mexico: U.S. Geological Survey Water Resources Investigations Report 93-4149.

Titus, F.B., Jr., 1963, Geology and ground-water conditions in eastern Valencia County, New Mexico: New Mexico Bureau of Mines and Mineral Resources Ground-Water Report 7.

Tolman, C.F., 1937, Ground water: New York, McGraw-Hill.

Wolfram, S., 1991, Mathematica (2nd edn.): Addison-Wesley, Redwood City, California.

Wright, H.E., 1946, Tertiary and Quaternary geology of the lower Rio Puerco area, New Mexico: Geological Society of America Bulletin, v. 57, p. 383-456.

Table 2.1 Calculated Transmissivity Ratios for the Hubbell Springs Fault

Fault	L_f (meters)	ΔWL (meters)	T_{hw}/T_f	T_{fw}/T_f	T_{hw}/T_{fw}
Hubbell Springs (Figure 2-1, A-A')	1800	138	20	2	10
Hubbell Springs (Figure 2-1, A-A')	1	138	20000	2000	10
Hubbell Springs (Figure 2-2, A-A')	7600	150	10	5	2

L_f = fault zone width; ΔWL = change in water level; T_{hw} = hangingwall transmissivity; T_{fw} = footwall transmissivity; T_f = fault transmissivity.
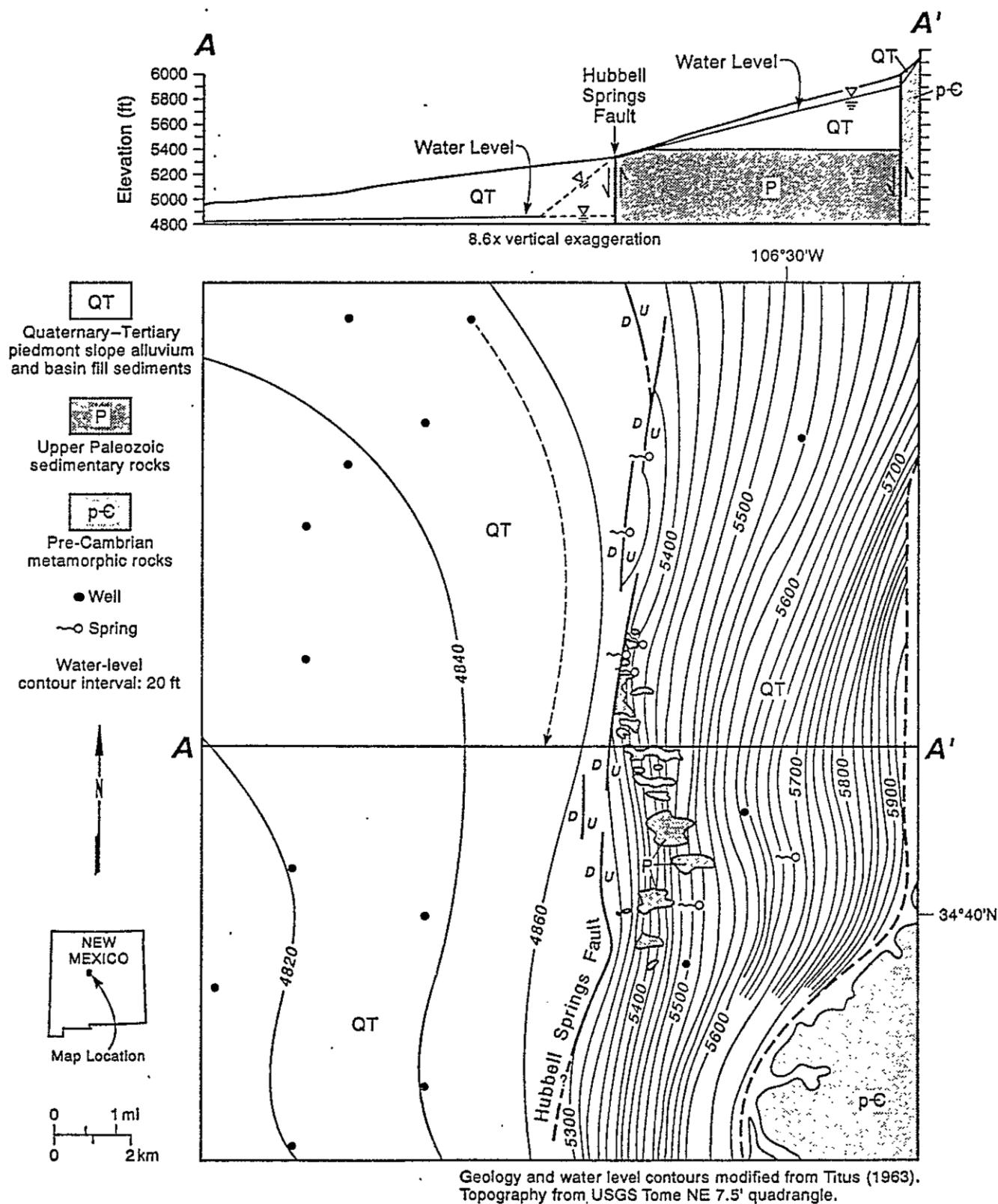
Figure 2-1. Water level contours and hydrogeologic cross-section across the Hubbell Springs fault, eastern margin of the southern Albuquerque Basin, New Mexico, based on limited field observations and water levels tabulated by Titus (1963).

2 - 24
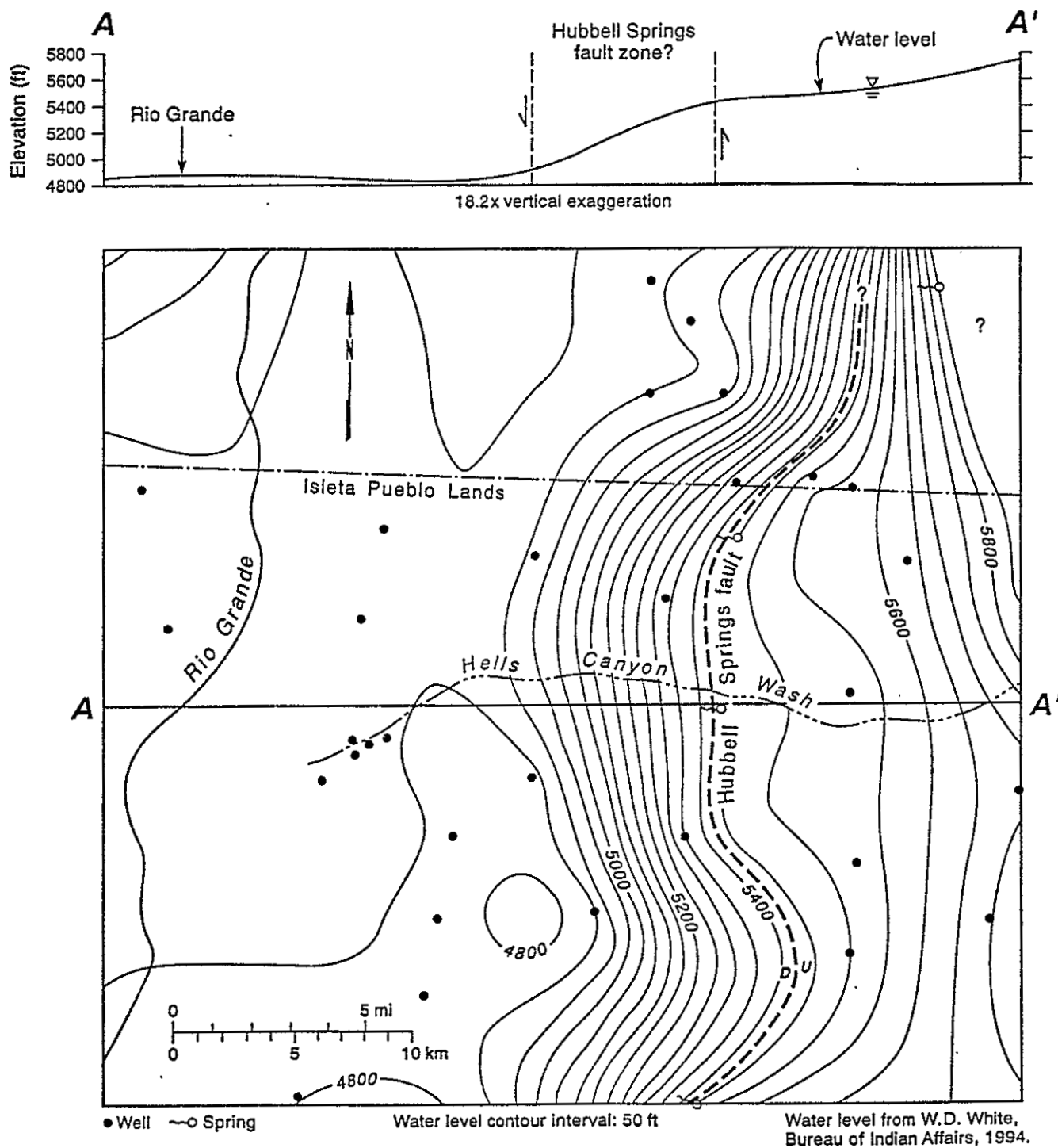
Figure 2-2. Water level contours across the Hubbell Springs fault near Hells Canyon Wash, on the northern portion of Isleta Pueblo and the southern portion of Kirtland Air Force Base. Redrawn from a map provided by W.D. White, Bureau of Indian Affairs, 1994.
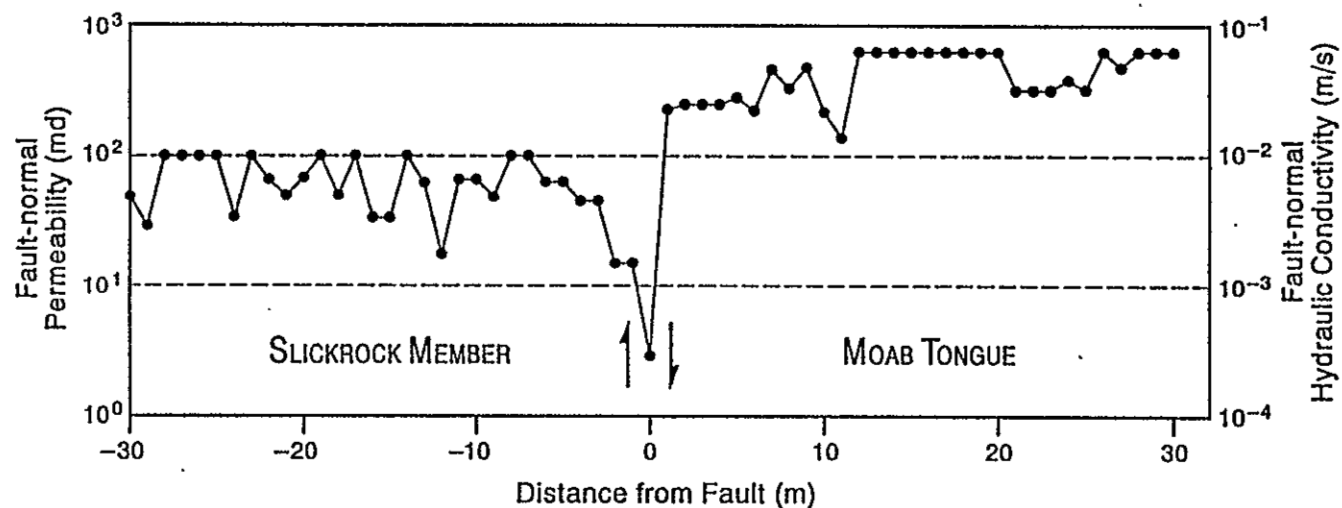
(after Antonellini & Aydin, 1994, AAPG Bulletin)

Figure 2-3. Permeability profile across two members of the Entrada Sandstone near Arches National Park, Utah juxtaposed by a small fault. Hydraulic conductivity was calculated by assuming isothermal flow of water at 20° C. This figure was modified from Antonellini and Aydin (1994). For reference, 1 md = 9.87 × 10⁻¹⁵ m².

For reference, $1 \text{ md} = 9.87 \times 10^{-15} \text{ m}^2$.
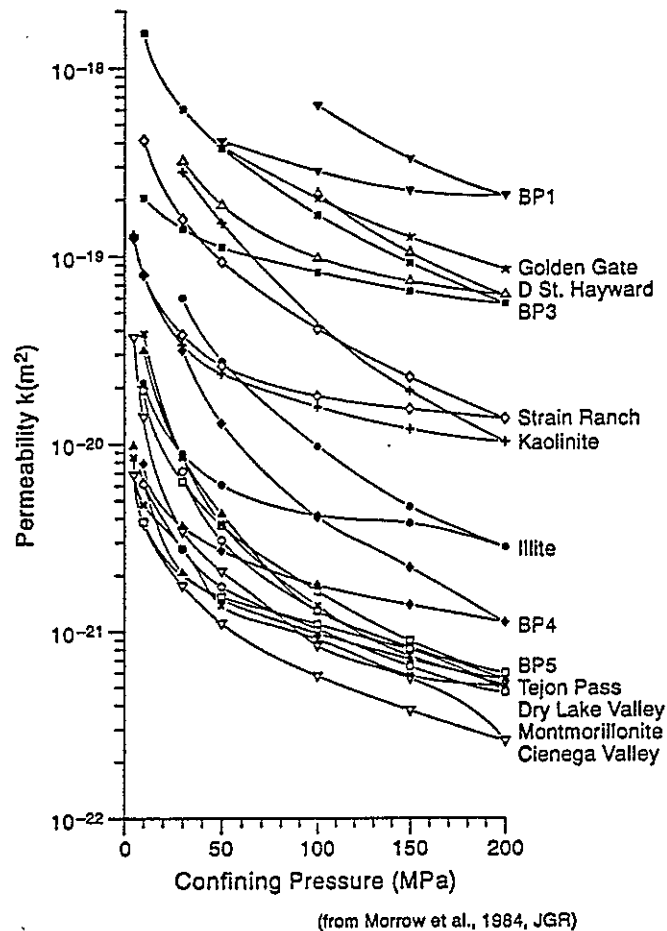
Figure 2-4. Laboratory-measured permeability of various fault gouge samples are a function of confining pressure, redrawn from Morrow et al (1984). Each sample was subjected to loading and unloading, and the loading curve for each is the higher of the two.
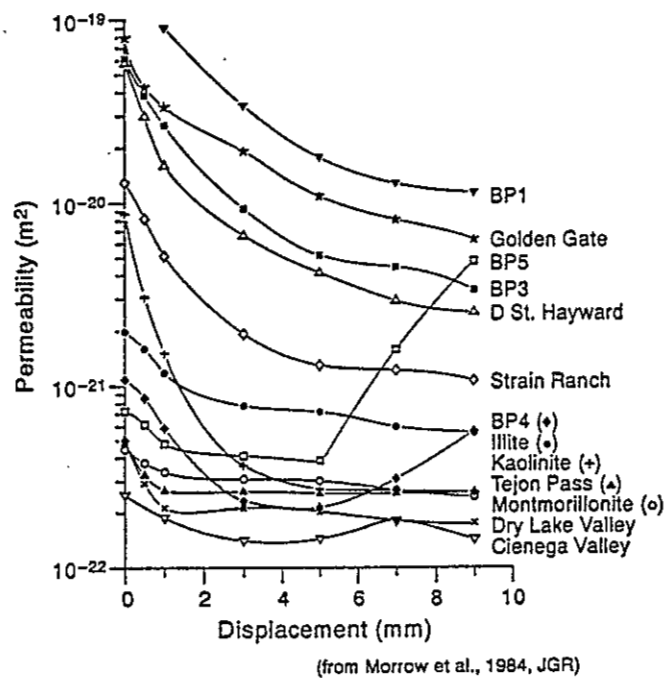
Figure 2-5. Laboratory-measured permeability of various fault gouge samples are a function of displacement under 200 MPa confining pressure, redrawn from Morrow et al (1984).
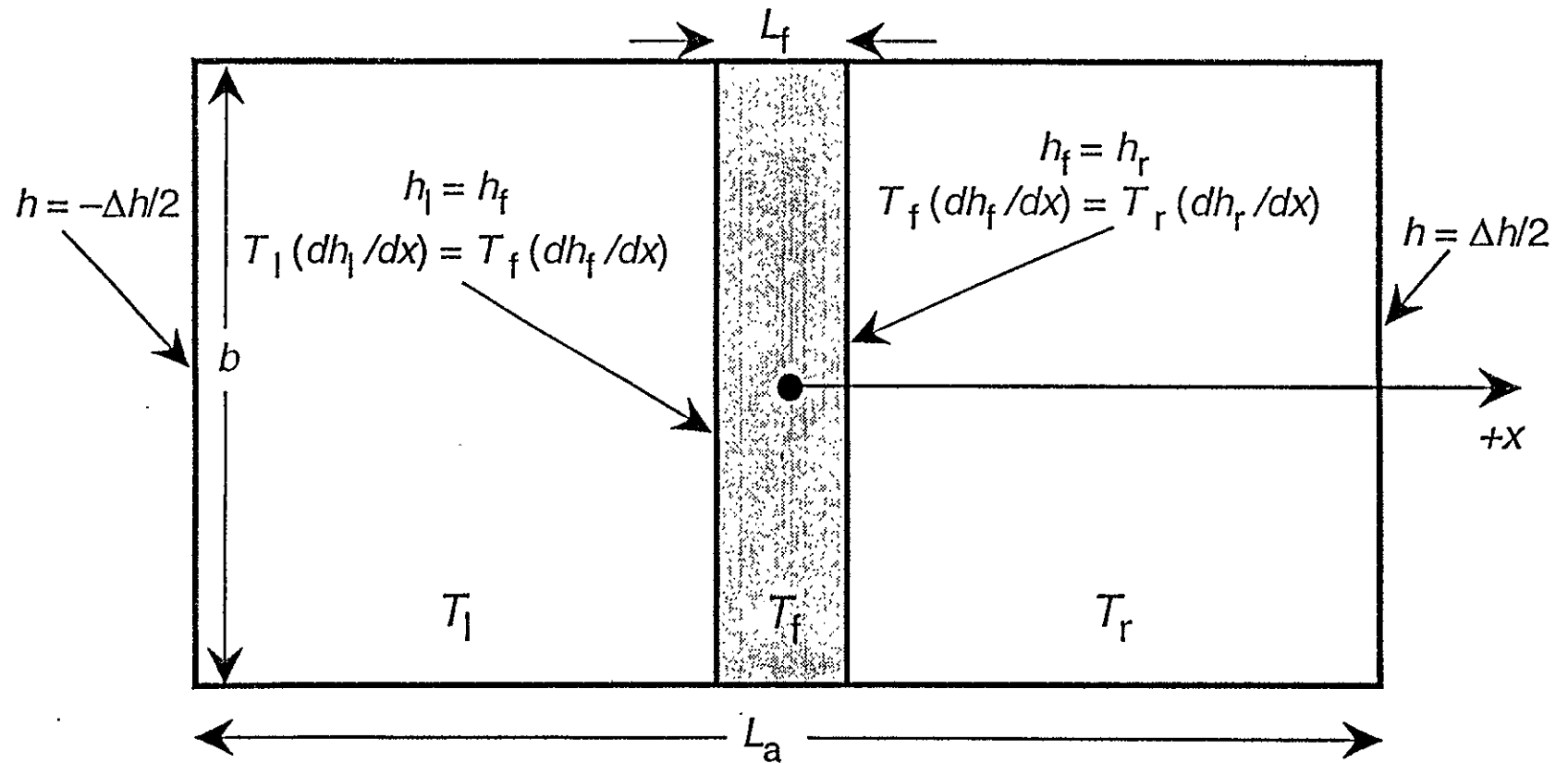
Figure 2-6. Schematic diagram and variable illustration of the idealized fault zone analyzed in this paper.
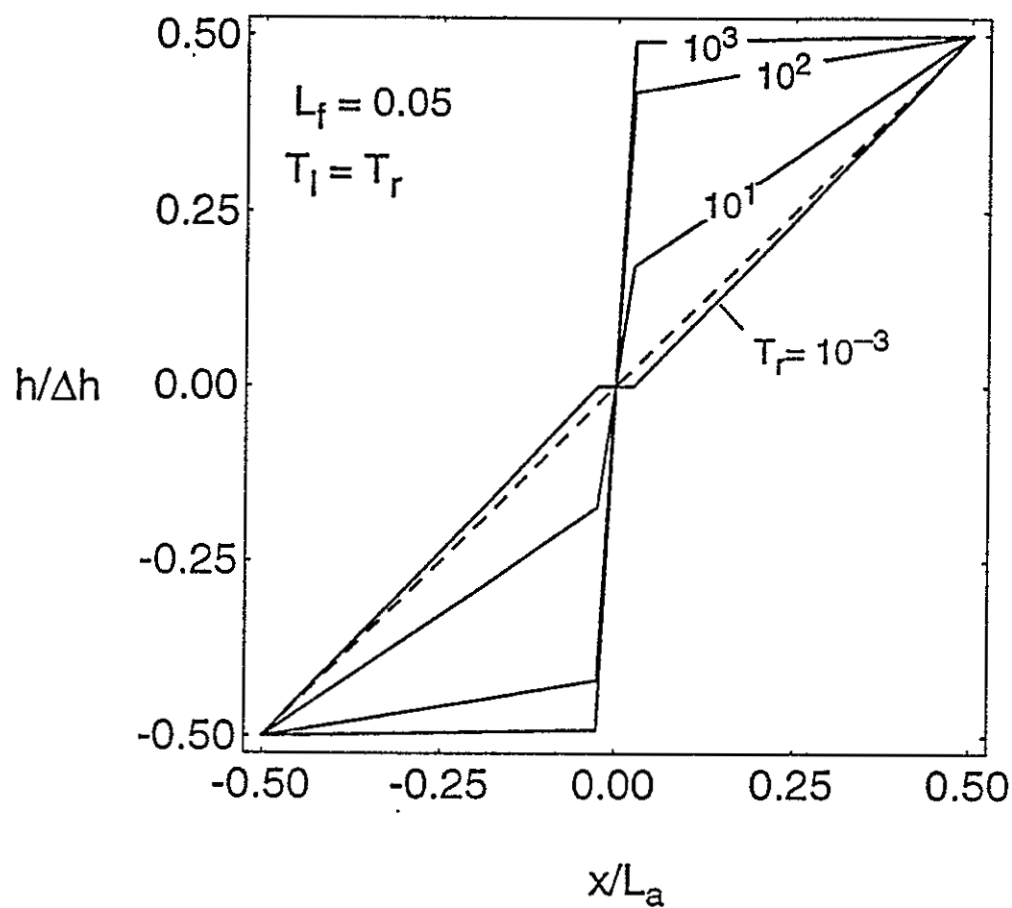
Figure 2-7. Head profiles across a fault juxtaposing two aquifers of equal transmissivity separated by a fault of dimensionless width $L_f = 0.05$. The dashed line indicates the unperturbed head profile that would exist in an unfaulted homogeneous aquifer.
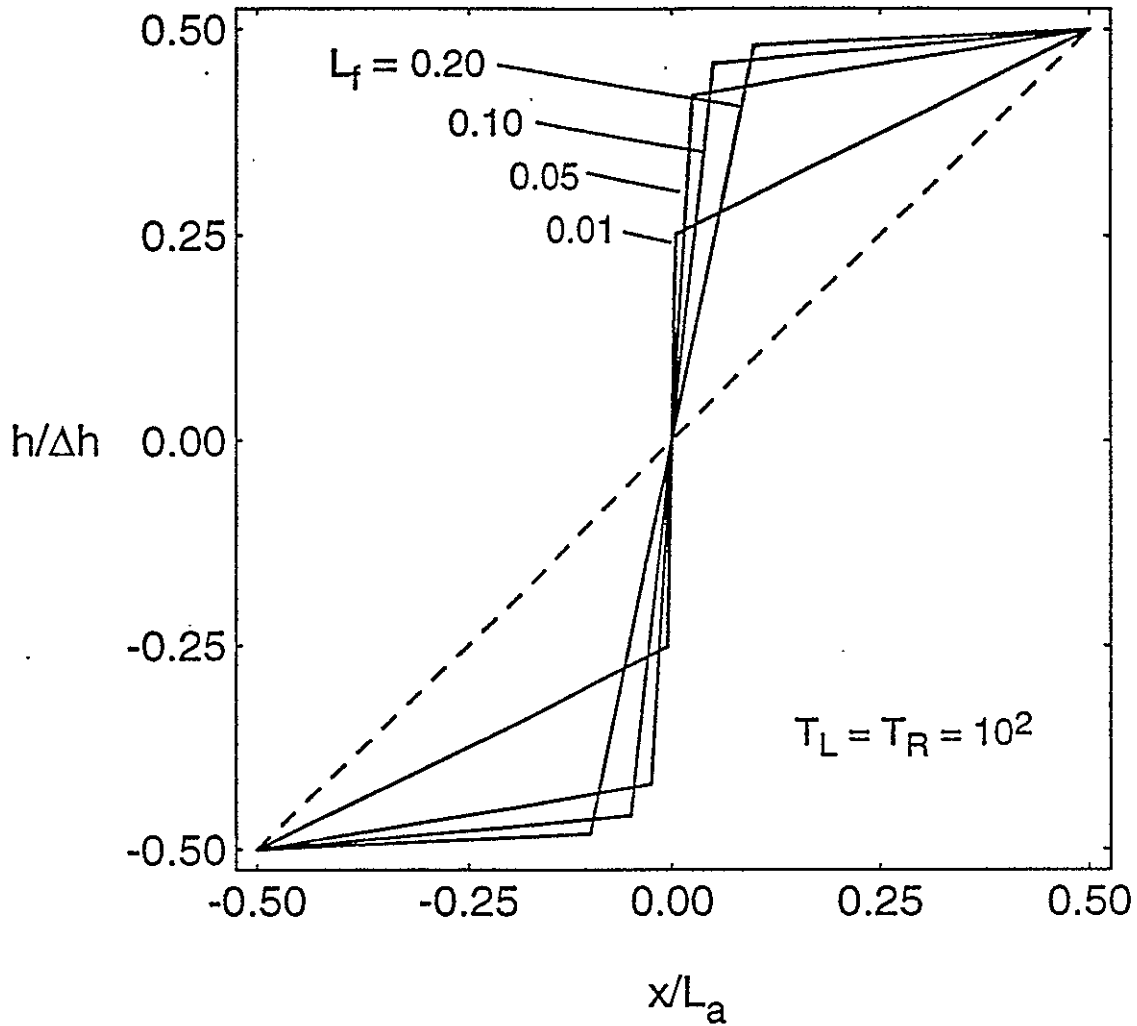
Figure 2-8. Head profiles across faults of different widths juxtaposing two aquifers of equal transmissivity. Fault transmissivity is two orders of magnitude lower than aquifer transmissivity in all cases, giving $T_l = T_r = 10^2$. The dashed line indicates the unperturbed head profile that would exist in an unfaulted homogeneous aquifer.
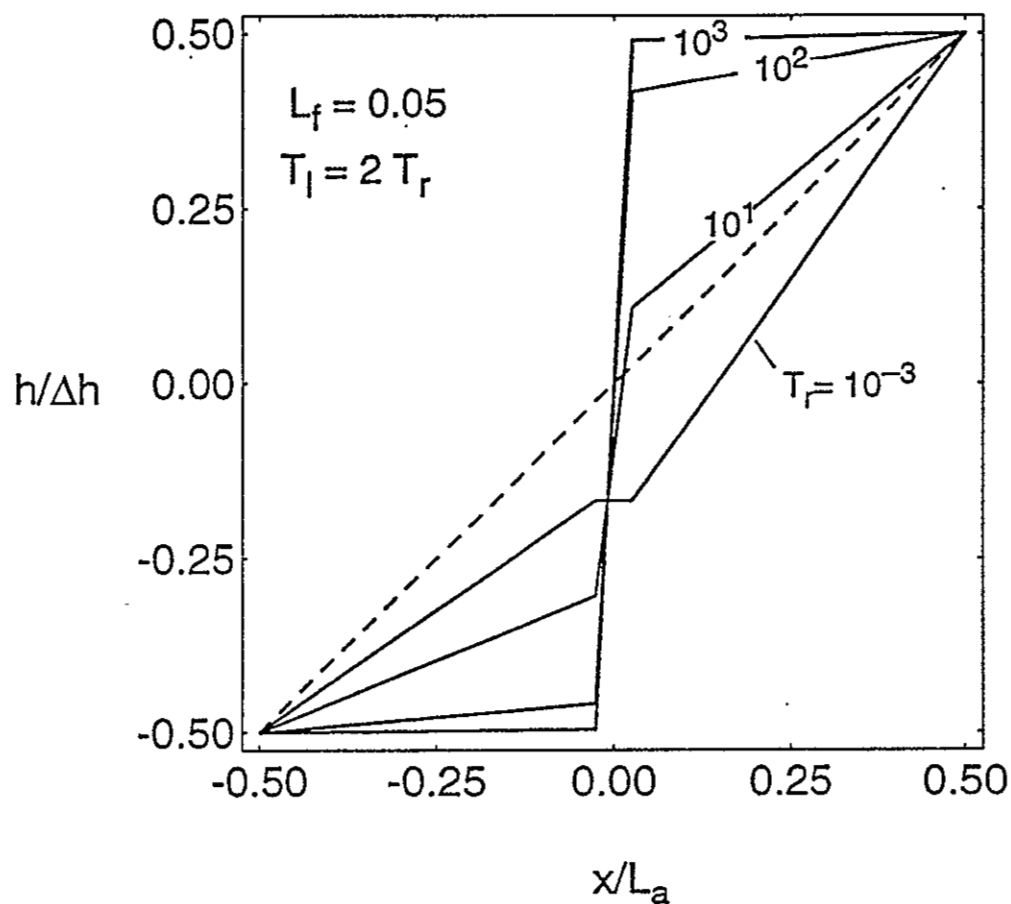
Figure 2-9. Head profiles across a fault juxtaposing two aquifers of unequal transmissivity separated by a fault of dimensionless width $L_f = 0.05$, with the higher transmissivity aquifer down-gradient from the fault. In this example, the down-gradient aquifer has twice the transmissivity of the up-gradient aquifer. The dashed line indicates the unperturbed head profile that would exist in an unfaulted homogeneous aquifer
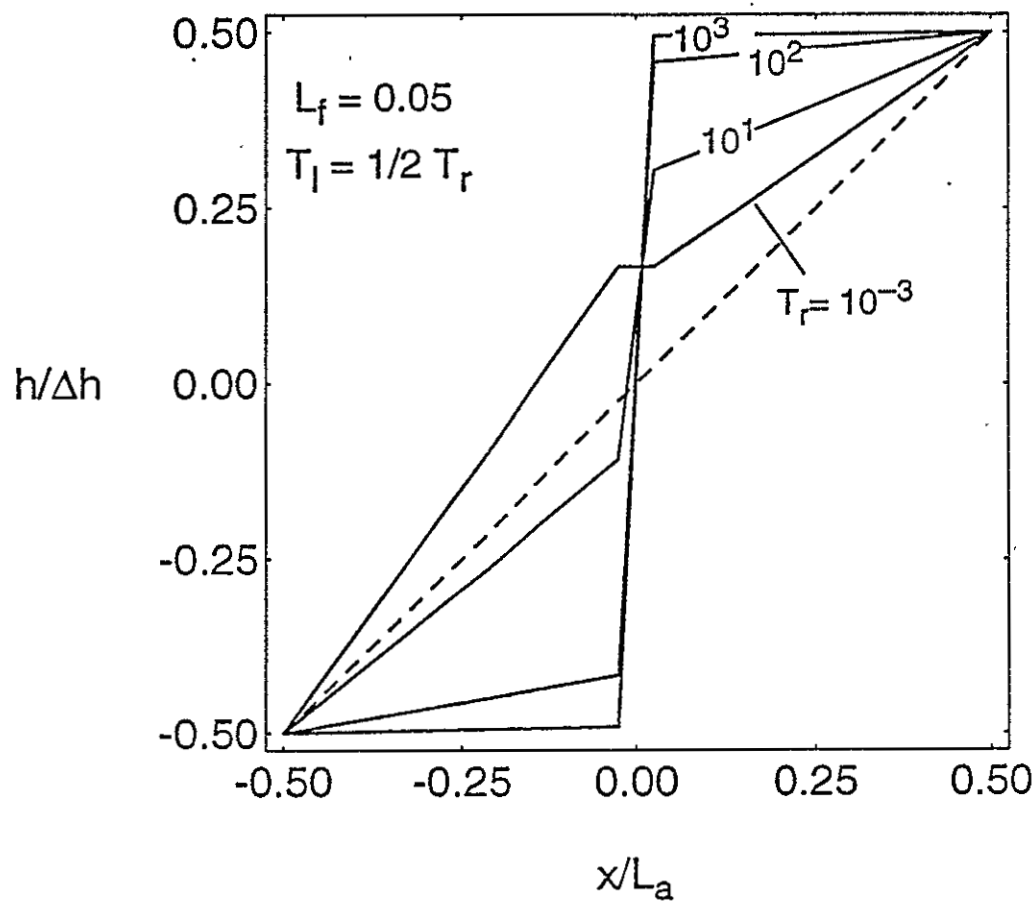
Figure 2-10. Head profiles across a fault juxtaposing two aquifers of unequal transmissivity, with the higher transmissivity aquifer up-gradient from the fault. Fault zone width is $L_f = 0.05$. In this example, the up-gradient aquifer has twice the transmissivity of the down-gradient aquifer. The dashed line indicates the unperturbed head profile that would exist in an unfaulted homogeneous aquifer.
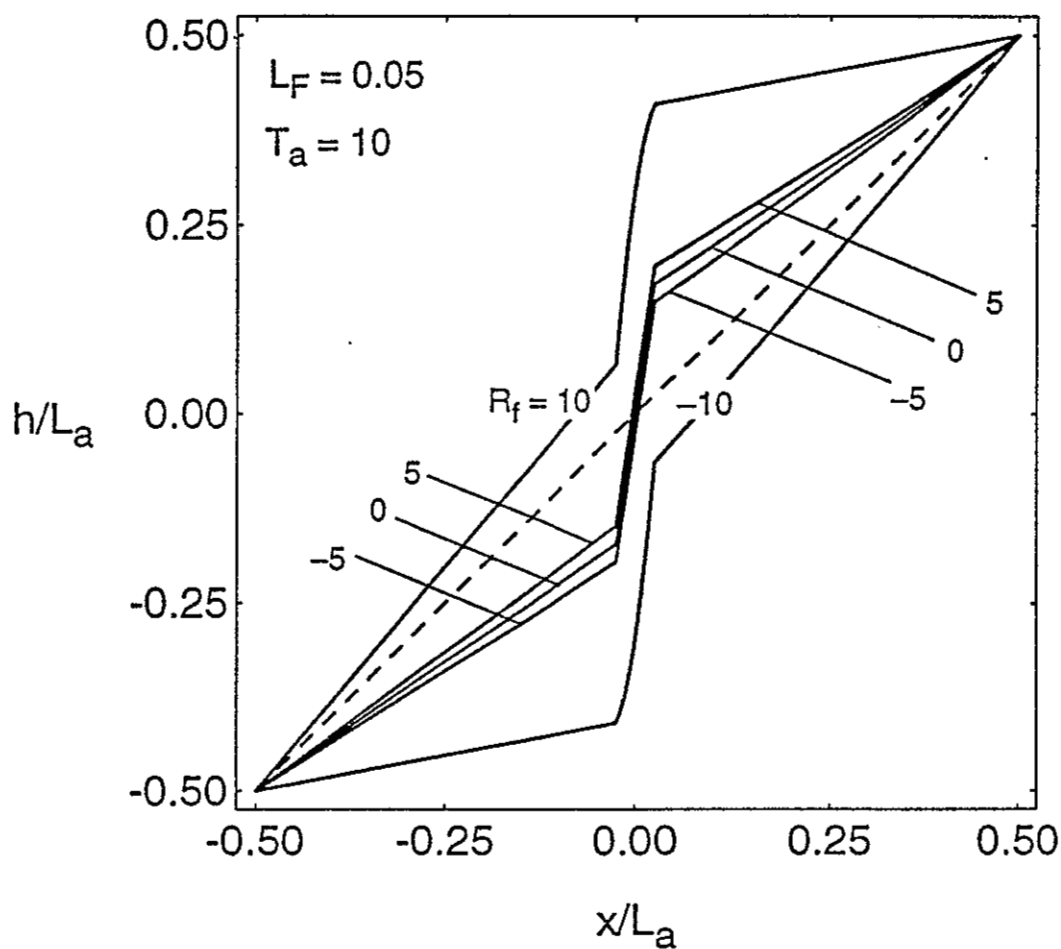
Figure 2-11. Head profiles across a low-transmissivity fault along which recharge or discharge occurs. Aquifers on either side of the fault are of equal transmissivity, in this case one order of magnitude more transmissive than the fault. Fault zone width is $L_f = 0.05$. Positive values of R_f indicate recharge from the fault to the aquifer, whereas negative values of R_f indicate discharge from the aquifer to the fault.
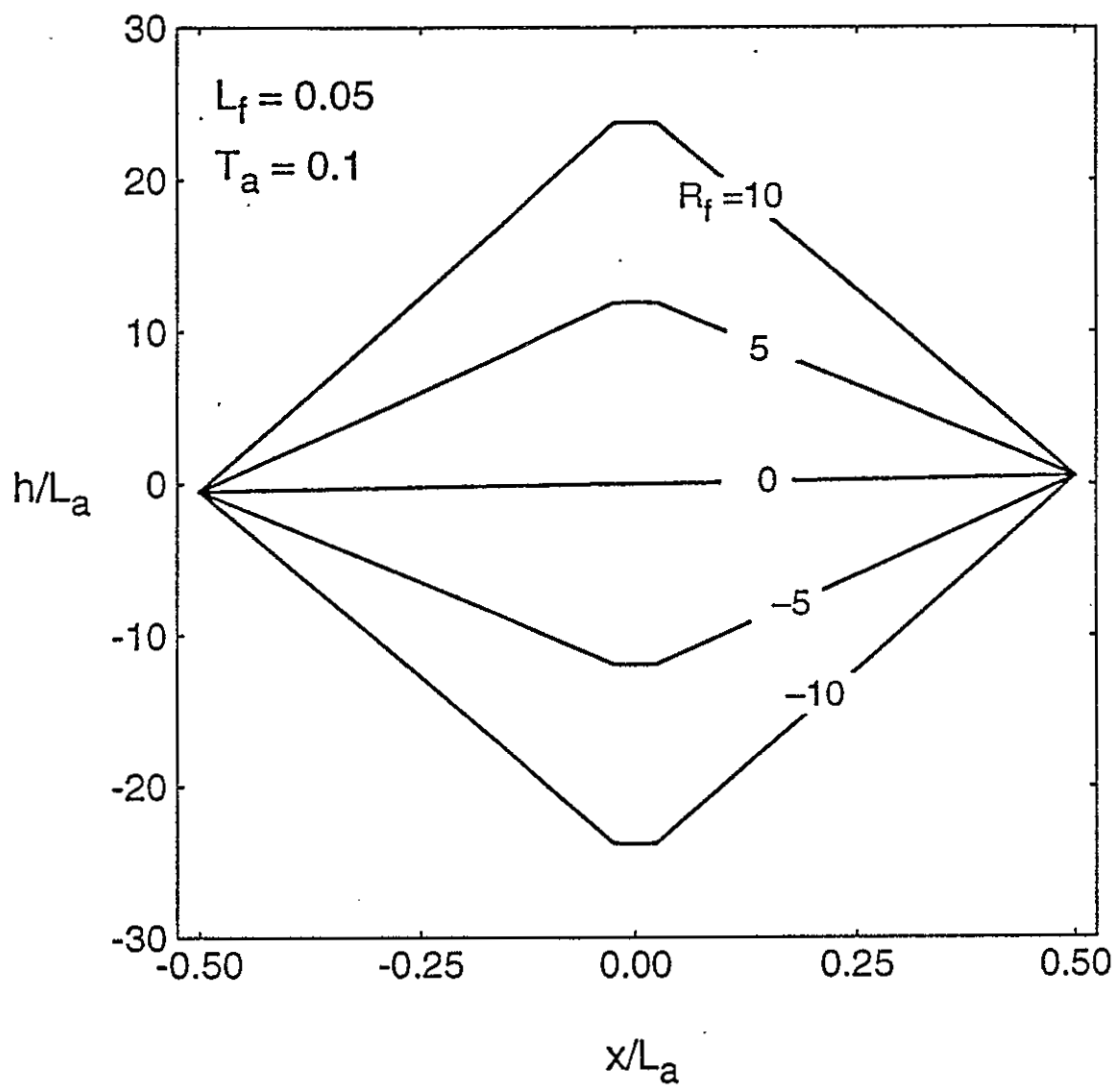
Figure 2-12. Head profiles across a high-transmissivity fault along which recharge or discharge occurs. Aquifers on either side of the fault are of equal transmissivity, in this case one order of magnitude less transmissive than the fault. Fault zone width is $L_f = 0.05$. Positive values of R_f indicate recharge from the fault to the aquifer, whereas negative values of R_f indicate discharge from the aquifer to the fault.
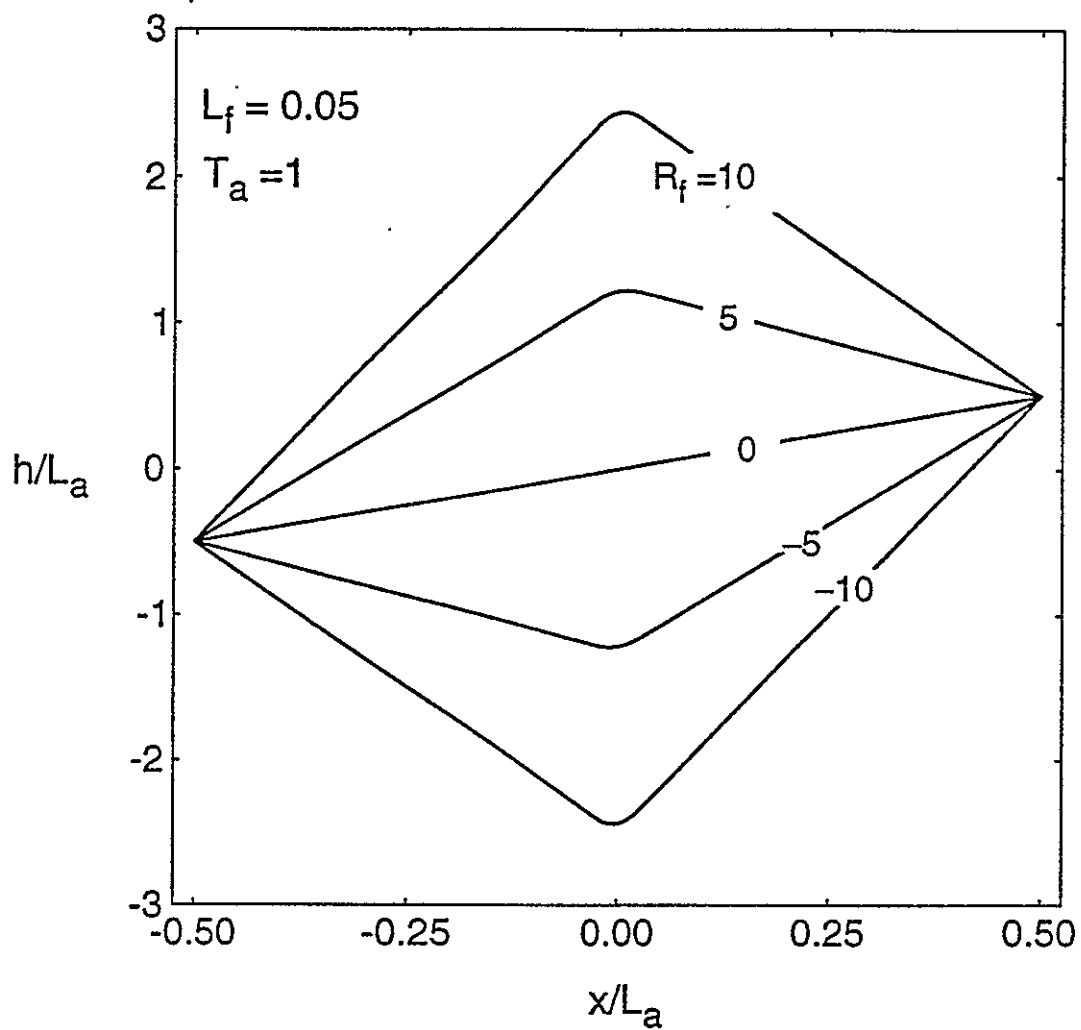
Figure 2-13. Head profiles across a fault along which recharge or discharge occurs, and which is equal in transmissivity to the adjacent aquifers. Fault zone width is $L_f = 0.05$. Positive values of R_f indicate recharge from the fault to the aquifer, whereas negative values of R_f indicate discharge from the aquifer to the fault.
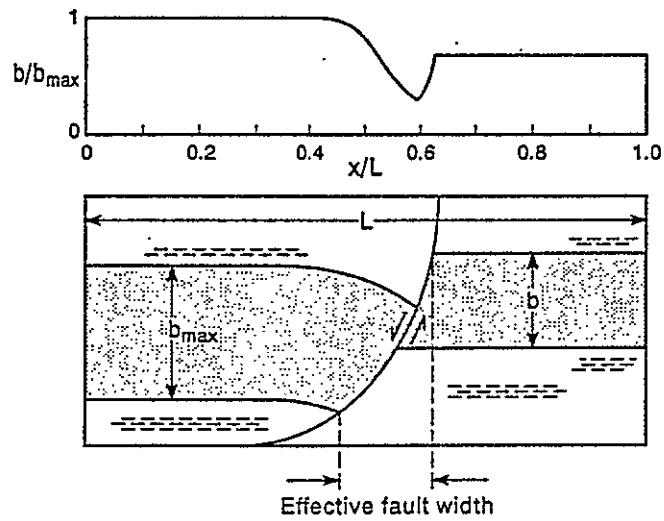
Figure 2-14. Changes in aquifer thickness in the vicinity of a non-vertical fault, illustrating the concept of effective fault width.
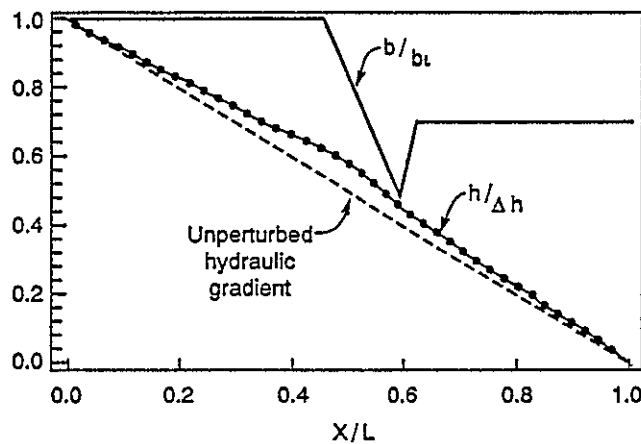
Figure 2-15. Results of a one-dimensional, steady-state flow simulation across a normal fault that has no hydraulic properties of its own but which thins the aquifer as illustrated. The b/b_l curve represents the dimensionless aquifer thickness and the $h/\Delta h$ curve represents vertically averaged hydraulic head. The dashed line represents the unperturbed hydraulic gradient that would exist in the absence of the fault and attendant changes in aquifer thickness.

Chapter 3

Patterns of Cementation Along the Sand Hill Fault, Albuquerque Basin, NM: Implications for Paleoflow Orientations and Mechanisms of Fault-Related Cementation

Peter Mozley and Laurel Goodwin
Department of Geoscience
New Mexico Tech, Socorro, NM 87801

SUMMARY

This chapter has presented preliminary results of an ongoing study of fault-related cementation in the Albuquerque Basin are presented in this chapter. Faults can act as either conduits or barriers to fluid flow, and the behavior with respect to flow of an individual fault can change over time as the character of the faulted units changes (see review by Knipe, 1993, and Chapter 2). The behavior of faults as barriers or conduits is critical to assessments of the volume, distribution, and accessibility of hydrocarbon and groundwater resources. As a result, interest in the factors influencing fluid flow in and adjacent to faults has increased as these fluid resources have, at least locally, been depleted. Yet the influence of faults on fluid flow in sedimentary basins remains poorly understood.

Some faults in the Albuquerque Basin strongly affect regional patterns of groundwater flow (Thorn et al., 1993; Haneberg, 1995, this report). In some cases this appears to be due to low permeability of the fault zone itself, rather than transmissivity differences of rocks on either side of the fault (e.e., Hubbell Springs and Rio Puerco faults). A likely cause of the low permeability associated with these faults is selective calcite cementation of the fault zone, which is commonly observed in faults exposed at the surface (Hawley, pers. com., 1994). Controls on the cementation of normal faults in the basin are poorly understood. Unpublished data suggests that the cementation is mainly associated with older structures, but this hypothesis has not been systematically evaluated (Hawley, pers. com., 1994).

The Sand Hill fault west of Albuquerque has been selectively cemented by calcite in a - 15 cm to 6 m wide zone. The margins of cemented areas are locally characterized by elongate patterns of cementation that have a strong subvertical orientation at the study site. These elongate cements appear to have formed from flowing groundwater, with the elongation oriented parallel to the groundwater flow direction at the time of calcite precipitation; consequently, they may be useful in constraining models of groundwater flow associated with Albuquerque Basin faults. Selective cementation such as that seen in the Sand Hill fault zone has been observed to be a common feature of faults in this and many other structural basins in the Southwest. Moreover, this style of cementation is clearly capable of significantly affecting regional patterns of groundwater flow. Cementation of the Sand Hill fault may have occurred through a variety of mechanisms, including: initial preferential flow along the fault, membrane filtration effects, pressure changes along the fault, and upward migration of deep basinal or hydrothermal fluids. Of these, initial preferential flow membrane filtration effects, pressure changes along the fault,

and upward migration of deep basinal and/or hydrothermal fluids seem the most likely mechanisms.

RECOMMENDATIONS FOR FUTURE WORK

Further work is needed in order to use the orientation data to constrain models of groundwater flow associated with faults, and to produce a conceptual model of cement distribution that will be useful in establishing the effect of cementation itself on groundwater resources.

Orientation of flow features. Thus far the orientation of the flow features (i.e., elongate cemented zones) has only been measured in a few outcrops. The orientation of flow features should be measured in a large number of outcrops and on other faults in order to have a data-set sufficient to allow use in constraining groundwater flow models. In addition, the orientation of elongate concretions that occur in the rocks on either side of the Sand Hill fault should be measured in selected horizons at varying distances from the fault. If these concretions formed at the same time as the oriented fault cements, it may be possible to directly measure the influence of the fault on groundwater flow in adjacent units.

Mapping cemented fault zones. Although cemented faults are common features in the Albuquerque Basin (Hawley, 1994, pers. com.), the distribution of the cemented zones has not been systematically described. As a first step, a basin-wide map should be constructed in collaboration with John Hawley, geologist involved in ongoing detailed field investigations of fault zones. Once such a map has been constructed it may be possible to observe relationships between the degree of cementation and parameters such as fault age, orientation, amount of displacement, etc. In addition, selected portions of the cemented faults should be mapped at a small scale in order to determine the continuity of cemented zones. Currently it is not known whether cementation is continuous or discontinuous on a scale of kilometers. Such information is critical to determining the influence of the cementation on regional groundwater flow. Finally, small-scale deformation features should also be systematically measured and related to both cement distribution and the orientation of flow features.

Geochemical analysis. Additional geochemical data should be obtained for fault cements. Our current geochemical data is from a single outcrop of the Sand Hill fault. By obtaining data from a variety of outcrops and faults it will be possible to determine whether the chemical homogeneity observed thus far is representative of the cemented faults as a whole. This information will be important in understanding the role faults play in the basin-wide migration of groundwater. For example, if the data vary widely from outcrop to outcrop, this would imply that different faults or portions of the same fault tap quite different fluid sources.

Chapter 3

Patterns of Cementation Along the Sand Hill Fault, Albuquerque Basin, NM: Implications for Paleoflow Orientations and Mechanisms of Fault-Related Cementation

Peter Mozley and Laurel Goodwin
Department of Geoscience, New Mexico Tech, Socorro, NM 87801

Abstract. — The Sand Hill fault NW of Albuquerque has been selectively cemented by calcite in a ~15 cm to 6 m wide zone. The margins of cemented areas are locally characterized by elongate patterns of cementation that have a strong subvertical orientation at the study site. These elongate cements appear to have formed from flowing groundwater, with the elongation oriented parallel to the groundwater flow direction at the time of calcite precipitation; consequently, they may be useful in constraining models of groundwater flow associated with Albuquerque Basin faults. Selective cementation such as that seen in the Sand Hill fault zone is a common feature of faults in the Albuquerque Basin, and is capable of significantly affecting regional patterns of groundwater flow. Cementation of the Sand Hill fault may have occurred through a variety of mechanisms, including: initial preferential flow along the fault, membrane filtration effects, pressure changes along the fault, and upward migration of deep basinal or hydrothermal fluids. Of these, initial preferential flow and pressure changes along the fault seem the most likely mechanisms.

INTRODUCTION

Faults can act as either conduits or barriers to fluid flow, and the behavior with respect to flow of an individual fault can change over time as the character of the fault rocks changes (See review by Knipe, 1993). The behavior of faults as barriers or conduits is critical to assessments of the volume, distribution, and accessibility of hydrocarbon and groundwater resources. As a result, interest in the factors influencing fluid flow in and adjacent to faults has increased as these fluid resources have, at least locally, been depleted. Yet the influence of faults on fluid flow in sedimentary basins remains poorly understood.

Some faults in the Albuquerque Basin strongly affect regional patterns of groundwater flow (Thorn et al., 1993; Haneberg, 1994, this report). In some cases this appears to be due to low permeability of the fault zone itself, rather than transmissivity differences of rocks on either side of the fault (e.g., Hubbell Springs and Rio Puerco faults; Haneberg, 1994, this report). A likely cause of the low permeability associated with these faults is selective calcite cementation of the fault zone, which is commonly observed in faults exposed at the surface (Thorn et al., 1993; Haneberg, 1994, this report; Hawley, pers. com., 1994). Controls on the cementation of normal faults in the basin are poorly understood. Unpublished data suggests that the cementation is mainly associated with older structures, but this hypothesis has not been systematically evaluated (Hawley, pers. com., 1994).

A variety of approaches have been used to investigate the influence of faults on fluid flow, including: (1) examination of fault-related permeability changes in rocks (e.g., Pittman, 1981; Antonellini and Aydin, 1994), (2) geochemical and isotopic analyses of fault-related cements to determine the chemistry and temperature of fluids migrating along faults (e.g., Burley et al., 1989), (3) modeling of fluid flow within faults and adjacent rocks given varying geometries and permeabilities of faults and lithologic packages (e.g., Forster and Smith, 1988; Bernard et al., 1989; Haneberg, 1994, this report), examination of changes in head across faults in modern hydrologic systems (e.g., Titus, 1963; Maclay and Small, 1983; Kolm and Downey, 1994), and analysis of reservoir pressure data and gas-oil-water interface locations in hydrocarbon reservoirs (e.g., Smith, 1980; Harding and Tuminas, 1988). In all of these cases, however, a key constraint — the orientation of flow with respect to the faults — has been lacking. In this paper we describe elongate patterns of cementation along the Sand Hill fault, a Tertiary normal fault in the Albuquerque Basin. These elongate patterns appear to record the orientation of fluid flow at the time of cementation, and thus provide a means of directly measuring patterns of fault-related flow at the outcrop scale. Although the emphasis of this paper is the elongate cements, we also briefly discuss possible mechanisms of preferential cementation of the Sand Hill and similar faults elsewhere in the basin.

STUDY AREA

The Sand Hill fault is located in the Albuquerque Basin a few miles NW of

Albuquerque, New Mexico (Fig. 3-1). One of the major normal faults bounding the western margin of the Rio Grande rift, it separates sedimentary rocks of the Lower Santa Fe Group (middle Miocene to late Oligocene) from those of the Middle Santa Fe Group (middle to late Miocene; Hawley and Haase, 1992). The Lower and Middle Santa Fe Group in this area consist of synrift alluvial, eolian and playa lake deposits (Hawley and Haase, 1992). The base of the Lower Santa Fe Group is offset by approximately 600 m near the study site (Hawley and Haase, 1992).

The Sand Hill fault is located along an escarpment separating the Llano de Albuquerque on the east from the active Rio Puerco floodplain on the west. This escarpment is characterized by badlands topography, with exceptional exposure. The nearly vertical fault is easily followed for nearly 50 km, and has been inferred to extend for another 15 km where exposure is poor (Kelley, 1977). This contribution is based on preliminary study of ~1 km of lateral exposure of the Sand Hill fault.

MACROSCOPIC FEATURES

The fault zone ranges from ~15 cm to 6 m wide within the study area. The zone consists of a single slip plane over most of this region, but a mappable splay significantly widens the zone in one area. A concentration of deformation bands is evident adjacent to the main slip plane. These deformation bands — narrow zones of cataclasis and/or volume change which accommodate up to a few centimeters of slip — are similar to those described previously in fault zones in porous sandstone (see review by Antonellini and Aydin, 1994), though they are locally thicker (up to 1 cm wide in these partially consolidated sedimentary rocks, vs. 0.5 - 2 mm in porous sandstones). Down-dip to nearly down-dip slickenside striae are locally evident on the main slip plane. Locally, pebbles in the surrounding sedimentary rocks are rotated such that their long axes are parallel to slickenside striae. In some areas, bedding is destroyed and beds are 'mixed' within a zone 1-2 m wide adjacent to the main slip surface. The slip planes and deformation bands are consistently cemented with calcite. Along much of the fault trace, the rock between deformation bands and slip plane(s) is cemented also, and the rock of the hanging wall and footwall adjacent to the fault zone is locally cemented. Where strongly cemented, the fault zone forms a positive topographic feature — locally resembling a wall — due to preferential erosion of the surrounding friable. largely uncemented sedimentary rocks (Fig. 3-2a).

Cementation patterns within the fault zone are striking (Fig. 3-2). While the bulk of the zone is characterized by a relatively homogeneous distribution of cement, the margins are locally irregular due to heterogeneous cementation. Preferentially cemented areas typically form well oriented, elongate features, which are subvertical within the area studied. These oriented features can be subdivided into three main morphological categories: fingers, columns, and ribs (Fig. 3-2b). The fingers are elongate three-dimensional features that protrude from the main cement zone; the columns are similar to the fingers, but the upper portion of the columns also are attached to the main cement zone; the ribs are similar to the fingers, but one side is entirely attached to the main cement zone. These features range from a few millimeters to a few centimeters in width and up to ten centimeters in length, and length/width ratios are highly variable. The features share the same preferred orientation and commonly merge, indicating that they are genetically related.

ANALYTICAL METHODS

Following preliminary field study, four oriented samples were obtained from various parts of the cemented fault zone. The samples were selected from areas in which fingers, columns, and ribs, and/or deformational structures had been identified. Each sample was cut perpendicular and, where appropriate, parallel to features of interest. All thin sections were impregnated with blue-dyed epoxy and polished for transmitted light, microprobe, cathodoluminescence, and UV/blue fluorescence examination.

The bulk composition of the samples was determined by point counting (300 points/sample). A MAAS/Nuclide model ELM-3 Luminoscope (Department of Geoscience, New Mexico Tech) and a Nikon microscope equipped with a UV/blue-fluorescence unit (Petroleum Recovery Research Center, New Mexico Tech) were used to characterize zonation in the calcite cements. Microstructural analysis was completed with a standard petrographic microscope.

An electron microprobe (JEOL-733 Superprobe, Institute of Meteoritics, University of New Mexico) was used to determine the elemental composition of calcite cements and evaluate compositional variation. Standard operating conditions were: 20 nA sample current and 1 - 10 micron beam diameter. Sample totals for all reported values are 100 +/- 2 %.

Isotopic analyses were performed under the supervision of Dr. Andrew Campbell

in the Department of Geoscience's stable isotope laboratory. The laboratory is equipped with a Finnigan MAT Delta E isotope ratio mass spectrometer.

FAULT CEMENTS AND MICROSTRUCTURES

Mineralogical and Chemical Composition of Cement

The cemented sandstones associated with the fault classify as lithic arkoses and feldspathic litharenites (classification of Folk, 1974). The main fault cement is micritic and sparry calcite (28 to 59 % of the whole rock), although small amounts of authigenic chert are present in a few of the samples (0 to 4.6 %). The calcite is extremely pure, with only minor substitution of Mg, and to a lesser extent Fe, Sr, Na, and Mn (Table 3-1; Fig. 3-3). Although there are differences in composition within the calcite cements, these differences are small (< a few mol%; Table 3-1). Micritic clasts and probable limestone fragments are present in small amounts (0 to 3%). The micritic clasts may be caliche intraclasts which are present in the Middle Santa Fe Group rocks near the fault. Alternatively, some of these clasts could represent previously cemented portions of the fault that were reworked during fault slip.

A variety of techniques were used in an attempt to detect chemical zonation in the calcite cement. In transmitted light, small-scale zonation (zones a few tens of microns thick) can be observed in places. This zonation is entirely symmetrical, rather than elongate, even within the oriented cemented features. Examination of these regions using back-scattered electron (BSE) imaging with the electron microprobe detected lines of inclusions (probably fluids, as no mineral matter could be detected) within the calcite; thus the zonation is not caused by variation in elemental composition. Indeed, no compositional zonation could be detected using BSE imaging. Cathodoluminescence examination also revealed no compositional zonation, as the authigenic calcite is uniformly non-luminescent. Trace amounts of calcite are characterized by a strong orange luminescence, but this calcite appears to be detrital (portions of probable caliche intraclasts and limestone fragments). Examination of the thin sections under UV and blue light, however, revealed zonation characterized by minor changes in the fluorescence of the calcite. Although this was the best of the methods employed to detect zonation, the fluorescence is so weak, and the zones so indistinct that it was not useful in elucidating cement stratigraphy.

The isotopic composition of the fault cements does not vary greatly. $\delta^{18}O$ values

range from 22.72 to 24.00 ‰ SMOW and ^{13}C values range from -4.26 to - 3.53 ‰ PDB (Table 3-2). These values are similar to those from subsamples of a concretion located near the fault zone in the Zia Formation (Table 3-2).

Deformation Features

Microscopic deformation features are present in the slip planes and deformation bands (Fig. 3-4). These features include: 1) Rotated elongate sand grains. Elongate grains that are oriented parallel to bedding in undeformed regions have been rotated into parallelism with the slip direction within the main slip plane (Fig. 3-4a). Rotated grains occur locally within a narrow zone less than a centimeter from the main slip plane, and within and adjacent to the deformation band. 2) Disrupted bedding in which sedimentary layering has been destroyed. This occurs in irregular patches less than a centimeter from the main slip plane and within a more regular, tabular zone near the deformation band. 3) Extensive cataclasis has occurred within the deformation band, as evidenced by a significant reduction in grain size and an increase in angularity of clasts (Fig. 3-4b). Less significant cataclasis is evident immediately adjacent to the deformation band. Elongate fragments are oriented parallel to the slip direction.

The amount of cement present within these deformed zones does not differ significantly from that present in undeformed areas. Either porosity is not reduced within slip planes and deformation bands, despite grain re-organization and cataclasis, or a high pore fluid pressure is maintained within zones of deformation, or the intergranular area increased following deformation to accommodate displacive calcite precipitation.

Elongate Cemented Zones

Only the samples obtained from the slip surface and deformation band show microscopic evidence of deformation. Samples containing the oriented elongate features are petrographically and chemically indistinguishable from undeformed samples that do not contain the features. In fact, the oriented cements are locally elongate at right angles to sand grains imbricated parallel to bedding (Fig. 3-4c). We had anticipated that it would be possible to observe elongate patterns of zonation in the calcite cement of the oriented samples but, as mentioned previously, no significant zonation was observed.

DISCUSSION

Origin of Oriented Patterns of Cementation

A variety of possible explanations for the origin of oriented patterns of cementation within the Sand Hill fault zone are explored in this section. We conclude that these features originated through groundwater flow, and therefore record paleoflow directions within the fault zone.

Deformation

A deformational origin might first be assumed for elongate features oriented parallel to a major fault surface. A number of observations, however, indicate that the oriented fingers, columns, and ribs within the Sand Hill fault zone are not the result of deformation. First and foremost, these features locally cross-cut undisturbed, subhorizontal bedding preserved within the fault zone. As noted earlier, the subvertical features are oriented at right angles to the bedding planes. Further, while macroscopic and microscopic evidence of deformation is abundant within slip planes and deformation bands, no such evidence is associated with the elongate, oriented cements.

Cemented sandstone beds with similar, though horizontally oriented (parallel to bedding), features are present in the nearby Lower Santa Fe Group. It is conceivable that some of these cemented beds could have rotated into the plane of the fault during slip. However, this possibility can be ruled out for the following reasons: (1) As mentioned above, the features locally cut vertically across horizontal bedding. (2) Although tilted bedding is observed within and adjacent to the fault zone, dips are typically less that 30° and vertical beds are absent. (3) The features have a consistent subvertical orientation; it is unlikely that rotated beds would have a consistent orientation. (4) Many of the three-dimensional features are probably too delicate to survive rotation.

Weathering

Three-dimensional features may be produced through the differential weathering of carbonate-cemented material (e.g., alveolar and tearpants weathering). It is conceivable that features like the fingers, ribs, and columns described here could result from weathering. Two factors, however, argue that they did not:

(1) Surface textures created by weathering rarely show a consistent preferred orientation. The orientation of these features, however, is consistently subvertical within

the study area. While one might argue that such a preferred orientation reflects preferential dissolution of some type of compositional zonation in the cements, there is no evidence for such zonation.

(2) The fault is located in an arid environment, thus carbonate precipitation rather than dissolution is the dominant process in weathering horizons (for example, a stage III-IV caliche caps the Llano de Albuquerque at the top of the escarpment). Furthermore, calcite cemented sandstone beds and concretions elsewhere in the Santa Fe Group do not show similar subvertical features and there is no evidence for significant dissolution of either the beds or the concretions. Finally, carbonate nodules in nearby paleosols and the active caliche at the top of the escarpment show no evidence of dissolution.

Groundwater Flow

Perhaps the strongest argument in favor of the flow interpretation is the striking similarity of these features to oriented concretions and beds observed in other units and elsewhere in the Santa Fe Group (Fig. 3-5; Todd, 1903; Meschter, 1958; Jacob, 1973; Raiswell and White, 1978; Parsons, 1980; Johnson, 1989; McBride et al., 1994; Mozley et al., 1994, this report). These oriented concretions and beds are the product of preferential cementation parallel to the groundwater flow direction. Although the mechanism for the elongation has not been examined in detail, it has been suggested that they form under conditions in which precipitation is transport-limited, and transport of dissolved species to the site of precipitation is greater in a particular horizon or orientation (Raiswell and White, 1978; J. R. Boles, pers. com., 1993).

Implications for Fluid Flow Along Faults

The most logical explanation for these three-dimensional oriented features is that they are the product of subvertical groundwater flow along the fault. These features show the orientation of flow during their precipitation, but in the absence of supporting geochemical or petrographic evidence, cannot be used to determine flow direction (i.e., 'up' vs. 'down'). Knowledge of paleoflow orientation can greatly assist in determining the influence of faults on fluid flow, and can be used to constrain models of paleo-groundwater flow in sedimentary basins such as the Albuquerque Basin (e.g., Thorn et al., 1993; Person and Garven, 1994; Haneberg, 1994, this report). These models, in turn, can aid in the assessment of groundwater and petroleum resources.

Controls on Fault Cementation

Because calcite-cemented zones along faults may significantly influence fluid flow in the Albuquerque Basin, it is desirable to develop a conceptual model of the subsurface distribution of fault-related cements. In order to develop such a model it is necessary to understand the mechanism(s) responsible for the selective precipitation of calcite along certain faults. A variety of possible mechanisms are capable of causing such selective cementation, including: initial preferential flow along the fault, membrane filtration effects across the fault, pore-pressure changes associated with the fault, and migration of deep basinal or hydrothermal fluids along the fault. In this section we discuss and evaluate the likelihood of these possible mechanisms in the case of the Sand Hill fault.

Initial preferential flow. If a fault becomes a zone of preferential groundwater flow, then a greater volume of dissolved chemical species will be transported through the fault zone than through the surrounding rocks. If the rate of cementation in the unit is limited by the transport of dissolved species to the site of precipitation, then zones experiencing greater groundwater flow will become preferentially cemented. The preferential cementation of coarser, presumably more permeable, stratigraphic horizons throughout the Santa Fe Group (Mozley et al., 1994, this report) indicates that pre-cementation permeability has been a controlling factor in the Santa Fe Group as a whole, and consequently is a likely mechanism in the case of the cemented faults.

Membrane filtration effects. Fine-grained sedimentary materials can act as geological membranes which are capable of affecting pore-water chemistry in a variety of ways. Groundwater passing through a geological membrane will become enriched in dissolved constituents on the upstream side of a membrane and depleted on the downstream side (e.g., Siever et al., 1965; Fritz and Eady, 1985; Demir, 1988; Fritz and Whitworth, 1994). Thus calcite precipitation can be induced by locally creating conditions favorable for calcite precipitation (e.g., higher concentrations of $Ca^{++}_{(aq)}$ and/or $HCO_3^{-}_{(aq)}$) on the upstream side of a membrane (Mitsoyannis and Saravacos, 1977; Fritz and Eady, 1985). Most reported membrane effects have occurred with clay-sized materials, though it is possible to have significant effects with silt-sized materials as well (Young and Low, 1965).

Geological membranes may become associated with faults in two main ways: (1) juxtaposition of a membrane lithology against a non-membrane lithology, or (2) formation of a membrane by deformation and grain-size reduction within the fault zone itself. In the case of the Sand Hill fault, the first of these mechanisms can be ruled out immediately,

because cementation commonly occurs in the fault zone where permeable sandstones are present on both sides of the fault (i.e., areas where no membrane lithology is present). The second mechanism is more likely, as cataclasis has resulted in considerable grain-size reduction in the deformation bands, and may locally have created zones fine-grained enough to act as membranes. Morrow et al. (1984) studied clay-rich and clay-poor fault gouge, and detemined that hydraulic conductivity ranged over four orders of magnitude, from 10^{-13} to 10^{-9} cm/s. Clayey sediments with hydraulic conductivities in this range are effective membranes (Whitworth, 1994, pers. com.). However, cementation occurs on both sides of the deformation bands, and if the membrane mechanism was solely responsible for cementation, cementation should have occurred preferentially on one side of the membrane.

Pressure changes along the fault. A drop in pore pressure can result in precipitation of calcite, by locally reducing P_{CO_2}. A variety of scenarios are capable of resulting in a reduction in the pore pressure of groundwater flowing through a fault zone. For example, in an unconfined system, upward flowing groundwater will experience a decrease in hydrostatic pressure, and a consequent decrease in P_{CO_2}.

Migration of deep basinal or hydrothermal fluids. Upward migration of deep basinal or hydrothermal fluids along faults could result in preferential cementation of the fault zone, as such fluids are commonly enriched in dissolved species such as $Ca^{++}_{(aq)}$. The $d^{18}O$ values of the fault calcites are compatible with a wide variety of fluid types, depending on the temperature of precipitation. The calcites either precipitated from ^{18}O-depleted waters (-7 to -12 per mil SMOW) at low temperatures (10 to 40 °C), or from ^{18}O-enriched waters at higher temperatures (Fig. 3-5). The elemental composition of the calcite, however, suggests that enriched basinal brines or hydrothermal fluids were not involved in the precipitation of the calcite. The calcites are extremely pure, and are virtually identical in composition to normal groundwater cements elsewhere in the Santa Fe Group (see Mozley et al., 1994, this report). Precipitation from enriched solutions should result in considerable substitution of other cations for Ca in the calcite lattice (Viezer, 1983).

In summary, although some mechanisms seem more likely than others, the cause of preferential cementation along the Sand Hill fault remains uncertain. Further work is necessary in order to narrow the list of choices.

RECOMMENDATIONS FOR FURTHER WORK

This chapter has presented preliminary results of an ongoing study of fault-related cementation in the Albuquerque Basin. Further work is needed in order use the orientation data to constrain models of groundwater flow associated with faults, and to produce a conceptual model of cement distribution that will be useful in establishing the effect of cementation itself on groundwater resources.

Orientation of flow features. Thus far the orientation of the flow features (i.e., elongate cemented zones) has only been measured in a few outcrops. The orientation of flow features should be measured in a large number of outcrops and on other faults in order to have a data-set sufficient to allow use in constraining groundwater flow models. In addition, the orientation of elongate concretions that occur in the rocks on either side of the Sand Hill fault should be measured in selected horizons at varying distances from the fault. If these concretions formed at the same time as the oriented fault cements, it may be possible to directly measure the influence of the fault on groundwater flow in adjacent units.

Mapping cemented fault zones. Although cemented faults are common features in the Albuquerque Basin (Hawley, 1994, pers. com.), the distribution of the cemented zones has not been systematically described. As a first step, a basin-wide map should be constructed in collaboration with John Hawley, beginning by using his unpublished data. Once such a map has been constructed it may be possible to observe relationships between the degree of cementation and fault parameters such as age, orientation, amount of displacement, etc. In addition, selected portions of the cemented faults should be mapped at a small scale in order to determine the continuity of cemented zones. Currently it is not known whether cementation is continuous or discontinuous on a scale of kilometers. Such information is critical to determining the influence of the cementation on regional groundwater flow. Finally, small-scale deformation features should also be systematically measured and related to both cement distribution and the orientation of flow features.

Geochemical analysis. Additional geochemical data should be obtained for fault cements. Our current geochemical data is from a single outcrop of the Sand Hill fault. By obtaining data from a variety of outcrops and faults it will be possible to determine whether the chemical homogeneity observed thus far is representative of the cemented faults as a whole. This information will be important in understanding the role faults play in the basin-wide migration of groundwater. For example, if the data vary widely from outcrop

to outcrop, this would imply that different faults or portions of the same fault tap quite different fluid sources.

REFERENCES CITED

Antonellini, M. and Aydin, A., 1994, Effect of faulting on fluid flow in porous sandstones: petrophysical properties: American Association of Petroleum Geologists Bulletin, v. 78, p. 355-377.

Bernard, D., Danis, M. and Quintard, M., 1989, Effects of permeability anisotropy and throw on the transmissivity in the vicinity of a fault, in A. E. Beck, G. Garven and L. Stegena, eds., Hydrogeological Regimes and Their Subsurface Thermal Effects, American Geophysical Union Geophysical Monograph 47: p. 119-128.

Burley, S. D., Mullis, J. and Matter, A., 1989, Timing diagenesis in the Tartan Reservoir (UK North Sea): constraints from combined cathodoluminescence microscopy and fluid inclusion studies: Marine and Petroleum Geology, v. 6, p. 98-120.

Demir, I., 1988, Studies of smectite membrane behavior: Electrokinetic, osmotic, and isotopic fractionation processes at elevated pressures. Geochimica et Cosmochimica Acta, v 52, p. 727-737.

Forster, C. B. and Smith, L., 1988, Groundwater flow systems in mountainous terrain: 2 controlling factors: Water Resources Research, v. 24, p. 1011-1023.

Friedman, I. and O'Neil, J. R., 1977, Compilation of stable isotope fractionation factors of geochemical interest (Data of Geochemistry, Sixth Edition, Chapter KK): US Geol. Surv. Prof. Paper 440-KK, 12 p.

Fritz, S. J. and Eady, C. D., 1985, Hyperfiltration-induced precipitation of calcite: Geochimica et Cosmochimica Acta, v. 49, p. 761-768.

Fritz, S. J. and Whitworth, T. M., 1994, Hyperfiltration-induced fractionation of lithium isotopes: ramifications relating to representativeness of aquifer sampling: Water Resources Research, v. 30, p. 225-235.

Haneberg, W.C., 1994, Faults as hydrogeologic units in the Albuquerque Basin, in, W.C. Haneberg and J.W. Hawley , eds., Characterization of hydrogeologic units in the northern Albuquerque Basin, New Mexico Bureau of Mines and Mineral Resources Open-File Report 402-C.

Harding, T. P. and Tuminas, A. C., 1988, Interpretation of footwall (lowside) fault traps sealed by reverse faults and convergent wrench faults: American Association of Petroleum Geologists Bulletin, v. 72, p. 738-757.

Hawley, J. W. and Haase, C. S., 1992, Hydrogeologic framework of the northern Albuquerque Basin: New Mexico Bureau of Mines and Mineral Resources Open-File Report 387, variously paged.

Jacob, A. F., 1973, Elongate concretions as paleochannel indicators, Tongue River Formation (Paleocene), North Dakota: Geological Society of America Bulletin, v. 84, p. 2127-2132.

Johnson, M. R., 1989, Paleogeographic significance of oriented calcareous concretions in the Triassic Katberg Formation, South Africa: Journal of Sedimentary Petrology, v. 59, p. 1008-1010.

Kelley, V. C., 1977, Geology of the Albuquerque Basin, New Mexico: New Mexico Bureau of Mines and Mineral Resources Memoir, No. 33, 59 p.

Knipe, R. J., 1993, The influence of fault zone processes and diagenesis on fluid flow, *in* A. D. Horbury and A. G. Robinson, eds., Diagenesis and basin development: Tulsa, Oklahoma, American Association of Petroleum Geologists, AAPG Studies in Geology No. 36, p. 135-151.

Kolm, K. E. and Downey, J. S., 1994, Diverse flow patterns in the aquifers of the Amargosa Desert and vicinity, southern Nevada and California: Bulletin of the Association of Engineering Geologists, v. 31, p. 33-47.

Maclay, R. W. and Small, T. A., 1983, Hydrostratigraphic subdivisions and fault barriers of the Edwards aquifer, south-central Texas, U.S.A.: Journal of Hydrology, v. 156, p. 127-146.

McBride, E. F., Picard, M. D. and Folk, R. L., 1994, Oriented concretions, Ionian Coast, Italy: evidence of groundwater flow direction: Journal of Sedimentary Research, v. A64, p. 535-540.

Meschter, D. Y.. 1958, A study of concretions as applied to the geology of uranium deposits: U.S. Atomic Energy Commission Technical Memorandum Report TM-D-1-14, 10 p. (Available on microfiche from the U.S. Geological Survey, Denver.)

Mitsoyannis, E. and Saravacos, G. D., 1977, Precipitation of calcium carbonate on reverse osmosis membranes: Desalination, v. 21, 235-240.

Morrow. C. A.; Shi, L. Q., and Byerlee, J. D., 1984, Permeability of fault gouge under confining pressure and shear stress: Journal of Geophysical Research, v. 89, 3193-3200.

Mozley, P.S., Beckner, J., and Davis, J.M., 1994, Calcite cementation in the Santa Fe Group, Albuquerque Basin, New Mexico: implications for groundwater studies, in, W.C. Haneberg and J.W. Hawley , eds., Characterization of hydrogeologic units in the northern Albuquerque Basin, New Mexico Bureau of Mines and Mineral Resources Open-File Report 402-C, p. 5-1 - 5-22.

Parsons, M. W., 1980, Distribution and origin of elongate sandstone concretions, Bullion Creek and Slope Formations (Paleocene), Adams County, North Dakota [unpubl. MS dissert.]: University of North Dakota, Grand Forks, North Dakota, 133 p.

Person, M. and Garven, G., 1994, A sensitivity study of the driving forces on fluid flow during continental-rift basin evolution: Geological Society of America Bulletin, v. 106, p. 461-475.

Pittman, E. D., 1981, Effect of fault-related granulation on porosity and permeability of quartz sandstones, Simpson Group (Ordovician), Oklahoma: American Association of Petroleum Geologists Bulletin, v. 65, p. 2381-2387.

Raiswell, R. and White, N. J. M., 1978, Spatial aspects of concretionary growth in the Upper Lias of northeast England: Sedimentary Geology, v. 20, p. 291-300.

Smith, D. A., 1980, Sealing and nonsealing faults in Louisiana Gulf Coast salt basin: American Association of Petroleum Geologists Bulletin, v. 64, p. 145-172.

Thorn, C. R., McAda, D. P. and Kernodle, J. M., 1993, Geohydrologic framework and hydrologic conditions in the Albuquerque Basin, Central New Mexico: U.S. Geological Survey Water-Resources Investigations Report 93-4149, 106 p.

Titus, F. B., 1963, Geology and ground-water conditions in eastern Valencia County, New Mexico: New Mexico Bureau of Mines and Mineral Resources Ground-water Report No. 7, v. 113 p.

Todd, J. E., 1903, Concretions and their geological effects: Geological Society of America Bulletin, v. 14, p. 353-368.

Veizer, J., 1983, Chemical diagenesis of carbonates: theory and application of trace element technique, in M. A. Arthur, eds., stable isotopes in sedimentary geology: Society of Economic Paleontologists and Mineralogists Short Course Notes No. 10, p. 3-1 to 3-100.

Young, A. and Low, P. F., 1965, Osmosis in argillaceous rocks: American Association of Petroleum Geologists Bulletin, v. 49, 1004-1008.

Table 3-1. Composition of calcite in cemented portions of the Sand Hill fault and in an oriented concretion from the Zia Formation near the fault. Data is from electron microprobe analysis.

Sample	Point	FeCO$_3$	MnCO$_3$	MgCO$_3$	CaCO$_3$	SrCO$_3$	Na$_2$CO$_3$	Type
SH-2	2	0.00	0.00	1.03	98.95	0.02	0.00	Fault cement
SH-2	3	0.00	0.00	0.52	99.44	0.04	0.00	Fault cement
SH-2	4	0.00	0.00	0.38	99.59	0.03	0.00	Fault cement
SH-2	5	0.24	0.00	0.45	99.28	0.03	0.00	Fault cement
SH-2	7	0.04	0.00	0.84	99.03	0.03	0.07	Fault cement
SH-2	8	0.04	0.00	0.41	99.45	0.04	0.08	Fault cement
SH-3	1a	0.00	0.00	1.10	98.69	0.10	0.11	Fault cement
SH-3	2	0.07	0.00	0.86	98.91	0.08	0.09	Fault cement
SH-3	3	0.00	0.00	1.40	98.46	0.06	0.09	Fault cement
SH-3	4	0.00	0.00	1.11	98.71	0.06	0.12	Fault cement
SH-3	5	0.09	0.00	1.43	98.27	0.06	0.15	Fault cement
SH-3	6	0.05	0.00	0.51	99.31	0.05	0.07	Fault cement
SH-3	7	0.05	0.00	0.95	98.85	0.03	0.12	Fault cement
SH-3	8	0.06	0.00	1.25	98.49	0.04	0.17	Fault cement
SH-3	10	0.00	0.00	0.52	99.41	0.02	0.06	Fault cement
SH-3	10a	0.00	0.00	0.83	99.10	0.02	0.04	Fault cement
SH-4b	1	0.03	0.00	0.62	99.34	0.00	0.00	Fault cement
SH-4b	3	0.04	0.00	1.31	98.65	0.00	0.00	Fault cement
SH-4b	4	0.00	0.00	0.99	99.01	0.00	0.00	Fault cement
SH-4b	2b	0.04	0.00	0.83	99.10	0.03	0.00	Fault cement
SH-4b	5	0.00	0.00	1.32	98.61	0.02	0.06	Fault cement
SH-4b	6	0.08	0.00	0.97	98.95	0.00	0.00	Fault cement
SH-4c	1a	0.00	0.00	0.92	98.99	0.03	0.06	Fault cement
SH-4c	2	0.08	0.00	0.77	99.08	0.02	0.06	Fault cement
SH-4c	3	0.09	0.00	1.02	98.81	0.00	0.08	Fault cement
SH-4c	4	0.05	0.00	0.67	99.18	0.03	0.08	Fault cement
SH-4c	5	0.00	0.03	0.31	99.62	0.00	0.04	Fault cement
SH-4d	1	0.12	0.00	1.15	98.65	0.04	0.04	Fault cement
SH-4d	1a	0.00	0.02	0.86	99.04	0.03	0.06	Fault cement
SH-4d	2	0.06	0.00	0.82	99.09	0.04	0.00	Fault cement
SH-4d	3	0.00	0.00	0.70	99.29	0.02	0.00	Fault cement
SH-4d	4	0.00	0.00	1.00	98.93	0.03	0.04	Fault cement
SH-4d	5	0.00	0.00	0.65	99.29	0.01	0.04	Fault cement
SH-4d	6	0.05	0.00	0.77	99.16	0.03	0.00	Fault cement
SH-5a	2	0.00	0.00	0.24	99.64	0.04	0.08	Zia concretion
SH-5a	3	0.00	0.00	0.24	99.67	0.02	0.08	Zia concretion
SH-5a	4a	0.00	0.00	0.29	99.57	0.05	0.09	Zia concretion
SH-5a	6	0.00	0.00	0.31	99.57	0.02	0.10	Zia concretion
SH-5b	1	0.00	0.00	0.25	99.75	0.00	0.00	Zia concretion
SH-5b	2	0.00	0.00	0.25	99.75	0.00	0.00	Zia concretion
SH-5b	3	0.00	0.00	0.19	99.81	0.00	0.00	Zia concretion

Table 3-2. Isotopic composition of cemented portions of the Sand Hill fault and an oriented concretion from the Zia Formation near the fault.

Sample	$\delta^{13}C$ (PDB)	$\delta^{18}O$ (SMOW)	Type
SH-1X	-3.53	24.00	Fault cement
SH-1Y	-3.99	23.80	Fault cement
SH-2	-4.02	23.46	Fault cement
SH-3x	-4.26	23.14	Fault cement
SH-3y	-3.86	23.39	Fault cement
SH-4X	-3.49	23.98	Fault cement
SH-4Y	-4.01	22.72	Fault cement
SH-5X	-4.15	22.71	Zia concretion
SH-5Y	-4.16	22.62	Zia concretion
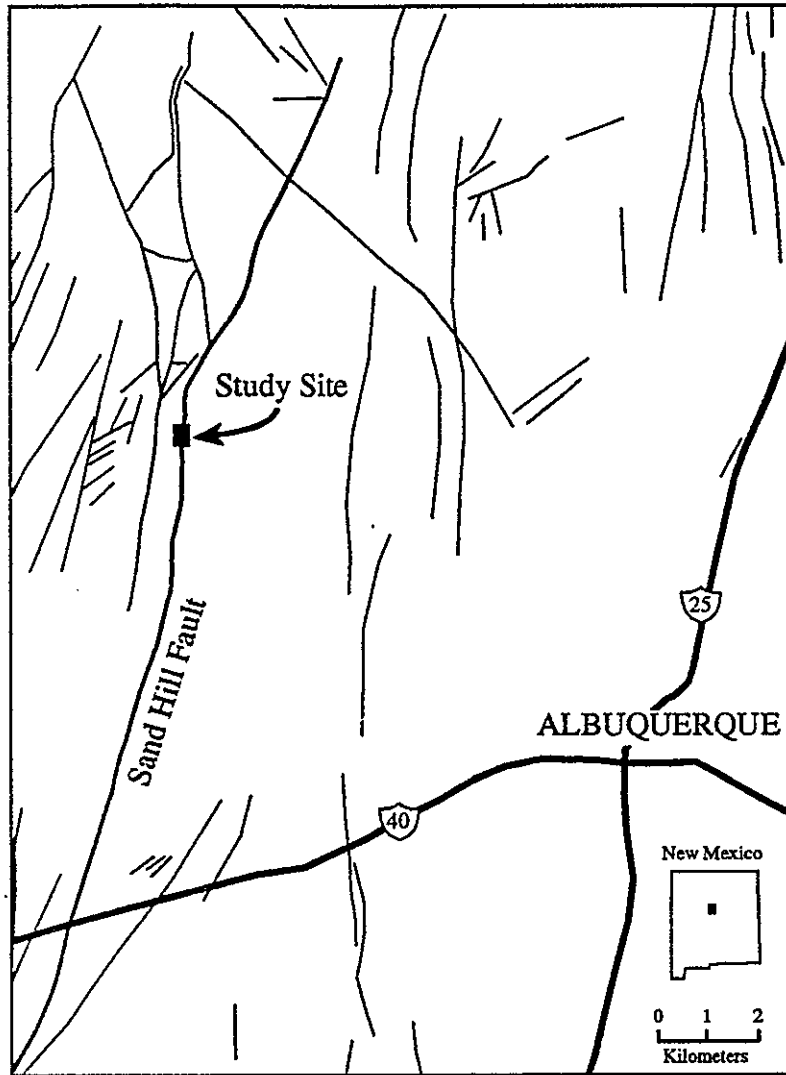
Figure 3-1. Index map showing the location of the Sand Hill fault and other faults in the NW Albuquerque Basin. Location of the study site is also shown.

Figure 3-2. Macroscopic features in Sand Hill fault zone. A: View facing west; person is nearly 2 m tall. Area where cementation is ~1.5 m in width; vertical cement fingers can be seen in upper part. B: View facing south. Sand Hill fault (SHF): only slip plane and adjacent deformation bands are cemented (light gray). Beds in hanging wall (left) are tilted to east near fault, consistent with east-side-down motion. Bedding (b) is disrupted adjacent to fault, within zone delineated by short dashed lines, and is homogeneously mixed in area marked (m); (a) marks younger alluvium. C: Vertical ribs and fingers. Note horizontal bedding, particularly in area of color change below lens cap (5 cm diameter). D: Vertical ribs and fingers along vertical surface. E: Vertical columns.
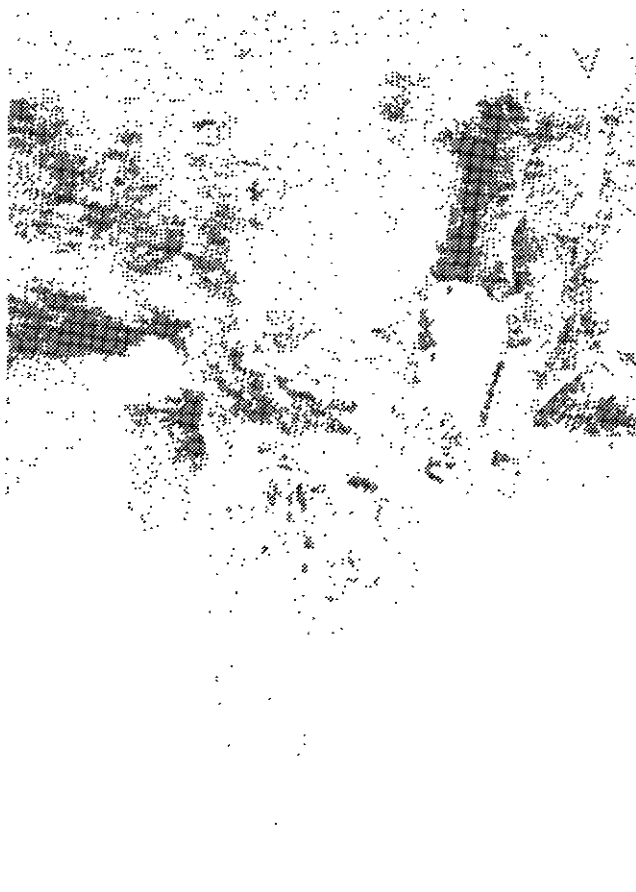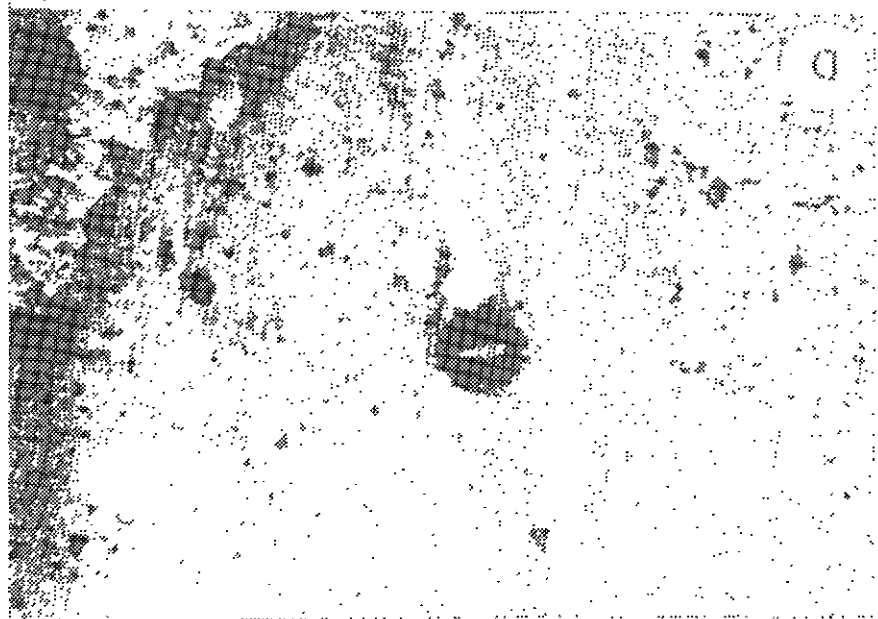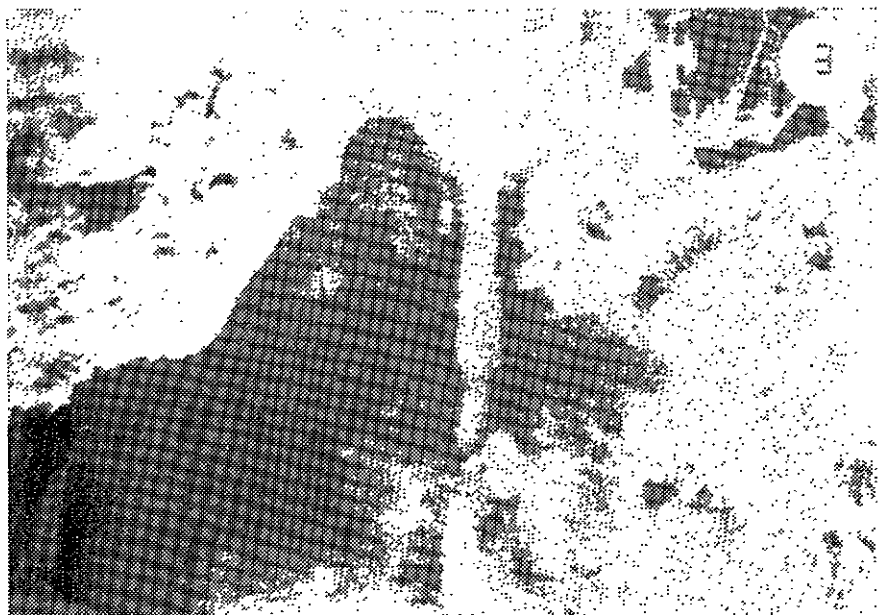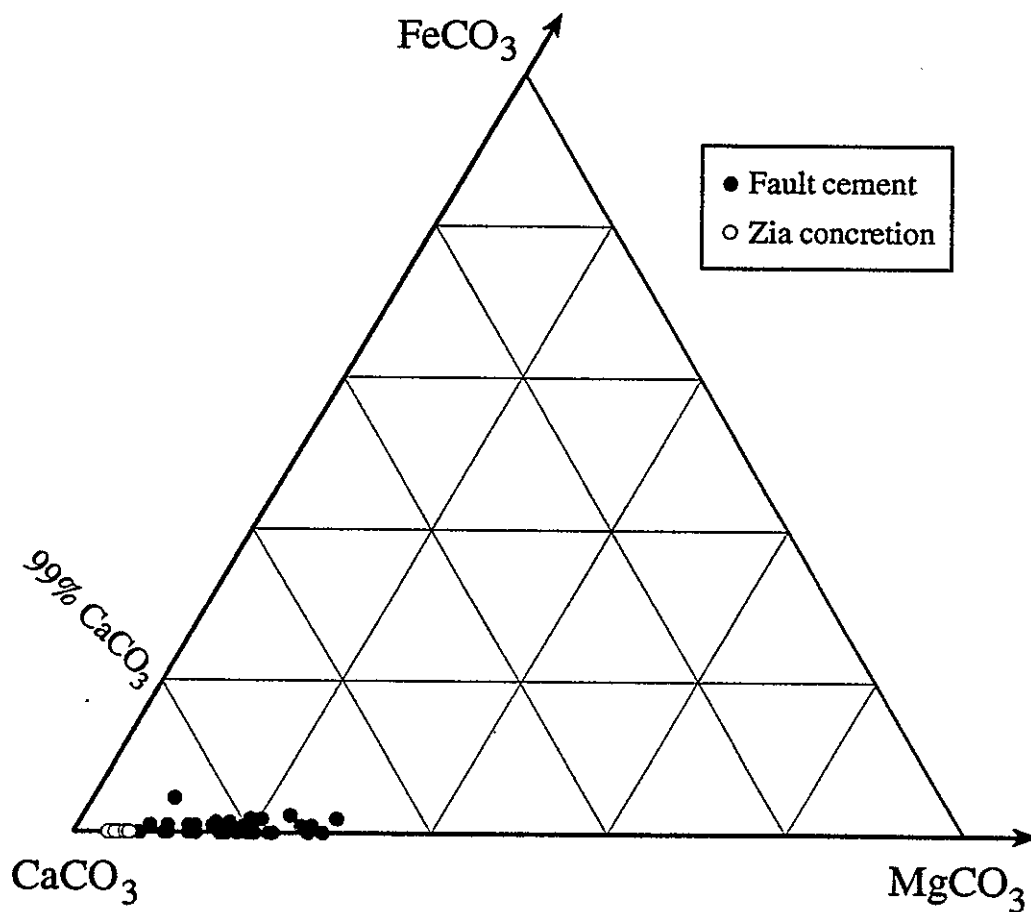
Figure 3-3. Ternary diagram showing composition of calcite in the cemented fault zone. The scale of the plot is at 95% $CaCO_3$.

Figure 3-4. Photomicrographs (plane light) of rocks from cemented areas in fault zone. Field of view is 4mm; each section is vertical. A: View to east of fabric in vertical finger which points upward. Elongate sand grains are aligned parallel to subhorizontal bedding. B: View to south. Disruption of subhorizontal, bedding-parallel alignment (left) by slip surface (S). Section is parallel to down-dip slickenside striae on S. Note rotation of elongate sand grains into S; sense of rotation records east-side-down motion. C: View to north of deformation band. Double-headed arrow indicates irregular boundary between zone of cataclasis (c) and zone of disrupted bedding where grains have not fractured. Elongate grains in both zones have been rotated parallel to slip direction (vertical). Farther from zone of cataclasis, elongate grains are aligned parallel to subhorizontal bedding.
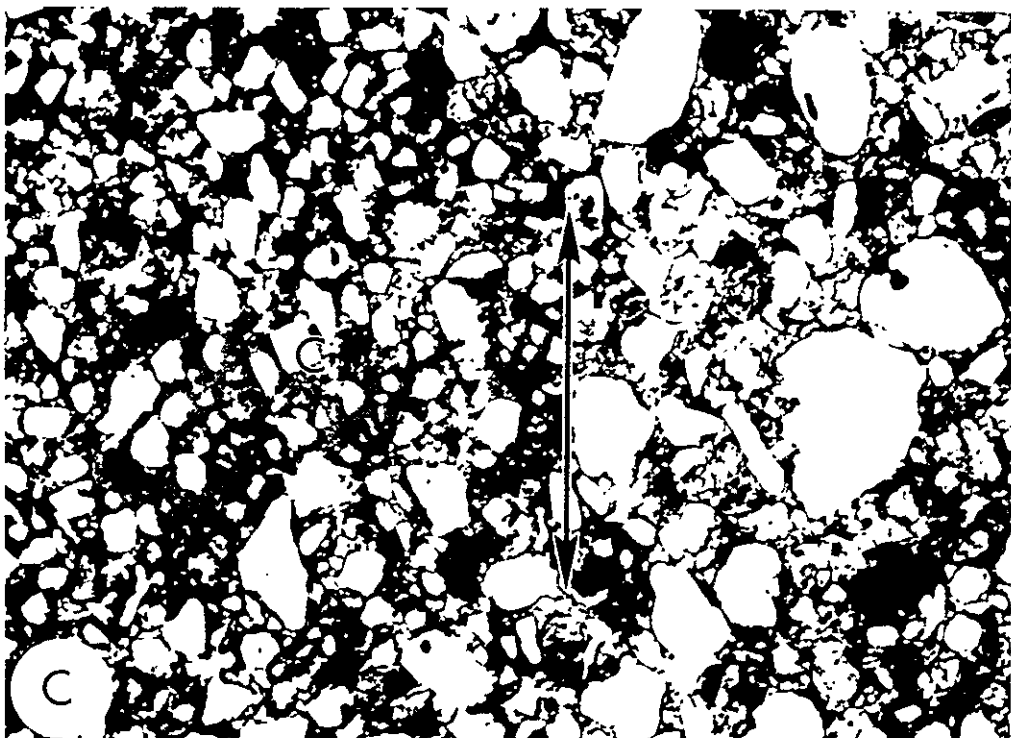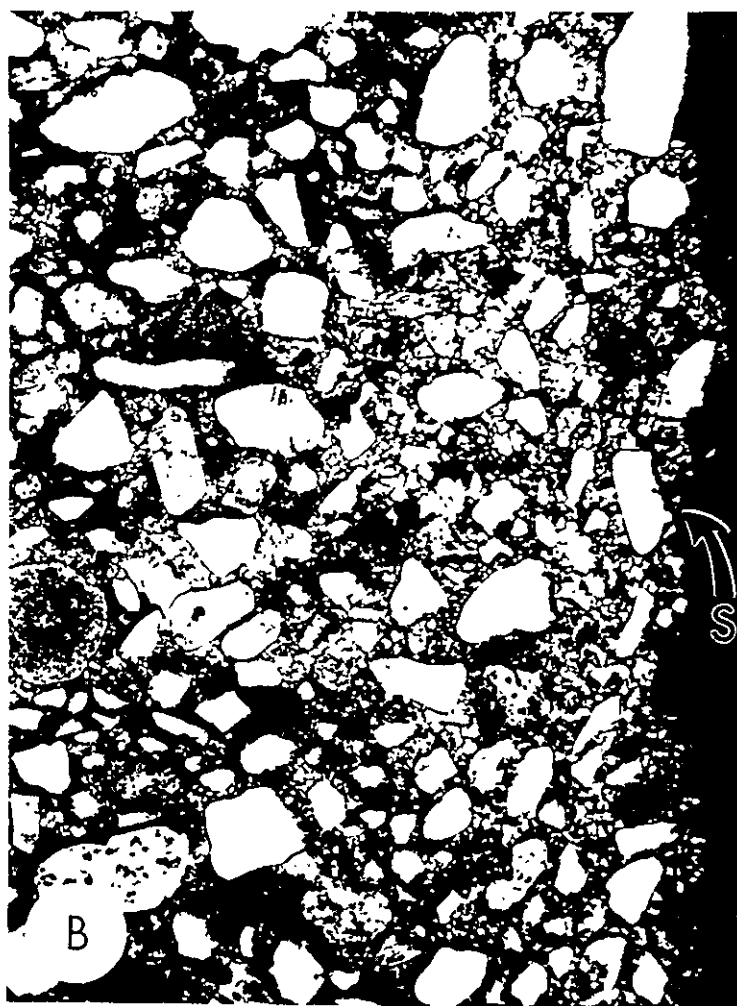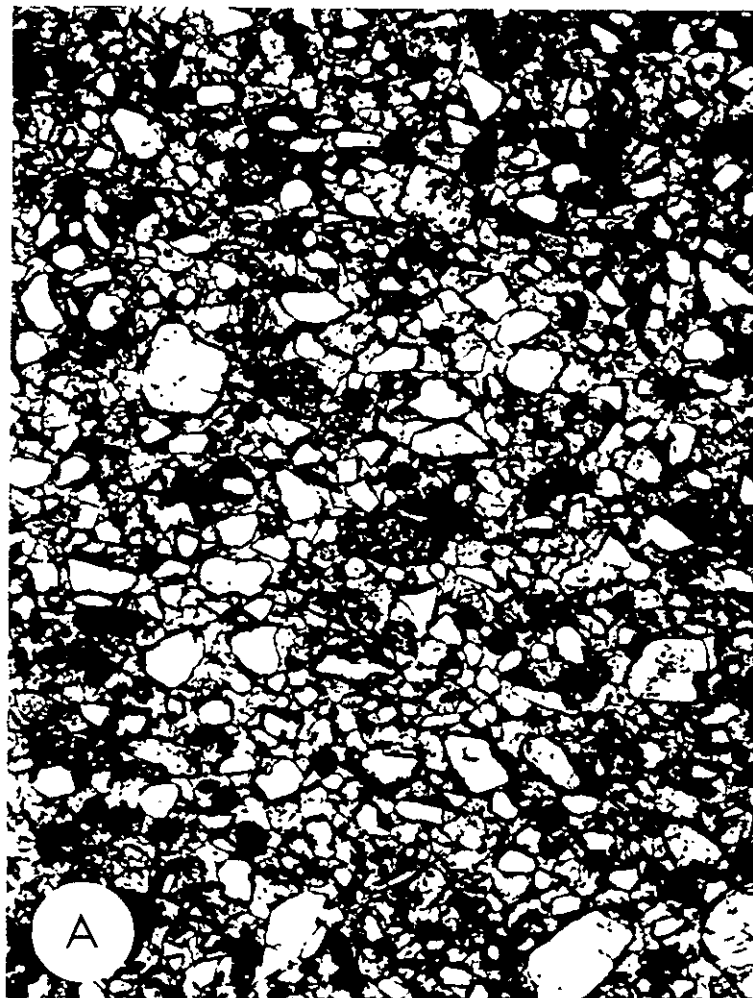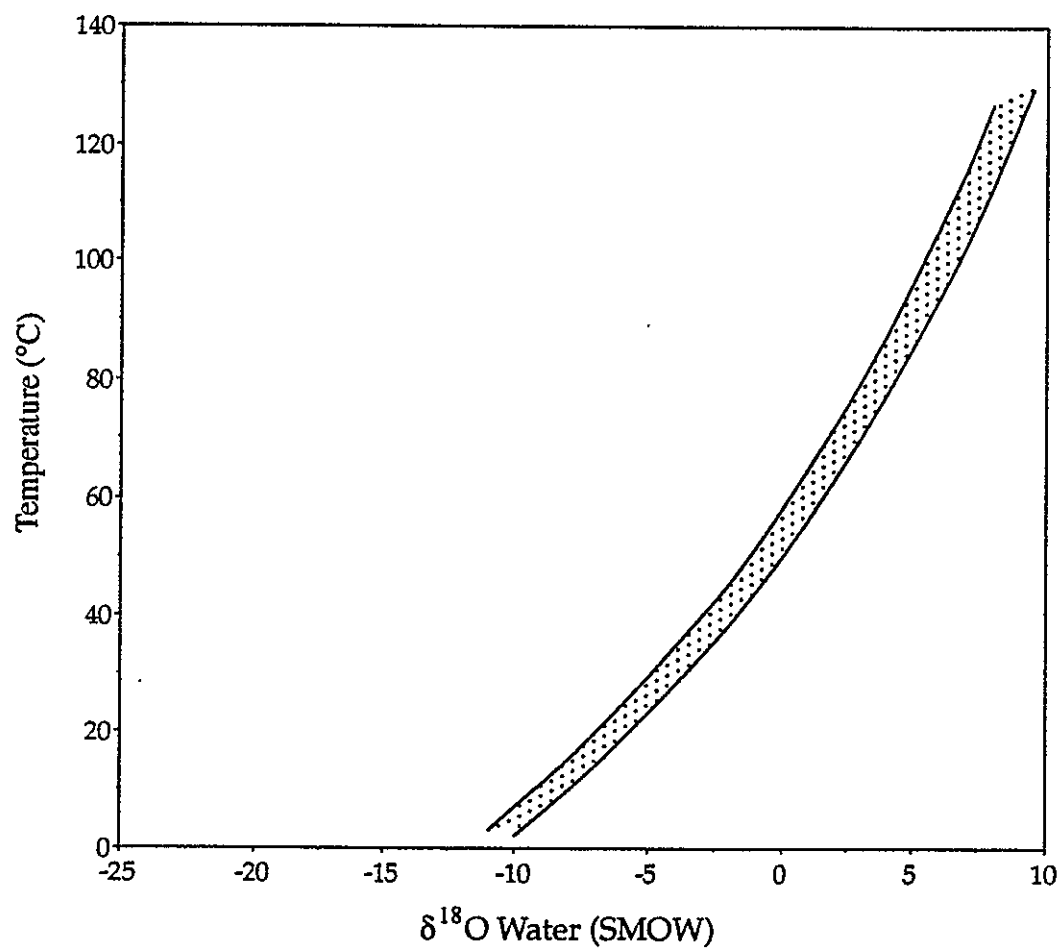
Figure 3-5. Possible temperatures and $\delta^{18}O$ values of water from which fault cements precipitated. Prepared using fractionation relationship of Friedman and O'Neil (1977) and data in Table 3-2.

Chapter 4

Compaction Curves and Virgin Specific Storage Estimates for Selected Albuquerque Basin Water Wells

William C. Haneberg
New Mexico Bureau of Mines and Mineral Resources, Socorro, NM 87801

PURPOSE AND SCOPE

The application of groundwater flow and transport models to real world problems requires quantitative knowledge of permeability and porosity characteristics of the aquifers being simulated. There are two basin purposes for the work described in this chapter:

1.   to quantify the spatial variability of porosity and permeability within the lithofacies that constitute the major aquifer zones in this and other major basins of the Rio Grande rift (originally defined by Hawley and Haase, and Hawley and Lozinsky, 1992: see Hawley, this volume)

2.   to determine whether these lithofacies represent legitimate hydrogeologic units with substantially different hydraulic characteristics. That is to say, can one quickly and inexpensively delineate useful hydrogeologic units on the basis of rotary drill cutting and geophysical log interpretation — which are the *de facto* standard data set for City of Albuquerque water supply wells — or are more detailed and expensive studies necessary?

The work described in the Chapter was undertaken in order to obtain first-order estimates of (1) the importance of sediment compaction in controlling porosity variability within basin-fill aquifer units, and (2) the compaction potential of the basin-fill aquifer system. To accomplish this, porosity logs were analyzed for five Albuquerque Basin water wells (Charles 5, Coronado 2, Gonzales 1, PSMW 19, and Zamora 1) shown in Figure 4-1[1]. These wells were selected because digital data files were either on-hand at or could be easily obtained by the New Mexico Bureau of Mines and Mineral Resources. Although digital log files are available for additional recent City wells, the expense of obtaining the files for more than an handful of wells was prohibitive. Scales of porosity variability were first examined by constructing porosity variograms on a lithofacies-by-lithofacies basis for the Charles 5. Athy- and Dickinson-type porosity curves were then fitted to geophysical log density porosity data sets. Depth-averaged virgin specific storage and specific compaction estimates were calculated using methods developed by Helm (1984). Finally the potential for land subsidence as a consequence of upper Santa Fe Group compaction is discussed in light of both the quantitative estimates made in the Chapter and the Cenozoic geomorphic history of the Albuquerque area.

---

[1]Figures and tables are located at the end of this Chapter.

CONCLUSIONS

Compaction curves fitted to geophysical log porosity data for the five water wells selected to this study show that depth-porosity relationships for upper Santa Fe Group sediments follow trends similar to those in other basins. Goodness-of-fit values were higher for Dickinson-type compaction curves than for Athy-type compaction curves in four of the five data sets examined, and suggest that compaction effects may account for 10% to 50% of the observed variability of porosity. The remainder is attributed to stratigraphic variability. Depth-averaged virgin specific storage values, calculated using Helm's method, range from about 2×10^{-4} to $5 \times 10^{-4} \text{m}^{-1}$. Specific compaction estimates, calculated by assuming that the effective aquifer thickness is nearly the same as a typical City well screen length of approximately 200 m, ranged from 0.02 to 0.10 m/m. The absence of widespread subsidence in the basin suggests that Santa Fe Group sediments in the Albuquerque Basin, like those in the El Paso area, are overconsolidated; thus, widespread land subsidence caused by the dewatering of upper Santa Fe Group aquifers should not become a significant problem until the preconsolidation stress is exceeded. Geomorphic evidence suggests that the overconsolidation is a consequence of the Pleistocene incision of the Rio Grande valley, which produced about 100 m of topographic relief and an estimated preconsolidation stress on the order of 1000 kPa (approximately 100 m drawdown). Collection and consolidation testing of undisturbed samples from representative clayey zones within the aquifer system will be necessary to more accurately assess subsidence potential and the aquifer preconsolidation stress.

Chapter 4

Compaction Curves and Virgin Specific Storage Estimates for Selected Albuquerque Basin Water Wells

William C. Haneberg
New Mexico Bureau of Mines and Mineral Resources, Socorro

Abstract.— Compaction curves fitted to geophysical log porosity data for five water wells in the Albuquerque metropolitan area show that depth-porosity relationships for upper Santa Fe Group sediments follow trends similar to those in other basins. Goodness-of-fit values were higher for Dickinson-type compaction curves than for Athy-type compaction curves in four of the five data sets examined, and suggest that compaction effects may account for 10% to 50% of the observed variability of porosity. The remainder is attributed to stratigraphic variability. Depth-averaged virgin specific storage values, calculated using Helm's method, range from about 2×10^{-4} to $5 \times 10^{-4} m^{-1}$. Specific compaction estimates, calculated by assuming that the effective aquifer thickness is nearly the same as a typical City well screen length of approximately 200 m, ranged from 0.02 to 0.10 m/m. The absence of widespread subsidence in the basin suggests that Santa Fe Group sediments in the Albuquerque Basin, like those in the El Paso area, are overconsolidated; thus, widespread land subsidence caused by the dewatering of upper Santa Fe Group aquifers should not become a significant problem until the preconsolidation stress is exceeded. Geomorphic evidence suggests that the overconsolidation is a consequence of the Pleistocene incision of the Rio Grande valley. which produced about 100 m of topographic relief and an estimated preconsolidation stress on the order of 1000 kPa (approximately 100 m drawdown). Collection and consolidation testing of undisturbed samples from representative clayey zones within the aquifer system will be necessary to more accurately assess subsidence potential and the aquifer preconsolidation stress.

INTRODUCTION

Hawley and Haase (1992) noted that geophysical logs from Albuquerque Basin water wells typically show a systematic decrease in porosity with depth. This relationship, which is not unique to the Albuquerque Basin, is generally believed to result from the compaction of sediments as they are buried and subjected to increasing lithostatic stresses. Athy (1930), Dickinson (1953), Baldwin and Butler (1985), and others have quantified depth-porosity relationships using logarithmic or exponential compaction curves for various basins. More than half of the sediment compaction predicted by generic

compaction curves occurs within 100 m of the surface, and about two-thirds of the sediment compaction occurs within 500 m of the surface (Haneberg, 1988).

The shallow depths of basin-fill aquifer systems— such as the upper Santa Fe Group in the Albuquerque area— make them especially susceptible to compaction. There may be, for example, significant changes in porosity and storage between the top and the bottom of a thick aquifer. For the same reason. porosity measurements obtained from outcrop samples at the surface may seriously overestimate porosity values at depth. Accurate assessment of the volume of groundwater available in a basin therefore requires some knowledge of depth-porosity relationships, which can be provided by compaction curves. Compaction curves are also important because they are, in essence, stress-strain curves that allow the hydrogeologist to predict the effects of groundwater overdraft by examining the effects of increasing effective stress on sediment compaction and, consequently, land subsidence at the Earth's surface. This is possible because the increase in lithostatic stress with depth is mechanically equivalent to the increase in effective stress caused by a decrease in hydraulic head (or, more specifically, pore water pressure). Predictions of aquifer system compaction potential are important because they provide some basis for including the economic costs of subsidence-induced infrastructure damage in groundwater development strategies.

Purpose and Scope

The work described in this Chapter was undertaken in order to obtain first-order estimates of (1) the importance of sediment compaction in controlling porosity variability within basin-fill aquifer units and (2) the compaction potential of the basin-fill aquifer system. To accomplish this, porosity logs were analyzed for five Albuquerque Basin water wells (Charles 5, Coronado 2, Gonzales 1, PSMW 19, and Zamora 1) shown in Figure 4-1[1]. These wells were selected because digital data files were either on-hand at or could be easily obtained by the New Mexico Bureau of Mines and Mineral Resources. Although digital log files are available for additional recent City wells, the expense of obtaining the files for more than a handful of wells was prohibitive. Scales of porosity variability were first examined by constructing porosity variograms on a lithofacies-by-lithofacies basis for the Charles 5. Athy- and Dickinson-type porosity curves were then fitted to geophysical log density porosity data sets. Depth-averaged virgin specific storage and specific compaction estimates were calculated using methods developed by Helm (1984). Finally, the potential for land subsidence as a consequence of upper Santa Fe

[1] Figures and tables are located at the end of this Chapter, following page 4-15.

Group compaction is discussed in light of both the quantitative estimates made in this Chapter and the Cenozoic geomorphic history of the Albuquerque area.

Hydrogeologic Setting

The geologic evolution and hydrogeologic setting of the Albuquerque Basin are discussed in detail by Hawley (Chapter 1, this report). The five wells analyzed in this Chapter are fortuitously distributed throughout the Albuquerque metropolitan area and, more importantly, were drilled in areas where Thorn et al. (1993) estimated that the horizontal hydraulic conductivity ranges from less than 7×10^{-5} m/s or 20 ft/day (Gonzales 1 and Zamora 1) to about 4×10^{-4} m/s or 100 ft/day (Charles 5). Horizontal hydraulic conductivity estimates for the Coronado 2 and PSMW 19 wells are not tabulated in Thorn et al. (1993), but they probably lie somewhere between the high and low values given above.

The five-fold range in average horizontal hydraulic conductivity observed among the wells analyzed in this Chapter can be understood in terms of the Hawley (Chapter 1, this volume; also see Hawley and Haase, 1992) lithofacies encountered in the wells. The Gonzales 1 well penetrates nearly equal net thicknesses of lithofacies Ib braided river gravels and lithofacies III basin-floor alluvial/playa/eolian deposits (see Hawley, this volume, Appendix F, for lithologic logs). The lithofacies Ib gravels, in particular, are pumice rich. The Zamora 1 penetrates alternating intervals of lithofacies Ib braided river gravels, lithofacies II basin-floor fluvial/eolian deposits, lithofacies IX basin-floor playa/alluvial flat deposits, and lithofacies III basin-floor alluvial/playa/eolian deposits. The upper portion of the Charles 5, in contrast, penetrates lithofacies Ib braided river gravels intermixed with only minor amounts of lithofacies III basin-floor alluvial/playa/eolian deposits, and lies within an elongated zone of high-conductivity axial river gravels deposited by the ancestral Rio Grande (Thorn et al., 1993).

Components and Magnitudes of Specifc Storage

Specific storage is the volume of water released from storage per volume of aquifer per unit of drawdown, and has units of reciprocal length (m^{-1} in this study). Specific storage is related to *storativity*, which is the product of specific storage and aquifer thickness. The storativity of a confined aquifer is somewhat analogous to the *specific yield* of an unconfined aquifer, except that the release of water from storage in a confined aquifer is accompanied by deformation of both the aquifer skeleton and the water, whereas water is released from storage in unconfined aquifers by gravity drainage with essentially no deformation.

Studies of the mechanical response of aquifer systems to pumping have shown that specific storage consists of three parts: a recoverable component associated with the elastic deformation of the aquifer, a recoverable component associated with the elastic expansion of water as it is brought from depth to the ground surface, and a non-recoverable or virgin component associated with plastic deformation of the aquifer. Virgin specific storage is typically one to two orders of magnitude greater than sum of the two elastic specific storage components.

Studies in basin-fill aquifer systems in Arizona and California have produced specific storage estimates for similar systems in the southwestern and western United States. Poland (1984) estimated specific storage components of 6.4×10^{-6} m^{-1} due to the elastic deformation of the aquifer skeleton, 1.9×10^{-5} m^{-1} due to the elastic expansion of water, and 6.7×10^{-4} m^{-1} due to inelastic deformation of San Joaquin Valley basin-fill sediments near Pixley, California. In this case, the ratio of virgin to elastic specific storage was approximately 80:1. Hanson (1989) estimated values of virgin specific storage ranging from 1.5×10^{-5} m^{-1} to 2.0×10^{-4} m^{-1} for basin-fill sediments at vertical extensometer sites in the Tucson Basin and Avra Valley, Arizona. Ratios of virgin to elastic specific storage therefore ranged from 2:1 to 27:1. Epstein (1987) used extensometer-derived elastic specific storage values of 8.0×10^{-6} m^{-1} to 1.0×10^{-5} m^{-1} and virgin specific storage values of 5.0×10^{-4} m^{-1} to 9.0×10^{-4} m^{-1} in computer simulations of land subsidence near Eloy, Arizona, yielding virgin to elastic specific storage ratios of 50:1 to 90:1.

Specific storage data for basin-fill sediments along the Rio Grande valley are limited. Kernodle (1992) was able to replicate observed land subsidence magnitudes in the El Paso, Texas area using an elastic specific storage value of 2.0×10^{-5} m^{-1} in a computer model. Because the observed subsidence magnitudes could be replicated using a specific storage value within the elastic range, Kernodle concluded that the El Paso aquifer has been overconsolidated. Vertical extensometer data collected during recent pumping tests in Albuquerque suggest that the depth-averaged elastic specific storage in the vicinity of the extensomter site is about 7×10^{-6} m^{-1}, and estimates derived using earth tide response at the same extensomter range from about 3.7×10^{-6} m^{-1} at a depth of 300 m to 5.6×10^{-6} m^{-1} at a depth of 50 m (C. Heywood, U.S. Geological Survey, personal communication, June 1, 1995). Haneberg and Freisen (1995) estimated subisdence near the center of the Mimbres Basin of southern New Mexico to be on the order of 0.5 m, compared to a water level decrease of approximately 35 m. These values yield a specific compaction estimate on the order of 1×10^{-2} and, assuming that the effective aquifer thickness is close to the typical agricultural well screen length of several tens of meters, an inelastic specific storage value on the order of 10^{-4} m^{-1}. This estimate is of the magnitude expected for virgin, rather than elastic,

specific storage, as one might expect for a basin that is characterized by land subsidence and earth fissures (Contaldo and Mueller, 1991).

SPATIAL VARIABILITY OF POROSITY IN THE CHARLES 5 WELL

Porosity curves for the selected Albuquerque Basin water wells are typically characterized by a 5 to 10% decrease in porosity with depth within the upper several hundred meters, which can be illustrated in different ways. Hawley and Haase (1992), for example, used visual examination of bulk density, sonic travel time, and various porosity geophysical logs as the basis of their conclusion that the systematic top-to-bottom decrease is a result of sediment compaction. Visual recognition of large-scale systematic changes or trends can be complicated, however, by the effects of small-scale stratigraphic variability. Small-scale varitions may occur on the scale of meters, decimeters, or centimeters; moreover, the magnitudes of small-scale variations may be as large as or even greater than the magnitude of change associated with the larger-scale trend upon which they are superimposed.

Data from the upper portion (110 - 549 m) of the Charles 5 well were used in the initial phase of this study to examine the nature of porosity variability within the upper Santa Fe Group aquifer system. The Charles 5 was a deep test hole with a total depth of 984 m (3230 ft), so only the upper portion of the well penetrating typical upper Santa Fe Group aquifer strata was analyzed in this part of the study. Log data were collected at 0.15 m (6 in) intervals, and only data from beneath the water table were used in the initial portion of the study.

The depths and combinations in which various lithofacies were encountered in the upper portion of the Charles 5 well, obtained from Hawley (this volume, Appendix F) are listed in Table 4-1. Characteristics of the individual lithofacies and sub-lithofacies are described below.

Lithofacies Ib.— River valley and basin-floor braided stream deposits. Sand and pebble gravel with lenses of silt and clay.

Lithofacies II.— Basin-floor fluvial and, locally, eolian deposits. Sand with lenses of pebbly sand, silt, and silty clay.

Lithofacies III.— Basin-floor alluvium and playa deposits with local eolian deposits. Interbedded sand, silt, and silty clay, with lenses of pebbly sand.

Lithofacies Vd.— Distal to medial piedmont slope alluvial fan deposits associated with large watersheds; allluvial fan distributary channels. Sand and gravel, with lenses of gravelly to nongravelly sand, silt, and clay.

Lithofacies Vf.— Distal to medial piedmont slope alluvial fan deposits associated with small watersheds; alluvial fan distributary channel and debris flow deposits. Gravelly sand, silt, and clay, with lenses of sand, gravel, and silty clay.

Lithofacies VII.— Distal to medial piedmont slope alluvial fan distributary channel and debris flow deposits. Indurated equivalent of Vd, Vf, and undifferentiated V.\

Basic Sample Statistics

A porosity cross-plot consisting of 2870 points shows that, although there is a general correlation between porosity values measured using the two different methods, density porosity tends to be slightly less than neutron porosity (Figure 4-2). There are also a number of points, from the top of the sampled interval, for which density porosity is greater than neutron porosity. Nonetheless, the cloud of points does plot sufficiently close to the 1:1 line to conclude that density porosity alone should be an adequate representative of the true porosity value for the aquifer system described in this Chapter. There is also some correlation between the 11-point variance and the 11-point mean of the porosity, with the highest means and variances obtained for the uppermost portion of the well penetrating lithofacies Ib (Figure 4-3).

Cumulative porosity distributions were calculated both for the entire upper portion of the Charles 5 well (110 - 549 m) as well as for each ocurrence of lithofacies encountered in the upper portion, and summized in a box plot (Figure 4-4). The two uppermost intervals, consisting of lithofacies Ib braided river gravels and mixed lithofacies Ib/III braided river gravels and basin-floor alluvial/playa/eolian deposits, have higher sample means and variances than do deeper intervals. Also, the shallower occurrence of lithofacies Ib has a significantly larger mean and variance than the deeper occurrence of lithofacies Ib. Cumulative distribution plots show that there can also be more difference between the porosity distributions from two occurrences of the same lithofacies than between occurences of different lithofacies (Figure 4-5) The same pattern occurs between the shallow and deep occurrences of mixed lithofacies Ib/III.

Scales of spatial variability can be investigated by calculating experimental variograms, which reflect the difference in magnitude between all possible pairs of spatially-correlated random variables separated by a specified distance or lag. The variogram statistic is (Isaaks and Srivastava, 1989)

$$\gamma(h) = \frac{1}{2N_h} \sum_{i,j|h_{ij}=h} (y_i - y_j)^2 \tag{1}$$

where $\gamma = \gamma(h)$ is the variogram statistic, h is the absolute value of the spatial separation or lag between each pair of data points, y is the spatially correlated random variable (*i.e.*, porosity in this study), and N_h is the number of data pairs separated by a lag of h. In contrast to statistics such as the sample mean and sample variance, which require relatively few data, variograms typically require several hundreds of data points. Features of an idealized variogram include the *sill*, the *range*, and the *nugget*. The sill is a plateau attained at some distance beyond which the variogram statistic is constant, and which is equal in magnitude to the sample variance. The range is the lag distance at which the sill is reached. A nugget is said to exist when the variogram has a non-zero value at a lag of $h = 0$, typically becausethere is spatial variability at a scale smaller than the lag increment used to construct the variogram from empirical data. Finally, a *hole effect* is said to exist if the variogram statistic fluctuates about the sill at large lag distances. The forms of real variograms, which can exhibit elaborate spatial correlation structures, commonly depart from the idealized example described above.

Empirical variograms were prepared in order to examine in detail the spatial variability of porosity both within each of the eight lithofacies intervals identified by Hawley (this volume, Appendix F and the undifferentiated upper portion of the well (Figures 4-6 and 4-7). Variogram lag intervals were 1.0 □ 0.5 m for the lithofacies intervals and 5.0 ± 2.5 m for the undifferentiated upper portion. The maximum lag distance calculated for each variogram was one-half the interval thickness, beyond which the number of data pairs and the quality of the variogram decreased sharply. Most of the empirical variograms show small ranges, typically on the order of a meter or so, as well as distinct hole effects that indicate cyclicity in the data. Nugget effects occurred for lithofacies Ib (110 -165 m), Ib/III (165 - 213 m), VI/VII 384 - 476 m , and the undifferentiated data set (110 - 549 m), implying the existence of correlation scales shorter than the minimum lag values of 1.0 and 5.0 m. Porosity variograms for lithofacies Ib/II (165 - 213 m), III (317 - 335 m), andII/Vd (335 - 384 m) do not reach a sill and may reflect underlying nonstationarity in the data set.

Model variograms were fitted to the empirical variograms by trial-and-error, beginning with a single exponential variogram of the form (Isaaks and Srivastava, 1989)

$$\gamma(h) = \sigma^2 \left[1 - \exp\left(-\frac{3h}{r} \right) \right] \tag{2}$$

or a single spherical variogram of the form

$$\gamma(h) = \sigma^2 \left[\frac{3h}{2r} - \frac{1}{2}\left(\frac{h}{r} \right)^3 \right] \tag{3}$$

where σ^2 is the sample variance, h is the lag distance, and r is the variogram range. No nuggets were allowed in the model variograms. If an empirical variogram could not be readily modeled using either of the two variograms shown above, a nested variogram was used beginning with two and, if necessary, proceeding to three levels of spatial correlation. In order to reduce the complexity of fitting nested variograms, it was arbitrarily decided that all components would be of the same type (*e.g.*, two exponential variograms could be nested, but not one exponential and one spherical). Each nested variogram component was weighted such that the weights summed to unity in order to insure that the sill would remain equal to the smaple variogram.

Fitted variogram types and ranges are summarized in Table 4-2, fitted variogram equations are given in Table 4-3 and the fitted variograms are plotted as solid lines in Figures 4-6 and 4-7. Six of the eight lithofacies variograms required nested models, with ranges from 0.5 to 25 m, whereas the undifferentiated variogram required a nested model with ranges of 2, 80, and 200 m. Thus, porosity in sediments penetrated by the upper portion of the Charles 5 varies at the bedding scale, the lithofacies scale, and the formation scale.

COMPACTION CURVES, VIRGIN SPECIFIC STORAGE, AND SPECIFIC COMPACTION

After the initial evaluation of porosity variability in the Charles 5 well was completed, compaction curves for the Charles 5, Coronado 2, Gonzales 1, PSMW 19, and Zamora 1 wells were estimated by fitting compaction curves to porosity data sets. Density porosity values were selected for the compaction curve analysis because they are common to virtually all Albuquerque Basin water well log suites, and porosity can be easily calculated if bulk density rather than denisty porosity is given on the log. Neutron porosity values, in contrast, are sometimes given in API units that cannot be converted directly to porosity. Sonic logs, from which porosity can also be calculated, are rare except for recent

wells. As illustrated in a previous section, there does not appear to be a significant difference between neutron and density porosity values for the upper portion of the Charles 5 well, and it is assumed that the same holds true for other Albuquerque Basin water wells. One would ideally like to corroborate geophysical log porosity estimates with core data; however, none were available for this project.

Model Compaction Curves

The two compaction curve models used were a negative exponential function of the form (Athy, 1930)

$$n = n_0 \exp\left(-z/z_.\right) \tag{4}$$

and a logarithmic function of the form (Dickinson, 1953)

$$n = n_0 + c \ln\left(z/z_.\right) \tag{5}$$

using theLevenberg-Marquardt algorithm for nonlinear curve fitting as implemented in the computer program *Mathematica* (Boyland et al., 1992; also see Press et al., 1992, p. 678-683 for a detailed description of the algorithm). In equations (4) and (5), n is porosity, z is depth, and n_0, c, and z_0 are empirical constants. Note. however, that n_0 and z_0 will have different values for each of the two compaction curve models. so that a value estimated by fitting one of the models to a data set cannot be inserted into the other model.

The empirical constants were constrained during the regressions so that $0 \le n_0 \le 1$, $500 \le z_0 \le 1500 \, \text{m}$, and $-1 \le c \le 0$. Data sets were read directly from ASCII files supplied by the geophysical logging contractors. and obviously spurious values near the top of the log were edited out by hand. Because density porosity values do not appear to change substantially between the saturated zone and the vadose zone, as many porosity values as possible were used for compaction curve fitting.

Calculation of Virgin Specific Storage

Assuming that the compressibility of water is negligible, that all deformation occurs as vertical compaction, and that all sediments are normally consolidated, virgin specific storage is related to porosity and the porosity gradient by (Helm, 1984)

$$S'_{skv} = -\frac{1}{(1-n)^2(G-1)}\frac{dn}{dz} \tag{6}$$

in which n is porosity, G is the specific gravity of the solids comprising the basin fill, and z is depth. This model implicitly assumes that the compacting sediments were originally homogeneous, with no large-scale changes in initial porosity or compressibility with depth. The average virgin specific storage between depths z_1 and z_2 can be found by integrating equation (6) as follows:

$$\overline{S}'_{skv} = \frac{1}{z_2-z_1}\int_{z_1}^{z_2} S'_{skv}\, dz \tag{7}$$

The dimensionless ratio of vertical aquifer compaction, sometimes referred to as specific compaction, to head decrease is given by (Helm, 1984)

$$\frac{\Delta b}{\Delta h} = (z_2-z_1)\,\overline{S}'_{skv} = \int_{z_1}^{z_2} S'_{skv}\, dz \tag{8}$$

where Δb is the decrease in aquifer thickness and Δh is the decrease in hydraulic head. Thus, the calculation of virgin specific storage and specific compaction is simple once a compaction curve is obtained for a given well.

Results

Fitted compaction curves are superimposed upon porosity logs for the five wells in Figures 4-8 through 4-12, and the best-fit compaction curve parameters are listed in Table 4-4.

Average virgin specific storage for all but one of the wells was on the order of 10^{-4} m^{-1}, and specific compaction ranged between 0.02 and 0.10. These values were averaged over the depth interval of 200 to 400 m, with the exception of the PSMW 19 results, which were averaged over the depth interval of 100 to 300 m because the well is only about 270 m deep. Most of the difference between the Athy and Dickinson curves occurs at very shallow depths, so the virgin specific storage and specific compaction estimates calculated using the two curves were similar. With the exception of the Gonzales 1 well, which is discussed below, goodness-of-fit (r^2) values ranged between 0.10 and 0.49, suggesting that the fitted compaction curves can account for about 10 to 50% of the observed porosity variability. These values are consistent with the weights assigned to the nested porosity variogram components for the undifferentiated upper portion of the Charles 5 well, in which the 80 and 200 m range components each accounted for 10% of the sill.

4-10

The only well for which problems were encountered was the Gonzales 1, for which porosity values were unusually high (in some cases approaching 1.0) above a depth of 125 m. The reason for these unusually high values is unclear, and the geophysical log for the nearby Gonzales 2 well gave no indication of similarly high values. Therefore, compaction curve fitting was performed using only porosity data collected between 125 and 550 m depth. Although the fitted Athy curve yielded reasonable but somewhat low values, the fitted Dickinson curve is very steep and yielded virgin specific storage and specific compaction values an order of magnitude smaller than the other wells. The fitted compaction curves for the Gonzales 1 were most likely affected by some combination of the absence of high porosity values at shallow depths and a systematic increase in porosity values at depths greater than 400 m.

DISCUSSION

Analysis of variograms constructed using porosity data from the Charles 5 geophysical logs shows that the porosity of the basin-fill sediments is spatially correlated in the vertical direction over scales ranging from decimeters to hundreds of meters. Nested or multi-component variograms were required to model the spatial correlation structure of porosity for six of the eight lithofacies intervals examined in this study, as well as for undifferentiated sediments penetrated by the upper portion of the Charles 5 well. Nested correlation structures imply that porosity in the upper Santa Fe Group is spatially correlated on several different scales (e.g., Gelhar, 1993). Small- to medium-scale variations in porosity, say those that occur over distances on the order one-half to ten meters, reflect differences in porosity among individual beds or architectural elements (Phillips and Wilson, 1989; Davis et al., 1993; Macfarlane et al., 1994). Large-scale variations, in this case those that occur over ranges of hundreds of meters or perhaps more, are inferred to be an effect of sediment compaction rather than a large scale stratigraphic changes; however, these changes may be difficult to discern because they contribute less to the total variability of porosity than do the small scale variations. For example, the modeled porosity variogram for the undifferentiated Charles 5 data set is weighted in such a manner that the 2 meter component contributes 80% of the variability whereas the 80 and 200 meter components each contribute 10% of the variability.

The inference of compaction-induced porosity variability is supported by three lines of evidence. First, similar systematic changes in porosity have been attributed to sediment compaction in many other basins (Athy, 1930; Dickinson, 1953; Baldwin and Butler, 1985), and it is unlikely that large scale stratigraphic variability in the Albuquerque Basin coincidentally follows the same pattern as compaction effects in other basins. Second, there is a correlation between porosity means and variances calculated on

a lithofacies-by-lithofacies basisfrom the Charles 5 data, and both the means and variances decrease with depth. One might expect more highly compacted (*i.e.*, more deeply buried) sediments to have smaller porosity means and variances than less highly (*i.e.*, less deeply buried) sediments. Third, lithofacies penetrated at shallow depths are more porous than occurrences of the same lithofacies penetrated at greater depths. In the Charles 5, for example, the shallow occurrence of lithofacies Ib is more porous than the deeper occurrence of lithofacies Ib.

Nonlinear fitting of Athy- and Dickinson-type compaction curves to porosity data sets from four wells in and around Albuquerque yielded virgin specific storage estimates on the order of 10^{-4} m^{-1} for depths of 200 to 400 m. These values are of the same magnitude as estimates obtained by others for other basin-fill aquifer systems in the western United States (*e.g.*, Poland, 1984; Epstein, 1987; Hanson, 1989). The geophysical logs for a fifth well, the Gonzales 1, contains unrealistically high porosity data for shallow depths and yields unusually small, and therefore unreliable, values. This illustrates the importance of collecting shallow porosity data to constraining compaction curve parameters. Specific compaction estimates for the same four wells ranged from 0.02 to 0.10, implying that long-term aquifer compaction may amount to as much as 10% of the water level decrease. The goodness-of-fit values obtained for the compaction curves suggest that compaction effects can account for 10% to 50% of the total porosity variability, which is in fair agreement with the value of 20% suggested by the nested variogram weights.

One of the most interesting results of this study is the finding that the Charles 5 well, which had the largest virgin specific storage estimate (that is to say, the greatest compaction potential), also has the highest average horizontal hydraulic conductivity. Unlike the other wells studied, the Charles 5 penetrates primarily lithofacies Ib river gravels, which one would not expect to be particularly compactible. One possible explanation is that the sample of four wells with reliable compaction curves is simply too small, and the calculation of the highest virgin specific storage value for the Charles 5 is a statistical fluke. Another possible explanation is that lithofacies Ib river gravels, which are pumice rich, are truly more compactible than the sediments penetrated by the other wells examined in this Chapter. Further analysis will be needed to discern between the two possibilities.

With the exception of isolated occurrences of subsidence and structural damage in the North Valley area, which are believed to have resulted from dewatering of the shallow alluvial aquifer and associated wetlands rather than the upper Santa Fe Group aquifer system (Kernodle, 1995), there is no convincing evidence of widespread land subsidence in the Albuquerque area despite heavy pumping and water level decreases that locally exceed 50 m (see Thorn et al., 1993 for water level decline maps). In

contrast, water level decreases of 35 m and less have produced widespread land subsidence and earth fissures in the Mimbres Basin south of Deming, New Mexico (Contaldo and Mueller, 1991; Haneberg and Friesen, 1995). The most likely explanation for the lack of subsidence in and around Albuquerque is that the upper Santa Fe Group aquifer system is overconsolidated, meaning that the aquifer system has in the past been subjected to greater lithostatic stress than it is being subjected to today. Holzer (1981) has shown that if an aquifer system has been overconsolidated, land subsidence is minimal until the reduction in effective confining stress brought about by groundwater overdraft exceeds the preconsolidation stress, which is the maximum stress to which the system has been subjected to in the past. Because the groundwater exerts an upward-directed buoyant force on the aquifer skeleton, a reduction in water level (and therefore pore water pressure) is mechanically equivalent to an increase the weight of the overlying sediments. Once the preconsolidation stress is exceeded, according to the data collected by Holzer (1981), land subsidence occurs rapidly.

The postulated overconsolidation of the upper Santa Fe Group aquifer system is probably a result of the Pleistocene incision of the Rio Grande valley, which produced geomorphic features such as the *Llano de Albuquerque*— a relic of the pre-incision basin floor— and stream terraces well above the current river level. The difference in elevation between the *Llano de Albuquerque* and the modern river level suggests that as much as 100 m of sediment may have been removed in some parts of the basin. Assuming that the pre-incision water table had the same relationship with the ground surface as did the Holocene pre-development water table, then, the preconsolidation stress for the upper Santa Fe Group aquifer system is should be equivalent to the pressure by a column of water equal in height to the inferred depth of incision (*i.e.*, a maximum of ~100 m H_2O or ~1000 kPa). Therefore, it would appear that there is little potential for widespread subsidence in the immediate future. Over the long term, however, there is a considerable potential for widespread land subsidence if drawdowns approach 100 m. It must be emphasized, however, that a preconoslidation stress of ~1000 kPa is based on subjective geomorphic criteria and is therefore highly speculative. More accurate estimates of the preconsolidation pressure, which are necessary to adequately assess the subsidence potential, can be obtained either by laboratory testing of samples or by continuing to withdraw groundwater and noting the amount of drawdown that is necessary to induce widespread land subsidence in the Albuquerque area.

RECOMMENDATIONS

The potential for aquifer system compaction and consequent land subsidence need to be analyzed in more depth and breadth. This can be accomplished by the purchase and analysis of additional digital geophysical log files for wells throughout the basin, culminating in the preparation of specific compaction

contour maps to delineate portions of the upper Santa Fe Group aquifer that are most susceptible to overdraft-induced compaction. The fitting of compaction curves, especially for large numbers of wells, cannot be done objectively and reliably by eye using paper copies of logs. Therefore, digital data files are essential. Undisturbed cores should also be collected from potentially compactible clay intervals within the aquifer system, and consolidation tests conducted in order to more accurately quantify the mechanical properties of these units. In particular, more reliable estimates of the preconsolidation stress must be obtained in order to assess the potential for widespread aquifer system compaction and land subsidence.

REFERENCES CITED

Athy, L.F., 1930, Density, porosity, and the compaction of sediments: AAPG Bulletin, v. 14, p. 1-24.

Baldwin, B. and Butler, C.O., 1985, Compaction curves: AAPG Bulletin, v. 69, p. 622-626.

Boyland, P., Keiper, J., Martin, E., Novak, J., Petkovsek, M., Skiena, S., Vardi, I., Wenzlow, A., Wickham-Jones, T., Withoff, D., 1992, Guide to Standard Mathematica Packages (2d ed.): Champaign, Illinois, Wolfram Research, Inc., 384 p.

Contaldo, G.J., and Mueller, J.E., 1991, Earth fissures of the Mimbres Basin, southwestern New Mexico: New Mexico Geology, v. 13, p. 69-74.

Davis, J.M., Lohman, R.C., Phillips, F.M., Wilson, J.L., and Love, D.W., 1993, Architecture of the Sierra Ladrones Formation, central New Mexico: Depositional controls on the permeability correlation structure: Geological Society of America Bulletin, v. 105, p. 998-1007.

Dickinson, G., 1953, Geological aspects of abnormal reservoir pressures in Gulf Coast Louisiana: AAPG Bulletin, v. 37, p. 410-432.

Epstein, C.J., 1987, Hydrologic and geologic factors affecting land subsidence near Eloy, Arizona: U.S. Geological Survey Water-Resources Investigations Report 87-4143.

Gelhar, L.W., 1993, Stochastic Subsurface Hydrology: Englewood Cliffs, NJ, Prentice-Hall, 390 p.

Haneberg, W.C., 1988, Some possible effects of consolidation on growth fault geometry: Tectonophysics, v. 148, p. 309-316.

Haneberg, W.C. and Friesen, R.L., 1995, Tilts, strains, and ground-water levels near an earth fissure in the Mimbres Basin, New Mexico: Geological Society of America Bulletin, v. 107, p. 316-326.

Hanson, R.T., 1989, Aquifer-system compaction, Tucson Basin and Avra Valley, Arizona: U.S. Geological Survey Water-Resources Investigations Report 88-4172.

Hawley, J.W. and Haase, C.S., 1992, Hydrogeologic framework of the northern Albuquerque Basin: New Mexico Bureau of Mines and Mineral Resources Open-File Report 387.

Helm. D.C.. 1984. Field-based computational techniques for predicting subsidence due to fluid withdrawal, in T.L. Holzer, editor, Man-Induced Land Subsidence: Geological Society of America Reviews in Engineering Geology VI. p. 1-22.

Holzer. T.L.. 1981, Preconsolidation stress of aquifer systems in areas of induced land subsidence: Water Resources Research. v. 17. p. 693-704.

Isaaks. E.H. and Srivastava. R.M.. 1989, Applied Geostatistics: New York, Oxford University Press, 561 p.

Kernodle. J.M.. 1995. Simulation of ground-water flow in the Albuquerque Basin, central New Mexico, 1901-1994, with projections to 2020: U.S. Geological Survey Water-Resources Investigations Report 94-4251, 114 p.

Kernodle. J.M.. 1992. Results of simulations by a preliminary numerical model of land subsidence in the El Paso, Texas. are: U.S. Geological Survey Water-Resources Investigations Report 92-4037.

Macfarlane. P.A.. Doveton. J.H.. Feldman, H.R., Butler, J.J., Jr., Combes, J.M., ad Collins, D.R., 1994, Aquifer/aquitard units of the Dakota aquifer system in Kansas: Methods of delineation and sedimentary architecture effects on ground-water flow and flow properties: Journal of Sedimentary Research, v. B64, p. 464-480.

Phillips. F.M.. and Wilson. J.L.. 1989, An approach to estimating hydraulic conductivity spatial correlation scales using geological characteristics: Water Resources Research. v. 25, p. 141-143.

Poland. J.F.. 1984. Mechanics of land subsidence due to fluid withdrawal, in J.F. Poland, editor, Guidebook to Studies of Land Subsidence Due to Ground-Water Withdrawal: UNESCO Studies and Reports in Hydrology 40. p. 37-54.

Press. W.H.. Teukolsky. S.A.. Vetterling, W.T., and Flannery, B.P., 1992, Numercial Recipes in FORTRAN (2d ed. : Cambridge. UK. University Press, 963 p.

Thorn. C.R.. McAda. D.P.. and Kernodle, J.M., 1993, Geohydrologic framework and hydrologic conditions in the Albuquerque Basin. central New Mexico: U.S. Geological Survey Water-Resources Investigations Report 93-4149. 106 p.

Table 4-1. Lithofacies encountered in the upper portion of the Charles Wells 5.

Depth feet	Depth meters	Lithofacies
0–98	0–30	Vf
98–540	30–165	Ib
540–700	165–213	Ib, III
700–870	213–265	Ib
870–1040	265–317	III, Ib
1040–1100	317–335	III
1100–1260	335–384	II, Vd
1260–1560	384–476	Vf, VII
1560–2020	476–616	III, V, VII

Table 4-2. Summary of fitted porosity variogram types and ranges, upper portion of Charles Wells 5

Lithofacies	Depth (m)	Variogram Type	Variogram Range(s) (m)
ALL	110 - 549	Nested Spherical	2, 80, 200
Ib	110 - 165	Exponential	1
Ib,III	165 - 213	Nested Exponential	1, 25
Ib	213 - 265	Exponential	4
III,Ib	265 - 317	Nested Spherical	1, 7.5
III	317 - 335	Nested Spherical	0.5, 3, 8
II,Vd	335 - 384	Nested Spherical	0.5, 7
Vf, VII	384 - 476	Exponential	1
III,V,VII	476 - 549	Nested Spherical	1, 8

Table 4-3. Summary statistics and modeled porosity variograms for the upper portion of the Charles 5 well

Lithofacies (Depth)	n	Mean	Variance	Modeled Variogram
All (110 - 549 m)	2870	0.40	0.0035	$\gamma(h) = 0.0035\left\{0.8\left[\frac{3}{2}\left(\frac{h}{2}\right) - \frac{1}{2}\left(\frac{h}{2}\right)^3\right] + 0.1\left[\frac{3}{2}\left(\frac{h}{80}\right) - \frac{1}{2}\left(\frac{h}{80}\right)^3\right] + 0.1\left[\frac{3}{2}\left(\frac{h}{200}\right) - \left(\frac{h}{200}\right)^3\right]\right\}$
Ib (110 -165 m)	358	0.44	0.0079	$\gamma(h) = 0.0079\left[1 - \exp\left(-\frac{3h}{1}\right)\right]$
Ib/III (165 - 213 m)	320	0.42	0.0049	$\gamma(h) = 0.0049\left\{0.9\left[1 - \exp\left(-\frac{3h}{1}\right)\right] + 0.1\left[1 - \exp\left(-\frac{3h}{25}\right)\right]\right\}$
Ib (213 - 265 m)	340	0.36	0.0019	$\gamma(h) = 0.0019\left[1 - \exp\left(-\frac{3h}{4}\right)\right]$
III/Ib (265 - 317 m)	340	0.39	0.0019	$\gamma(h) = 0.0019\left\{0.3\left[\frac{3}{2}\left(\frac{h}{1}\right) - \frac{1}{2}\left(\frac{h}{1}\right)^3\right] + 0.7\left[\frac{3}{2}\left(\frac{h}{7.5}\right) - \frac{1}{2}\left(\frac{h}{7.5}\right)^3\right]\right\}$
III (317 - 335 m)	120	0.43	0.0026	$\gamma(h) = 0.0026\left\{0.3\left[\frac{3}{2}\left(\frac{h}{0.5}\right) - \frac{1}{2}\left(\frac{h}{0.5}\right)^3\right] + 0.6\left[\frac{3}{2}\left(\frac{h}{3}\right) - \frac{1}{2}\left(\frac{h}{3}\right)^3\right] + 0.1\left[\frac{3}{2}\left(\frac{h}{8}\right) - \frac{1}{2}\left(\frac{h}{8}\right)^3\right]\right\}$
II/Vd (335 - 384 m)	317	0.37	0.0013	$\gamma(h) = 0.0013\left\{0.7\left[\frac{3}{2}\left(\frac{h}{0.5}\right) - \frac{1}{2}\left(\frac{h}{0.5}\right)^3\right] + 0.3\left[\frac{3}{2}\left(\frac{h}{7}\right) - \frac{1}{2}\left(\frac{h}{7}\right)^3\right]\right\}$
Vf/VII (384 - 476 m)	597	0.40	0.0015	$\gamma(h) = 0.0015\left[1 - \exp\left(-\frac{3h}{1}\right)\right]$
III/V/VII (476 - 549 m)	478	0.38	0.0017	$\gamma(h) = 0.0017\left\{0.5\left[\frac{3}{2}\left(\frac{h}{1}\right) - \frac{1}{2}\left(\frac{h}{1}\right)^3\right] + 0.5\left[\frac{3}{2}\left(\frac{h}{8}\right) - \frac{1}{2}\left(\frac{h}{8}\right)^3\right]\right\}$

Table 4-4. Best-fit compaction curve parameters and virgin specific storage estimates for selected Albuquerque Basin water wells

	Athy (1930) Model $n = n_0 \exp(-z/z_0)$					Dickinson (1953) Model $n = n_0 + c \ln(z/z_0)$					
	n_0	z_0 (meters)	r^2	$\bar{S}'_{skv}$ (meters⁻¹)	$\Delta b / \Delta h$	n_0	c	z_0 (meters)	r^2	$\bar{S}'_{skv}$ (meters⁻¹)	$\Delta b / \Delta h$
Charles 5	0.49	1690	0.41	4.2×10^{-4}	0.08	0.30	-0.084	851	0.49	4.8×10^{-4}	0.10
Coronado 2	0.39	2094	0.093	2.2×10^{-4}	0.04	0.31	-0.032	752	0.13	1.6×10^{-4}	0.03
Gonzales 1	0.32	3222	0.85	1.1×10^{-4}	0.02	0.32	-0.0057	492	0.053	2.6×10^{-5}	0.005
PSMW 19	0.33	1875	0.10	2.0×10^{-4}	0.04	0.28	-0.024	365	0.17	2.4×10^{-4}	0.05
Zamora 1	0.39	1451	0.27	2.8×10^{-4}	0.06	0.29	-0.041	635	0.32	1.8×10^{-4}	0.04
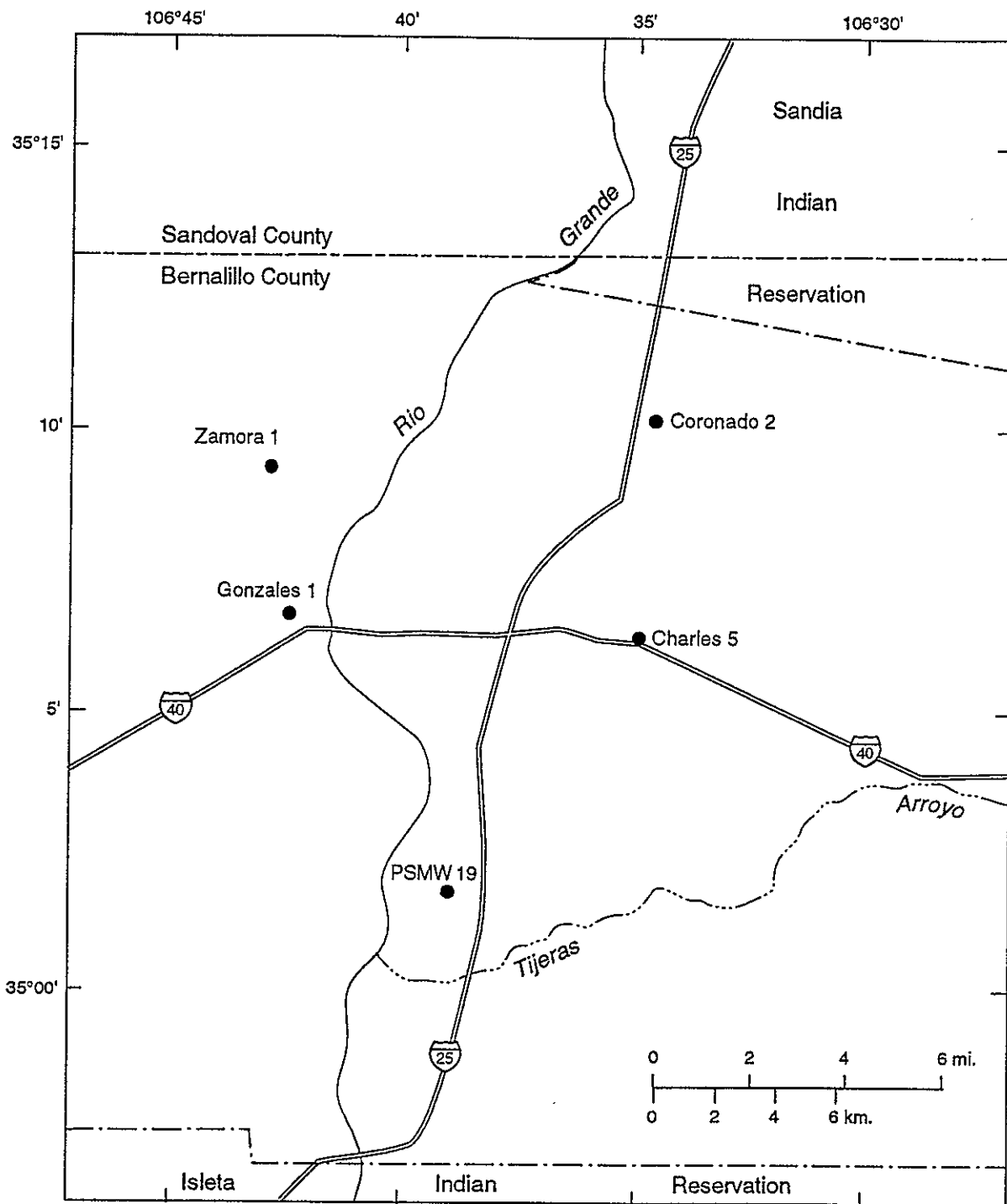
Figure 4-1. Index map of the Albuquerque area showing locations of wells referenced in this chapter.
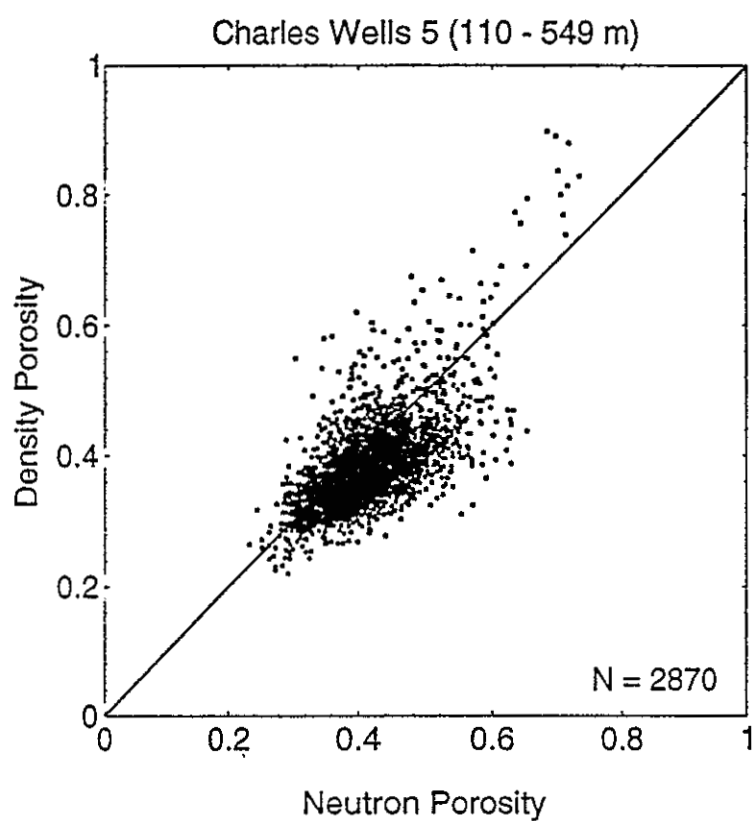
Figure 4-2. Neutron-density porosity cross-plot for the upper portion of the Charles Wells 5.
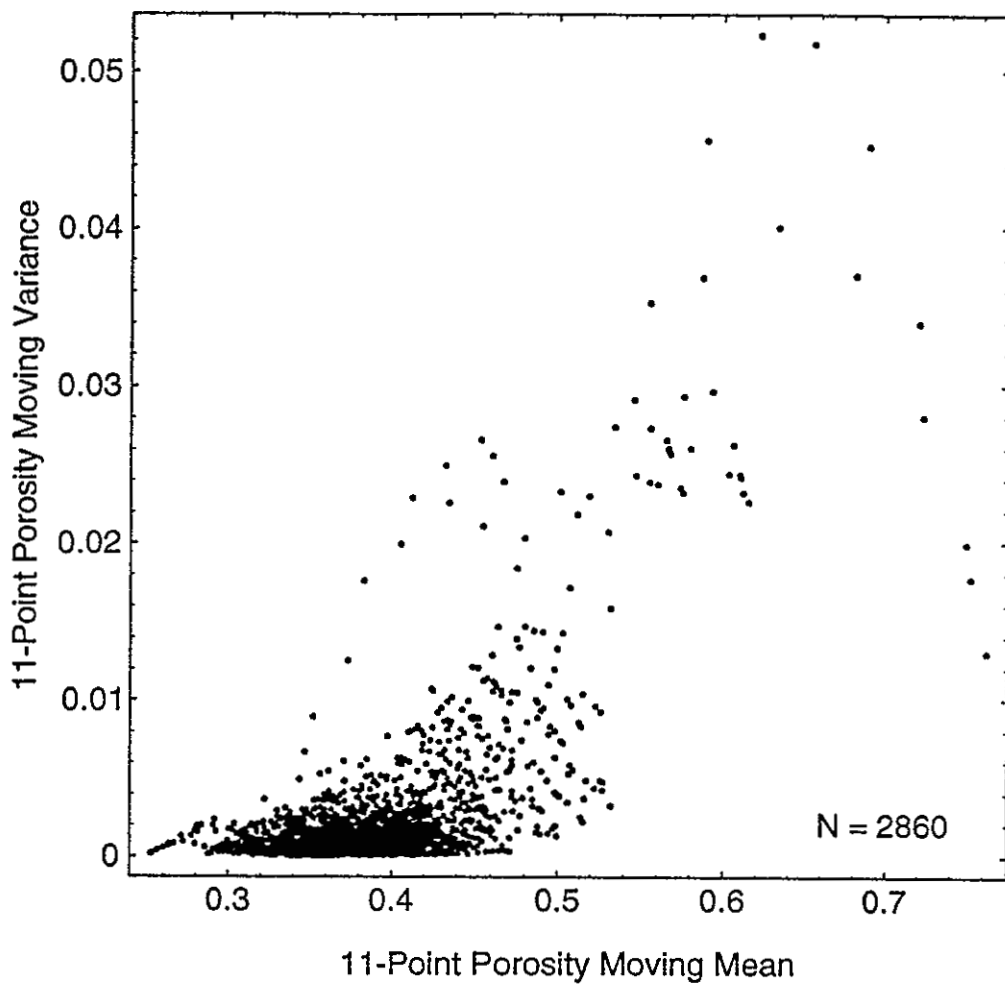
Figure 4-3. Plot of moving sample variance as a function of moving sample mean for the upper portion of the Charles Wells 5.

Charles Wells 5 (110 - 549 m)
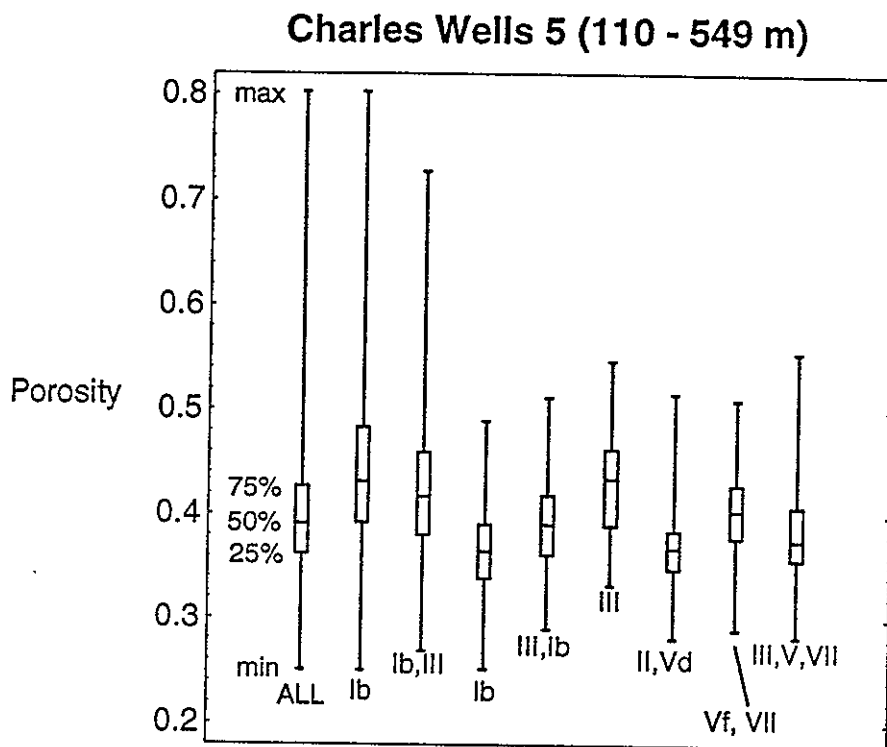
Figure 4-4.   Geophysical log porosity quartiles by lithofacies, upper portion of the
               Charles Wells 5.

Charles Wells 5 Selected Lithofacies
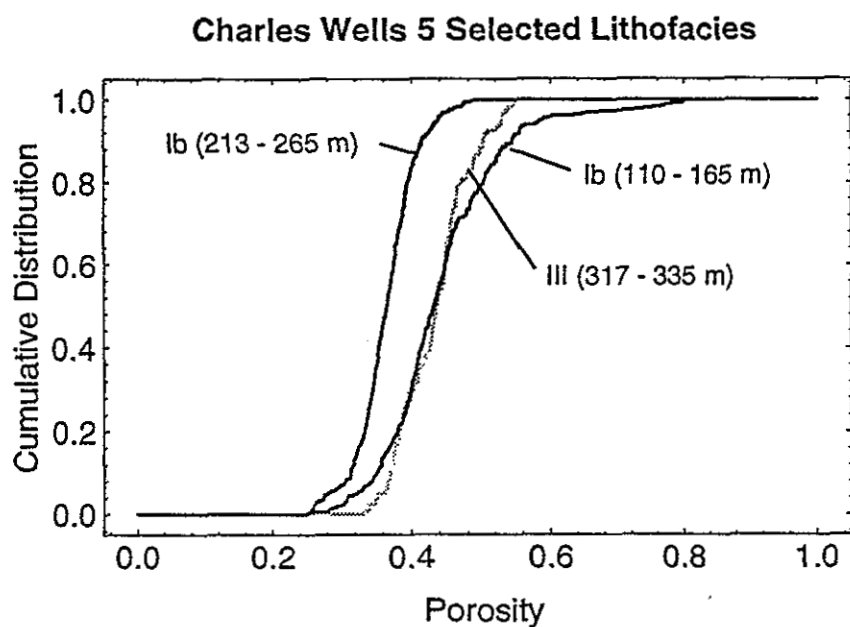
Figure 4-5. Cumulative distributions of porosity distributions for the two unmixed occurrences of lithofacies Ib and the single unmixed occurrence of lithofacies III from the upper portion of the Charles Wells 5.

Charles Wells 5 (110 - 549 m)
Porosity Variograms
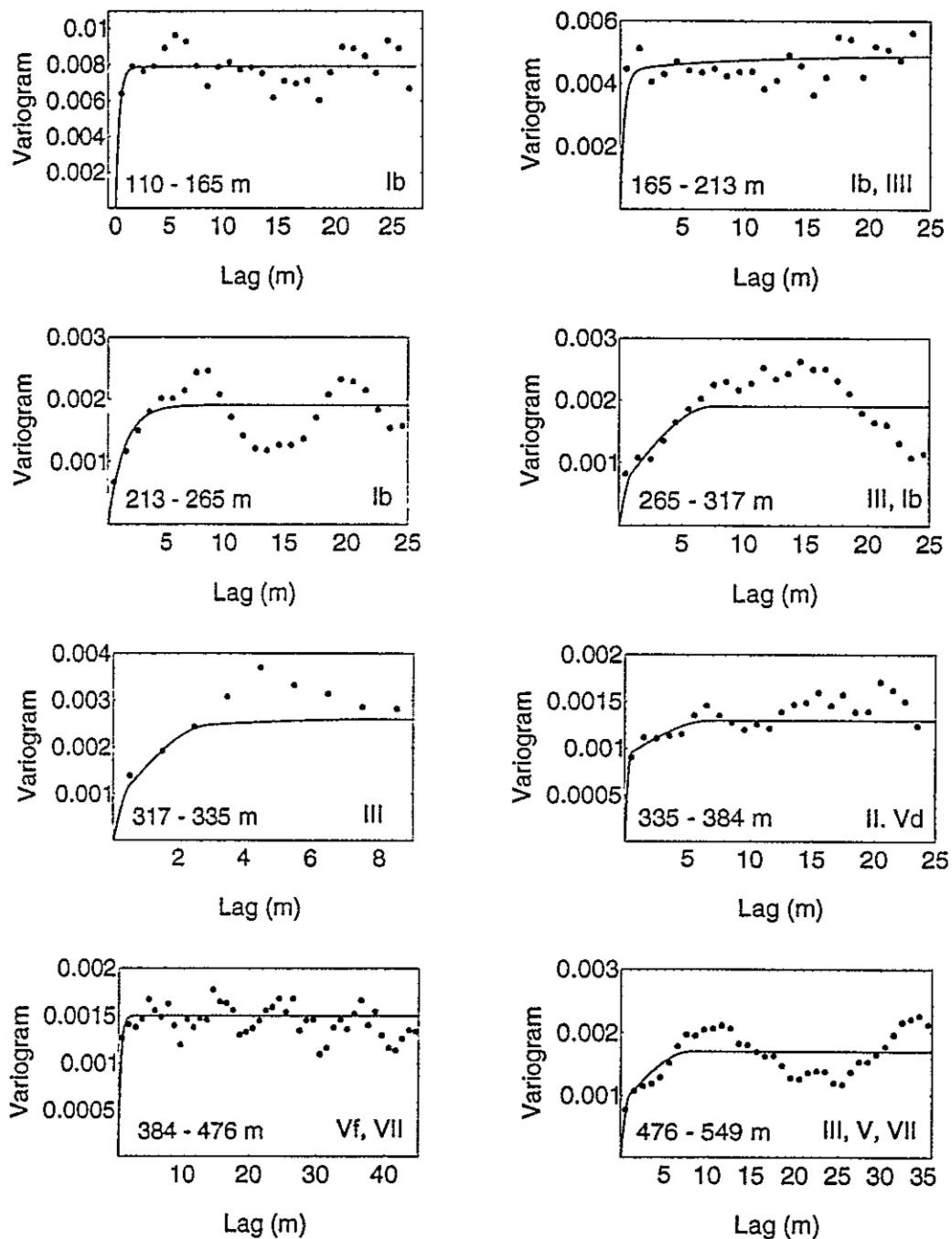
Figure 4-6. Experimental and fitted porosity variograms for the depth intervals listed in Table 4-1 and statistically summarized in Table 4-2. Equations for fitted variograms are given in Table 4-3.
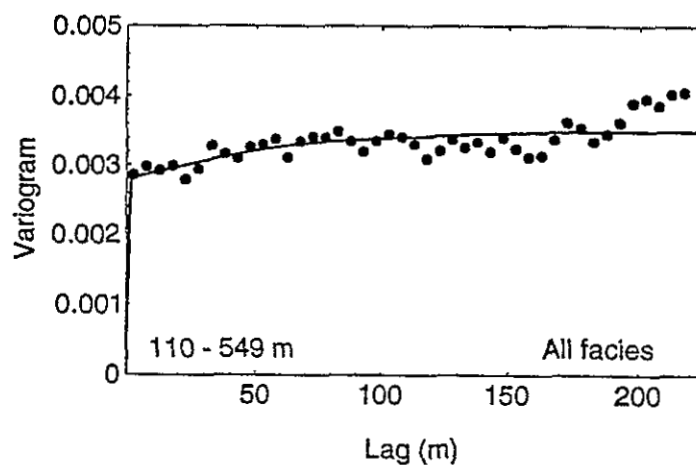
Figure 4-7. Experimental and fitted variograms for undifferentiated RMS porosity data from the upper portion of the Charles Wells 5. Fitted variogram equations are given in Table 4-3.
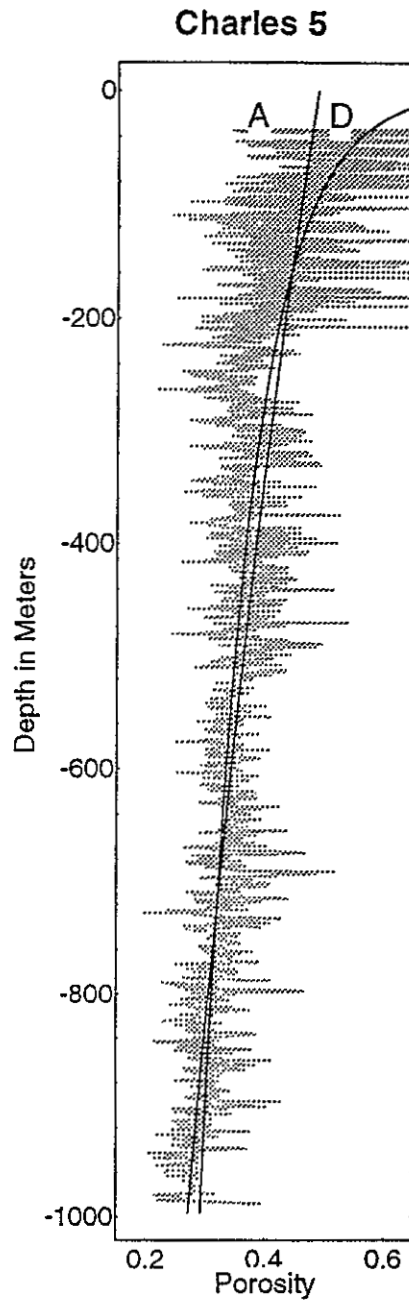
Figure 4-8. Best-fit Athy (1930) and Dickinson (1953) compaction curves superimposed upon the density porosity log for the Charles Wells 5. "A" denotes the Athy curve and "D" denotes the Dickinson curve. Compaction curve parameters are listed in Table 4-4.
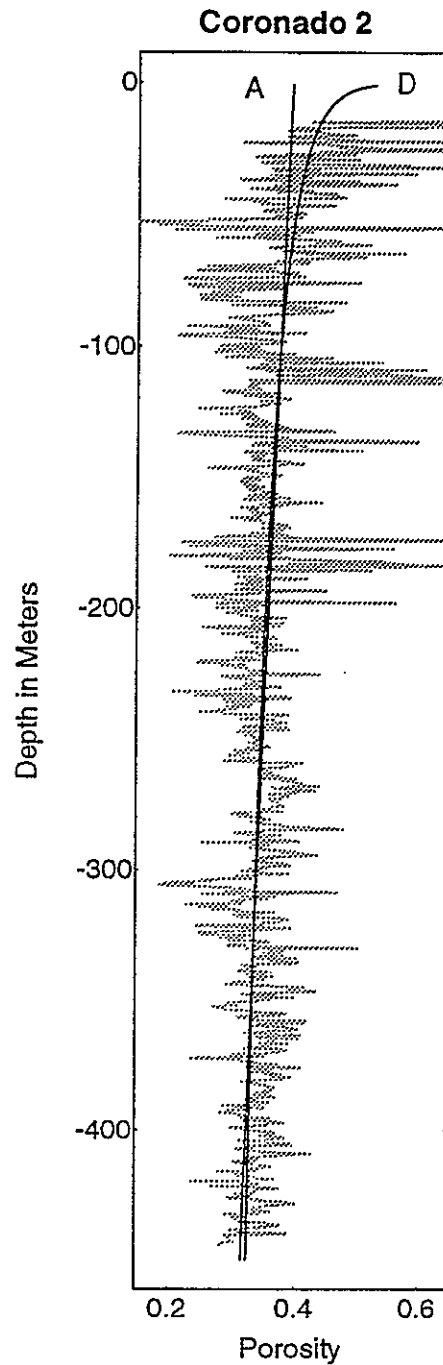
Coronado 2

Figure 4-9. Best-fit Athy (1930) and Dickinson (1953) compaction curves superimposed upon the density porosity log for the Coronado 2 well. "A" denotes the Athy curve and "D" denotes the Dickinson curve. Compaction curve parameters are listed in Table 4-4.
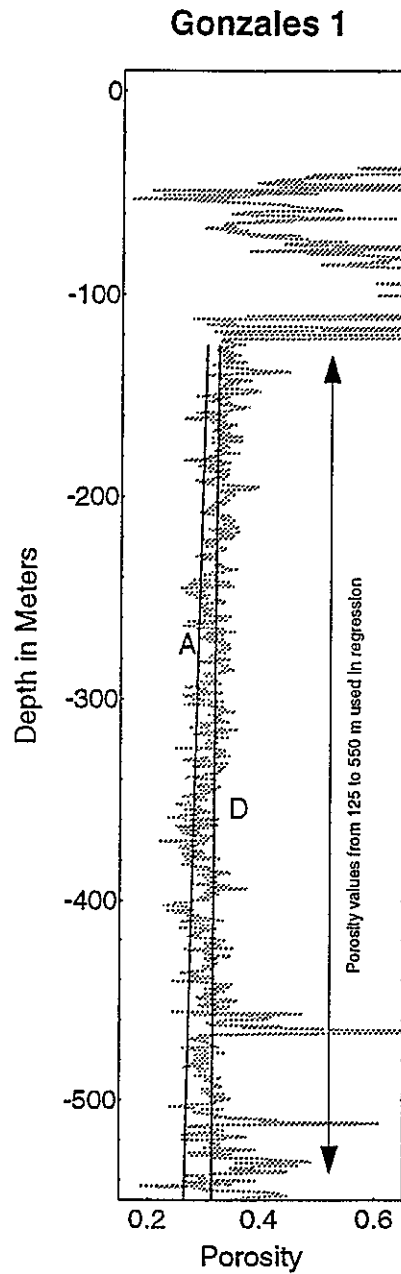
Gonzales 1

Figure 4-10. Best-fit Athy (1930) and Dickinson (1953) compaction curves
superimposed upon the density porosity log for the Gonzales 1. "A"
denotes the Athy curve and "D" denotes the Dickinson curve. Compaction
curve parameters are listed in Table 4-4.
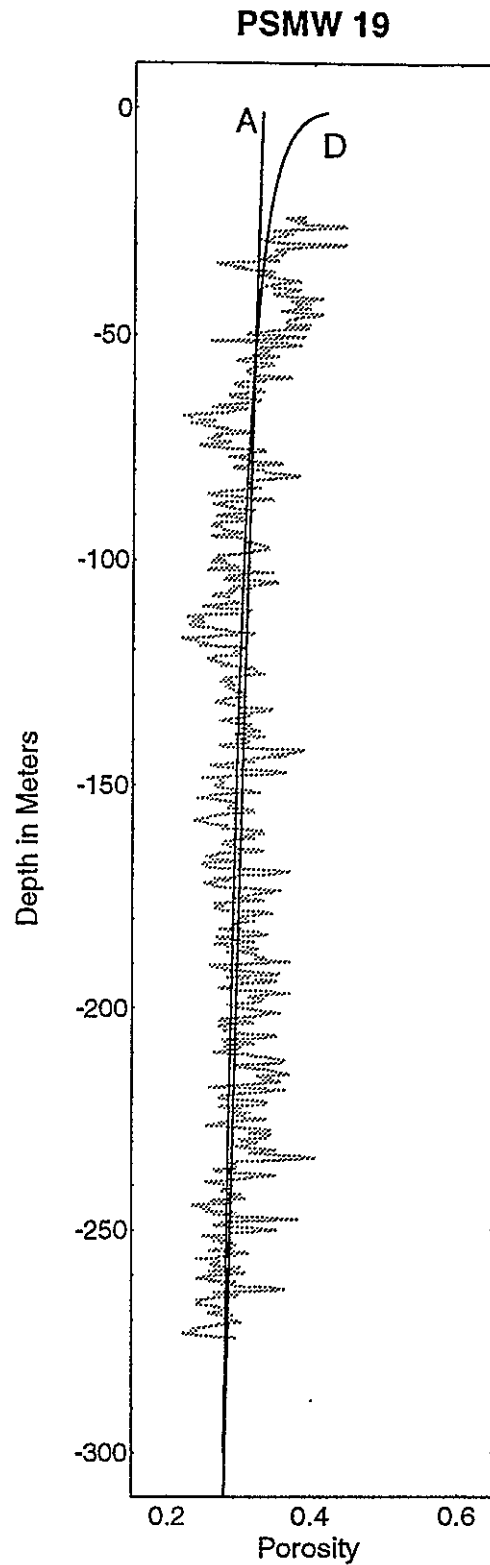
PSMW 19

Figure 4-11. Best-fit Athy (1930) and Dickinson (1953) compaction curves
superimposed upon the density porosity log for the PSMW 19 well. "A"
denotes the Athy curve and "D" denotes the Dickinson curve. Compaction
curve parameters are listed in Table 4-4.
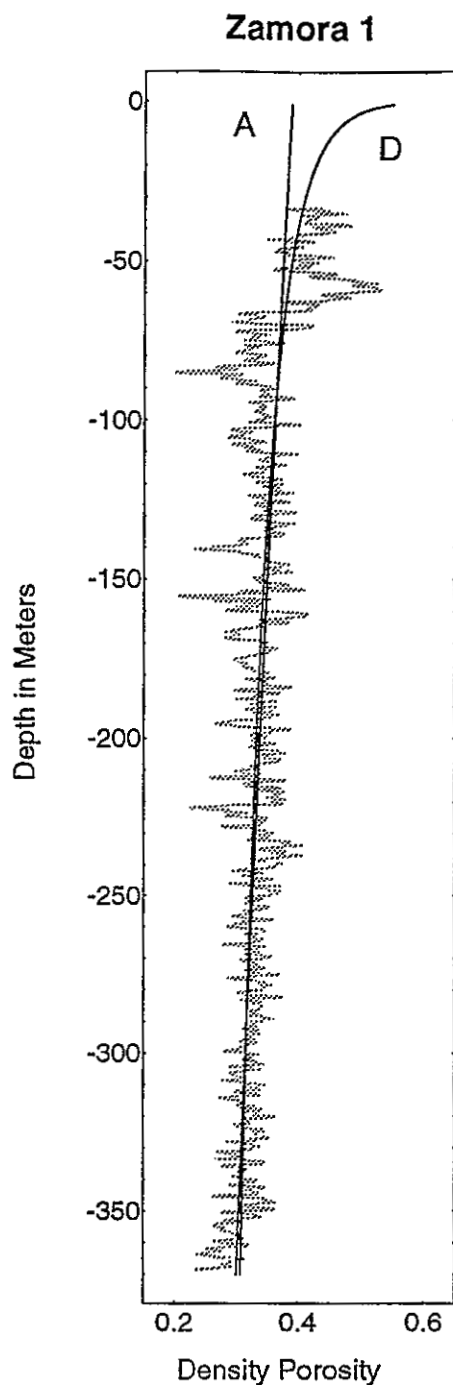
Figure 4-12. Best-fit Athy (1930) and Dickinson (1953) compaction curves superimposed upon the density porosity log for the Zamora 1 well. "A" denotes the Athy curve and "D" denotes the Dickinson curve. Compaction curve parameters are listed in Table 4-4.

Chapter 5

Calcite Cementation in the Santa Fe Group, Albuquerque Basin, NM: Implications for Groundwater Studies

Peter Mozley and Joe Beckner
Department of Geoscience
New Mexico Tech, Socorro, NM 87801

J. Matthew Davis
Department of Earth Sciences
University of New Hampshire, Durham, NH 03824

PURPOSE AND SCOPE

The hydrologic properties of sedimentary rocks are controlled by primary depositional features such as grain size and sorting, as well as diagenetic alterations that affect the pore structure (i.e., precipitation, dissolution, and compaction). Several studies have addressed the question of depositional controls on hydraulic properties in the Albuquerque Basin (Hawley and Haase, 1992; Davis et al., 1993). However, the effect of diagenesis on these properties has not been examined in detail. As part of the current project, we are investigating zones of calcite cementation in the Santa Fe Group. Calcite is the most volumetrically important cement in the unit. In places it completely cements sandstone and conglomerate beds, forming aquicludes several meters thick and 1000's of meters wide. The spatial distribution of these cements needs to be taken into account when attempting to model groundwater flow in Santa Fe Group aquifers.

This chapter presents preliminary results from an ongoing study of calcite cementation in the Santa Fe Group. We have examined the spatial distribution of the cements and their petrographic and geochemical characteristics. Most of the work to date has focused on cementation in the ancestral upper Rio Puerco facies of the Sierra Ladrones Formation, and the Zia Formation, through all major units were examined on a reconnaissance basis.

SUMMARY

Calcite cementation in the Santa Fe Group appears to be controlled by two main factors: depositional facies and primary depositional texture. Calcite is most abundant in deposits of the ancestral Rio Grande tributaries (e.g., upper Rio Puerco), closed-basin fluvial facies, and piedmont facies. It is least abundant in the ancestral axial Rio Grande facies. Regardless of depositional environment, coarser grained and better sorted sediments tend to be preferentially cemented. This suggests that cementation was in part controlled by pre-cementation permeability, perhaps due to a greater flux of Ca^{++} and/or HCO_3- in permeable horizons. Portions of the Santa Fe Group contain abundant elongate calcite concretions that formed parallel to the orientation of

groundwater flow at the time of their precipitation. In the Sierra Ladrones Formation the orientation of these concretions corresponds well with the orientation of the permeability correlation structure, as determined from prior mapping and permeameter measurements. In cases where the paleo-groundwater flow closely corresponds with the direction of fluvial deposition, measurement of concretion orientations in alluvial rocks may provide a means of rapidly estimating the correlation structure over large areas.

RECOMMENDATIONS FOR FUTURE WORK

This report is preliminary and further work is needed to produce a complete and quantitative data set. The following list details additional information that is needed:

1. Subsurface data from conventional cores. This study has focused on outcrop examination of calcite cementation. This is due to the ease at which the geometry and distribution of cementation can be observed in outcrop. Calcite cements are commonly reported to occur in the subsurface (e.g., Titus, 1963; Hawley and Haase, 1992; Hawley, 1994, this report), but little is known about their subsurface distribution. The principal problem in examining cementation in the subsurface of the Albuquerque Basin is a lack of suitable sample materials. For example, cemented fragments are commonly present in cuttings, but it is difficult to tell whether these fragments represent interclasts of previously cemented Santa Fe Group materials, or are part of a cemented horizon that was fragmented during drilling. Conventional core material is needed to see whether or not patterns of cementation observed in outcrop are representative of the subsurface cements as well.

2. Data from a greater variety of units. Thus far we have only examined the ancestral Rio Puerco facies of the Sierra Ladrones Formation and the Zia Formation in detail. With the exception of two samples from the Zia formation, all the petrographic data obtained has been from ancestral Rio Puerco samples. More information is needed from other units throughout the basin.

3. Quantification of permeability and cementation data. Our interpretation that cement distribution is controlled locally be pre-cementation permeability is based upon visual estimates of grain-size and sorting made in the field. Quantitative permeability data are needed to confirm this relationship. Because the pre-cementation permeability cannot be directly measured, it will be necessary to dissolve cemented samples in acid and estimate permeability by grain-size analysis (see Panda and Lake, 1994), this data can then be compared to the permeability of uncemented samples also estimated by grain-size analysis.

Likewise, out data on the degree of cementation is based upon qualitative visual observations. The degree of cementation should be quantified by determining the percentage calcite present in selected samples using a Chittick apparatus.

4. *Additional petrographic and geochemical data.* Thus far we have only examined the petrography and geochemistry of the ancestral Rio Puerco cements in any detail. Additional data is needed from the other units.

Chapter 5

Calcite Cementation in the Santa Fe Group, Albuquerque Basin, NM: Implications for Groundwater Studies

Peter Mozley and Joe Beckner, Department of Geoscience, New Mexico Tech, Socorro, NM 87801

J. Matthew Davis, Department of Earth Sciences, University of New Hampshire, Durham, NH 03824

Abstract. — Calcite is the most abundant cement in the Santa Fe Group. Calcite cemented zones commonly form laterally extensive aquicludes that should be taken into account when modeling groundwater flow in the basin. Calcite cementation in the Santa Fe Group appears to be controlled by two main factors: depositional facies and primary depositional texture. Calcite is most abundant in tributaries to the ancestral Rio Grande, closed-basin fluvial facies, and piedmont facies. It is least abundant in the ancestral Rio Grande facies. Regardless of depositional environment, coarser grained and better sorted sediments tend to be preferentially cemented. This suggests that cementation was in part controlled by pre-cementation permeability, perhaps due to a greater flux of Ca^{++} and/or HCO_3^- in permeable horizons. Portions of the Santa Fe Group contain abundant elongate calcite concretions that formed parallel to the orientation of groundwater flow at the time of their precipitation. In the Sierra Ladrones Formation the orientation of these concretions corresponds well with the orientation of the permeability correlation structure, as determined from prior mapping and permeameter measurements. In cases where the paleo-groundwater flow closely corresponds with the direction of fluvial deposition, measurement of concretion orientations in alluvial rocks may provide a means of rapidly estimating the correlation structure over large areas.

INTRODUCTION

The hydrologic properties of sedimentary rocks are controlled by primary depositional features such as grain size and sorting, as well as diagenetic alterations that affect the pore structure (i.e., precipitation, dissolution, and compaction). Several studies have addressed the question of depositional controls on hydraulic properties in the Albuquerque Basin (Hawley and Haase, 1992; Davis et al., 1993). However, the effect of diagenesis on these properties has not been examined in detail. As part of the current project, we are investigating zones of calcite cementation in the Santa Fe Group. Calcite is the most volumetrically important cement in the unit. In places it completely cements sandstone and conglomerate beds, forming aquicludes several meters thick and 1000's of

meters wide. The spatial distribution of these cements needs to be taken into account when attempting to model groundwater flow in Santa Fe Group aquifers.

This chapter presents preliminary results from an ongoing study of calcite cementation in the Santa Fe Group. We have examined the spatial distribution of the cements and their petrographic and geochemical characteristics. Most of the work to date has focused on cementation in the ancestral Rio Puerco facies of the Sierra Ladrones Formation, and the Zia Formation, though all major units were examined on a reconnaissance basis.

METHODS

Field Work

Outcrops of the Santa Fe Group were examined throughout the Albuquerque Basin. Representative stratigraphic sections were measured using a Jacob's staff. The lateral extent of cemented beds was determined by measuring the longest straight-line segment of continuous cementation exposed in the outcrop. In many cases the full lateral extent of the bed could not be determined due to limited exposure, so lateral continuity may be considerably greater than the reported values in some cases. Zia stratigraphic sections were described by Beckner, whereas all other sections were described by Mozley.

Petrographic Analysis

Thin sections were prepared from cemented zones in the ancestral Rio Puerco facies of the Sierra Ladrones Formation and from a single concretion in the Unnamed Member of the Zia Formation. No thin sections were prepared for the other units. Samples were impregnated with blue-dyed epoxy prior to thin-section preparation in order to differentiate between true porosity and porosity created by grain plucking during thin section preparation. All thin sections were examined on a standard petrographic microscope, as well as on microscopes equipped with cathodoluminescence and UV/blue fluorescence units (MAAS/Nuclide model ELM-3 Luminoscope, Department of Geoscience, New Mexico Tech; and Nikon fluorescence unit, Petroleum Recovery Research Center, New Mexico Tech). Thin sections were also examined using back-scattered electron imaging on an electron microprobe (JEOL 733-Superprobe, Institute of Meteoritics, University of New Mexico).

Geochemical Analysis

The elemental composition of calcite cements in all the thin sections was determined by microprobe analysis using carbonate standards. Standard operating conditions were: 20 nA sample current and 1 - 10 micron beam diameter. Sample totals for all reported values are 100 +/- 2 %.

PETROLOGY AND GEOCHEMISTRY OF CEMENTED ZONES

Thus far we have only examined cements in the ancestral Rio Puerco facies of the Sierra Ladrones Formation in detail. The cemented zones consist mainly of mixtures of micrite, microspar, sparite (sometimes poikilotopic), and minor amounts of detrital carbonate. Under cathodoluminescence examination the authigenic calcite is non-luminescent, whereas the detrital carbonate is characterized by orange luminescence. Faint zonation was observed in some of the cements under UV/blue fluorescence examination.

The elemental composition of the calcite is close to the $CaCO_3$ end-member, with only minor substitution of other cations (mainly Mg) for Ca in the calcite structure (Table 5-1. Fig. 5-1). The elemental composition of the calcite is very similar to that of calcite in the cemented zone of the Sand Hill fault (Mozley and Goodwin, 1994, this report).

SPATIAL DISTRIBUTION OF CALCITE CEMENTS IN THE SANTA FE GROUP

Relationship to Facies and Depositional Texture

The distribution of calcite cement in the Santa Fe Group is strongly controlled by facies and depositional texture (Table 5-2; Figs. 5-2 through 5-7). Carbonate cements are most abundant in the tributaries to the ancestral Rio Grande (i.e., ancestral Rio Puerco), closed-basin fluvial facies, and piedmont facies. Calcite cement is least abundant in the ancestral Rio Grande facies. Within a particular facies, coarser grained and better sorted units tend to contain the most cement (Figs. 5-2 through 5-7). Lateral continuity of cemented horizons varies considerably among the different facies examined (Table 5-2).

The most laterally continuous horizons were observed in the closed-basin fluvial, eolian, and playa lake facies (>1 km). The least laterally continuous horizons were observed in the ancestral Rio Grande deposits (max. observed 9 m).

Although most of the authigenic calcite in the Santa Fe Group occurs as a pore-filling cement, the playa lake facies of the Zia Formation contains two horizons of synsedimentary carbonate. These layers are characterized by highly irregular shapes and are interpreted to be lacustrine tuffa deposits (Lozinsky, 1988). In addition, small calcite nodules (<2 cm diameter) are present throughout the Santa Fe Group. These nodules are preferentially associated with finer grained lithologies and may be pedogenic.

Controls on Cement Distribution

There are a variety of possible controls on the distribution of calcite cements in sedimentary rocks, including: presence of nucleating material, proximity to a source of calcium or bicarbonate, pH, membrane filtration effects, changes in the rate of deposition, changes in pore pressure, past water-table configuration, and pre-cementation permeability. The preferential cementation of coarser grained and better sorted horizons in outcrops of the Santa Fe Group indicates that a fundamental control on calcite distribution was pre-cementation permeability (permeability increases with increasing grain size and sorting). This suggests that sediments that originally had the greatest permeability and connectivity of permeable packages became preferentially cemented by calcite. A possible explanation for this relationship is that cementation was limited by the availability of dissolved calcium and/or bicarbonate, and greater amounts of these dissolved components were available in the best portions of the aquifer (i.e., areas that experienced the greatest flux of aqueous species). However, this relationship alone does not adequately explain the observed distribution of calcite, because the highly permeable ancestral Rio Grande facies is one of the least cemented facies. The lower amounts of calcite in the ancestral Rio Grande facies probably results from differences in the pore-water chemistry of the different facies at the time of cement precipitation. The ancestral Rio Grande facies pore waters may have contained less calcium, bicarbonate, and/or had a lower pH than the tributary, closed-basin fluvial, and piedmont facies. An alternative explanation for the smaller amounts of calcite in the ancestral Rio Grande deposits is that calcite cements were once abundant, but have undergone selective dissolution in the unit. Macroscopic examination of ancestral Rio Grande cement zones, however, provides no evidence for large-scale cement dissolution. The morphology of cemented horizons in the ancestral Rio Grande is

identical to that of cements in the other units, and the surface of the cemented zones show no evidence of dissolution.

Although synsedimentary, pedogenic and unsaturated-zone calcite cements are present in the Santa Fe Group, the strong relationship between grain size and cementation indicates that the most volumetrically significant cements formed in the saturated zone (i.e., saturated flow tends to be concentrated in coarser-grained rocks; Domenico and Schwartz, 1990). In addition, the preferential cementation of the base of coarse-grained layers that overlie very fine grained layers in the piedmont facies indicates that some of the piedmont calcites formed in perched aquifers.

Effect of Cementation on Groundwater Resources

Calcite cementation in the Santa Fe Group greatly reduces permeability and porosity forming both local and regional aquitards and aquicludes. The impact of cementation on aquifer quality is invariably negative, particularly because it disproportionately affects the best portions of the aquifer (i.e., beds with initial high permeability and porosity). In extreme cases this has led to a wholesale inversion of aquifer quality, in which beds that were initially the best portions of the aquifer are now the worst. In addition to reducing overall aquifer quality, laterally continuous zones of cementation can have a major effect on vertical fluid flow, perhaps resulting in compartmentalization in some cases. Such compartmentalization could result in significant production loss in wells that are screened on only one side of a laterally extensive cement horizon.

ORIENTED CONCRETIONS AND THEIR RELATIONSHIP TO THE PERMEABILITY CORRELATION STRUCTURE

A striking feature of many of the cemented zones is a pattern of elongation that has a consistent orientation within a few degrees of variation at any given portion of the outcrop (Fig. 5-8). These elongate zones occur as isolated concretions and as large tabular beds, where the elongation is seen as ribs and furrows on the top and base, and elongate projections at the edges. Such elongate cements have been noted in a large number of units, and are generally believed to result from precipitation from flowing groundwater, with the cement orientation reflecting the orientation of groundwater flow at the time of precipitation (Todd, 1903; Schultz, 1941; Colton,1967; Jacob, 1973; Parsons, 1980;

Meschter, 1958; Raiswell and White, 1978; Theakstone, 1981; Fastovsky and Dott, 1986; Pirrie, 1987; Johnson, 1989; McBride et al., 1994). In the Santa Fe Group, elongate zones of cementation have been observed in the ancestral Rio Puerco and ancestral Rio Grande facies of the Sierra Ladrones Formation, in playa lake deposits of the Popotosa Formation at the Gabaldon Badlands, and in fluvial and eolian facies of the Zia Formation. We have mapped the orientation of the concretions in the Sierra Ladrones Formation over a large area (Fig. 5-9) and are currently mapping the orientation of concretions in the Zia Formation.

A popular means of quantifying flow through heterogeneous reservoirs and aquifers is the stochastic approach, which requires information on the permeability correlation structure. The permeability correlation structure summarizes the directions and distances over which the permeability is correlated in space. Estimation of the permeability correlation structure generally requires hundreds of spatially distributed permeability measurements (often referred to as hard data) which is often prohibitive due to cost and time constraints. One approach to minimizing the data requirements for estimation of the permeability correlation structure is to incorporate "soft" geologic information. Phillips and Wilson (1989) suggested that under certain conditions the correlation lengths can be estimated from the average dimensions of geologic units. The other approach is to measure the structure directly by obtaining permeability data in several space dimensions using a permeameter (Goggin et al. 1988; Dreyer et al., 1990; Davis et al., 1993). The former approach suffers from the general lack of sufficient exposure to measure the dimensions and directions of preferred orientation. The latter approach, though certainly the most accurate measure, requires exceptionally well exposed outcrops, and is extremely time consuming.

As part of a previous study (Davis et al., 1993), the permeability correlation structure of ancestral Rio Puerco deposits at a site near Bosque, NM was estimated from geologic mapping and in-situ permeability measurement and was interpreted as being largely controlled by depositional processes. The overall permeability correlation structure at the site corresponds well with paleocurrent data (as shown by Davis et al., 1993), and remarkably well with the concretion orientations measured in the same site (Fig. 5-11, a, b, and c). The paleocurrent orientations show greater dispersion than the concretion orientations (Fig. 5-11 b and c; mean resultant length is 0.53 for paleocurrent orientations versus 0.84 for the concretions), which is to be expected given the wide variation in paleocurrent orientations in most fluvial environments.

The orientation of elongate concretions appears to be a reliable proxy for the permeability correlation structure, at least in this case. This is not surprising, as previous studies of alluvial rocks have shown a strong relationship between paleocurrent data and concretion orientation (Jacob, 1973; Parsons, 1980; Theakstone, 1981; Fastovsky and Dott, 1986; Johnson, 1989); and primary depositional texture (controlled in large part by current direction) should be the major control on the correlation structure. Further work will be necessary to document the relationship in other areas.

We have restricted our interpretation to alluvial rocks, because the relationship between paleocurrent direction and concretion orientation is less clear for non-alluvial environments. Although Colton (1967) and Pirrie (1987) noted a correlation between concretion orientation and paleocurrent direction in marine mudstones and shallow marine sandstones, respectively, McBride et al. (1994) concluded that concretion orientation in the shallow marine and beach sandstones they examined is not related to primary depositional fabric. We speculate that the reason for the strong correlation in alluvial rocks is that the alluvial concretions form relatively early, from groundwater moving subparallel to the downstream direction. This is supported by observations that groundwater flow in alluvial valleys is commonly dominated by downstream or underflow components (Larkin and Sharp, 1992). In the Sierra Ladrones Formation the high degree of anisotropy may have also largely controlled the groundwater flow directions, damping out oscillations in the natural hydraulic gradient. In cases that are more isotropic a larger degree of variability in groundwater flow direction and thus concretion orientation may be present.

RECOMMENDATIONS FOR FUTURE WORK

This report is preliminary and further work is needed to produce a complete and quantitative data set. The following list details additional information that is needed:

1. *Subsurface data from conventional cores.* This study has focused on outcrop examination of calcite cementation. This is due to the ease at which the geometry and distribution of cementation can be observed in outcrop. Calcite cements are commonly reported to occur in the subsurface (e.g., Titus, 1963; Hawley and Haase, 1992; Hawley, 1994, this report), but little is known about their subsurface distribution. The principal problem in examining cementation in the subsurface of the Albuquerque Basin is a lack of suitable sample materials. For example, cemented fragments are commonly present in

cuttings, but it is difficult to tell whether these fragments represent intraclasts of previously cemented Santa Fe Group materials, or are part of a cemented horizon that was fragmented during drilling. Conventional core material is needed to see whether or not patterns of cementation observed in outcrop are representative of the subsurface cements as well.

2. *Data from a greater variety of units.* Thus far we have only examined the ancestral Rio Puerco facies of the Sierra Ladrones Formation and the Zia Formation in detail. With the exception of two samples from the Zia Formation, all the petrographic data obtained has been from ancestral Rio Puerco samples. More information is needed from other units throughout the basin.

3. *Quantification of permeability and cementation data.* Our interpretation that cement distribution is controlled locally by pre-cementation permeability is based upon visual estimates of grain-size and sorting made in the field. Quantitative permeability data are needed to confirm this relationship. Because the pre-cementation permeability cannot be directly measured, it will be necessary to dissolve cemented samples in acid and estimate permeability by grain-size analysis (see Panda and Lake, 1994), this data can then be compared to the permeability of uncemented samples also estimated by grain-size analysis.

Likewise, our data on the degree of cementation is based upon qualitative visual observations. The degree of cementation should be quantified by determining the percentage calcite present in selected samples using a Chittick apparatus.

4. *Additional petrographic and geochemical data.* Thus far we have only examined the petrography and geochemistry of the ancestral Rio Puerco cements in any detail. Additional data is needed from the other units.

REFERENCES CITED

Colton, G. W., 1967, Orientation of carbonate concretions in the Upper Devonian of New York: U. S. Geological Survey Professional Paper, v. 575-B, p. B57-B59.

Davis, J. M., Lohmann, R. C., Phillips, F. M., Wilson, J. L. and Love, D. W., 1993, Architecture of the Sierra Ladrones Formation, central New Mexico: Depositional controls on the permeability correlation structure: Geological Society of America Bulletin, v. 105, p. 998-1007.

Domenico, P. A. and Schwartz, F. W., 1990, Physical and chemical hydrogeology: New York, John Wiley and Sons, 824 p.

Dreyer, T. A. S. and Walderhaug, O., 1990, Minipermeameter-based study of permeability trends in channel sand bodies: American Association of Petroleum Geologists Bulletin, v. 74, p. 359-374.

Fastovsky, D. E. and Dott, R. H., 1986, Sedimentology, stratigraphy, and extinctions during the Cretaceous-Paleogene transition at Bug Creek, Montana: Geology, v. 14, p. 279-282.

Gelhar, L. W., Chandler, M. A., Kocurek, G. and Lake, L. W., 1983, Three dimensional stochastic analysis of macrodispersion in aquifers: Water Resources Research, v. 19, p. 161-180.

Goggin, D. J., Chandler, M. A., Kocurek, G. and Lake, L. W., 1988, Patterns of permeability in eolian deposits: Page Sandstone (Jurassic), northeastern Arizona: Society of Petroleum Engineers Formation Evaluation, v. 3, p. 297-306.

Hawley, J. W. and Haase, C. S., 1992, Hydrogeologic framework of the northern Albuquerque Basin: New Mexico Bureau of Mines and Mineral Resources Open-File Report 387, variously paged.

Jacob, A. F., 1973, Elongate concretions as paleochannel indicators, Tongue River Formation (Paleocene), North Dakota: Geological Society of America Bulletin, v. 84, p. 2127-2132.

Johnson, M. R., 1989, Paleogeographic significance of oriented calcareous concretions in the Triassic Katberg Formation, South Africa: Journal of Sedimentary Petrology, v. 59, p. 1008-1010.

Larkin, R. G. and Sharp, J. M. J., 1992, On the relationship between river-basin geomorphology, aquifer hydraulics, and ground-water flow direction in alluvial aquifers: Geological Society of America Bulletin, v. 104, p. 1608-1620.

Lozinsky, R. P., 1988, Stratigraphy, sedimentology, and sand petrology of the Santa Fe Group and pre-Santa Fe Group Tertiary deposits in the Albuquerque basin, central New Mexico [unpubl. Ph.D. dissert.]: Socorro, New Mexico, New Mexico Institute of Mines and Technology, 298 p.

Lozinsky, R. P., Hawley, J. W. and Love, D. W., 1991, Geologic overview and Pliocene-Quaternary history of the Albuquerque Basin, central New Mexico, in B. Julian and J. Zidek, eds., Field guide to geologic excursions in New Mexico and adjacent areas of Texas and Colorado.: Bulletin New Mexico Bureau of Mines and Mineral Resources, p. 157-162.

McBride, E. F., Piracy, M. D. and Folk, R. L., 1994, Oriented concretions, Ionian Coast, Italy: evidence of groundwater flow direction: Journal of Sedimentary Research, v. A64, p. 535-540.

Meschter, D. Y., 1958, A study of concretions as applied to the geology of uranium deposits: U.S. Atomic Energy Commission Technical Memorandum Report TM-D-1-14, 10 p. (Available on microfiche from the U.S. Geological Survey in Denver.)

Mozley, P.S., and Goodwin, L.G., 1994, Patterns of cementation along the Sand Hill fault, Albuquerque basin, NM: implications for paleoflow orientations and mechanisms of fault-related cementation, in, W.C. Haneberg and J.W. Hawley (eds.), *Characterization of hydrogeologic units in the northern Albuquerque Basin*, New Mexico Bureau of Mines and Mineral Resources Open-File Report 402-C, p. ___.

Panda, M. N. and Lake, L. W., 1994, Estimation of single-phase permeability from parameters of particle-size distribution: American Association of Petroleum Geologists Bulletin, v. 78, p. 1028-1039.

Parsons, M. W., 1980, Distribution and origin of elongate sandstone concretions, Bullion Creek and Slope Formations (Paleocene), Adams County, North Dakota [unpubl. MS thesis]: University of North Dakota, Grand Forks, North Dakota, 133 p.

Phillips, F. M. and Wilson, J. L., 1989, An approach to estimating hydraulic conductivity spatial correlation scales using geological characteristics: Water Resources Research, v. 25, p. 141-143.

Pirrie, D., 1987, Oriented calcareous concretions from James Ross Island, Antarctica: British Antarctic Survey Bulletin, v. 75, p. 41-50.

Raiswell, R. and White, N. J. M., 1978, Spatial aspects of concretionary growth in the Upper Lias of northeast England: Sedimentary Geology, v. 20, p. 291-300.

Schultz, C. B., 1941, The pipy concretions of the Arikaree: University of Nebraska State Museum Bulletin, v. 2, p. 69-82.

Theakstone, W. H., 1981, Concretions in glacial sediments at Seglvatnet, Norway: Journal of Sedimentary Petrology, v. 51, p. 191-196.

Todd, J. E., 1903, Concretions and their geological effects: Geological Society of America Bulletin, v. 14, p. 353-368.

Table 5-1. Composition of calcite in authigenic cements (micrite and sparite) and caliche intraclasts. All samples are from cemented zones in Ancestral Rio Puerco deposits near Bosque, NM. Data is from electron microprobe analysis.

Sample	Point	$FeCO_3$	$MnCO_3$	$MgCO_3$	$CaCO_3$	$SrCO_3$	Na_2CO_3	Type
31194-1	1	-	-	0.25	99.72	0.02	-	Sparite
	2	-	-	0.33	99.65	0.01	-	Sparite
	3	-	-	0.49	99.47	0.03	-	Micrite
	4	-	-	0.68	99.27	0.04	-	Micrite
	5	-	-	1.24	98.72	0.03	-	Sparite
31194-3	2	0.09	-	1.75	97.97	0.08	0.07	Caliche
	3	0.19	-	1.35	98.22	0.13	0.09	Caliche
	4	0.54	0.16	0.78	98.47	0.02	-	Caliche
	5	-	-	1.32	98.57	0.03	0.07	Caliche fracture
	6	0.03	-	1.31	98.54	0.04	0.07	Caliche fracture
	7	-	-	0.35	99.59	-	0.05	Sparite
	8	-	-	0.63	99.27	0.03	0.05	Sparite
	9	-	-	0.41	99.55	0.03	-	Sparite
31194-7aa	1	0.08	-	0.51	99.40	-	-	Sparite
	2	-	-	0.73	99.26	-	-	Sparite
	3	-	-	1.57	98.42	-	-	Micrite
	4	0.04	-	0.95	99.01	-	-	?
	5	0.06	-	0.63	99.30	-	-	?
31194-7e	1	-	-	0.76	99.23	-	-	Sparite
	2	-	-	0.22	99.77	-	-	Sparite
	3	-	-	0.96	99.03	-	-	Sparite
	4	-	-	0.87	99.12	-	-	Micrite
	5	-	-	1.69	98.20	0.09	-	Micrite
31194-8	1	-	-	3.00	96.86	0.08	0.04	Sparite
	3	0.33	0.040	1.58	97.96	0.07	-	Micrite
	5	0.04	-	1.57	98.26	0.06	0.05	Sparite
	7	-	-	2.06	97.78	0.07	0.08	Sparite
31194-10a	1	0.05	-	1.61	98.24	0.05	0.03	Sparite
	2	0.07	0.020	1.62	98.22	0.06	-	Sparite
	4	0.03	-	1.27	98.62	0.06	-	Sparite
	5	-	-	1.63	98.29	0.02	0.05	Sparite

Table 5-2. Summary of calcite cement relationships in the Santa Fe Group, Albuquerque Basin. Hydrostratigraphic units noted are described in Hawley and Haase (1992).

Facies/units	Lithologic associations	Cement abundance	Lateral continuity	Controls on cementation	Outcrops examined
Piedmont slope (Hydrostrat. unit: USF-1)	Cement occurs mainly in grain-supported conglomerates and medium to very coarse grained sandstones.	Abundant to absent	Proximal: often minimal (<5 m) due to lateral termination of coarse-grained rock types. Distal: Continuous cemented zones (>500 m) common.	Cementation controlled by pre-cementation permeability. Some cementation may have occurred in perched aquifers.	Upper Santa Fe Gp. Tijeras Arroyo & W of Placitas; Sierra Ladrones Fm, Arroyo de la Parida.
Ancestral Rio Puerco (Hydrostrat. unit: USF)	Coarser grained sandstones and to a lesser extent conglomerates preferentially cemented. Very poorly sorted conglomerates not well cemented.	Abundant	Highly variable (<1m to >200m).	Cementation controlled by pre-cementation permeability.	Upper Santa Fe Gp. Sierra Ladrones Fm W, NW, & SW of Belen.
Ancestral Rio Grande (Hydrostrat. unit: USF-2)	Coarser grained sandstones and conglomerates preferentially cemented, but relationship is not very strong.	Rare	Minimal (maximum observed = 9 m).	Cementation controlled by pre-cementation permeability.	Upper Santa Fe Gp. Sierra Ladrones Fm, S Alb., Black Mesa, Isleta Pueblo, I25 between Belen & Socorro, Johnson Hill area.
Closed basin fluvial (Hydrostrat. unit: LSF)	Coarser grained sandstones preferentially cemented.	Abundant	Highly variable (<1m to >2km).	Cementation controlled by pre-cementation permeability.	Lower Santa Fe Gp. Zia Fm in outcrops W of Rio Rancho; Popotosa Fm, W of Lemitar.
Eolian (Hydrostrat. unit: LSF)	Coarser grained, bioturbated sandstones preferentially cemented.	Abundant to absent	Highly variable (<1m to >1km).	Cementation controlled by pre-cementation permeability, and is related in some way to pedogenesis.	Lower Santa Fe Gp. Zia Fm in outcrops W of Rio Rancho.
Playa (Hydrostrat. unit: LSF)	Coarser grained sandstones preferentially cemented. Syndepositional carbonates locally important.	Rare to abundant	Highly variable (<1m to >2km).	Cementation controlled by pre-cementation permeability and depositional environment.	Lower Santa Fe Gp. Zia Fm in outcrops W of Rio Rancho; Popotosa Fm, Gabaldon Badlands.
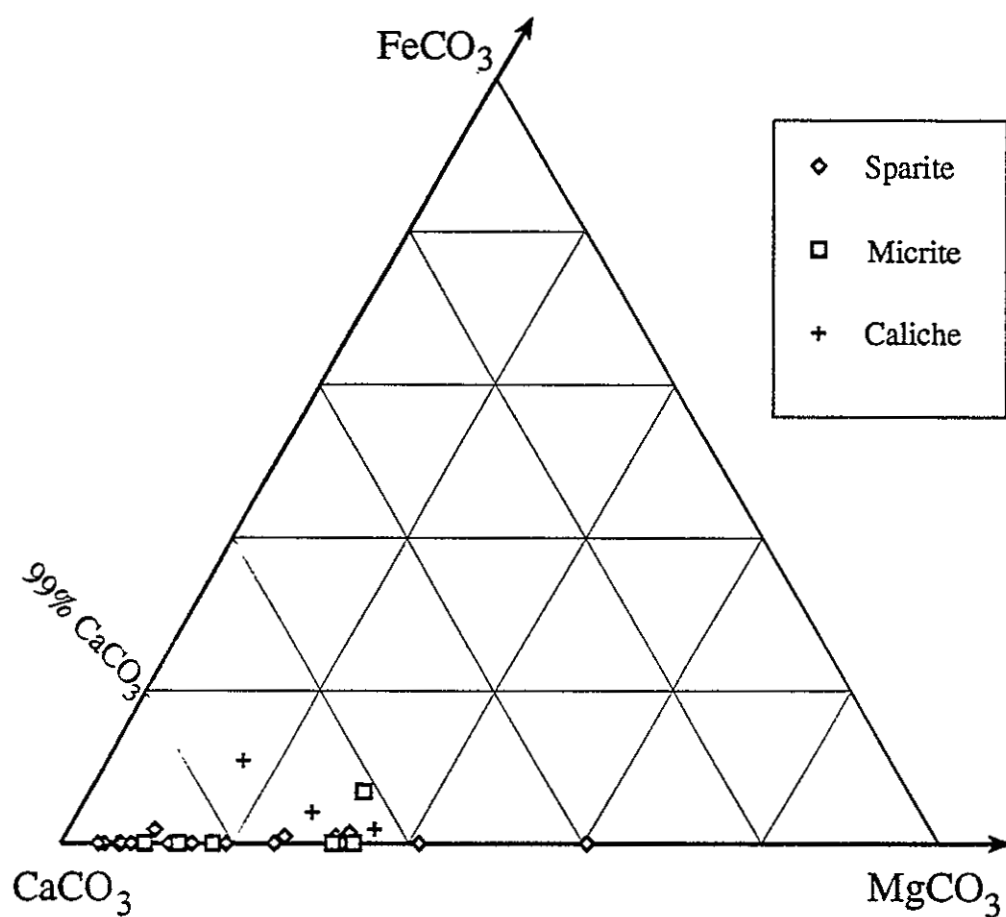
Figure 5-1. Ternary diagram showing composition of calcite in cements and caliche nodules from the ancestral Rio Puerco facies of the Sierra Ladrones Formation. The scale of the plot is at 95% CaCO₃.

Symbol	Lithology	Symbol	Structure
	Conglomerate		Imbrication
	Sandstone		Current ripples
	Silty sandstone		Wavy parallel bedding
	Shaly sandstone		Trough cross-strat.
	Sandy shale/mudstone		Low-angle tabular bedding
	Shale/mudstone	o o o o	Pebbles/granules
	Caliche		Trace fossils
			Planar lamination
			Rip-up clasts
			Convolute bedding

Figure 5-2. Key to lithologic and structural symbols used in Figs. 5-3 through 5-7.
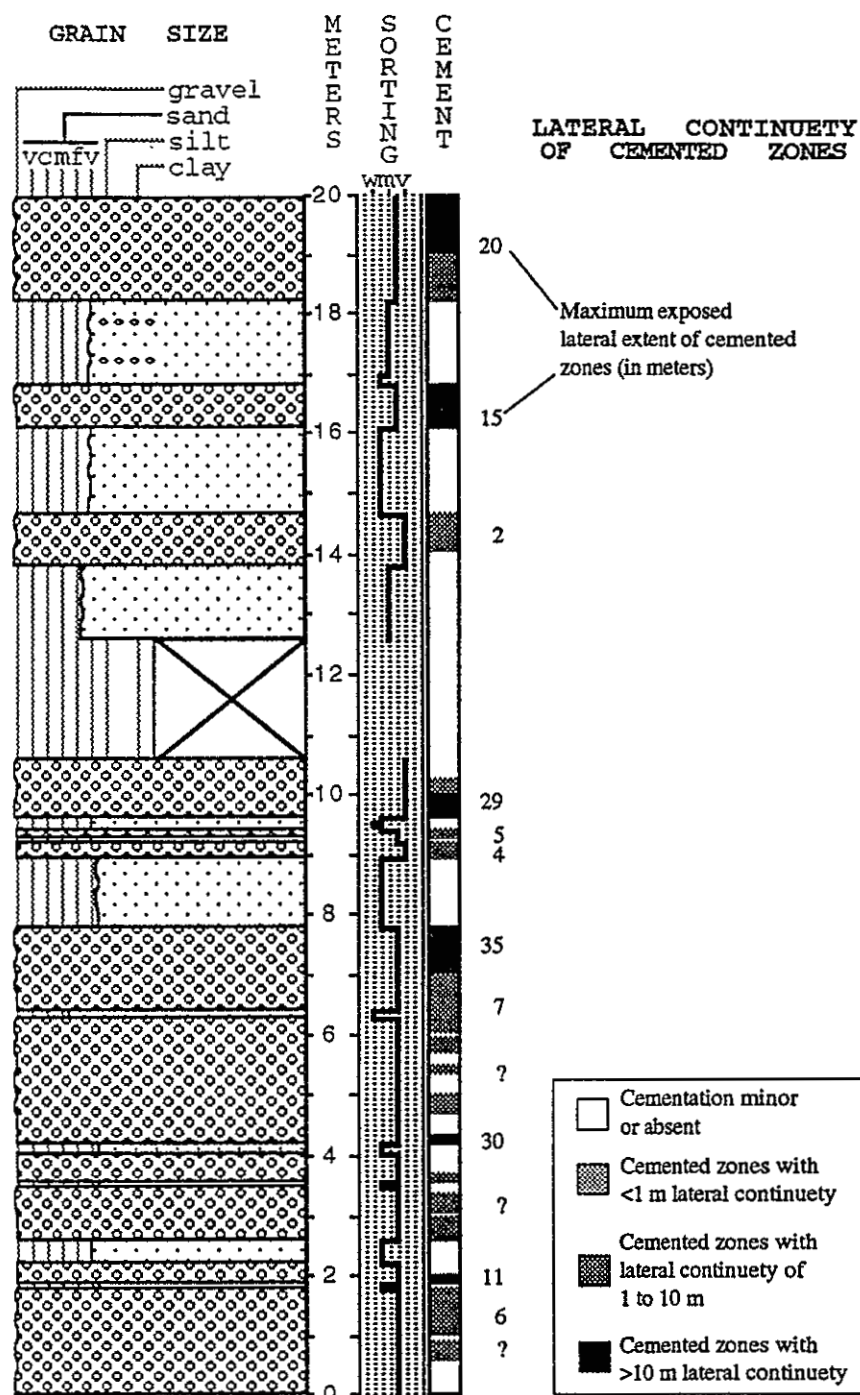
Figure 5-3. Stratigraphic column of Upper Santa Fe Group piedmont slope deposits, near Placitas, NM.
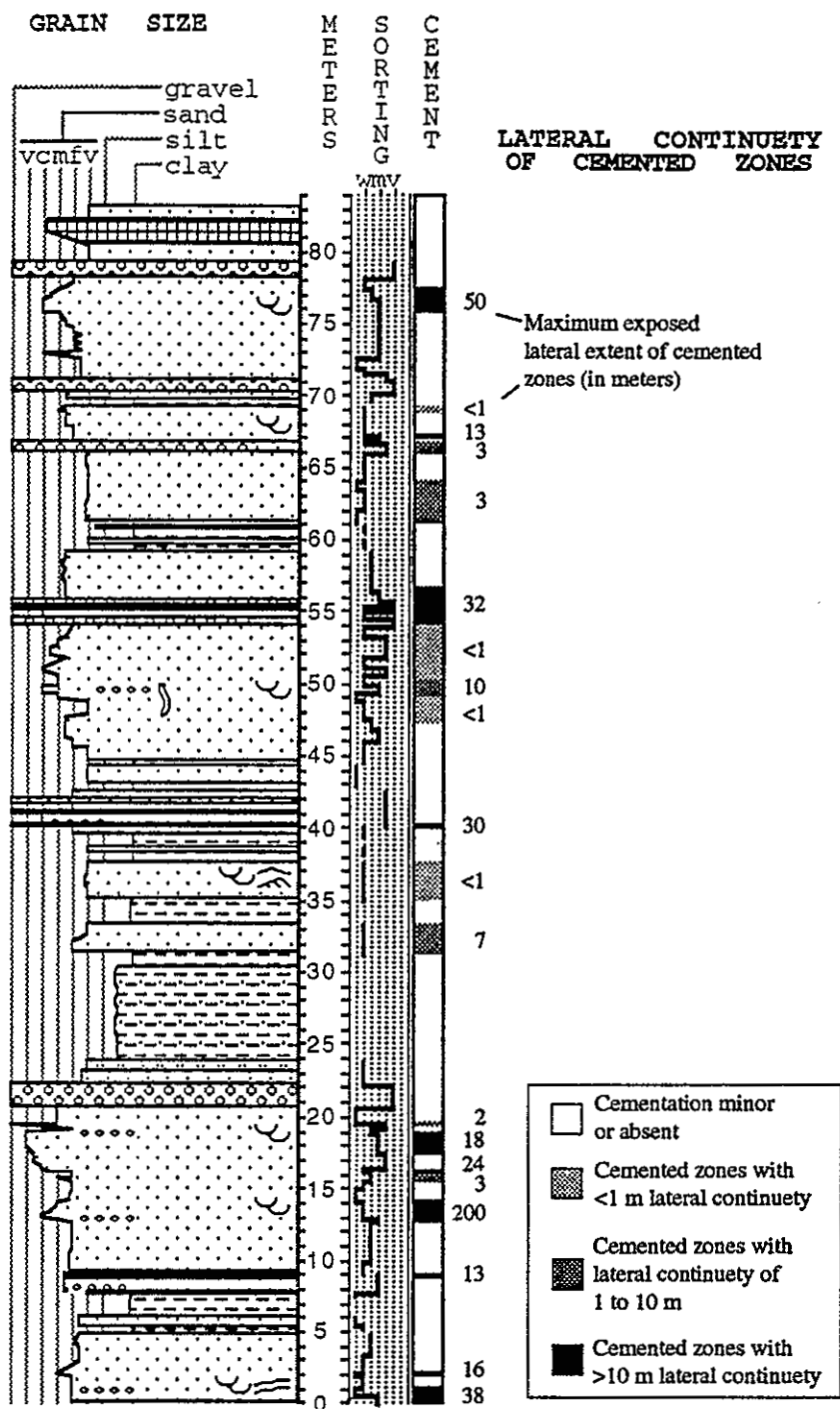
Figure 5-4. Stratigraphic column of ancestral Rio Puerco deposits near Bosque, NM.
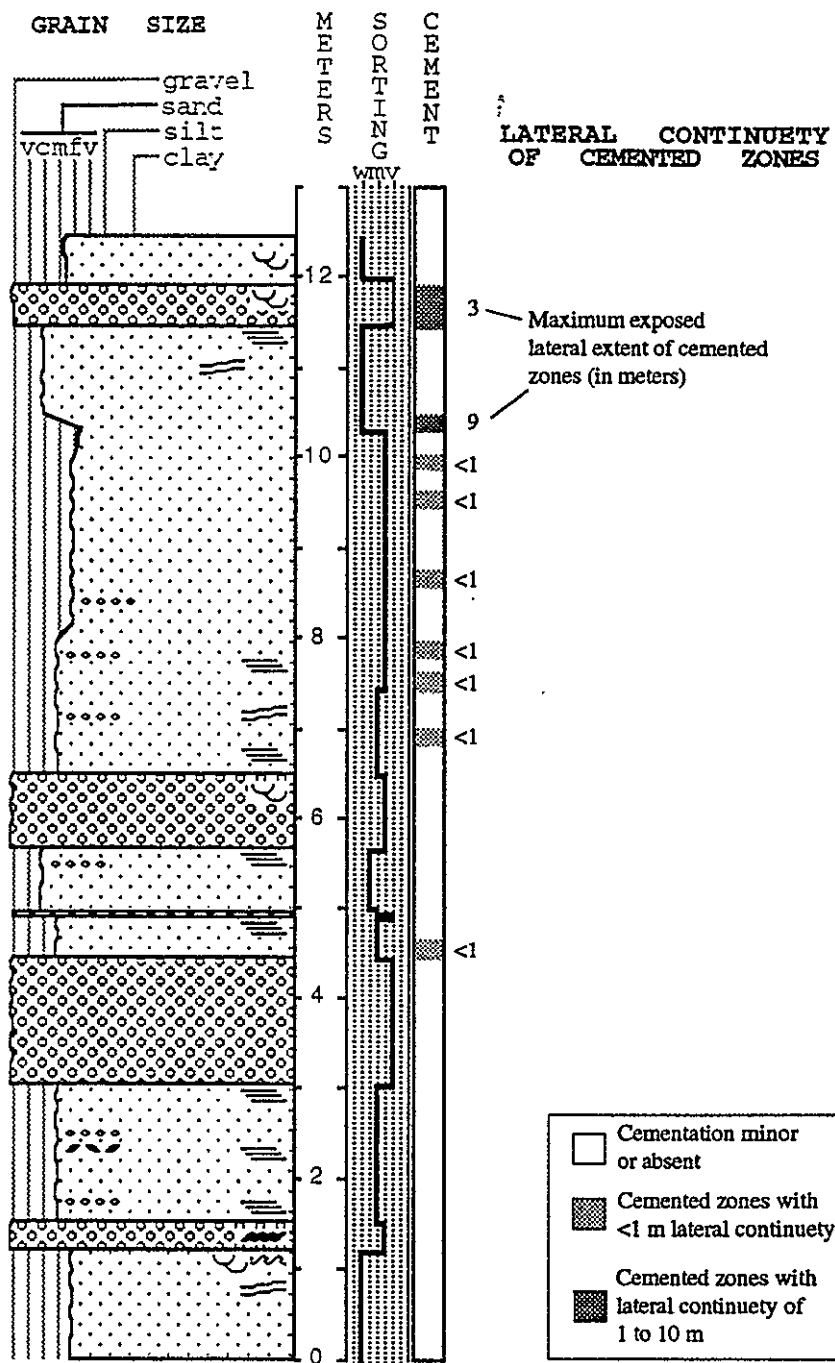
Figure 5-5. Stratigraphic column of ancestral Rio Grande deposits near the Rio Bravo exit on Interstate 25.
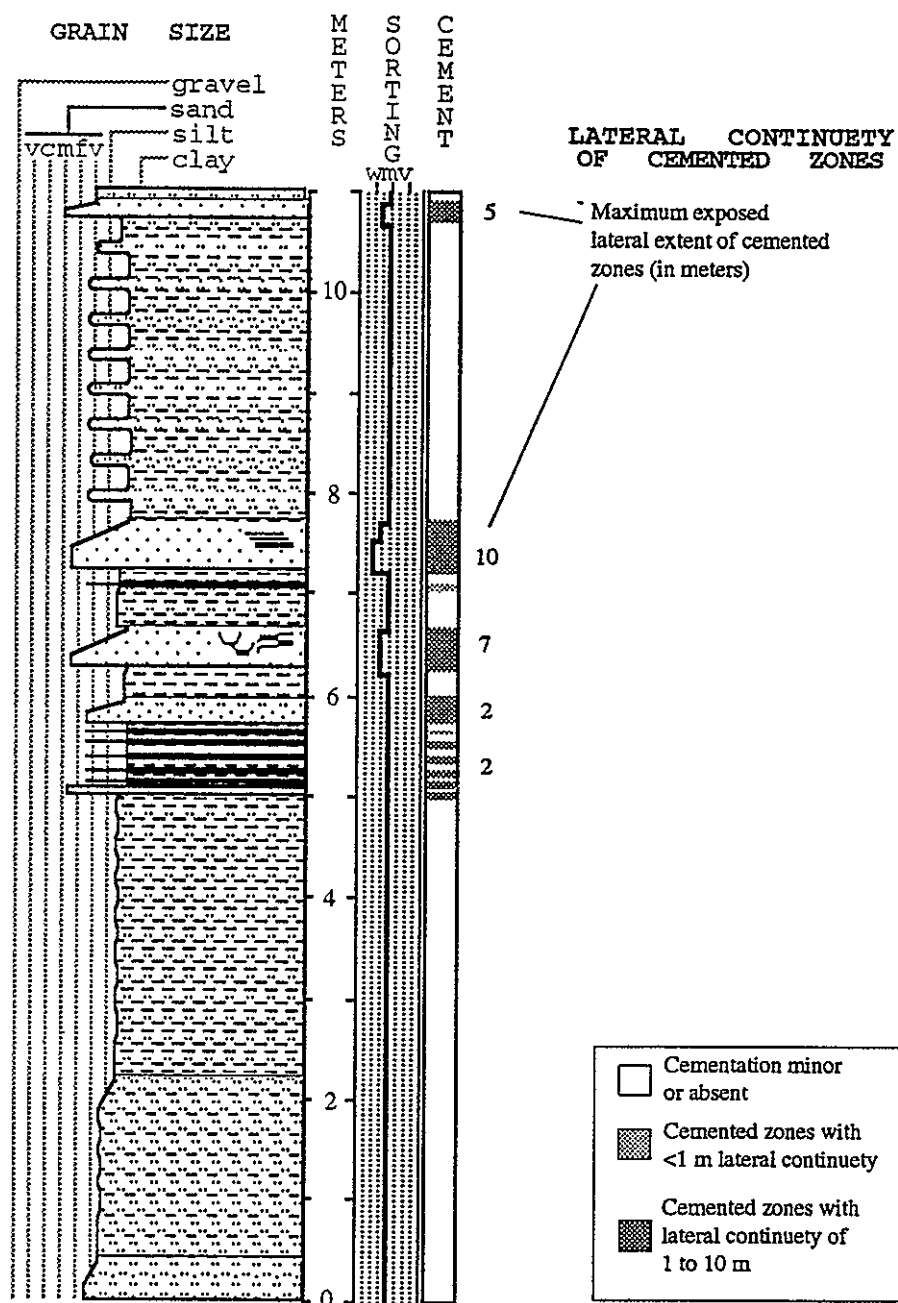
Figure 5-6. Stratigraphic column of closed-basin fluvial deposits in the Zia Formation west of Rio Rancho.
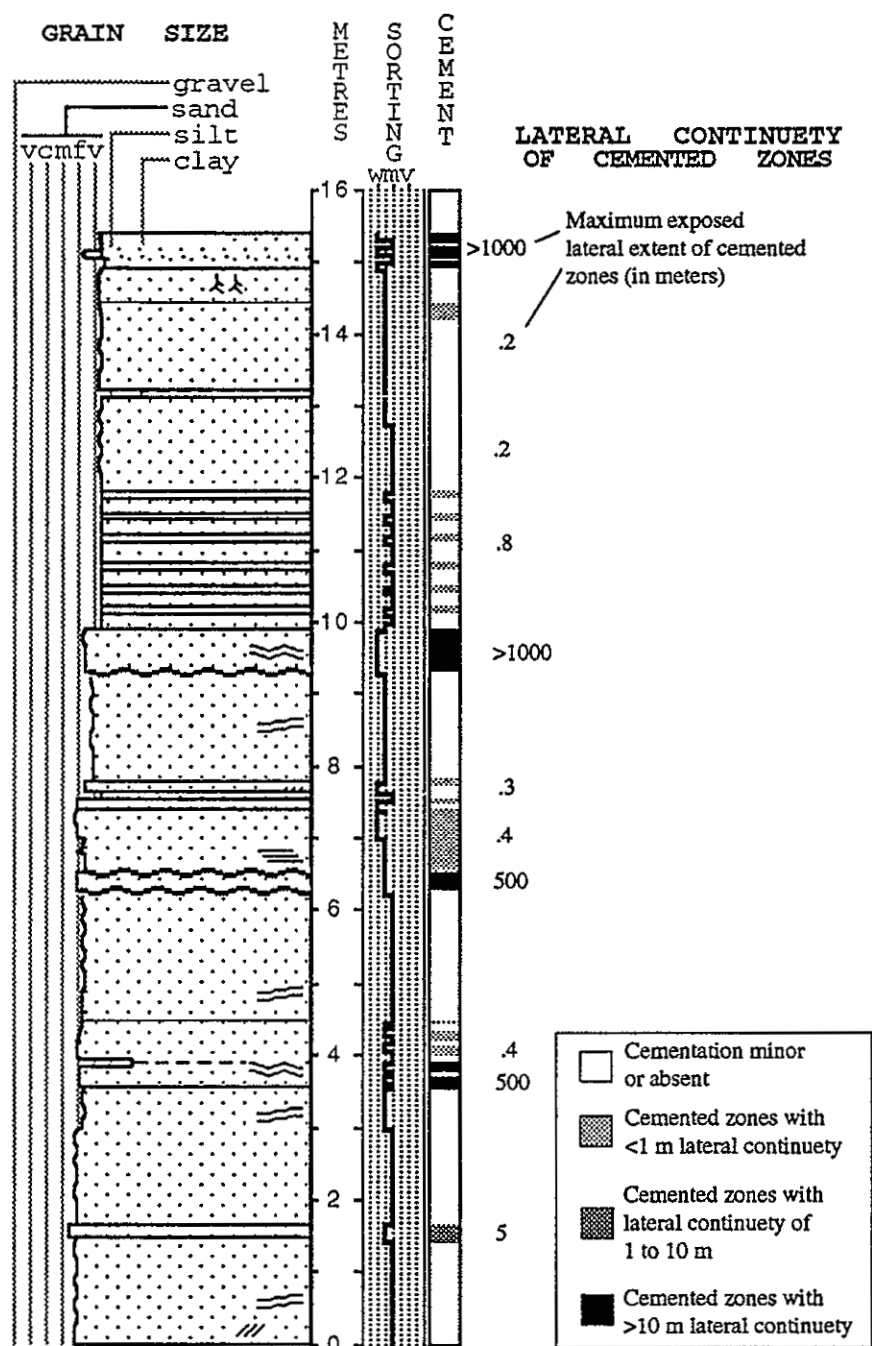
Figure 5-7. Stratigraphic column of eolian deposits in the Zia Formation west of Rio Rancho.

Figure 5-8. Elongate oriented concretion from the ancestral Rio Puerco facies of the Sierra Ladrones Formation. Lens cap is five centimeters in diameter.
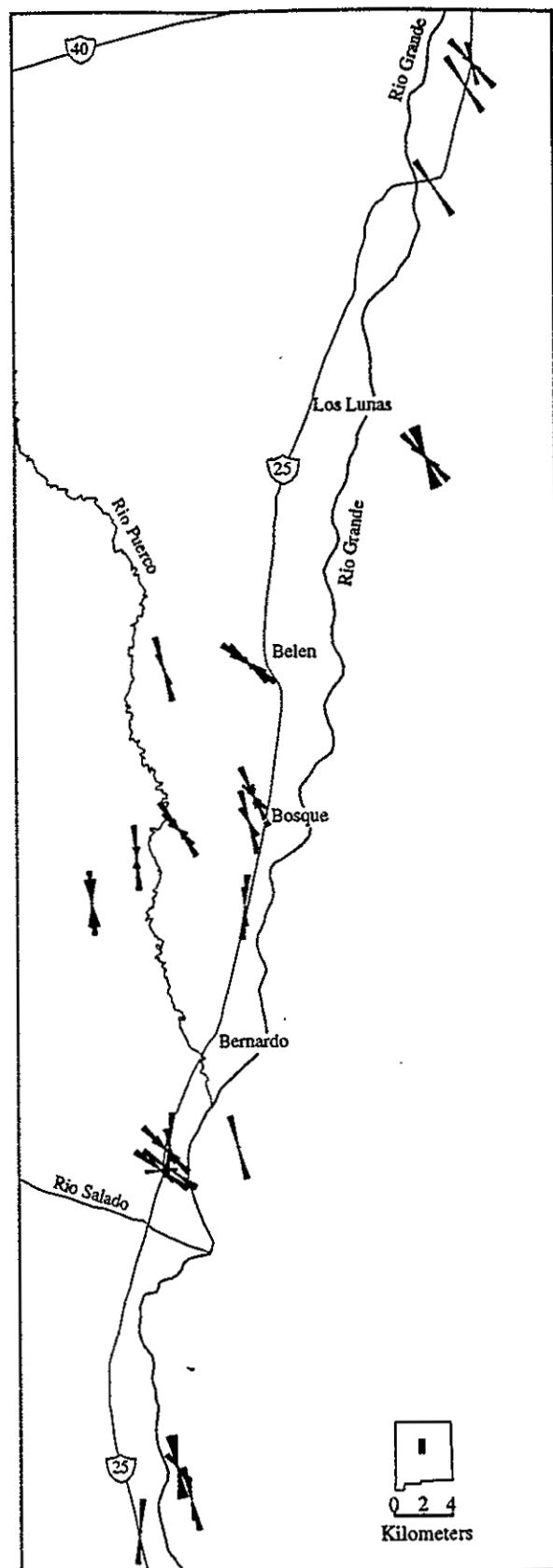
Figure 5-9. Map showing orientation of elongate concretions in the Sierra Ladrones Formation. Orientations are represented by rose diagrams (circular histograms).
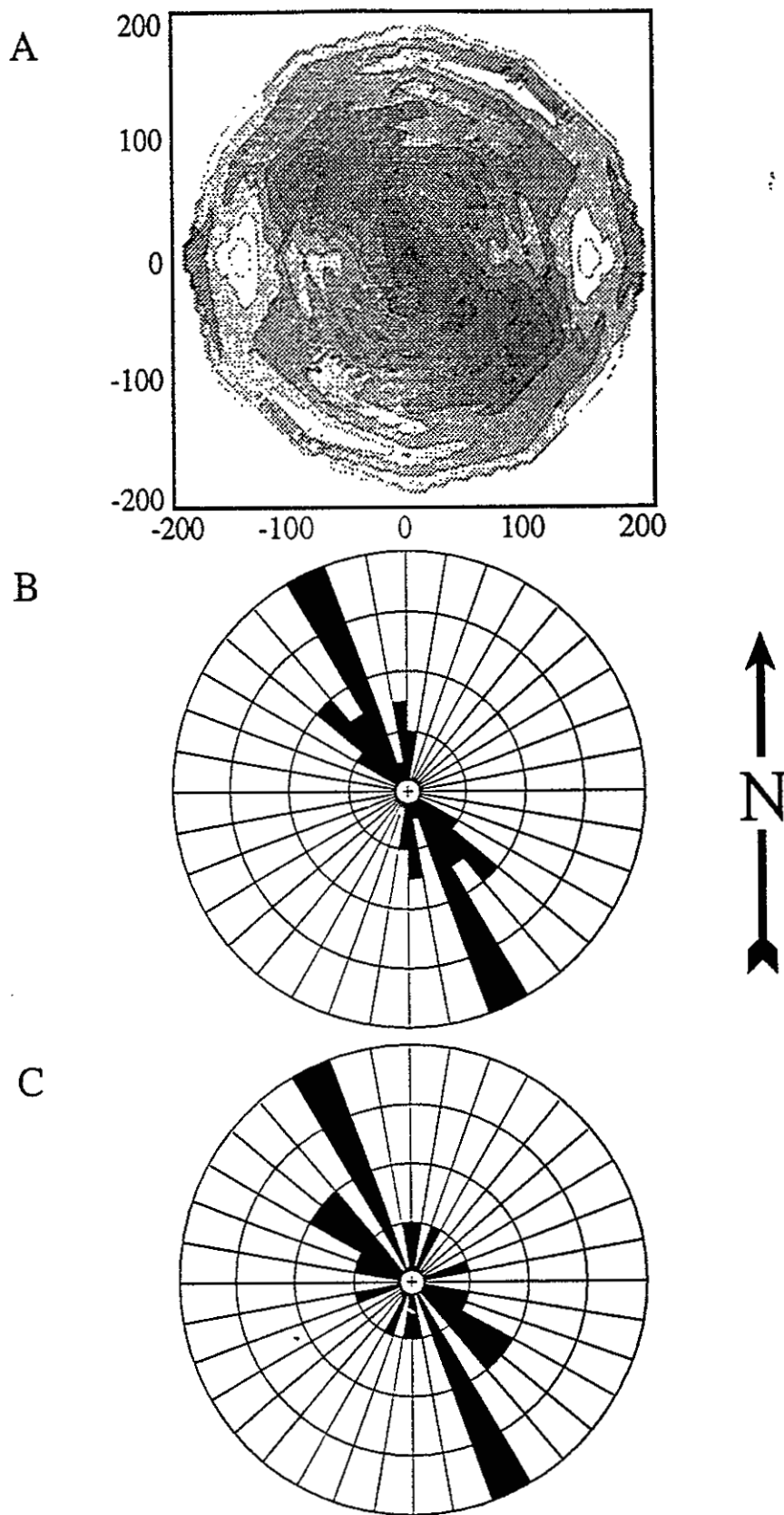
Figure 5-10. Orientation of permeability structure, concretions, and paleocurrents in the same outcrop. (A) Azimuthal horizontal variogram using log-permeability data set; constructed by combining estimates of N0°E, N60°E, N90°E, N30°E, and N60°W; the orientation of greatest correlation is N30°W (From Davis et al., 1993). (B) Rose diagram showing orientation of elongate concretions (N = 23); the vector mean is N28°W, 95% confidence angle is 14°. (C) Rose diagram showing orientation of paleocurrents (N = 14); the vector mean is N39°W, 95% confidence angle is 37°.

Chapter 6

Petrology and Diagenesis of the Santa Fe Group in the Northern Albuquerque Basin, New Mexico

John M. Gillentine
New Mexico Tech, Socorro, NM 87801

PURPOSE AND SCOPE

Diagenesis refers to the collective physical and chemical changes in sediments as they are progressively buried by younger sediment. Its impact on groundwater resources comes about not only through alterations to the original mineralogical composition of sediment, but through modifications to the porosity and permeability of those sediments as well. Chemical reactions between groundwater and aquifer minerals result in the release of certain ionic species into solution, and the fixing by precipitation of certain other species into secondary or "authigenic" minerals.

This portion of the study expands on earlier characterization of the hydrogeologic framework of the Albuquerque basin (Hawley and Haase, 1992) by exploring in greater detail the sedimentary petrology and diagenesis of aquifer zones in the middle and lower Santa Fe Group. The approach was to examine the primary and secondary components of basin-fill, and then, from the results of this examination, to draw inferences regarding the geochemical environment that would account for the observed alterations. Specific questions addressed in this study are:

1. Can systematic changes in the physical or chemical character of sediments be recognized at progressively greater well depths?

2. Can distinct diagenetic zones or facies be identified that represent differing chemical conditions in various depth intervals?

3. Is authigenesis linked to primary mineralogy and depositional fabric (lithofacies), to an evolving pore-fluid chemistry, or both?

Data for the study were obtained from sidewall core samples and cuttings of four municipal wells located in different parts of the basin (Figure 6-1).

SUMMARY

Forty-seven side-wall cores from four wells were examined using petrographic and scanning electron microscopy to determine the distribution and relative abundance of both detrital and authigenic minerals as well as aquifer porosity characteristics. An electron microprobe was used to determine the chemical compositions of selected minerals. Authigenic clays are relatively

abundant in all samples examined. Zeolites are often associated with authigenic clay and tend to occur in medium- to coarse-grained sands with a relatively high volcanic rock fragment content, but are not limited to such sands. For example, zeolites were found in COA wells Charles Wells 5 and 6 (Ch-5 and 6) east of the Rio Grande, but they were not found in wells SAF-1 or Cerro Colorado 1 (CC-1), which are west of the Rio Grande, despite the presence of volcanic rock fragments in the latter two wells. Therefore, parent mineralogy may not be the only controlling factor for zeolite precipitation. Authigenic carbonates were not abundant in the four wells examined. In general there is no relationship between porosity and depth in the four wells examined.

TABLE OF CONTENTS

LIST OF TABLES

LIST OF FIGURES

Figure 6-1. Index map of Albuquerque Basin area showing location of Albuquerque Municipal Wells: Charles Wells 5 and 6 (Ch5 & 6), Cerro Colorado 1 (CC1) and Soil Amendment Facility 1 (SAF1). Map base from Thorn et al. (1993, Fig. 16); see Plate 3 (Hawley, this report) for revised locations of major faults and buried axial-channel boundaries.

Figure 6-2. Ternary diagram of detrital modes (after Folk, 1974). Q = quartz; F = feldspar; R = rock fragments; URF = undifferentiated rock fragments; VRF = volcanic rock fragments; SRF = sedimentary rock fragments. Definition of parameters in Appendix A. Differences in sandstone composition between west mesa wells (CC1 and SAF1, solid symbols) and east mesa wells (CW5 and CW6, open symbols) is the result of differences in respective source area.

Figure 6-3. Distribution of authigenic minerals with depth occurrence. Mineral abundance, expressed in terms of relative pore volume, is independent of burial depth.

Figure 6-4. Cement groups plotted according to texture of host sediment. Zeolites and Zeolites + clay occur in coarser grained, less sorted sands, whereas carbonate and carbonate + clay occur in finer grained, better sorted sands. Grain Size and sorting from Appendix A, Table 2; cement groups from Appendix C.

Figure 6-5. Total macroporosity of each core sample, as a percentage of 300 point counts. Porosity generally decreases with increasing well depth, suggesting porosity loss to compaction and occlusion by mineral cements. Wide differences in porosity of samples from similar depths reflect the extreme heterogeneity in sedimentary texture.

Figure 6-6. Secondary porosity resulting from framework grain dissolution, alteration and fracture, expressed as a percentage of 100 porosity point counts. Secondary porosity generally increases with depth, suggesting diagenetic modifications to original porosity are more pronounced in deeper aquifer zones.

Figure 6-7. Minus-cement porosity versus total cement for each of the dominant cement types (after Houseknecht, 1987). NE-SW diagonal lines are lines of equal intergranular volume (post-cementation/compaction); NW-SE diagonal line separates graph into a cementation-dominated field (above) and a compaction-dominated field (below).

Figure 6-8. Relative abundance of framework grains versus well depth from Cerro Colorado 1. Definition of counted parameters in Appendix A.

Figure 6-9. Relative abundance of framework grains versus well depth for SAF 1. Definition of counted parameters in Appendix A.

Figure 6-10. Relative abundance of framework grains versus well depth for Charles Wells 5. Definition of counted parameters in Appendix A.

Figure 11. Relative abundance of framework grains versus well depth for Charles Well 6. Definition of counted parameters in Appendix A.

Chapter 6

Petrology and Diagenesis of the Middle and Lower Santa Fe Group in the Northern Albuquerque Basin, New Mexico

John Michael Gillentine
New Mexico Institute of Mining and Technology
Socorro, New Mexico

ABSTRACT — Santa Fe Group sediments within the northern Albuquerque Basin mirror the basin's complex geologic setting and tectonic history, containing fragments of Precambrian plutonic and metamorphic rocks, Paleozoic and Mesozoic sedimentary rocks, and Cenozoic volcanic rocks shed from surrounding uplands. Sidewall-core samples of basin-fill deposits obtained from four Albuquerque municipal wells located in basin areas both west and east of the Rio Grande Valley classify as feldsarenite, lithic arkose or feldspathic litharenite. Differences in grain composition across the basin indicate dissimilar provenance. Plutonic and metamorphic sediments were probably derived from the northwest, whereas volcaniclastic sediments originated in the Jemez, Espinosa or Latir volcanic fields to the north. Abundant quartz (some grains with recycled overgrowths) in West Mesa cores were possibly derived from Cretaceous rocks that crop out to the west. Differences in the primary composition of cores were found not to control authigenesis because soluble detrital minerals are present in quantities more than adequate to provide the chemical species necessary for secondary mineral precipitation. Authigenic minerals are zeolite and calcite cements, and smectite or illite/smectite occurring as pore-fillings and alterations of framework aluminosilicates. Not all phases are present in all wells, and no systematic occurrence of any one phase is discernable in any given well. Changes in pore-water chemistry and mineral mass during the formation of the authigenic minerals were modeled using the program PHREEQE. Results of simulations using City of Albuquerque water quality data indicate that water at the well head is not in equilibrium with authigenic minerals observed in thin section. Precipitation of individual model phases or combinations of phases required pore waters of distinctly different chemistry, suggesting the aquifer system is compartmentalized into discrete chemical zones. Available data does not allow definition of zone boundaries, but it is apparent from the sample set that they may be very small, perhaps on the order of cubic meters.

INTRODUCTION

Recent concern over the quality and long-term availability of groundwater within the Albuquerque basin, and the growing realization that groundwater resources within Bernalillo County are more limited than previously thought to be, has sparked interest for new research into the character of Santa Fe Group deposits that comprise the aquifer (Thorn, et al., 1993; Kernodle et al., 1995; Hawley and Haase, 1992;

6-1

Hawley et al., 1995). As shallower aquifer zones in the Albuquerque-Rio Rancho Metropolitan area are depleted, progressively deeper groundwater reserves will be developed, where factors controlling transmissivity, conductivity and water quality are less well understood.

This portion of the study expands on earlier work characterizing the hydrogeologic framework of the northern Albuquerque Basin (Section IV in Hawley and Haase, 1992) by exploring in greater detail the sedimentary petrology and diagenesis of aquifer zones in the Middle and Lower Santa Fe Hydrostratigraphic Units (MSF and LSF). The approach was to examine the primary and secondary mineralogical components of basin fill, and from the results of this examination infer the geochemical environment that would account for the observed alterations. Data for the study were obtained from sidewall core samples of four Albuquerque municipal wells located in both the West Mesa (Llano de Alburquerque) and East Mesa (NE Heights) areas of the basin (Figure 6-1). Specific questions addressed in this study are:

1. Can systematic changes in the physical or chemical character of sediments be recognized in progressively older deposits penetrated by deep wells?

2. Can distinct diagenetic zones or facies be identified that represent differing chemical conditions in various depth and stratigraphic intervals?

3. Is authigenesis linked to primary mineralogy and depositional fabric (lithofacies), to an evolving pore-fluid chemistry, or both?

Diagenesis refers to the collective physical and chemical changes in sediments as they are progressively buried by younger deposits. Its impact on Albuquerque Basin groundwater resources comes about not only through alterations to the original mineralogical composition of the Santa Fe Group basin fill, but through modifications to the porosity and permeability of these sediments as well. Chemical reactions between groundwater and aquifer minerals result in the release of certain ionic species into solution, and the fixing by precipitation of certain other species into secondary or

authigenic minerals. Special technical terminology used in this chapter is defined in the following glossary.

GLOSSARY

Aphanitic
igneous texture consisting of crystalline aggregates whose grain size is too small to be identifiable with the unaided eye.

Axiolitic
divitrification fabric of volcanic rock that emanates outward from a central or axial plane of relict glass shard.

Fabric
inclusive term for both texture and structure.

Felsitic
groundmass texture of volcanic rock consisting of equigranular mosaic of equant or elongate silicate minerals.

Felted
birefringent microlites of euhedral feldspar oriented sub parallel to each other as result of flow of magma.

Fragmental
texture of igneous rock produced by explosive eruption or other volcanic process; fragmental rocks are typically structureless and exhibit no size-sorting of constituent grains.

Granoblastic
fabric of metamorphic rock consisting of mosaic of equidimensional, anhedral grains.

Groundmass
fine-grained matrix of porphyritic igneous rock.

Microlitic
groundmass texture of volcanic rock consisting of microscopic feldspar laths; term includes felted and trachytic textures.

Phenocryst
relatively large mineral crystals present within groundmass of porphyritic igneous rock.

Poikilitic
intergrowth texture where detrital grains are enclosed within larger crystals of another mineral (typically an authigenic mineral).

Porphyritic
igneous texture consisting of large mineral crystals (phenocrysts) residing within an appreciably finer-grained matrix, or groundmass.

Spherulitic
devitrification fabric of volcanic rock where spherical to ellipsoidal clusters of radiating fibrous crystals lie in a glassy, or occasionally felsic, aphanitic matrix.

Structure
relationship of groups or aggregates of grains, such as bedding or folds in bedding, flow structures in volcanic rocks.

Texture
relationship between individual grains and grains immediately surrounding them, specifically grain size, shape and sorting.

GEOLOGIC SETTING

The Rio Grande rift extends for nearly 600 miles (1000 km) from Leadville, Colorado, to Chihuahua, Mexico, and shares scale and geophysical characteristics with such systems as the Rhinegraben and East African rifts (Olsen et al., 1987; Ingersoll et al., 1990). The northern portion of the north-south trending rift consists of four linked axial basins: the upper Arkansas, San Luis, Espanola and Albuquerque Basins from north to south, respectively. The rift bifurcates near Socorro, New Mexico and widens toward the south into smaller, sub-parallel basins in basin-and-range style extension (Chapin, 1988). Located within the central part of the rift zone, the Albuquerque Basin Complex is physiographically distinct from adjacent basins because of its scale. It covers an area of approximately 4250 square miles (11,000 km^2) (Kelley, 1977), and has structural blocks vertically offset by as much as 35,000 ft. (10 km) (May and Russel, 1994). The Basin Complex is bounded on the east by the Sandia, Manzano and Los Pinos uplifts and on the west and northwest by the Lucero and Nacimiento uplifts. It comprises structural and geohydrologic subdivisions previously referred to as the Santo Domingo and Albuquerque-Belen Basins, which, in turn, include a group of intra-basin structural lows (depressions) and highs that are described in other sections of this report (cf. plates 1-17. Appendix G-J)..

Geological and geophysical investigations of the deep subsurface, (including oil and gas exploration wells, gravity surveys, and seismic profiling) have shown that the internal geometry of the basin consists of at least two groups of down-faulted basins (grabens) dominated by an eastward-dipping half-graben complex north of the Tijeras (transverse) structural trend, and a westward-dipping half-graben to the south (Lozinsky, 1994; Russell and Snelson, 1994; Hawley et al., 1995). This style of linked half-graben architecture, where the polarity of down-dropped margins alternates along the length of the rift, is typical of Rio Grande basins (Chapin, 1988), as well as of other continental rifts systems worldwide (e.g., Rosendahl et al., 1986). Structural linkages between parallel, right-stepping rift segments are thought to occur at transfer,

or accommodation zones of nested fault systems that conserve the regional extensional strain, and "accommodate" changes in graben polarity (Rosendahl et al., 1986). Alternatively, rift segments may be linked by offset, or "dogleg" segments that propagate in a direction oblique to the regional extensional direction (Nelson et al., 1992). According to these workers, rift-offsets are characterized by a bimodal fault pattern, with a dip-slip component in the normal segment and an oblique-slip component in the offset segment. Non-plane strain in Albuquerque Basin offsets may have resulted in lesser dip-slip displacement relative to the normal, north-south trending basin segments, and produced inter-graben structural saddles that separate the Santo Domingo, Central Albuquerque, and Belen subbasins. Differential displacement would coincide with significant rotation of structural blocks (Nelson et al., 1992). The length of subbasin segments and the position of rift-segment joins are thought to be inherited from pre-existing (Laramide to Precambrian), northeast-trending lineaments (Chapin and Cather, 1994).

The asymmetric geometry of the Albuquerque Basin has exerted an important influence on diagenesis by controlling the distribution of sedimentary facies within the basin. Geometry controls not only the original composition of the basin-fill by determining clastic input from various source-terranes, but also has a significant influence on sediment transport energy and burial rate, sedimentary texture and degree of compaction (Allen and Allen, 1990).

Evidence for the timing of rift initiation comes from (1) radiometric ages of basalts, basaltic andesites and dacites interbedded with basal coarse clastics of the Popotosa Formation (Bachman and Mehnert, 1978; Osburn and Chapin, 1983), (2) ages of rift-related dike intrusions (Aldrich et al., 1986; Henry and Price, 1986), and (3) ages of the youngest mid-Tertiary ignimbrites of the northwest Mogollon-Datil volcanic field that sheeted across the pre-rift topography near Lemitar, New Mexico (Chamberlin, 1983; Osburn and Chapin, 1983; McIntosh et al., 1986). The combined evidence points toward a 28-27 Ma. age for the onset of rifting, which is supported by the shift in regional magmatism from intermediate, caldera-related lavas to predominantly basaltic, rift-related lavas by 26-24 Ma. (Dungan et al., 1989).

PREVIOUS WORK

Stratigraphy And Stratigraphic Nomenclature

Excellent summaries of previous stratigraphic work are given by Spiegel and Baldwin (1963), Galusha and Blick (1971), Kelley (1977) and Tedford (1982). The original term used by Hayden (1869) to describe the unconsolidated alluvium near the City of Santa Fe was "Santa Fe marls." This was modified to "Santa Fe Formation" by Darton (1922), who surveyed the region in a very general way during a statewide reconnaissance into the oil and gas and economic minerals potential of New Mexico. He mapped the entire Albuquerque Basin as QT -- alluvium (Recent) and Santa Fe Formation (Miocene and Pliocene), reporting an average thickness of the Santa Fe as ±450 ft. Although it was generally understood that the "Santa Fe Formation" comprised most of the unconsolidated deposits within the Rio Grande Depression from Colorado to Texas (Bryan, 1938), no formal type locality or unit subdivisions were specified until Denny (1940) published a map of the Pojoaque-Nambe area north of Santa Fe. He limited the Santa Fe Formation to "those deformed and predominantly fluviatile deposits of the Santa Fe region that contain the [mammalian] vertebrate fauna" (p.680); he placed the Santa Fe in the mid-Miocene to upper Pliocene.

In the Albuquerque area, some of the earliest detailed work was done by Bryan and McCann (1937, 1938), who preserved the definition of the Santa Fe as a regional unit, but recognized also the individuality of adjacent structural basins along the length of the rift. Despite discontinuity of outcrop, shifts in provenance and fragmentary fossil evidence, they were able to trace the Santa Fe Formation from Hayden's generalized type locality into the northwest Albuquerque Basin on the basis of similar faunal ages and depositional style between basins. Bryan and McCann (1937) informally named three sandstone members along the north-west flank of the Llano de Alburquerque (i.e., Ceja Mesa), the lower gray, middle red, and upper buff, that underlie Pleistocene pediment and terrace gravels (the "Ortiz gravels" first described by Ogilvie, 1905). However, this broad, three-fold subdivision has not been adopted by all workers. Galusha (1966) formally introduced the Zia Sand Formation, which is roughly equivalent to the lower gray member of Bryan and McCann, but placed it

below the Santa Fe Formation. Galusha and Blick (1971) stated that the three divisions are "not applicable to beds of the type area of the Santa Fe Group." Bailey et al. (1969) also departed from the three-member subdivision, describing and naming the Cochiti Formation in the southeastern Jemez Mountains. This unit, consisting of volcanic detritus derived from the Keres Group, was mapped to where it grades into coarse red granitic sands beneath Santa Ana Mesa. They narrowly defined the Santa Fe Formation, bounding it below by the Zia Sand Formation of Galusha (1966), and above by the Cochiti Formation. The fact that the Cochiti grades into beds of the Santa Fe Formation and is time-equivalent to the Santa Fe led Kelley (1977) to assert that it is equivalent to the middle red member and thus only a facies of the Santa Fe.

Kottlowski (1953) first proposed raising the Santa Fe to group status, a practice followed by Spiegel and Baldwin (1963), who used the term "Santa Fe Group" to describe a section of basin fill that included basal "mid Miocene (?)" volcanic flows and "Pleistocene (?)" Ortiz gravels. They subdivided the basin-fill of the La Cienega-Seton Village area near Santa Fe into the Tesuque and Ancha Formations, and extended the Santa Fe Group to include areas adjacent to, but outside of the Rio Grande trough itself. Galusha and Blick (1971) originally suggested restricting the use of the term Santa Fe Group to the Espanola Basin type-locality, but subsequent workers have tended to use the much broader stratigraphic concept formally introduced by Bryan in 1938 (Hawley, 1978; Tedford, 1981; Chapin, 1988).

In a comprehensive study of the Albuquerque Basin, Kelley (1977) did not subscribe to group status for the Santa Fe, believing that mappable units were too indistinct to be elevated above member status. However, he did further define Bryan and McCann's (1937) three broad subdivisions, formally renaming two of the units Zia ("lower gray") and Ceja ("upper buff") members. Kelley argued that pervasive lateral and vertical interfingering of units precludes finer stratigraphic subdivision.

This complex interfingering and gradation of units, combined with relatively rapid changes in unit thickness, compositional variability and incomplete exposure, have made stratigraphic correlation difficult. Consequently, there has been considerable inconsistency in the stratigraphic nomenclature. Despite arguments that

favor a limited definition of the Santa Fe (splitting as opposed to lumping), current practice is to consider the syn-rift basin-fill in a regional context by using the group terminology and by making allowance for local variability (e.g., Chapin, 1988; Ingersoll et al., 1990).

Hawley and Haase (1992) subdivided the entire basin-fill into three units: 1) pre-Santa Fe Tertiary deposits, 2) Santa Fe Group deposits, and 3) post Santa Fe Group Quaternary deposits. In their conceptual model of basin hydrogeology, Santa Fe Group deposits were subdivided into Lower, Middle and Upper hydrostratigraphic units on the basis of shifts in depositional style over time, and roughly correspond to Bryan and McCann's (1937) and Kelley's (1977) formational subdivisions. Pre-Santa Fe units include the Galisteo and Baca Formations and consist primarily of sandstones, siltstones and mudstones of non-volcanic origin. A third pre-Santa Fe unit was identified in the southern Albuquerque basin by Lozinsky (1988, 1994) and referred to informally as the "unit of Isleta Well No. 2." It differs from the underlying pre-Santa Fe units in that it is mostly volcanogenic, correlating with Datil Group volcanic and volcanic-related sequences. Post Santa Fe Quaternary deposits consist of Pleistocene-Holocene valley-fill, inset stream terraces and alluvial fan deposits.

Basin Evolution

Current concepts of the basin's tectonic and depositional history are reviewed by Chapin and Cather (1994), Lozinsky (1994), May and Russell (1994), Russell and Snelson (1994), and Hawley et al. (1995). Lower Santa Fe Group units deposited from about 28-15 Ma. indicate an internal drainage system, and consist of fine-grained, playa-type mudstones and siltstones in the basin floor that intertongue laterally with eolian and basin-margin piedmont units. Increased tectonism and rapid sedimentation from about 15-5 Ma. deposited units of the Middle Santa Fe Group, which is the thickest sequence in the section and is marked by the appearance of fluvial deposition in the basin floor. After about 5 Ma., infilling of the basin's half graben segments had progressed to where the ancestral Rio Grande became a through-going system, integrating the sediments of adjacent basins. Upper Santa Fe Group deposits are thus

comprised of axial river sands and overbank fines in the deeper, central basin that intertongue laterally with poorly sorted sands and conglomerates of coalescing piedmont aprons at the uplifted basin margins. After about 1 Ma. the ancestral Rio Grande and Rio Puerco river systems began to incise the Santa Fe Group valley fill, leaving the Llano

de Alburquerque geomorphic surface between the two river valleys. Post-Santa Fe Group Quaternary units are mostly backfill sequences that consist of coarse and poorly sorted fluvial-terrace deposits and the modern floodplain sediments of the Rio Grande and Puerco Valleys (Lambert, 1968; Lambert et al., 1982; Machette, 1985; Hawley and Love, 1991).

Basin-Fill Diagenesis

Walker et al. (1978), in their overview paper on diagenesis of first-cycle alluvium in the desert southwest, found that Santa Fe Group outcrops sampled along the Rio Grande rift share textural and mineralogical similarities with outcrop samples of Pliocene (?) fanglomerates from Baja, California, and with core samples of Plio-Pleistocene Gila Group deposits near Tucson, Arizona. These workers maintained that arkosic sediments of arid-region basins characteristically exhibit a decrease in textural maturity following the onset of diagenesis through precipitation of authigenic clay minerals, and an increase in mineralogical maturity through dissolution and replacement of framework grains. Disequilibrium between granitic and volcaniclastic detritus and circulating groundwater were believed to result in geologically rapid post-depositional alteration. Unless ions released by intrastratal dissolution are later precipitated as cementing agents, groundwaters may remove these ions completely from interstitial pore spaces.

Groundwater removal of dissolved constituents was apparently not a major factor in Santa Fe Group diagenesis at San Diego Mountain near Las Cruces, New Mexico (Mack and Grigsby, 1985). Early precipitation of hematite as a grain-rimming cement was succeeded by pore-filling calcite cements of progressively higher

Fe^{2+}/Mn^{2+} ratios, suggesting that pore waters became progressively reducing over time. Persistence throughout the section of mechanically infiltrated clays and authigenic calcium smectite void-filling cements further suggests that diagenetic reactions were controlled by an essentially closed-system pore fluid evolution. The conspicuous absence of authigenic zeolite and feldspar was attributed by the authors to the stability of early calcite cements, which inhibited later chemical interaction between detrital grains and pore solutions. Calcite cementation was also linked to the absence of any well-defined trend in compaction, despite the 3000 ft (950 m) thickness of section.

An earlier diagenetic survey of the Albuquerque Basin was made by Mozley et al. (1992). Calcite and zeolite cements were identified in thin-sectioned sidewall cores, and grain-rimming authigenic smectite was detected in SEM. Intragranular porosity (from dissolution of soluble framework grains) was defined by insoluble clay coatings surrounding "ghost grains," and by preferentially dissolved feldspars and volcanic rock fragments.

METHODS
Sampling

Four wells drilled within the last ten years by the City of Albuquerque provided the basic data for the present study (Figure 6-1). Charles Wells 5 and Charles Wells 6 are Water Utility Division production wells located east of the Rio Grande in the Albuquerque Northeast Heights. Cerro Colorado 1 and Soil Amendment Facility 1 (SAF 1) are Solid Waste and Public Works Department exploratory wells located on the west mesa. These four wells are unique among city wells because they were sidewall-cored in selected sandy intervals. Sidewall cores more successfully preserve the character of sediments than do rotary cuttings. However, few core samples could be obtained from depths less than about 2000 ft because shallower Santa Fe strata are poorly consolidated. Drill cuttings were also collected from these wells at ten foot intervals, but incompletely lithified samples were seldom preserved.

Thin-Section Preparation

Selected sidewall cores from sandy intervals were thin-sectioned by a commercial laboratory. All thin-sections were vacuum-impregnated with a blue-dyed epoxy to distinguish true porosity from porosity created during thin-section preparation. Most samples were stained for potassium feldspar, and many for plagioclase feldspar. Selected thin-sections were hand polished with aluminum oxide paste for microprobe analysis.

Sandstone Petrography

The modal composition of forty-nine thin-sections was determined using a Swift Model F automated point-counter. Counting was done under plane-polarized light with occasional use of cross-polarized light. Three hundred points were counted per sample using a modified version of the Gazzi-Dickinson method (Gazzi, 1966; Dickinson, 1970) that allowed simultaneous tracking of both the mineralogy of grains and the type of rock fragment within which they occur. This method helped assess the potential contribution of unstable minerals to pore solutions, as well as revealed subtle differences in the content of lithic fragments between samples from different wells. Authigenic mineral counts and diagenetic textures, such as framework grain dissolution and alteration, were also recorded.

Point-Count Parameters

Each thin-section point was assigned a category based on clast lithology, type of pore space, or authigenic mineralogy. These categories, and the recalculated parameters used in ternary classification (QFR) diagrams are outlined in Appendix 6-A. Clast lithologies are discussed under Sandstone Petrology, and descriptions of porosity and authigenic mineralogy are presented in the Diagenesis section.

A separate count of 100 points was made of each sample that tallied only pore space. This tabulation, and the definition of porosity terms used, are located in Appendix 6-B.

Point-count Error

The reliability of point-counting results is related to the total number of points counted, and is expressed in terms of the standard deviation (van der Plas and Tobi, 1965). At a 95% confidence level, modal compositions of the units sampled are within four- to six percent of the values reported in Appendix 6-A (+/- 2σ). Because the Santa Fe Group is heterogeneous, the values reported cannot be reliably extrapolated to units outside the immediate vicinity of the sidewall cores.

Scanning Electron Microscopy

It became apparent early in the petrographic study that some important textural relationships and mineral identities could not be resolved using standard petrographic methods alone. Scanning electron microscopy, with its greater depth of field and significantly higher magnification, defined many fine-scale features not otherwise discernable.

Two different scanning electron microscopes were used: a Hitachi HHS-2R located at the electron microscopy facility of New Mexico Tech, and a Hitachi S-450 located at the University of New Mexico Institute of Meteoritics. Both machines were equipped with a Tracor Northern energy dispersive X-ray analysis system (EDS). Starting accelerating voltages ranged from 15 to 20 keV. Small chips of core material (5-10 mm in diameter) were cemented onto carbon stubs, and sputter-coated with a 200 to 500 angstrom-thick carbon coating under a 200 to 300 angstrom-thick gold/palladium coating. Total coating thicknesses are on the order of 700 angstroms. Coating materials conduct electrical current away from the specimen, facilitating clearer imaging. Unfortunately, an inverse relationship exists between image clarity and EDS resolution. Thicker coatings produce sharper micrographs but mute the X-ray spectra of mineral constituents. The choice of coating materials and thickness was thus a compromise between two objectives.

Electron Microprobe Analysis

Chemical compositions of framework grains and selected authigenic minerals were determined using the University of New Mexico Institute of Meteoritics Jeol "Superprobe" Model 733.

Electron microprobe analysis determines elemental compositions by focusing an electron beam within a small area of polished sample. The Jeol Model 733 uses a tungsten filament and accelerating voltages of 10-30 keV. Beam diameter ranged from 1-5μm, and beam current from 10^{-9} to 10^{-7} amps. X-rays emitted from the sample are diffracted by spectrometer crystals within the probe, and collected in a wavelength dispersive (WDS) detection system. Comparing the emission spectra of the sample to the spectra of a standard of known composition determined the composition of the sample. Feldspar and volcanic rock fragment compositions are based on a rhyolite glass standard; clay compositions are from a biotite standard. Error associated with microprobe analysis is a function of element concentration and spectrometer count rate, and is given in Appendix 6-D as weight percent of each element.

X-Ray Diffraction Analysis

Analyses of sidewall cores taken from clay-rich zones in Charles Wells 5, Thomas 5 and 7, SAF-1 and Cerro Colorado wells were done in the New Mexico Bureau of Mines and Mineral Resources X-Ray Facility. Results of these analyses were first reported by Mozley et al. (1992).

Mineralogy of the less-than-two micron clay fraction was determined from oriented clay mineral aggregates (i.e., with preferred c-axis orientations) sedimented onto glass slides. Oriented samples were analyzed on a Rigaku DMAXA diffractometer using monochromatic (Ni-filtered) CuKα radiation at a scanning rate of two degrees 2θ per minute. Samples were solvated in ethylene glycol and then heated to 375° C as an aid to mineral identification. Such treatments result in the expansion of smectite or smectite-like interlayers within the material, and produce shifts in XRD patterns that are characteristic of the particular mineral species. The samples were

analyzed only for the major clay minerals kaolinite, chlorite, illite, smectite and interlayered illite/smectite.

Zeolite mineralogy was determined using random powder mounts of air-dried material ground in a mortar and pestle. Random orientations obtain more complete diffraction data for comparison to standard powder diffraction files by maximizing the number of crystal reflections. Because of the low relative abundance of zeolite crystals, the scanning rate was reduced to 0.6 degrees 2θ per minute.

Cathodoluminescence Microscopy

One problem encountered in routine petrographic work was distinguishing between authigenic sparry calcite and corroded carbonate lithoclasts. Differences in luminescence of authigenic and detrital carbonates provided a relatively quick and qualitative means of resolving carbonate identity. A Nuclide ELM Luminoscope, mounted on a Nikon petrographic microscope, was used with accelerating voltages ranging from about 10 to 15 keV. Only a small group of representative, carbonate-rich thin-sections were chosen for analysis. These samples were polished manually with an aluminum oxide paste.

SANDSTONE PETROLOGY
Primary Composition

The most abundant detrital grains are quartz, feldspar and various rock fragments, with lesser amounts of biotite, muscovite and various heavy minerals (Appendix 6-A, Table A-1). Volcanic rock fragments are the most abundant and most petrographically varied lithic type, followed by granitic/gneissic fragments, sedimentary rock fragments and trace metamorphic rock fragments. Using Folk's (1974) mineralogical classification scheme, sidewall core samples classify as lithic arkose, feldsarenite, or feldspathic litharenite (Figure 6-2).

Quartz

Monocrystalline quartz in the sampled intervals is mainly of the common or plutonic variety (Folk, 1974), with straight to slightly undulose extinction, entrained inclusions and occasional microlites. Common quartz is believed to be characteristic of a granitic source area. Volcanic quartz, with straight extinction, almost no inclusions, and the preserved bipyramidal crystal habit of beta quartz, is also prevalent in some intervals. Volcanic grains typically have embayed margins.

Polycrystalline quartz varieties are mostly equigranular granoblastic types (quartzites), with straight grain boundaries that form triple-junctions with adjacent grains. Some stretched and schistose metamorphic types also occur, with granulated to crenulated grain boundaries, strong undulosity, and aligned muscovite, sillimanite or chlorite inclusions. No attempt was made to quantify quartz varieties on a genetic basis.

Feldspar

Plagioclase feldspars are typically monocrystalline, but also occur with quartz in granitic-gneissic rock fragments (discussed below). Within volcanic rock fragments, plagioclase occurs either as tabular microphenocrysts or as microlytic or felted lathwork within the groundmass. Polysynthetic lamellar twinning is diagnostic of plagioclase, but untwinned, anhedral grains are also common that are either of metamorphic origin or lie on the {010}cleavage. Concentric compositional zoning is evident in a number of microphenocrysts.

Microprobe results (Appendix 6-D, Table D-1) show that a typical monocrystalline plagioclase from Charles Wells 5 has a composition ranging from $An_{13.7}$ (oligoclase) to $An_{28.2}$ (oligoclase-andesine), but may also contain up to 7% potassium. A small orthoclase content may account for the fact that many feldspar grains accept both plagioclase and alkali feldspar stains.

Alkali feldspars occur in both high temperature (disordered) and low temperature (ordered) forms, the latter being more prevalent. Discrete, monocrystalline grains are most often grid-twinned microcline or untwinned orthoclase, as are granitic-

gneissic rock fragments that occur with quartz, +/- muscovite. A typical monocrystalline K-feldspar from Charles Wells 5 has a composition ranging from 3.1% to 13.4% sodium (Appendix 6-D, Table D-1).

Granitic-gneissic rock fragments are polymineralic grains of muscovite, biotite, chlorite or sillimanite that occur with quartz and feldspar and are plotted together with feldspar at the F-pole on the QFL diagram (Figure 6-2). Perthitic or myrmekitic intergrowths, while not abundant, are not uncommon within granitic-gneissic fragments, and are often associated with vacuolized feldspars. Vacuolization refers to minute gas or fluid inclusions incorporated within a mineral grain either during or after its formation. Some skeletal or microporous polycrystalline quartz grains were observed that may in fact be granitic rock fragments with perthitic intergrowths.

Lithic Fragments

Volcanic rock fragments are the most abundant and most varied lithic type, with compositions ranging from rhyolitic ash-flow tuffs (ignimbrites) to andesites to basalts. Silicic volcanics are typically fragmental, with microphenocrysts of sanidine or quartz embedded in an aphanitic to felsitic or glassy groundmass. Intermediate volcanics consist of plagioclase feldspar microphenocrysts (often with compositional zonation) +/- biotite, pyroxene or amphibole in a felted, or occasionally trachytic, groundmass. Mafic volcanics, with sphene or olivine microphenocrysts and microlitic plagioclase laths, are less common, and often display iddingsite or opaque Fe-Ti oxide alteration. Skeletal or ghost microphenocrysts within a coherent groundmass are common, reflecting selective dissolution of components during diagenesis.

Pumiceous fragments are typically rust-brown in plane light, display axiolitic or spherulitic devitrification, and are either isotropic or exhibit a "streaky" form of petrographic extinction. Microprobe analysis (Appendix 6-D, Table D-1) of the groundmass of a vitroclast sample from Charles Wells 5 was found to have the general formula

$$(K_{.511}Na_{.200}Fe_{.017}Ca_{.007}Ti_{.005}Ba_{.002}Mg_{.001})Al_{.745}Si_{3.246}O_{8.000}$$
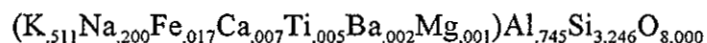
which has a similar composition and an Al/Si ratio similar to, but slightly lower than sanidine. Microprobe results indicate that pumiceous rock fragments were derived from a rhyolitic or latitic magma. Pumice fragments generally accept alkali feldspar stain.

Siliceous volcanic rock fragments are fine-grained and look very much like chert in cross-polarized light, but exhibit a combination of relict microphenocrysts, microlytic fabic and heavy minerals. These grains are distinguished from undifferentiated rock fragments (discussed below) by the presence of plagioclase and/or alkali feldspar stains over the entire grain surface.

Sedimentary rock fragments include sandstone/siltstone rock fragments, carbonate lithoclasts and chert. Sandstone/siltstone rock fragments, defined by fine-grained quartz and feldspar in a detrital clay matrix, have grain boundaries that are mostly ragged and indistinct. Siltstone abundance may be underestimated in fine-grained samples that contain abundant detrital clay. Intact fragments of quartz arenites were not found, though a number of well-rounded monocrystalline grains were observed to have partially rounded quartz overgrowths. If these overgrowths are remnants of an earlier generation cement, they represent clasts recycled from a texturally more mature sandstone (Folk, 1974).

Carbonate lithoclasts are nowhere abundant, and are essentially absent from west mesa wells. In most cases carbonate grains are comminuted and appear sparitic, perhaps as a result of weathering and transport rather than recrystallization. Intact foraminifera were found in two samples, both in Charles Wells 6, and were tentatively identified as nodosariids.

Chert consists of microcrystalline quartz (an aggregate of equidimensional grains that form a birefringent mosaic) and/or chalcedonic quartz (sheaf-like bundles of radiating fibers). Chert is differentiated from fine-grained siliceous rock fragments by the absence of feldspar staining.

Undifferentiated rock fragments are a fairly common and problematic rock type that could not be identified with certainty. These grains are siliceous, very fine-grained, have low birefringence and are apparently polycrystalline in a way resembling

chert. Extinction boundaries of these clasts are more "feathery" and indistinct than chalcedonic quartz boundaries, and extinction undulosity is more irregular. Color in plane-polarized light ranges from pale yellow-gold to pale green. In a few samples, rock fragments with features otherwise characteristic of undifferentiated rock fragments were found to contain feldspar and amphibole microphenocrysts, clearly indicating a volcanic origin. Yet other samples were found to contain relict twinning and vacuolization--characteristics of monocrystalline plutonic feldspar. Only those grains that could not be classified as either feldspar or volcanic rock fragments were categorized as undifferentiated rock fragments. QFL diagrams will be skewed towards the lithics pole, should many of these grains be in fact altered feldspar.

Metamorphic rock fragments are extremely rare, with the exception of several quartzite fragments (counted as polycrystalline quartz). The few metamorphic grains encountered are granoblastic polycrystalline quartz + sericitized feldspar $\pm$ biotite, tabulated as granitic-gneissic rock fragments. Foliated rock fragments are not common probably because of their inherent instability and because annealing of such grains would render them unrecognizable within the sand fraction (Blatt and Christie, 1963).

Heavy Minerals were defined for point-counting purposes as all mineral grains, excluding micas, having a specific gravity greater than that of quartz (specific gravity 2.89; Folk, 1974). Amphiboles, pyroxenes, olivines or sphene, occurring as members of volcanic lithic fragments, were identified on the basis of crystal habit and pleochroism. These grains were seldom pristine. Tourmaline, zircon, Al_2O_3 polymorphs, amphiboles and pyroxenes were also observed within granitic-gneissic lithic fragments. Unless heavy minerals occurred as discrete grains, they were recalculated using standard point counting methods as lithic fragments.

Allogenic Clay

Allogenic clay was differentiated from authigenic clay by particle morphology and distribution with respect to detrital sand-sized grains (Wilson and Pittman, 1977). Petrographically, detrital clays are variegated, occurring in patches or swaths of medium to dark reddish brown (plane-polarized light). High-order yellow interference

colors are typically masked by the mineral color. Under high magnification and reduced opening of the iris diaphragm, the variable relief of numerous individual clay particles stands out in the form of multiple Becke lines. With the SEM, detrital clay flakes were seen to be preferentially aligned sub-parallel to the surfaces of sand grains, and to have ragged and irregular terminations.

Sidewall core samples are interpreted to contain both syndepositional and mechanically infiltrated clays (classification of Wilson and Pittman, 1977). Dispersed matrix is probably the most common mode of occurrence, particularly where silt-sized grains are abundant. Thin, intercalated lamina occur in only a few of the thin-sectioned cores, and no biogenic or biogenically introduced clay was observed. Intraformational, or "rip-up" clasts are not common, but may not have been recognizable due to diagenetic or sampling-induced alterations. Detrital clays are ductile and easily deformed, and their origin could not always be determined with certainty. Furthermore, the coring process and possible desiccation during storage may have destroyed morphological and textural properties of some clay samples that would facilitate their identification.

DIAGENESIS
Authigenic Composition

Diagenetic minerals present in the samples are clays (smectite and interlayered illite/smectite), zeolites and calcite. Not all phases are present in all wells, and no systematic occurrence of any one phase is discernable with increasing depth. Most sidewall cores contain more than a single authigenic component, but typically contain only one, or perhaps two components in significant quantity. Samples were thus grouped in Appendix 6-C according to dominant authigenic mineralogy. Thin-sections having more than one cement in excess of an arbitrary 10% of pre-cement porosity were placed in a two-cement category. Samples were considered "uncemented" if they contained no secondary minerals in excess of 10% of pre-cement porosity.

Smectite, Illite and Interlayered Illite/Smectite

All of the samples examined with SEM contained abundant clay, determined from particle morphology to consist of both authigenic and detrital varieties. In thin-section, authigenic clay was interpreted to occur where irregularly distributed patches of microporosity were observed. These patches or zones were seen to be uniformly colorless, have low birefringence, and to completely fill pore spaces (Plates 6-1A and 6-2A). Undeformed zones extend into narrow recesses where adjacent framework grains meet, but are absent at points of grain-grain contact (Plate 6-1). Microporous zones returned clay-like compositions when microprobed (Appendix 6-D, Table 2).

Using the terms and identification criteria of Wilson and Pittman (1977), authigenic clay is identified as either a pore-filling phyllosilicate cement or a psuedomorphous replacement of framework grains. Pore-fillings are defined by these workers as clay that partially or completely plugs interstitial pore space, and displays no apparent alignment or preferred orientation of particles. Psuedomorphous replacement is defined as clay that replaces unstable detrital grains, or infills voids left by framework grain dissolution. The compositional purity of both modes of authigenic clay (Plates 6-1A and 6-2A) results in uniformity in color and texture (Wilson and Pittman, 1977), as well as a "clear transparency" (Dickinson, 1970). The concentric color zonation criteria of Dickinson (1970) was not observed in thin-section samples, but Wilson and Pittman (1977) state this is a relatively uncommon feature.

The irregular or spotty distribution of material and the absence of flame-like wisps or drapes about detrital grains, suggest it is not dispersed detrital matrix or mechanically infiltrated clay (Wilson and Pittman, 1977; Dickinson, 1970). The occurrence of undeformed patches of microporosity within narrow, angular recesses of grain contacts indicates in situ growth, rather than allogenic material squeezed between rigid grains. Where framework grain alteration is sufficiently advanced, psuedomorphous replacements may have extended into pore spaces and become indistinguishable from phyllosilicate cement. Clay was only point-counted as replacement where relict lithic fragments or microphenocrysts were observed (framework microporosity, Appendix 6-C).

Chemical compositions of representative authigenic clay from Charles Wells 5 are shown in Appendix 6-D, Table 2. Both Na^+- and non-Na^+ clay varieties were identified, which have the following average formulas:

$$(Na_{.52}K_{.31}Ca_{.28})(Al_{1.52}Fe_{.08}Mg_{.03})Si_{3.96}O_{11}$$
$$(K_{.08}Ca_{.06})(Al_{.66}Mg_{.30}Fe_{.27}Ti_{.16})Si_{4.51}O_{11.}$$
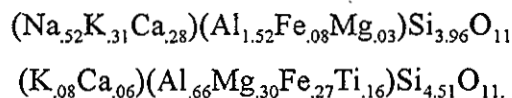
The analytical difficulty associated with hydrous minerals of characteristically high cation exchange capacity (Brindley, 1981) is reflected in the low totals in Appendix 6-D. The results shown are considered semi-quantitative. The presence of octahedral magnesium and abundant tetrahedral silica in both clay species indicates that the samples belong to the dioctahedral group of (smectitic) phyllosilicate minerals. The non-Na^+ clays are also characterized by titanium substitution within the octahedral site.

Chemical compositions of morphologically similar clays vary, even at the scale of a thin-section, but at least some of this variability may result from interstratifications of different clay mineral species. Illite and smectite differ principally in the degree of cation substitution possible within their respective crystal unit cells, and in the variable hydration states of smectite. The similarity of unit cell allows illite and smectite structural sheets to stack on top of each other in any sequence from completely random to regularly ordered (Brindley, 1981). Microprobe analysis necessarily averages the chemical compositions of mixed-layer illite/smectite.

Morphology of Albuquerque samples observed with SEM suggests that smectite or smectite-like material are the dominant clay species (Plates 6-1, 6-2 and 6-3). The ragged-edged, crenulated or webby to flaky appearance, while not diagnostic in-and-of itself, is characteristic of smectite or a smectite-dominated illite/smectite (Welton, 1984). The regularity of the illite/smectite layer stacking is not distinguishable with SEM. Based on XRD analyses, Mozley et al. (1992; their Table 5, Appendix G) report that selected core samples have a consistently greater abundance of smectite than of other phases. Illite, illite/smectite and kaolinite are of lesser abundance. XRD analysis does not, however, distinguish between authigenic and detrital clay species.

Kaolinite

Kaolinite is a common weathering product of feldspars and mafic volcanic rocks, but was not observed in thin section or with SEM in any of the Albuquerque cores. It is typical of environments with high permeability and large fluid volumes (so-called leaching environments) whereas smectites, which were observed, are characteristic alteration products in alkaline environments and drier climates (Carroll, 1970). An earlier study by Mozley et al. (1992) reported small amounts of kaolinite in Cerro Colorado 1 and SAF 1 using XRD techniques, but they did not identify it in thin section. The earlier XRD study located kaolinite only in clayey-silty cores, indicating its occurrence is limited to finer-grained sediments. Its absence in the sandier cores selected for petrographic work raises the possibility that kaolinite in clayey zones is detrital.

Zeolites

Zeolites were observed in a number of samples from Charles Wells 5 and Charles Wells 6, and in one sample from SAF 1. Where they occur, zeolites form in pore spaces as clusters of euhedral to subhedral crystals, and are often (but not always) associated with authigenic clay. Petrographically, zeolites are length-fast, have high relief and low birefringence (.006-.008), and are colorless in plane polarized light (Plate 6-2A). Crystal size is on the order of 20 to 30 microns.

With SEM, zeolites are seen to have prismatic habit, and to be flattened along the b-axis and elongated along the c-axis (Plate 6-4). Chemical composition of five zeolite samples from Charles Wells 5 (2992.1 feet) are shown in Appendix 6-D, Table D-3. The crystal morphology visible with SEM, combined with microprobe and XRD analyses, identify the zeolite species as a calcium-rich, low silica variety of the heulandite group.

Oxide totals in Appendix 6-D, Table D-3 are low--76% to 85%. However, microprobe results are given on an anhydrous basis. Idealized heulandite, $CaAl_2Si_7O_{18} \cdot 6H_2O$ (Woods and Garrels, 1987), has a molecular weight of 686.79, of which water comprises 15.74%, by weight. Adding approximately six formula units of

non-structural water to the results in Table D-3 brings the oxide totals up to acceptable values, and demonstrates that unbound water within the framework channelways of zeolites reasonably accounts for deficiencies in microprobe analytical results. Analysis number 1 (Table D-3) has an oxide total of 96.6%, which may reflect greater retention of structural water by this sample, at the expense of calcium and magnesium.

Some workers (e.g., Mason and Sand, 1960; Mumpton, 1960) consider heulandite as one end-member of a heulandite-clinoptilolite structural series, with clinoptilolite as the potassium-sodium, high silica end-member. However, Hay (1966) points out that the two species may be ion-exchange varieties of the same mineral. Inconsistencies in physical properties and extent of cation substitutions led Tschernich (1992) to argue for abandonment of the clinoptilolite nomenclature, reasoning that compositional and structural variations should be addressed using descriptive modifiers. For purposes of this report, zeolites are referred to simply as heulandite.

Mason and Sand (1960) defined heulandite according to the ratio $Ca^{2+}+Sr^{2+}+Ba^{2+}$: $Na^{+}+K^{+}$. On this basis, Albuquerque basin zeolites have less $Na^{+}+K^{+}$ and less $Ca^{2+}+Sr^{2+}+Ba^{2+}$ than the natural heulandite sample of Johnson, et al. (1985), but a similar value of $Al^{3+}+Si^{4+}$. Albuquerque samples also have less $Na^{+}+K^{+}$ than either the high or low silica heulandite varieties reported by Tschernich (1992), but similar ratios of Al^{3+} to Si^{4+} as varieties with similar $Ca^{2+}+Sr^{2+}+Ba^{2+}$. Some of the alkali cations in Albuquerque zeolites may have been evacuated by sample dehydration during storage and sample preparation. Also, chemical compositions reported in the literature are for large crystals (millimeters to centimeters), which tend toward high-calcium, low-silica content (Tschernich, 1992). Because all of the exchangeable cations (the alkali and alkaline earth metals) are located on two crystal lattice sites, sample compositions may deviate from published compositions because of differences in crystal size and cation exchange capacity.

In an earlier report (Mozley et al., 1992), Albuquerque zeolites were tentatively identified as the variety stilbite. This conclusion was based on preliminary XRD analyses of material present in relatively low abundance. Additional analyses and refinements to XRD techniques now confirm the zeolite species as heulandite.

According to Hay (1978), zeolite formation is associated with one of several processes: 1) hydrothermal alteration; 2) low-grade, regional metamorphism; 3) saline, alkaline lake (playa) or saline, alkaline soil deposition; and 4) percolation of meteoric water in open hydrologic systems. Of these, only the last two are pertinent to the Albuquerque Basin. Each of these two types of deposit has a characteristic mineral zonation associated with its occurrence. Arid-region lacustrine or playa deposits are characterized by a concentric, lateral zonation in facies inward from fresh tuffaceous material on the basin periphery, to alkalic zeolites, to analcime, and finally to authigenic alkali feldspar at the basin center (Sheppard and Gude,1968; Surdam and Sheppard, 1978). The distribution of facies is believed related to evaporative concentration of sodium carbonate-bicarbonate waters. In open hydrologic systems, downward-percolating meteoric waters react with detrital minerals and become progressively enriched in silica and alkaline metals, producing a vertical zonation in groundwater chemistry and authigenic minerals (Hay, 1978). Upper zones, typically consisting of fresh glass and smectite, are generally in sharp contact with underlying clinoptilolite/heulandite and analcime zones, indicating a significant increase in solution pH and ionic strength as descending pore waters react with volcanic materials.

Vertical zeolite zones were not detected over the depths sampled (heulandite is the single zeolite species observed) but the absence of vertical zonation does not rule out a hydrologic mechanism for zeolite precipitation. Zeolites precipitated preferentially in medium to coarse-grained, moderately to poorly sorted sands (discussed below), suggesting a correlation between zeolite occurrence and sediment with higher permeability. Greater fluid flux through permeable aquifer zones enhances dissolution of framework grains (Sullivan and McBride, 1991; Siebert et al., 1984) and ultimately impacts the saturation state of migrating fluids. Lateral zonation associated with playa deposits cannot be evaluated from bore-hole data.

Calcite

The Santa Fe Group is mostly uncemented in outcrop but commonly contains discontinuous bands and lenses of calcite-cemented, sediment-filled channels, cut-and-

fill structures and concretionary sands. In thin section, micrite comprises most of the matrix of a few fine-grained samples or occurs as isolated poikilitic crystals in some coarser-grained samples (Plates 6-1A and 6-1B). There is an apparent tendency for calcite to occur in finer grained, better sorted sands, but the correlation between the relative abundance of calcite and grain size is weak (discussed below).

Carbonate lithoclasts were nearly always brecciated, and thus easily mistaken for secondary sparite. Cathodoluminescence microscopy was useful in differentiating the two carbonate origins, but point-counting was done exclusively under plane polarized or cross polarized light. Cathodoluminescence was used only as a qualitative guide.

Core Depth and Secondary Mineralization

Secondary minerals observed in this study are essentially low temperature and pressure varieties, the occurrences of which are unsystematic with respect to depth of burial. Figure 6-3 illustrates the distribution of authigenic minerals by core depth, and indicates the absence of a discernable trend in mineralization over the intervals sampled.

Influence of Primary Mineralogy and Sedimentary Texture

The formation of secondary clay and zeolites is typically attributed to chemical decomposition of sediment containing abundant volcanic rock fragments and feldspars (e.g., Hay, 1966; Colella et al., 1978; Reeves, 1978), but the correlation of authigenic mineral suites to a specific sandstone composition is typically weak (Hay, 1966). The single West Mesa sample containing zeolites (SAF; 1440 feet), for example, has no volcanic lithic fragments, has a relatively low plagioclase content, but does contain an abundance of undifferentiated rock fragments. No zeolites were observed in volcanic glasses of Cerro Colorado No. 1 (below 1500 feet), perhaps indicating some additional control on zeolite precipitation besides detrital composition.

The relationship between secondary mineral precipitation and sedimentary texture was evaluated by estimating the grain size and sorting of uncut sidewall core

plugs using visual comparitors (Swanson, 1981; Tucker, 1982). These estimates are considered a first approximation of sedimentary texture.

The range in grain size in cored intervals covers the entire sand spectrum, extending from very fine lower- to very coarse upper sand (0.06 to 2.00 mm; Appendix 6-A, Table 2). The most commonly occurring grain size (mode) is nearly as diverse, ranging from very fine upper- to medium lower sand. Mean grain size was calculated using the relation $\phi16\% + \phi50\% + \phi84\%/3$; sorting, expressed as the standard deviation in grain size, was calculated using the relation $\phi84\% - \phi16\%/2$ (modified from Folk, 1974). Grain roundness varies from angular to subround.

Authigenic mineralization is evident throughout the observed range of sedimentary texture (Figure 6-4). Though occurrences may span a range in grain size and degree of sorting, the general trend is that zeolites and zeolites + clay form in coarse-grained, less sorted sediments; calcite and calcite + clay forms in medium to fine-grained, well sorted sediments; and clay replacements of framework grains develop in medium-grained, moderately sorted sediments. Uncemented samples may be either fine-grained or coarse-grained, but are generally better sorted than mineralized samples. The apparent preference of authigenic minerals for a specific grain-size class is not necessarily reflected in the relative abundance of that mineral, however. Correlation coefficients calculated for number of mineral occurrences and several primary sedimentological parameters are shown in Table 6-1. No strong relationships are seen in Table 6-1 between authigenic mineralization and sedimentary composition and texture, the highest correlations being between zeolite occurrence and sorting ($r = 0.56$), between zeolite occurrence and the ratio of standard deviation/mean grain size ($r = 0.58$), and between clay alteration and percent lithics ($r = 0.55$). Correlations indicate, in general, that zeolites are more likely to occur in coarser-grained, less sorted sediments containing volcanic rock fragments. Phyllosilicate and calcite cement abundance are less predictable from primary sedimentological considerations alone.

Table 6-1. Correlation coefficients calculated for authigenic mineral abundance and primary sedimentological parameters. Primary mineral percentages are based on point-count parameters recalculated using the Gazzi-Dickinson method, which emphasizes mineralogical content over lithic type. The ratio of sorting to grain size (std dev/mean phi) is a means of combining two textural parameters into a single variable.

Zeolite (%)	Clay Alteration (%)	Calcite (%)	
-0.42	0.02	0.03	Mean Phi
0.56	-0.01	-0.08	Std Deviation
0.58	0.02	-0.12	Std Dev/Mean Phi
0.38	0.55	-0.30	% Lithics
-0.15	-0.15	0.24	% Feldspar
-0.23	-0.39	0.08	% Quartz
-0.39	-0.33	-0.01	% URF
0.43	0.39	0.09	% VRF
-0.13	-0.15	-0.19	% SRF
-0.29	-0.44	-0.33	Intergranular Macroporosity

The quantity of authigenic minerals that precipitate is not appreciably affected by texture, but it is apparent that certain environmental conditions must be met before a particular authigenic suite can develop. Poor correlation between secondary mineral abundance and primary sedimentological composition is explained in part by the fact that soluble feldspars and lithic fragments occur with such abundance throughout the Santa Fe Group that authigenesis is not limited by the absence of a necessary solute. In the geochemical modeling section of this report, each of the observed authigenic minerals was simulated by simply dissolving increased amounts of oligoclase: the specific chemical species released into model pore solutions remained the same.

These observations suggest that the presence or absence of secondary minerals in sidewall cores is related more to the hydrologic properties of aquifer zones than to specific sediment composition. Sedimentary texture is important insofar as providing an environment conducive to nucleation and crystal growth, and in it's affect on the movement of groundwater .

<p style="text-align: center;">Porosity and Framework Grain Dissolution</p>

Variability in original porosity is related to grain sorting and to the abundance of fines within the primary sediment (Beard and Weyl, 1973). During diagenesis, porosity may be enhanced by dissolution of framework grains, occluded by precipitation of secondary minerals, or reduced by burial compaction (Beard and Weyl, 1973; Siebert et al., 1984; Houseknecht, 1987).

Porosity of Albuquerque core samples is shown in Figures 6-5 and 6-6. Total macroporosity, reported as a percentage of total sample volume, generally decreases with depth (Figure 6-5) though there is considerable scatter amongst data points. The implication of this decrease in total porosity is that porosity occlusion and compaction become more pronounced at depth. Secondary porosity also displays considerable variability, but in general increases with depth (Figure 6-6), supporting the notion that diagenetic modifications to original porosity become greater in deeper parts of the basin. The distribution of authigenic minerals, however, does not support this conclusion (Figure 6-3) because secondary mineral precipitation is inconsistent with depth.

Secondary porosity generated by intrastratal solution of framework grains results in skeletal grains with a remnant, identifiable structure (Plate 6-2D); ghost grains, identified by an insoluble clay or cement residue (Plate 6-4D); or oversized pores that suggest framework grain dissolution by conspicuous pore size. Selective dissolution of microphenocrysts produces euhedral or lath-shaped voids within volcanic rock fragments (Plate 6-1A). Skeletal grain content of Albuquerque samples ranges from 2.3 to 4.3 percent of total sandstone volume, and averages 3.08 percent

(Appendix 6-B; summarized below in Table 6-2). Nearly 50 percent of grains showing skeletal characteristics (i.e., with relict grain margins) are plagioclase, 25 percent are K-feldspar, and 18 percent are volcanic rock fragments (Appendix 6-B, Table B-2b). Skeletal grain content is slightly higher for East Mesa wells Charles Wells 5 and Charles Wells 6 than for West Mesa wells, but no trend in skeletal grain content is seen with depth.

Table 6-2. Average skeletal grain content (all mineralogies) for each well; percent of 300 point counts

	Cerro Colorado	SAF 1	Charles Wells 6	Charles Wells 5
mean	2.52	2.28	3.21	4.33
std dev	2.33	1.27	1.64	1.69

Processes commonly advanced for chemically aggressive pore fluids are dissociation of organic acids and the resulting generation of CO_2 during organic diagenesis (e.g., Surdam et al., 1984; Lundegard and Land, 1986; Kharaka et al., 1986), leaching of mineral matter in the shallow subsurface by meteoric water in equilibrium with atmospheric CO_2 (Bloch and Franks, 1993), hydrolysis reactions between minerals and groundwater (Bjørlykke, 1983) and microbial metabolic processes (e.g., Tan, 1980; Robert and Berthelin, 1986). Geochemical reactions in the CO_2-organic acid system of hydrocarbon reservoirs play an important role in the generation of secondary porosity. However, the organic carbon of oil-field waters is associated with kerogen-rich rocks not found in the Santa Fe Group, and may not be present in the Santa Fe except in relatively small concentrations. The second and third processes, hydrolysis reactions and mineral leaching, are similar processes that both impart an alteration to the silicate structure, but differ from each other in regard to the fate of chemical reaction products. In open hydrologic systems with relatively high fluid flow rates, soluble reaction products (such as aluminum hydroxides) are supposedly removed or leached from their site of formation rather than accumulated in intergranular pore spaces (Bloch and Franks, 1993). Physical removal of products by

groundwater flow facilitates the forward reaction and further dissolution, in accordance with LeChatelier's Principle. Hydrolysis differs from leaching in that it is in theory a reversible reaction that permits establishment of an equilibrium between reactant detrital grains and product minerals. If this equilibrium is reached, for example in constricted pore spaces with limited exposure to circulating fluids, dissolution of detrital grains will be significantly slowed or stopped. Factors influencing the rate of feldspar hydrolysis and silicate solubility are mineralogical composition of the sediment, grain size, fracturing and degree of alteration before deposition, acidity of porewaters and the duration of exposure to pore fluids (Bjørlykke, 1983).

The importance of microbial metabolism, the fourth process, in the synthesis of organic acids and production of CO_2 is well established (Stevenson, 1967; Tan, 1980), and those compounds most effective in dissolving aluminosilicate minerals are also strong chelating agents believed responsible for the mobilization and transport of decomposed mineral matter out of the soil profile (Stevenson, 1967; Stevenson and Fitch, 1986). Although qualitative estimates of microbial biomass and activity are difficult to obtain, arid and semiarid soils are known to contain most of the same major taxa of micro-organisms contained in less extreme climates (Kieft, 1991). The distribution of acid-generating microbial colonies is patterned about what has been termed "fertile islands" of low population density perennial plants. Microbial populations are most active in the upper 5-20 cm of the vertical soil profile, though some fungi populations are known to extend to depths of around 10 m (Kieft, 1991).

Microbial decomposition in the shallow subsurface of the Albuquerque Basin requires that skeletal grains have survived burial and the effects of burial compaction. Bloch and Franks (1993) determined that dissolution of plagioclase feldspars in the San Joaquin Basin of California was mostly generated in the shallow subsurface, and that delicate dissolution structures were protected from compaction by the high rigid-grain content of the sands. Burial depths of samples in the Albuquerque Basin are considerably less than the 2,900 feet to 13,000 feet sampled in the San Joaquin Basin, so it is feasible that skeletal structures produced in the shallow subsurface have survived to their present depths.

In order to evaluate possible dissolution mechanisms, the following calculations were made to estimate the amount of material released into solution, and to compare that estimate to the amount of material potentially dissolved by organic acid generation. Soluble minerals anorthite, Ca-glass, microcline, sanidine, K-glass, albite and Na-glass have molar volumes, in cm^3/mol, ranging from 100.07 for albite to 100.79 for anorthite to 116.50 for K-glass (Robie et al., 1979). The mean molar volume for these minerals is 106.88 cm^3/mol, or 9.4 $mmol/cm^3$. If 3% of Albuquerque Basin sediment exhibits framework grain dissolution (Table 2), then

$$(9.4 \text{ mmol/cm}^3) (0.03) = 0.28 \text{ mmol mineral matter/cm}^3 \text{ sediment}$$

has been released into pore solution. The amount of acid required to hydrolyze this sediment is given by the dissociation reaction of oligoclase, the most abundant detrital feldspar. Assuming no conservation of aluminum,

$$4 \text{ NaAlSi}_3\text{O}_8 \cdot \text{CaAl}_2\text{Si}_2\text{O}_8 + 16 \text{ H}_2\text{O} + 24 \text{ H}^+ \rightleftharpoons 4 \text{ Na}^+ + \text{Ca}^{2+} + 6 \text{ Al}^{3+} + 14 \text{ H}_4\text{SiO}_4$$
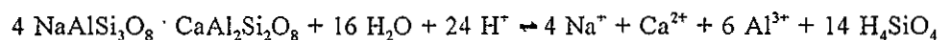
requires 24 mmol acid per mmol oligoclase dissolved. If 24 mmol acid are required per mmol of sediment dissolved, and there is 0.28 mmol of dissolved sediment per cm^3, then

$$(24 \text{ mmol H}^+/\text{mmol Olig})(0.28 \text{ mmol dissolved Olig/cm}^3) = 6.72 \text{ mmol H}^+$$

is required per cm^3 sediment dissolved.

According to Tan (1986), acetic acid concentrations in temperate-region soils are on the order of 0.7 to 1.0 mmol/100 g. Assuming a perfectly efficient utilization of available H^+ ions and a density of sediment approximately equal to that of quartz (the most abundant mineral),

$$(7.0 \times 10^{-3} \text{ to } 1.0 \times 10^{-2} \text{ mmol/g sediment}) (2.65 \text{ g/cm}^3) =$$
$$1.86 \times 10^{-2} \text{ to } 2.65 \times 10^{-2} \text{ mmol acid/cm}^3 \text{ sediment}$$

is available, two orders of magnitude less than necessary to account for the observed dissolution. The rate at which organic acids are replenished is highly variable, but the paucity of vegetation and low soil-moisture content of arid and semiarid region soils place constraints on the biotic contribution to framework grain dissolution possible in Albuquerque Basin sediments. The calculations above, though crude, suggest that

dissolution is perhaps enhanced or initiated by soil microbial processes early in the sediment burial history, but that microbial metabolism alone is inadequate to generate sufficient quantities of acid. The effects of biochemical reactions in deeper parts of the basin are unknown.

The solubilities of aluminosilicate minerals such as oligoclase are strongly dependent on the partial pressure of CO_2 which, when dissolved in groundwater, equilibrates with carbonic acid (Freeze and Cherry, 1979). CO_2 in groundwater may be derived from the atmosphere or generated by biochemical reaction. Unless CO_2 is available at constant partial pressure (so-called "open systems"), H_2CO_3 is consumed by mineral dissolution reactions. Carbonic acid consumption is particularly high in carbonate terranes. However, high pCO_2 may be preserved in groundwater if water-rock reactions in soil or vadose zones are minimal. It is probable that framework grain dissolution in Albuquerque Basin cores indicate pore water whose flow path was primarily through crystalline Precambrian rocks, rather than through Paleozoic limestones.

Compaction

There is no strong petrographic evidence for significant mechanical compaction in the middle to lower Santa Fe Group. What evidence there is exists in the form of biotite, muscovite or argillaceous rock fragments bent and distorted about rigid framework grains, and in the nature of framework grain contacts. Most samples have floating or tangential (point) contacts, but some samples have mostly longitudinal contacts.

To assess the relative importance of compaction to diagenesis and porosity reduction, a plot of minus-cement porosity versus total cement was constructed following the technique of Houseknecht (1987). The diagram (Figure 6-7) assumes an original, uncompacted porosity of about 44%, which is an estimate based on naturally and artificially packed sands that are well sorted or better (Beard and Weyl, 1973). The diagonal lines in Figure 6-7 are lines of equal intergranular macroporosity determined from 300 point-counts; samples are grouped by their dominant cement (Appendix 6-C) and plotted as separate data series on the diagram. "Uncemented" samples contain less than about 4% cement, and cluster near the y-axis at around 25-

30% minus-cement porosity (plus two outliers at 2 and 12%). The remaining samples are scattered across the diagram, plotting on either side of the dividing line between the cementation and compaction fields.

Because of their relatively large crystal size and tendency to encompass several grains, carbonate cements occupy the largest pore volume of any cement type, and are more capable than zeolites or clay of preserving original intergranular spacing upon burial. Though calcite-cemented samples are among the group of samples in Figure 7 with the highest minus-cement porosity, zeolite and clay samples are also present, suggesting porosity reduction by compaction has not been an active process. On the other hand, uncemented samples have less minus-cement porosity than most samples, possibly indicating moderate compaction of at least some of the cores.

A problem with Houseknecht's method of estimating porosity loss, pointed out by Pate (1989) and Ehrenberg (1989), is that there is a dynamic reduction in bulk sediment volume as compaction progresses. Point-counting can only address existing intergranular volume and relate it to an empirical estimate of original porosity. Porosity loss due to compaction will thus be slightly higher than indicated by Houseknecht's figure.

Houseknecht assumes for the diagram that sands are well-sorted or better, that grains are of similar sphericity, are nonductile, and have minimal secondary porosity. Ideally, only samples with similar textural characteristics will have been selected for compaction analysis. Because the Albuquerque sample set is relatively small, all sample data was used in the construction of Figure 6-7 regardless of textural characteristics: restricting the sample set would result in too few data points for comparison. None-the-less, the exercise was largely inconclusive.

LITHOFACIES AND INDICATORS OF PROVENANCE

Lithofacies, as defined by Hawley and Haase (1992); Hawley et al. (1995), are shown for each sample on Table C-1, Appendix 6-C. An underlying assumption in subdividing core samples into lithofacies is that volcanic rock fragments indicate fluvial deposition, due to the absence of an immediate source area. Thin sections

provide no indication whether the fluvial system was a through-going, interbasinal system or a closed, internally drained system, but studies of regional sediment dispersal patterns (e.g., Ingersoll et al., 1990; Love and Young, 1983; Lozinsky and Tedford, 1991) suggest cores are from stratigraphic levels that pre-date a through-going axial Rio Grande. Regional volcanic centers capable of supplying volcaniclastics to the Albuquerque basin include the Latir-Questa volcanic field (Dungan et al., 1979), the older volcanic pile of the Jemez Mountains (Keres Group of Bailey et al., 1969), the Espinaso Formation (Smith et al., 1991), or the Mogollon-Datil field (Chamberlin et al., 1994).

Volcanic rock fragments, silicified rock fragments and feldspars from deep crustal sources are petrographically similar once they have become altered. These grains were collectively termed "undifferentiated rock fragments" where they could not be distinguished from one another. Because volcanic or undifferentiated rock fragments are present in all thin sections, a fluvial origin cannot be ruled out for any of the core. Fine-grained samples may indicate termination of the drainage system in a low energy basin floor or playa environment.

The occurrence within the same thin section of granitic-gneissic and volcanic rock fragments indicates considerable mixing of sediment from diverse source areas. Possible mechanisms for sediment mixing include 1) stream-channel integration of fluvially-derived volcaniclastics with piedmont alluvium delivered to the axial basin by up-stream arroyo systems, such as the ancestral Tijeras or Embudo; 2) fluvial transport of volcanic debris and plutonic-metamorphic rocks, both derived from an area to the north; 3) incision of pre-existing fluvial facies by piedmont arroyos that downcut into the footwall block of subsiding rift segments, reworking the volcanic component into prograding alluvial fans.

Granitic and metamorphic detritus within the Gabaldon Badlands section of the Sierra Ladrones Formation was interpreted by Lozinsky and Tedford (1991) to have originated in a source area to the northwest. Unless the Sandia block was sufficiently uplifted by early to mid Santa Fe time to expose Precambrian basement, sediment within the Albuquerque Basin would have come from the same plutonic-metamorphic

source area as sediment in basins to the south, such as the Gabaldon section. A Sandia-Manzano source area for granitic-gneissic and sedimentary rock fragments in West Mesa cores is improbable because of the east-dipping structure of the north Albuquerque Basin.

Volcanic detritus in West Mesa wells is mostly pumiceous, displaying devitrification textures and a high degree of alteration to clay. Volcanic rock fragments occur below depths of 1300 feet in Cerro Colorado, and below 2000 feet in SAF 1. Though transport distances for these clasts are conceivably quite large, a likely source area for West Mesa volcanic rock fragments is the older volcanic pile of the Jemez mountains (Keres Group of Bailey et al., 1969) or deposits of the Latir-Questa caldera system (Lipman and Reed, 1989; Dungan et al., 1989).

Although clast lithologies described earlier in the Sandstone Petrology section occur in virtually all core samples, there is a noticeable difference in the modal composition of samples from East and West Mesa wells (Figure 6-2). West Mesa samples Cerro Colorado 1 and SAF 1 are more quartzose and less feldspathic than East Mesa samples, and generally contain fewer volcanic rock fragments. Higher percentages of monocrystalline quartz, and the presence in some samples of recycled quartz overgrowths suggest a contribution to the West Mesa from an older sedimentary source, probably Mesozoic rocks of the Colorado Plateau region to the west and northwest.

In Figures 6-8 to 6-11, the relative abundance of framework grains is plotted against well depth for each of the four wells. East Mesa wells show a higher degree of variability in clast abundance across their depth profile (Figures 6-10 and 6-11) than do West Mesa wells (Figures 6-8 and 6-9). This implies a more dynamic sediment delivery system for East Mesa wells (both of which are located in a zone of inferred mixing of ancestral Rio Grande and Tijeras Arroyo fan deposits). The greater mineralogical maturity and consistency in grain abundance of West Mesa wells implies a more stable sediment supply.

GEOCHEMICAL MODELING

Changes in pore water chemistry and mineral mass during low-temperature diagenesis were modeled using the FORTRAN IV program PHREEQE (Parkhurst et al., 1990). The purpose of modeling was to evaluate mineral phase coexistence and to determine whether those phases could be produced sequentially from a simple starting solution. PHREEQE, one of a series of programs developed by the United States Geological Survey to simulate geochemical equilibrium, calculates the pH, pe, ionic strength, and saturation state of a solution, and the mass transfer of minerals into or out of the aqueous phase.

Methods

Thermodynamic data for clay and zeolite species are not widely available, so data for minerals whose formulas are similar to, but simpler than the sample minerals were obtained from the literature. Microprobe results indicate clay species contain Na^+ and Ca^{2+} in approximately equal amounts and contain relatively lesser amounts of K^+. Zeolites are calcic heulandite. For simulation purposes, idealized Ca-smectite, Na-smectite, illite and calcite were modeled using mineral formula and free energies and enthalpies of formation from Woods and Garrels (1987); data for calcic heulandite is from Johnson et al. (1985). Equilibrium constants and free energies and enthalpies of reaction were calculated for mineral dissociation reactions and input to the program. Because the temperature of Albuquerque Basin waters is variable, the Van't Hoff equation was used by the program to address the temperature dependence of equilibrium constants. Activity coefficients were calculated using the Debye-Hückel formula.

Two separate fluid evolution schemes were tried. In the first scheme, products of feldspar, aegerine, actinolite and biotite dissociation reactions were added to a pure-water starting solution and allowed to equilibrate with the simplified authigenic phases. In the second scheme, water quality data supplied by the City of Albuquerque Water Utilities Division for CW6, SAF1 and CC1 was input to the program and defined as the starting solution. Mean values for seventeen analytes, sampled during the period

January 1992 to April 1994, were used. The addition of dissolved components was also required in the latter scheme to bring the solution to equilibrium with all the simulated phases. Reaction input in the second scheme was defined by dissolution of oligoclase.

<div align="center">Results</div>

Each of the authigenic phases was successfully simulated in scheme 1 by dissolving sufficient quantities of detrital minerals into a pure water starting solution (Table 6-3). However, no paragenetic relationships could be defined: trials involving multiple phases always resulted in metastable or non-sensical solutions that had saturation indices greater than zero, or that dissolved non-existing authigenic phases. In contrast, trials using water quality data as a starting solution, the second scheme, simulated both paragenesis and mass transfer in the precipitation of each product mineral.

Table 6-3. Pore fluid composition and saturation state in the K_2O-Na_2O-CaO system: results of geochemical simulation using PHREEQE (Parkhurst et al., 1993) and a pure-water starting composition.

Equilibrium Mineral Phase	Solution pH	Solution Alkalinity $(x10^{-5})$	Detrital Minerals Dissolved/kg H_2O (mol $x10^{-6}$)
heulandite	8.6366	4.4038	0.8468
Ca-smectite	8.7066	5.8446	1.1239
illite	8.8063	9.2807	1.7847
Na-smectite	8.8064	9.2860	1.7860
calcite	7.0466	6.2882E-3	1.1056E-3

Table 6-4 lists the results of simulations using water analyses from CW6, CC1 and SAF1. Shown are the mineral phase (or phases) maintained in equilibrium with the solution, the solution stability (defined by its saturation index) and the number of

micro moles of each phase dissolved or precipitated in reaching equilibrium. Results of trials using water quality data (scheme 2) are discussed below by well-of-origin.

Charles Wells 6

The initial solution, using CW6 water analyses as a starting point, is supersaturated with respect to all model phases (Table 6-4). Trial number 9, a two-phase equilibria (point A, Table 6-4), is the first simulation to result in a stable solution. Each of the single-phase trials, and most multiphase trials are supersaturated in at least one other phase. Some trials produced non-sensical results. For example, trial 6 (Ca-smectite/heulandite) resulted in a stable solution (i.e., no saturation index greater than zero) but required destruction of 118 mmol authigenic smectite before any smectite had yet been formed by the model. The only way that the model could produce phases other than heulandite and calcite was by hydrolyzing detrital oligoclase. Trial 23 (point B) introduces Ca-smectite into the system by dissolving 77.18 mmol oligoclase; 230 mmol heulandite precipitate in the reaction, and 3 mmol calcite dissolve (leaving 61.7 mmol calcite from point A). The mass value of 0.0 mmol for Ca-smectite means that the solution is just saturated with respect to smectite, but no smectite has yet formed. In trial 27 (point C), illite enters the system following the addition of 747 mmol oligoclase. Each of the existing phases continued to precipitate in this step, including a very large amount of calcite (1.6 x 10^6 μmol). A fraction of this calcite (73 mmol) was lost in the final step (trial 28, point D) to bring Na-smectite into the system. The pH, alkalinity and ionic strength of the pore fluid became progressively elevated as the fluid equilibrated with each additional phase.

Cerro Colorado 1

In trial number 1 (point A, Table 6-3) a very small amount of heulandite precipitates as the first equilibrium phase. No other phases could be generated without addition of dissolved oligoclase. Trial 12 (point B) resulted in the introduction of three additional phases to the system, calcite, Ca-smectite and illite, following addition of 575 mmol oligoclase. The final phase, Na-smectite, was introduced in trial 13

(point C, Table 6-3) after 1,936 mmol dissolved oligoclase were added to solution. Again, the pore fluid became increasingly alkaline with reaction progress, but less so than in CW6.

Soil Amendment Facility 1

The reaction path modeled for SAF1 is similar to that of CC1 in that heulandite equilibrated with the starting solution (trial 1, point A) and in that the second step in the reaction path was a multiphase equilibria (trial 12, point B). The SAF1 path differs from the CC1 and CW6 paths in its failure to introduce Na-smectite as a product phase, and in the relatively low amount of heulandite produced. No reactions beyond point B succeeded without consuming more product phases than were present in the system.

Discussion of Modeling Results

In the model, feldspar hydrolysis resulted in a step-wise progression in products where each new phase continued to precipitate as subsequent phases equilibrated with the solution. Heulandite, the first phase to precipitate in the model, was predicted to occur in abundance in all wells. However, a discrepancy exists between the model and the system it mimics. Heulandite was not observed with its projected frequency, and thin-section samples were seldom seen to possess more than one or two authigenic phases. This is explained in part by the simplifications used in constructing the model. Modeling illite and the calcium and sodium smectites as independent phases was a way to simulate interstratified clays of varying composition. Busenberg (1978) noted chemical compositions of clay precipitated from artificial feldspar weathering experiments (with high initial Ca, Mg and SiO_2 concentrations) were not only complex, but varied over time. Differences between the discrete product sequence predicted by the model and petrographic observation is diminished if clay phases are considered collectively. The failure of the model to precipitate Na-smectite in SAF1 likely indicates clays formed in these waters are more calcic than their counterparts in the other wells. Zeolites, which can form from the same starting materials as clay, are

favored by lower ratios of hydrogen to sodium, potassium and calcium, and by lower activities of magnesium (Hay, 1978).

Table 6-4 shows that heulandite precipitated from the starting solution without affecting the solution's ending pH, alkalinity or ionic strength (trial 1, all wells). The formation of additional phases, however, required dissolution of detrital minerals and produced a change in pore fluid chemistry. Water quality analyses (the starting solution) must therefore reflect either 1) the composition of the shallow aquifer only, and implies that total dissolved solids increase with depth; or 2) the average composition of water mixed from a number of relatively small aquifer compartments, some of which may equilibrate with secondary minerals. Water in middle and lower Santa Fe Group aquifer zones has had a longer residence time, relative to the shallow aquifer, within which to hydrolyize detrital grains. Deeper water is also less susceptible to dilution by recharge. However, there is no data to either confirm or deny the assertion that water quality data reflects only the shallow aquifer. Water analyses, collected at the wellhead, do not pertain to a specific depth, and sidewall cores were collected from depths below the screened interval. The alternate idea, that water chemistry varies across discrete aquifer zones, requires that pockets of more saline water be isolated from meteoric recharge. Such pockets are conceivable within fine-grained sediments that act as barriers to groundwater flow. But petrographic observations suggest authigenesis occurs in "cleaner" sands lacking silt and detrital clay, with supposedly higher permeability. Low fluid flux through clean sandy zones, or restricted communication between sandy zones and meteoric recharge may result from impeding lenses or beds of fine-grained material (or cemented or gouge-filled faults in certain areas). Outcrop analogs of the Middle and Lower Santa Fe consist of discontinuous sandy lenses that are traceable for only several meters before pinching out against silty or clayey units (Galusha and Blick, 1971; Lozinsky, 1988; Lozinsky and Tedford, 1991). In all probability, both depth and small-scale aquifer compartmentalization may operate to promote diagenesis.

Though there is no apparent correlation between framework-grain dissolution and authigenesis, it is reasonable to assume, based on conservation of mass arguments,

6-40

that precipitation is associated with dissolution. The low correspondence may indicate transport (dispersion) of dissolved constituents away from their grain of origin. The quantity of dissolved mineral matter, calculated from point-counts of intragranular macroporosity, is 0.28 moles per liter of water (Diagenesis/Dissolution Processes section). This is two orders of magnitude greater than required by the model to equilibrate with the last clay phase (Table 6-4). Many of the products of mineral hydrolysis must therefore have remained in solution, dispersed throughout the aquifer matrix.

Table 6-4. Pore-fluid composition, saturation state and mineral mass transfer in the K_2O-Na_2O-CaO system upon equilibration with authigenic mineral phases: results of geochemical simulation using PHREEQE (Parkhurst et al., 1993) and water quality data supplied by Albuquerque Water Utilities Division. Thermodynamic data for clays from Woods and Garrels (1987) and for zeolites from Johnson et al. (1985). Upper-case letters identify the reaction path that allows each phase to enter the system.

CHARLES WELLS 6

Trial No.		Equilibrium Mineral Phase	Saturation Index + supersaturation - undersaturation					Mass μmol/kg H₂O + dissolution - precipitation					Solution Chemistry			
			heulandite	Ca-smectite	Na-smectite	illite	calcite	heulandite	Ca-smectite	Na-smectite	illite	calcite	pH	alk (10⁻³)	I (10⁻³)	oligoclase dissolved/kg H₂O (mol)
		initial solution	11.2033	5.3706	4.6332	4.0120	0.2894						7.675	1.856	9.0	0.0
1		heulandite	0.0	-7.6630	-8.4004	-8.8532	0.2894	-0.7415					7.6751	1.85	9.0	0.0
2		Ca-smectite	6.5958	0.0	-0.7375	-1.2849	0.2952		-0.6333				7.6806	1.85	9.0	0.0
3		Na-smectite	7.2288	0.7375	0.0	-0.5569	0.2952			-0.6299			7.6806	1.85	9.0	0.0
4		illite	7.7124	1.3049	0.5674	0.0	0.2929				-0.6331		7.6784	1.85	9.0	0.0
5		calcite	11.1945	5.8720	5.1358	4.3109	0.0					-64.726	7.4197	1.72	8.9	0.0
6		Ca-smec/heul	0.0	0.0	-0.7351	-1.5949	-0.4008	-138.128	+118.107				7.0492	1.615	8.7	0.0
7		Na-smec/heul	0.0	0.7307	0.0	-0.8591	-0.4119	-140.203		+120.356			7.0422	1.615	8.7	0.0
8		illite/heul	0.0	1.2405	0.5060	0.0	-0.2134	-139.726			+123.803		7.2189	1.728	8.8	0.0
9	A	calcite/heul	0.0	-7.1512	-7.8874	-8.5441	0.0	-0.74153				-64.680	7.4197	1.720	8.9	0.0
10		illite/Ca-smec	8.2117	0.0	-0.7333	0.0	1.3621		-376.896		+381.205		8.3988	2.150	9.1	0.0
11		Na-smec/Ca-smec	4.1333	0.0	0.0	-0.7312	-2.6216		-1.867E+4	+1.867E+4			7.7516	1.850	6.3	0.0
12		calcite/Ca-smec	6.1475	0.0	-0.7362	-1.4850	0.0		-0.6346			+65.7749	7.4200	1.720	8.9	0.0
13		illite/Na-smec	7.9668	0.7409	0.0	0.0	0.7650			-117.053	+117.953		8.1493	1.943	9.1	0.0
14		calcite/Na-smec	6.7795	0.7362	0.0	-0.7583	0.0			-0.6325		-65.774	7.4200	1.719	8.9	0.0
15		calcite/illite	7.4403	1.5059	0.7697	0.0	0.0				-0.6361	-65.347	7.4199	1.720	8.9	0.0
16		Ca-smec/Na-smec/heul	0.0	0.0	0.0	-1.1152	-3.3189	-1.201E+2	-1.795E+4	+1.805E+4			7.1242	1.645	6.1	0.0
17		Ca-smec/illite/heul	0.0	0.0	-0.7315	0.0	+0.9623	-143.491	-379.170		+527.868		8.3833	2.155	9.0	0.0
18		Ca-smec/heul/calcite	0.0	0.0	-0.7380	-1.3340	0.0	-139.974	+120.045			+141.111	7.3683	1.897	9.0	0.0
19		illite/heul/calc	0.0	1.0959	0.3601	0.0	0.0	-141.075			+126.233	+66.921	7.3945	1.871	9.0	0.0
20		illite/heul/calc/Ca-smec	0.0	0.0	-0.6966	0.0	0.0	-92.703	-1.515E+3		+1.618E+3	-1.036E+3	7.9512	0.899	7.0	0.0
21		Nasm/heul/calc/Casm/il	0.0	0.0	0.0	0.0	0.0	-496.981	-3.3615E+4	+3.4529E+4	-120.589	+2.9734E+3	9.6587	9.555	12.1	0.0
22		calcite/heul/Ca-smec	0.0	0.0	-0.7380	-1.3340	0.0	-139.974	+120.045			+141.111	7.3683	1.897	9.1	0.0
23	B	Ca-smec/heul/calcite	0.0	0.0	-0.7046	-1.2704	0.0	-230.773	0.0			+2.972	7.4384	1.733	8.7	7.718E-5
24		Na-smec/heul/calcite	0.0	0.7036	0.0	-0.5561	0.0	-236.527		0.0		2.959	7.4389	1.748	8.7	7.976E-5
25		illite/heul/calcite	0.0	1.2511	0.5492	0.0	0.0	-246.796			0.0	+2.8878	7.4397	1.785	8.7	8.473E-5
26		Nasm/Casm/heu/calc	0.0	0.0	0.0	1.2743	0.0	-6.228E+3	-581.215	0.0		+93.484	10.1591	25.30	13.6	3.228E-3
27	C	illite/Ca-smec/heul/calc	0.0	0.0	-0.4880	0.0	0.0	-1.102E+3	-894.679		0.0	-1.644E+3	8.8771	0.987	5.6	7.466E-4
28	D	Nasm/il/Casm/heu/calc	0.0	0.0	0.0	0.0	0.0	-6.235E+3	-507.694	0.0	-124.347	+73.199	10.1566	25.11	13.5	3.243E-3

Table 6-4 (continued).

CERRO COLORADO 1

Trial No.		Equilibrium Mineral Phase	Saturation Index (+ supersaturation, - undersaturation)					Mass µmol/kg H$_2$O (+ dissolution, - precipitation)					Solution Chemistry			
			heulandite	Ca-smectite	Na-smectite	illite	calcite	heulandite	Ca-smectite	Na-smectite	illite	calcite	pH	alk (10^{-3})	I (10^{-3})	oligoclase dissolved per kg H$_2$O (mol)
		initial solution	10.1107	5.3816	4.9559	4.0161	-0.2638						7.180	3.094	18.4	0.0
1	A	heulandite	0.0	-6.3833	-6.8090	-7.5969	-0.2640	-0.7421					7.180	3.095	18.4	0.0
2		calcite	10.1494	4.9967	4.5658	3.7868	0.0					+126.539	7.3815	3.354	18.7	0.0
3		Ca-smectite	5.4886	0.0	-0.4257	-1.2948	-0.2621		-0.6338				7.1816	3.096	18.4	0.0
4		illite	6.6146	1.3128	0.8870	0.0	-0.2628				-0.6337		7.1809	3.096	18.4	0.0
5		Na-smectite	5.8541	0.4257	0.0	-0.8746	-0.2621			-0.6322			7.1816	3.096	18.4	0.0
6		heul/Ca-smec	0.0	0.0	-0.4188	-1.3660	-0.6507	-180.045	+154.103				6.8772	2.789	18.0	0.0
7		heul/calcite	0.0	-6.8136	-7.2444	-7.8709	0.0	-0.7420				+126.621	7.3817	3.348	18.6	0.0
8	B	Ca-smec/heul/calcite	0.0	0.0	-0.4350	-1.0047	0.0	-184.759	+158.923			+391.323	7.3304	3.569	18.9	0.0
9		Ca-smec/heul/calcite	0.0	0.0	-0.4172	-0.9163	0.0	-305.648	0.0			+18.195	7.4249	3.396	18.6	1.024E-4
10		Na-smec/heul/calcite	0.0	0.4169	0.0	-0.4927	0.0	-310.797		0.0		+18.430	7.4256	3.411	18.6	1.047E-4
11		illite/heul/calc	0.0	0.9013	0.4849	0.0	0.0	-321.338			0.0	+18.869	7.4269	3.447	18.6	1.097E-4
12	B	illite/Ca-smec/heul/calc	0.0	0.0	-0.2564	0.0	0.0	-888.508	-694.275		0.0	-1.106E+3	8.3957	2.751	17.4	5.752E-4
13	C	Nasm/il/Casm/heu/calc	0.0	0.0	0.0	0.0	0.0	-3.497E+3	-545.602	0.0	-382.764	-103.575	9.6707	14.57	22.4	1.936E-3

SOIL AMENDMENT FACILITY 1

Trial No.		Equilibrium Mineral Phase	Saturation Index (+ supersaturation, - undersaturation)					Mass µmol/kg H$_2$O (+ dissolution, - precipitation)					Solution Chemistry			
			heulandite	Ca-smectite	Na-smectite	illite	calcite	heulandite	Ca-smectite	Na-smectite	illite	calcite	pH	alk (10^{-3})	I (10^{-3})	oligoclase dissolved per kg H$_2$O (mol)
		initial solution	8.9366	3.0945	2.6739	2.1637	-0.0040						8.2730	1.541	8.5	0.0
1	A	heulandite	0.0	-7.2949	-7.7155	-8.0903	-0.0034	-0.7416					8.2742	1.541	8.5	0.0
2		calcite	8.9363	3.0872	2.6665	2.1591	0.0					+0.4618	8.2765	1.548	8.5	0.0
3		Ca-smectite	6.2875	0.0	-0.4206	-0.8830	0.0057		-0.6058				8.2829	1.543	8.5	0.0
4		illite	7.0542	0.8997	0.4791	0.0	0.0017				-0.5697		8.2788	1.542	8.5	0.0
5		Na-smectite	6.6485	0.4207	0.0	-0.4680	0.0055			-0.5899			8.2826	1.543	8.5	0.0
6		heul/Ca-smec	0.0	0.0	-0.4068	-1.5306	-1.1505	-105.071	+89.824				7.2449	1.364	8.3	0.0
7		heul/calcite	0.0	-7.3009	-7.7215	-8.0938	0.0	-0.7416				+0.3931	8.2773	1.542	8.5	0.0
8		Ca-smec/heul/calcite	0.0	0.0	-0.4330	-0.8010	0.0	-116.875	+107.248			+190.524	8.1525	1.778	8.7	0.0
9		Ca-smec/heul/calcite	0.0	0.0	-0.3876	-0.5442	0.0	-221.042	0.0			+0.8635	8.4261	1.706	8.5	8.046E-5
10		Na-smec/heul/calcite	0.0	0.3806	0.0	-0.1315	0.0	-268.567		0.0		+3.501	8.4537	1.899	8.6	1.041E-4
11		illite/heul/calcite	0.0	0.4959	0.1191	0.0	0.0	-293.831			0.0	+5.020	8.4689	2.002	8.6	1.167E-4
12	B	illite/Ca-smec/heul/calc	0.0	0.0	-0.2864	0.0	0.0	-485.600	-99.619		0.0	-116.778	9.0008	2.424	8.6	2.387E-4
13		Nasm/il/Casm/heu/calc	0.0	0.0	0.0	0.0	0.0	-4.138E+3	+141.404	0.0	-102.375	+1.612E+3	9.9864	20.54	16.3	2.027E-3
14		Nasm/Casm/heu/calc	0.0	0.0	0.0	0.9227	0.0	-4.135E+3	+80.244	0.0		+1.630E+3	9.9892	20.71	16.3	2.017E-3

CONCLUSIONS

Basic questions underlying this investigation concern the factors controlling diagenesis, and what effect these factors have had on water quality and availability. These questions were approached by examining both the allogenic and authigenic composition of the basin-fill, and by drawing certain inferences about the geochemical conditions that would account for the observed mineral species and textures. While the set of sidewall cores on which the study is based provided a unique glimpse into the geochemical environment of the lower Santa Fe Group, they were collected selectively from sandy intervals in only a few widely separated wells. Thin-sectioned samples display a high degree of textural and compositional variability, both between wells and within the same well. Over the course of the investigation, it proved difficult to group samples by common characteristics and to define consistent patterns or trends within the groupings. Framework grain types are not homogeneously distributed, nor are the products of their dissolution and alteration. Despite the small sample population, some generalizations may be drawn.

Provenance

Differences in clast composition between East and West Mesa wells suggest dissimilar provenance, and down-hole variations in clast abundance imply that a more dynamic sediment delivery system existed on the East Mesa. Plutonic and metamorphic sediments were probably derived from the northwest, while volcaniclastic sediments originated in the Jemez, Espinaso or Latir volcanic fields to north. West Mesa wells CC1 and SAF1 have a west to northwest sedimentary source area (of predominantly Mesozoic rocks) not shared by East Mesa wells CW5 and CW6.

Dissolution

Skeletal grain content of Albuquerque samples ranges from 2 to 4 percent of total sandstone volume, and is slightly higher for East Mesa wells than for West Mesa wells. While dissolution of framework grains may be initiated or enhanced by microbial processes early in the sediment burial history, prolonged contact with

groundwater (hydrolysis) is a more plausible mechanism for the generation of secondary porosity. Feldspar hydrolysis has released approximately 0.3 moles dissolved mineral matter per liter of water, far more than the 3×10^{-3} moles required by the geochemical model to equilibrate with the last phase in the paragenetic sequence. "Surplus" solutes are dispersed through deeper aquifer zones.

Cementation and Alteration

Diagenetic minerals present in the samples are clay (smectite and interlayered illite/smectite), zeolites and calcite. Zeolites are most often (but not always) associated with clay. Calcite occurs as both isolated, poikilitic crystals encompassing several adjacent pores, and micritic patches restricted to a single pore. Clay is interpreted petrographically to occur in microporous zones as a pore-filling or a psuedomorphous replacement of framework grains.

Results of geochemical simulations indicate the pH, alkalinity and ionic strength of pore waters become progressively elevated as feldspar dissolves to precipitate each phase in the system. A theoretical paragenesis of model phases, based on thermodynamic considerations alone, is heulandite-calcite-Ca smectite-illite-Na smectite. Though modeled as discrete species, clay phases are actually compositional variants of a more or less generic phyllosilicate structure.

Equilibrium conditions existing at a local scale control both the occurrence and speciation of diagenetic minerals. These conditions are in turn determined by aquifer heterogeneity and the hydrodynamic properties of groundwater within small-scale aquifer compartments.

REFERENCES

Aldrich, M. J., Jr., Chapin, C. E., and Laughlin, A. W., 1986, Stress history and tectonic development of the Rio Grande Rift, New Mexico: Journal of Geophysical Research, vol. 91, no. B6, pp. 6199-6211.

Allen, P. A. and Allen, J. R. L., 1990, Basin analysis-principles and applications: Blackwell Scientific, Oxford, England, pp. 228-238.

Bachman, G. O., and Mehnert, H. H., 1978, New K-Ar dates and the late Pliocene to Holocene geomorphic history of the central Rio Grande region, New Mexico: Geological Society of America Bulletin, vol. 89, pp. 283-292.

Bailey, R. A., Smith, R. L., and Ross, C. S.,1969, Stratigraphic nomenclature of volcanic rocks in the Jemez Mountains, New Mexico: United States Geological Survey Bulletin 1274-P, 19 pp.

Beard, D. C., and Weyl, P. K., 1973, Influence of texture on porosity and permeability of unconsolidated sand: American Association of Petroleum Geologists Bulletin, vol. 57, pp. 349-369.

Blatt, H. and Christie, J. M.,1963, Undulatory extinction in quartz of igneous and metamorphic rocks and its significance in provenance studies of sedimentary rocks: Journal of Sedimentary Petrology, vol. 33, pp. 559-579.

Bloch, S. and Franks, S. G., 1993, Preservation of shallow plagioclase dissolution porosity during burial: implications for porosity prediction and aluminum mass balance: AAPG Bulletin, vol. 77, no. 9, pp. 1488-1501.

Bjorlykke, K., 1983, Diagenetic reactions in sandstones in Parker, A. and Sellwood, B. W. (eds.), Sediment Diagenesis: Reidel Publishing Co., pp. 169-213.

Brindley, G. W., 1981, X-ray identification (with ancillary techniques) of clay minerals, in Longstaffe, F. J. (ed.), Clays and the resource geologist: Mineralogical Association of Canada Short Course Handbook, Vol. 7, pp. 22-35.

Bryan, K., 1938, The Ceja del Rio Puerco: a border feature of the basin and range province in New Mexico, II. Geomorphology: Journal of Geology, vol. 46, no. 1, pp. 1-16.

Bryan, K, and McCann, F. T., 1937, The Ceja del Rio Puerco: a border feature of the basin and range province in New Mexico, I. Stratigraphy and structure: Journal of Geology, vol. 45, no. 8, pp. 801-828.

Busenberg, E., 1978, The products of the interaction of feldspars with aqueous solutions at 25· C: Geochimica et Cosmochimica Acta, vol. 42, pp. 1679-1679.

Carroll, D., 1970, Clay minerals: a guide to their X-ray diffraction: Geological Society of America Special Paper 126, 80 pp.

Chamberlin, R. M.,1983, Cenozoic domino-style crustal extension in the Lemitar Mountains, New Mexico: a summary: New Mexico Geological Society Guidebook 34, pp. 111-118.

Chamberlin, R. M., Kues, B. D., Cather, S. M., Barker, J. M., and McIntosh, W. C., 1994, Mogollon Slope, West-Central New Mexico and East-Central Arizona: New Mexico Geological Society Guidebook 45, 335 pp.

Chapin, C. E., 1988, Axial basins of the northern and central Rio Grande rifts, in Sloss, L. L., ed., Sedimentary Cover--North American craton: U.S.; the Geology of North America vol. D-2: Boulder, Colorado, Geological Society of America, p. 165-170.

Chapin, C. E. and Cather, S., 1994, Tectonic setting of the axial basins of the northern and central Rio Grande rift: Geological Society of America, Special Paper 291, pp. 5–25.

Colella, C., Aiello, R. and Porcelli, C., 1978, Hydration as an early stage in the zeolitization of natural glass, in Sand, L. B. and Mumpton, F. A. (eds.), Natural zeolites: occurrence, properties, use: Pergamon Press Ltd., Oxford, pp. 345-350.

Darton, N. H., 1922, Geologic structure of parts of New Mexico: United States Geological Survey Bulletin 726, pp. 173-275.

Denny, C. S., 1940, Santa Fe Formation in the Espanola Valley, New Mexico: Geological Society of America Bulletin vol. 51, pp. 677-694.

Dickinson, W. R., 1970, Interpreting detrital modes of graywacke and arkose: Journal of Sedimentary Petrology, vol. 40, no. 2, pp. 695-707.

Dungan, M. A., Thompson, R. A., and Stormer, J. S., 1989, Rio Grande rift volcanism: northeastern Jemez zone, New Mexico: New Mexico Bureau of Mines and Mineral Resources Memoir 46, pp. 435-483.

Ehrenberg, S. N., 1989, Assessing the relative importance of compaction processes and cementation to reduction of porosity in sandstones: Discussion; compaction and porosity evolution of Pliocene sandstones, Ventura Basin, California: Discussion: American Association of Petroleum Geologists Bulletin, vol. 73, no. 10, pp. 1274-1276

Faure, G., 1991, Principles and applications of inorganic geochemistry: Macmillan Publishing Company, New York, NY, variously paginated.

Freeze, R. A., and Cherry, J. A., 1979, Groundwater: Prentice-Hall, Inc., Englewood Cliffs, N. J., p. 95.

Folk, R. L., 1974, Petrology of Sedimentary Rocks: Hemphill Publishing Company, Austin, 182 pp.

Galusha, T., 1966, The Zia Sand Formation, new early to medial Miocene beds in New Mexico: American Museum Novitates 2271, 12 pp.

Galusha, T., and Blick, J. C., 1971, Stratigraphy of the Santa Fe Group, New Mexico: American Museum of Natural History Bulletin, vol. 144 article 1, 128 pp.

Gazzi, P., 1966, Le arenarie del flysch sopracretaceo dell'Appennino modenese; correlazioni con il flysch di Monghidoro: Mineralogica e Petrografica Acta, vol. 12, pp. 69-97.

Hawley, J. W., compiler, 1978 Guidebook to the Rio Grande rift in New Mexico and Colorado: New Mexico Bureau of Mines and Mineral Resources, Circular 163, 241 pp.

Hawley, J. W., and Haase, C. S., 1992, Hydrogeologic framework of the northern Albuquerque basin: New Mexico Bureau of Mines and Mineral Resources Open-File Report 387

Hawley, J. W. and Love, D. W., 1991, Quaternary and Neogene landscape evolution: A transect across the Colorado Plateau and Basin and Range provinces in west-central and central New Mexico, in Julian, B., and Zidek, J., eds., Field guide to geologic excursions in New Mexico and adjacent areas of Texas and Colorado: New Mexico Bureau of Mines & Mineral Resources, Bulletin 137, pp. 105-148 (130-133).

Hawley, J. W., Haase, C. S., and Lozinsky, R. Pp., 1995, An underground view of the Albuquerque Basin, in Ortega-Klett, C., ed., Proceedings of the 39th Annual New Mexico Water Conference, "The water future of Albuquerque and Middle Rio Grande Basin": New Mexico Water Resources Research Institute Report 290, pp. 37-55.

Hay, R. L., 1978, Geologic occurrence of zeolites, in Sand, L. B. and Mumpton, F. A. (eds.), Natural zeolites: occurrence, properties, use: Pergamon Press Ltd., Oxford, pp. 135-143.

Hay, R. L., 1966, Zeolites and zeolitic reactions in sedimentary rocks: Geological Society of America Special Paper No. 85.

Hayden, F. V., 1869, Preliminary field report of the United States Geological Survey of Colorado and New Mexico: U. S. Government Printing Office, Washington, D. C., 155 pp.

Henry, C. D., and Price, J. G., 1986, Early basin and range development in trans-Pecos Texas and adjacent Chihuahua: magmatism and orientation, timing, and style of extension: Journal of Geophysical Research, vol. 91, no. B6, pp. 6213-6224.

Houseknecht, D. W., 1987, Assessing the relative importance of compaction processes and cementation to reduction of porosity in sandstones: American Association of Petroleum Geologists Bulletin, vol. 71, pp. 633-642.

Ingersoll, R. V., Cavazza, W., Baldridge, W. S., and Shafiqullah, M., 1990, Cenozoic sedimentation and paleotectonics of north-central New Mexico: Implications for initiation and evolution of the Rio Grande rift: Geological Society of America Bulletin, vol. 102, pp. 1280-1296.

Johnson, G. K., Flowtow, H. E., and O'Hare, P. A. G., 1985, Thermodynamic studies of zeolites: heulandite: American Mineralogist, vol. 70, pp. 1065-1071.

Kelley, V. C., 1977, Geology of Albuquerque basin, New Mexico: New Mexico Bureau of Mines and Mineral Resources Memoir 33, 60 pp.

Kharaka, Y. K., Law, L. M., Carothers, W. W., and Goerlitz, D. F., 1986, Role of organic species dissolved in formation waters from sedimentary basins in mineral diagenesis, in Gautier, D. L. (ed.), Roles of organic matter in sediment diagenesis: Society of Economic Paleontologists and Mineralogists Special Publication 38, pp. 111-112.

Kieft, T. L., 1991, Soil microbiology in reclamation of arid and semiarid lands, in Skujins, J. (ed), Semiarid lands and deserts: soil resource and reclamation: Marcel Dekker, Inc., New York, pp. 209-256.

Kottlowski, F. E., 1953, Tertiary-Quaternary sediments of the Rio Grande valley in southern New Mexico: New Mexico Geological Society Guidebook 4, pp. 144-148.

Lambert, P. W., 1968, Quaternary stratigraphy of the Albuquerque area, New Mexico: unpublished Ph.D. dissertation, University of New Mexico, 329 pp.

Lambert, P. W., Hawley, J. W., and Wells, S. G., 1982, Supplemental road-log segment III-S: Urban and environmental geology of the Albuquerque area: New Mexico Geological Society, Guidebook 333, pp. 977-124.

Love, D. W. and Young, J. D., 1983, Progress report on the late Cenozoic geologic evolution of the lower Rio Puerco, in Chapin, C. E. and Callender, J. F. (eds), Socorro II: New Mexico Geological Society 34th Field Conference Guidebook, pp. 277-284.

Lozinsky, R. P., 1988, Stratigraphy, sedimentology, and sand petrology of the Santa Fe Group and pre-Santa Fe Tertiary deposits in the Albuquerque basin, central New Mexico: Unpublished Ph.D. dissertation, New Mexico Institute of Mining and Technology, 298 pp.

Lozinsky, R. P., 1994, Cenozoic stratigraphy, sandstone petrology, and depositional history of the Albuquerque Basin, central New Mexico: Geological Society of America, Special Paper 291, pp. 73-81.

Lozinsky, R. P. and Tedford, R. H., 1991, Geology and paleontology of the Santa Fe Group, southwestern Albuquerque basin, Valencia County, New Mexico: New Mexico Bureau of Mines and Mineral Resources Bulletin 132, pp. 8-24.

Lundegard, P. D. and Land, L. S., 1986, Carbon dioxide and organic acids: their role in porosity enhancement and cementation, Paleogene of the Texas Gulf Coast, in Gautier, D. L. (ed.), Roles of organic matter in sediment diagenesis: Society of Economic Paleontologists and Mineralogists Special Publication 38, pp. 129-146.

Machette, M. N., 1985, Calcic soils of the southwestern United States, in Weide, D. L., ed., Quaternary soils and geomorphology of the American Southwest: Geological Society of America Special Paper 203, pp. 1-21.

Mack, G. H., and Grigsby, J. D.,1985, Mechanical and chemical diagenesis of the Haynor Ranch and Rincon Valley formations (Santa Fe Group, Miocene), San Diego Mountain, New Mexico: New Mexico Geology, vol. 7 no. 3, pp. 45-48.

Mason, B. and Sand, L. B., 1960, Clinoptilolite from Patagonia. The relationship between clinoptilolite and heulandite: American Mineralogist, vol. 45, pp. 341-350

May, S. J. and Russell, L. R., 1994, Thickness of the syn-rift Santa Fe Group in the Albuquerque Basin and its relation to structural style: Geological Society of America, Special Paper 291, pp. 113-123.

McIntosh, W. C., Sutter, J. F., Chapin, C. E., Osburn, G. R., and Ratte, J. C., 1986, A stratigraphic framework for the eastern Mogollon-Datil volcanic field based on paleomagnetism and high-precision $^{40}Ar/^{29}Ar$ dating of ignimbrites--a progress report: New Mexico Geological Society Guidebook 37, pp. 183-195.

Mozley, P. S., Chamberlin, R., Gillentine, J. M., and Lozinsky, R. P., 1992, Petrologic date, in Hydrogoeologic framework of the northern Albuquerque Basin; New Mexico Bureau of Mines and Mineral Resources, Open-File Report 387, pp. IV-1 to IV-17.

Mumpton, F. A., 1960, Clinoptilolite redefined: American Mineralogist, vol. 45, pp. 351-369

Nelson, R. A., Patton, T. L. and Morley, C. K., 1992, Rift-segment interaction and its relation to hydrocarbon exploration in continental rift systems: American Association of Petroleum Geologists Bulletin, vol. 76, no. 8, pp. 1153-1169.

Ogilvie, I. H.,1905, The high-altitude conoplane; a topographic form illustrated in the Ortiz Mountains: American Geologist, vol. 36, pp. 27-34.

Olsen, K. H, Baldridge, W. S., and Callender, J. F., 1987, Rio Grande rift: an overview: Tectonophysics, vol. 143, pp. 119-139.

Osburn, G. R., and Chapin, C. E.,1983, Ash-flow tuffs and cauldrons in the northeast Mogollon-Datil volcanic field: a summary: New Mexico Geological Society Guidebook 34, pp. 197-204.

Pate, C. R., 1989, Assessing the relative importance of compaction processes and cementation to reduction of porosity in sandstones: Discussion: American Association of Petroleum Geologists Bulletin, vol. 73, no. 10, pp. 1270-1273.

Parkhurst, D. L., Thorstenson, D. C., and Plummer, L. N.,1993, PHREEQE: a geochemical reaction model based on an ion-pairing aqueous model, version 2.1: International Ground Water Modeling Center, Colorado School of Mines, Golden, Colorado.

Plas, L. van der, and Tobi, A. C., 1965, A chart for judging the reliability of point counting results: American Journal of Science, vol. 263, pp. 87-90.

Reeves, C. C., Jr., 1978, Economic significance of playa lake deposits, in Matter, A. and Tucker, M. E. (eds.), Modern and ancient lake sediments: International Association of Sedimentologists Special Publication 2, pp. 279-290.

Robert, M. and Berthelin, J., 1986, Role of biological and biochemical factors in soil mineral weathering, in Huang, P. M. and Schnitzer, M. (eds), Interactions of soil minerals with natural organics and microbes: Soil Science Society of America Special Publication No. 17, pp. 453-495.

Robie, R. A., Hemingway, B. S., and Fisher, J. R., 1979, Thermodynamic properties of minerals and related substances at 298.15∞ K and 1 bar pressure and at higher temperatures: U. S. Geological Survey Bulletin 1452.

Rosendahl, B. R., Reynolds, K. J., Lorber, P. M., Burgess, C. F., McGill, J., Scott, D., Lambiase, J. J., and Derksen, S. J., 1986, Structural expressions of rifting: lessons from Lake Tanganyika, Africa, in Frostick, L. E., et al., eds., Sedimentation in the African Rifts: Special Publications of the Geological Society of London 25, pp. 29-43.

Sheppard, R. A. and Gude, A. J., 1968, Distribution and genesis of authigenic silicate minerals in tuffs of Pleistocene Lake Tecopa, Inyo County, California: United States Geological Survey Professional Paper 597, 38p.

Siebert, R. M., Moncure, G. K., and Lahann, R. W., 1984, A theory of framework grain dissolution in sandstones, in McDonald, D. A., and Surdam, R. C., (eds.), Clastic Diagenesis: AAPG Memoir 37, pp. 163-175.

Smith, G. A., Larsen, D., Harlan, S. S., McIntosh, W. C., Erskine, D. W., and Taylor, S., 1991, A tale of two volcaniclastic aprons: field guide to the sedimentology and physical volcanology of the Oligocene Espinaso Formation and Miocene Peralta Tuff, north-central New Mexico, in Julian, B. and Zidek, J. (eds.) Field guide to geologic excursions in New Mexico and adjacent areas of Texas and Colorado: New Mexico Bureau of Mines and Mineral Resources Bulletin 137, pp. 87-103.

Spiegel, Z., and Baldwin, B., 1963, Geology and water resources of the Santa Fe area, New Mexico: United States Geological Survey Water-Supply Paper 1525, 258 pp.

Stevenson, F. J., 1967, Organic Acids in Soils, in McLaren, A. D. and Peterson, G. H. (eds), Soil Biochemistry: Marcel Dekker, Inc., New York, pp. 119-146.

Stevenson, F. J., and Fitch, A., 1986, Chemistry of complexation of metal ions with soil solution organics, in Huang, P. M. and Schnitzer, M. (eds), Interactions of soil minerals with natural organics and microbes: Soil Science Society of America Special Publication No. 17, pp. 29-58.

Sullivan, K. B. and McBride, E. F., 1991, Diagenesis of sandstones at shale contacts and diagenetic heterogeneity, Frio Formation, Texas: AAPG Bulletin, vol. 75 no. 1, pp. 121-138.

Surdam, R. C., Boese, S. W., and Crossey, L. J., 1984, The chemistry of secondary porosity, in McDonald, D. A., and Surdam, R. C., (eds.), Clastic Diagenesis: AAPG Memoir 37, pp. 127-149.

Surdam, R. C., and Sheppard, R. A., 1978, Zeolites in saline, alkaline-lake deposits, in Sand, L. B. and Mumpton, F. A. (eds.), Natural zeolites: occurrence, properties, use: Pergamon Press Ltd., Oxford, pp. 145-174.

Swanson, A. G., 1981, Sample examination manual, American Association of Petroleum Geologists Methods in Exploration Series, Tulsa, Oklahoma.

Tan, K. H., 1986, Degradation of soil minerals by organic acids, in Huang, P. M. and Schnitzer, M. (eds), Interactions of soil minerals with natural organics and microbes: Soil Science Society of America Special Publication No. 17, pp. 1-27.

Tan, K. H., 1980, The release of silicon, aluminum, and potassium during decomposition of soil minerals by humic acid: Soil Science, vol. 129 no. 1, pp. 5-11.

Tedford, R. H, 1981, Mammalian biochronology of the late Cenozoic basins of New Mexico: Geological Society of America Bulletin, Part I, v. 92, pp. 1008–1022.

Tedford, R. H., 1982, Neogene stratigraphy of the northwestern Albuquerque basin: New Mexico Geological Society 33, pp. 273-278.

Thorn, C. R., McAda, D. P., and Kernodle, J. M., 1993, Geohydrologic framework and hydrologic conditions in the Albuquerque Basin, central New Mexico, U.S. Geological Survey, Water-Resources Investigations Report 93-4149, 106 pp.

Tschernich, R. W., 1992, Zeolites of the world: Geoscience Press, Inc. Phoenix, Az., pp. 246-273.

Tucker, M. E., 1982, The field description of sedimentary rocks: Geological Society of London Handbook Series, Open University Press, Buckinghamshire; Halsted Press, New York, 112 p.

Walker, T. R., Waugh, B., and Crone, A. J., 1978, Diagenesis in first-cycle desert alluvium of Cenozoic age, southwestern United States and northwestern Mexico: Geological Society of America Bulletin, vol. 89, pp. 19-32.

Welton, J. E., 1984, SEM petrology atlas: American Association of Petroleum Geologist Methods in Exploration Series, No. 4, variously paginated.

Wilson, M. D., and Pittman, E. D., 1977, Authigenic clays in sandstones: recognition and influence on reservoir properties and paleoenvironmental analysis: Journal of Sedimentary Petrology, vol. 47, no. 1, pp. 3-31.

Woods, T. L. and Garrels, R. M., 1987, Thermodynamic values at low temperature for natural inorganic materials: an uncritical summary: Oxford University Press, New York, variously paginated.

LIST OF FIGURES

Figure 6-1. Index map of Albuquerque Basin area showing location of Albuquerque Municipal Wells: Charles Wells 5 and 6 (Ch5 & 6), Cerro Colorado 1 (CC1) and Soil Amendment Facility 1 (SAF1). Map base from Thorn et al. (1993, Fig. 16); see Plate 3 (Hawley, this report) for revised locations of major faults and buried axial-channel boundaries.

Figure 6-2. Ternary diagram of detrital modes (after Folk, 1974). Q = quartz; F = feldspar; R = rock fragments; URF = undifferentiated rock fragments; VRF =_volcanic rock fragments; SRF = sedimentary rock fragments. Definition of parameters in Appendix A. Differences in sandstone composition between west mesa wells (CC1 and SAF1, solid symbols) and east mesa wells (CW5 and CW6, open symbols) is the result of differences in respective source area.

Figure 6-3. Distribution of authigenic minerals with depth occurrence. Mineral abundance, expressed in terms of relative pore volume, is independent of burial depth.

Figure 6-4. Cement groups plotted according to texture of host sediment. Zeolites and Zeolites + clay occur in coarser grained, less sorted sands, whereas carbonate and carbonate + clay occur in finer grained, better sorted sands. Grain Size and sorting from Appendix A, Table 2; cement groups from Appendix C.

Figure 6-5. Total macroporosity of each core sample, as a percentage of 300 point counts. Porosity generally decreases with increasing well depth, suggesting porosity loss to compaction and occlusion by mineral cements. Wide differences in porosity of samples from similar depths reflect the extreme heterogeneity in sedimentary texture.

Figure 6-6. Secondary porosity resulting from framework grain dissolution, alteration and fracture, expressed as a percentage of 100 porosity point counts. Secondary porosity generally increases with depth, suggesting diagenetic modifications to original porosity are more pronounced in deeper aquifer zones.

Figure 6-7. Minus-cement porosity versus total cement for each of the dominant cement types (after Houseknecht, 1987). NE-SW diagonal lines are lines of equal intergranular volume (post-cementation/compaction); NW-SE diagonal line separates graph into a cementation-dominated field (above) and a compaction-dominated field (below).

Figure 6-8. Relative abundance of framework grains versus well depth from Cerro Colorado 1. Definition of counted parameters in Appendix A.

Figure 6-9. Relative abundance of framework grains versus well depth for SAF 1. Definition of counted parameters in Appendix A.

Figure 6-10. Relative abundance of framework grains versus well depth for Charles Wells 5. Definition of counted parameters in Appendix A.

Figure 6-11. Relative abundance of framework grains versus well depth for Charles Well 6. Definition of counted parameters in Appendix A.

Figure 6-1. Index map of Albuquerque Basin area showing location of Albuquerque Municipal Wells: Charles Wells 5 and 6 (Ch5 & 6), Cerro Colorado (CC1) and Soil Amendment Facility 1 (SAF1). Map base from Thorn et al. (1993, Fig. 16); see Plate 3 (Hawley, this report) for revised locations of major faults and buried axial-channel boundaries

Figure 6-2. Ternary diagram of detrital modes (after Folk, 1974). Q = quartz, F = feldspar; R = rock fragments; URF = undifferentiated rock fragments; VRF = volcanic rock fragments; SRF = sedimentary rock fragments. Definition of parameters in Appendix A. Differences in sandstone composition between west mesa wells (CC1 and SAF1, solid symbols) and east mesa wells (CW5 and CW6, open symbols) is the result of differences in respective source area.
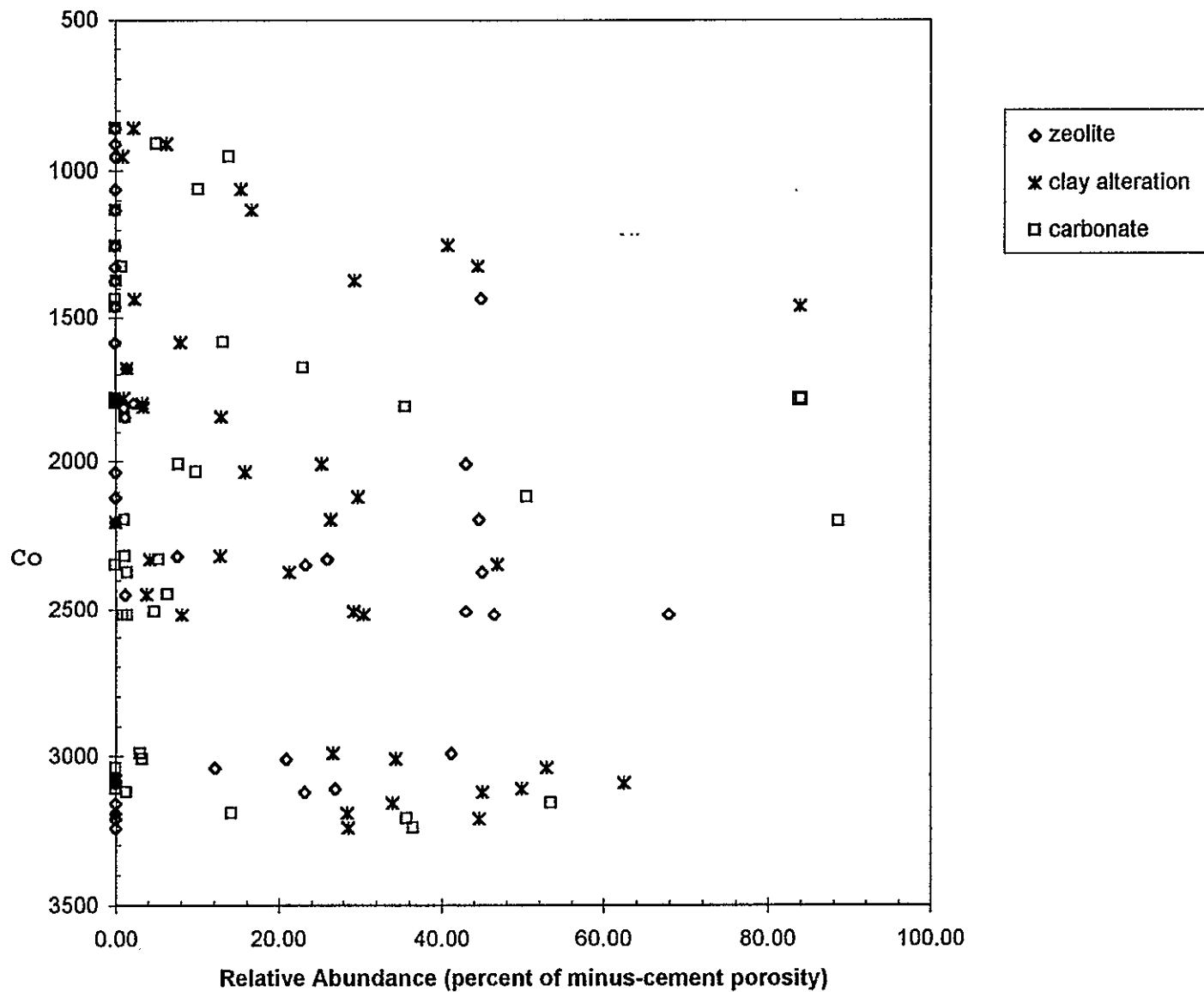
Figure 6-3. Distribution of authigenic minerals with depth of occurrence. Mineral abundance expressed in terms of relative pore volume, is independent of burial depth.

Figure 6-4. Cement groups plotted according to texture of host sediment. Zeolites and zeolites + clay occur in coarser grained, less sorted sands, whereas carbonate and carbonate + clay occur in finer grained, better sorted sands. Grain size and sorting from Appendix A, table 2; cement groups from Appendix C.

Figure 6-5. Total macroporosity of each core sample, as a percentage of 300 point counts. Porosity generally decreases with increasing well depth, suggesting porosity loss to compaction and occlusion by mineral cements. Wide differences in porosity of samples from similar depths reflect the heterogeneity in sedimentary texture.
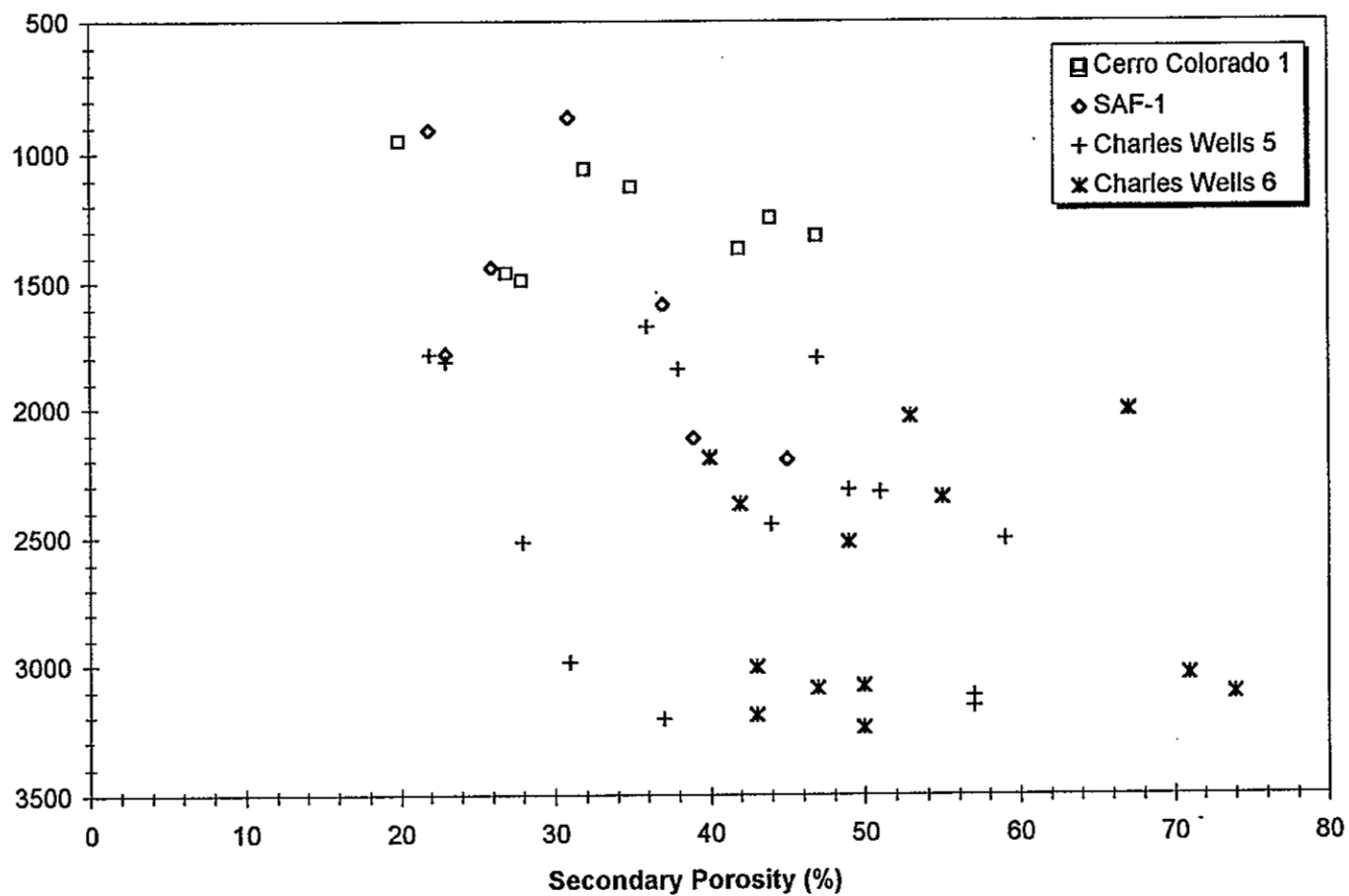
Figure 6-6. Secondary porosity resulting from framework grain dissolution, alteration and fracture, expressed as a percentage of 100 porosity point counts. Secondary porosity generally increases with depth, suggesting diagenetic modifications to original porosity are more pronounced in deeper aquifer zones.
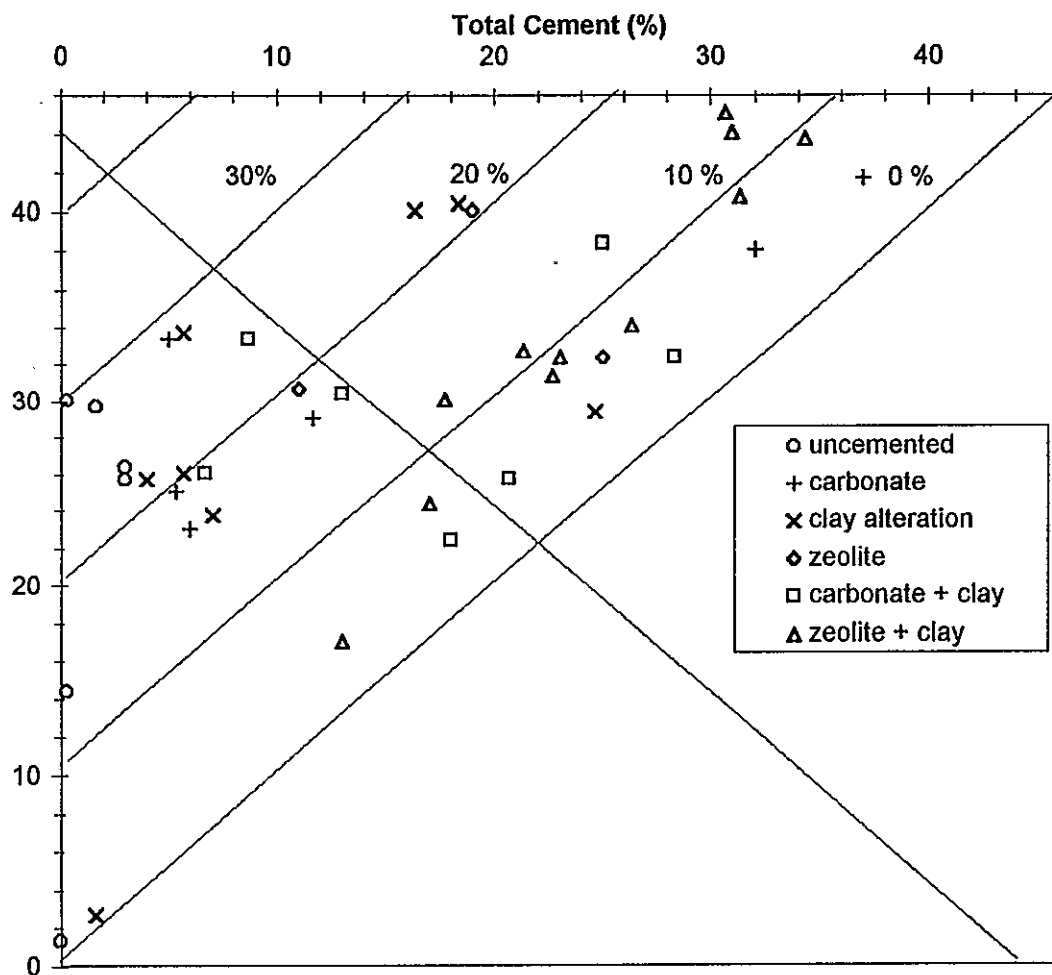
Figure 6-7. Minus-cement porosity versus total cement for each of the dominant cement types (after Houseknecht, 1987). NE-SW diagonal lines are lines of equal intergranular volume (post-cementation/compaction); NW-SE diagonal line separates graph into a cementation-dominated field (above) and a compaction-dominated field (below).

Cerro Colorado 1
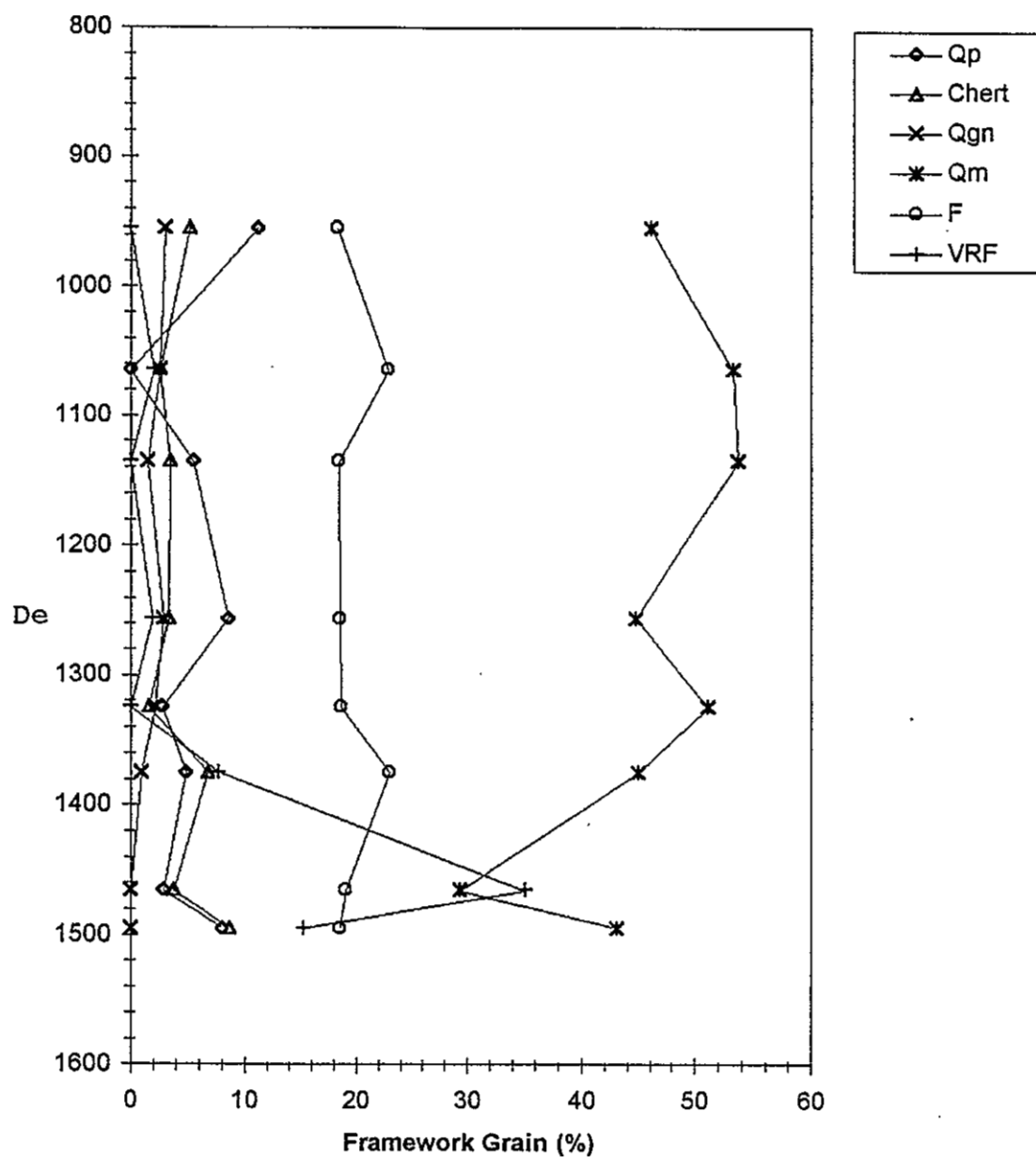
Figure 6-8. Relative abundance of framework grains versus well depth for Cerro Colorado 1. Definition of counted parameters in Appendix A.

Soil Amendment Facility 1
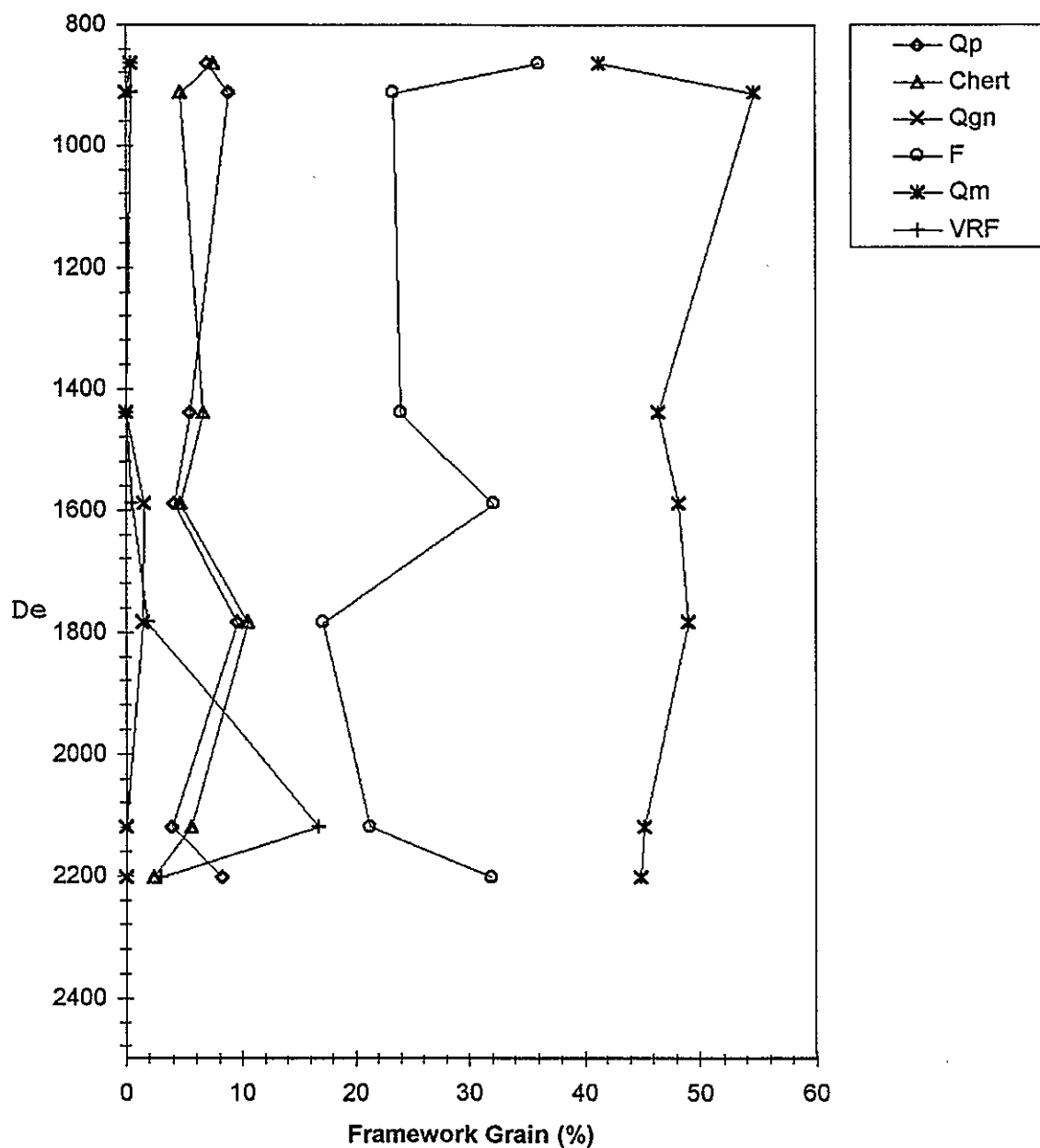
Figure 6-9. Relative abundance of framework grains versus well depth for SAF 1. Definition of counted parameters in Appendix A.

Charles Wells 5
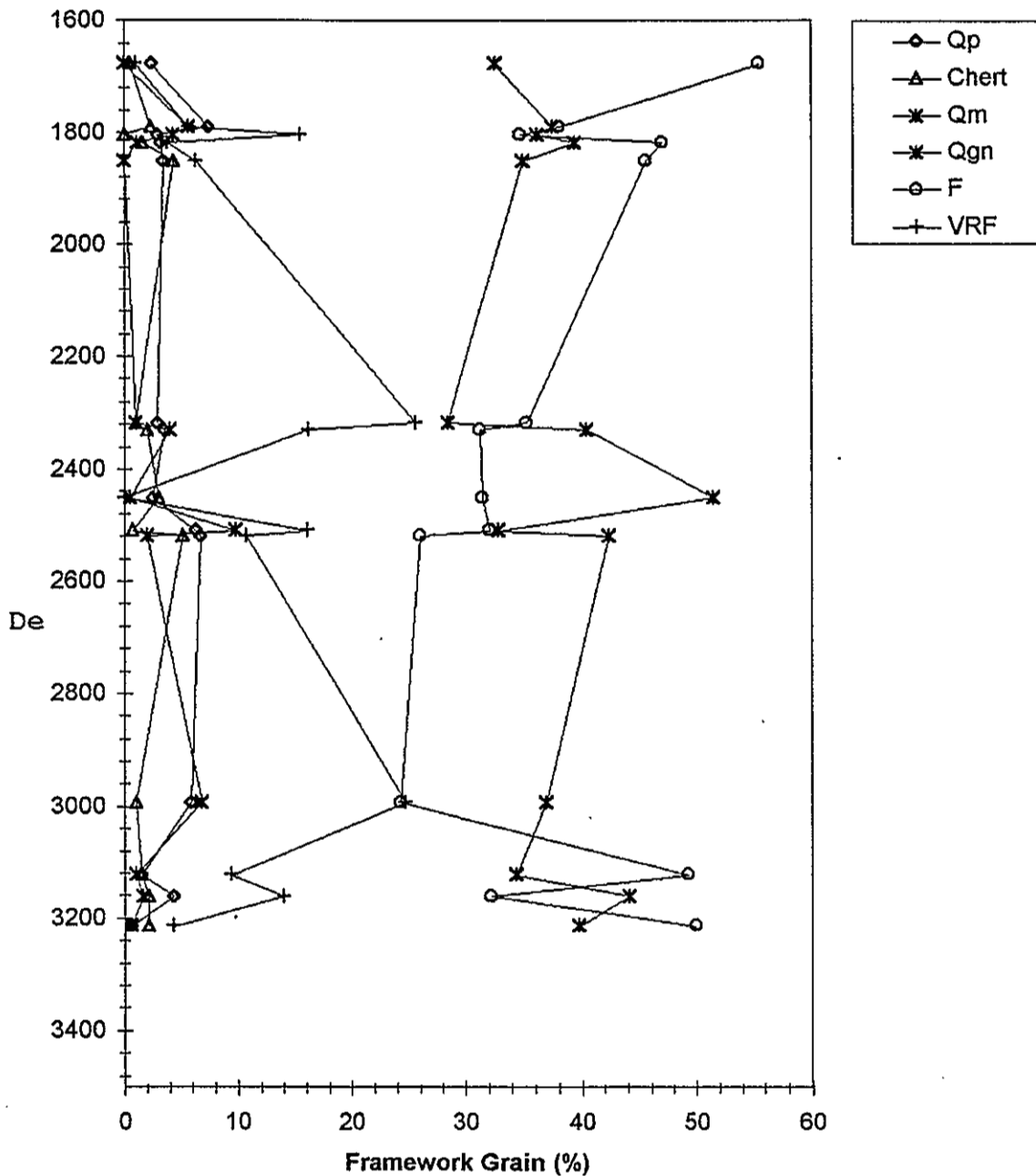
Figure 6-10. Relative abundance of framework grains versus well depth for Charles Wells 5. Definition of counted parameters in Appendix A.

Charles Wells 6
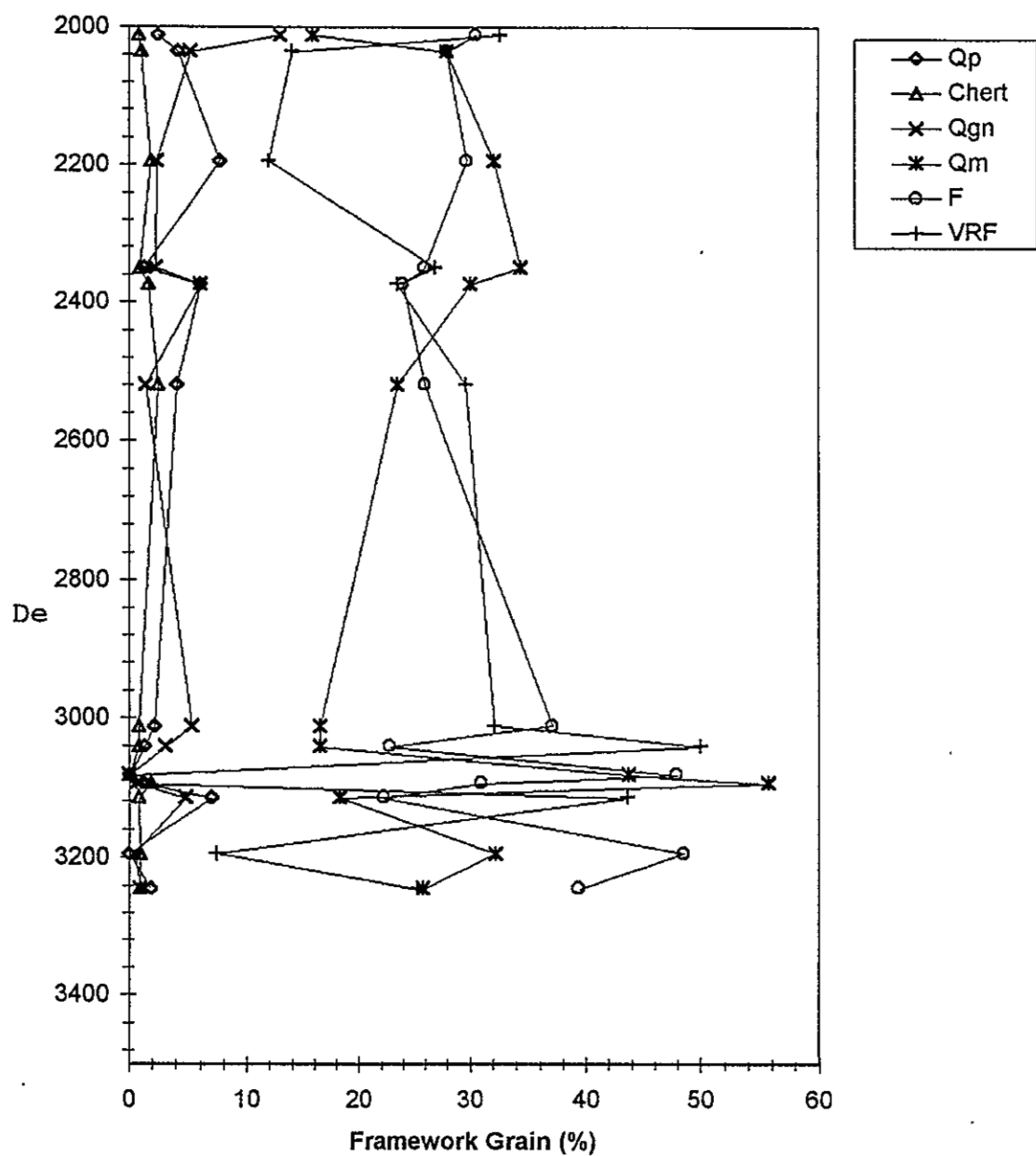
Figure 6-11. Relative abundance of framework grains versus well depth for Charles Well 6. Definition of counted parameters in Appendix A.

APPENDIX 6-A

Counted Parameters and Recalculated Parameters

APPENDIX A

Counted Parameters

Framework Grains

Qm: monocrystalline quartz
Qp: polycrystalline quartz
P: monocrystalline plagioclase feldspar
K: monocrystalline alkali feldspar
gn: polymineralic rock fragment of granitic or gneissic origin
Q_v: quartz phenocryst within volcanic rock fragment
P_v: plagioclase phenocryst within volcanic rock fragment
K_v: alkali feldspar phenocryst within volcanic rock fragment
V_g: groundmass of volcanic rock fragment
V_s: fine-grained, siliceous volcanic rock fragment
V_p: pumice or pumiceous volcanic rock fragment
Q_s: quartz within sedimentary rock fragment
Q_c: chert
F_s: feldspar within sedimentary rock fragment
S_m: fine-grained matrix of sandstone or siltstone sedimentary rock fragment
S_c: carbonate rock fragment (limestone)
U: undifferentiated rock fragment

Non-framework Grains

M: biotite, muscovite or chlorite
HM: heavy mineral
Opq: opaque mineral
DC: allogenic (detrital) clay
Cmt: pore-filling mineral growth (zeolite, calcite or phyllosilicate cement)
MP: intergranular macroporosity

Recalculated Parameters

Standard Method

% Q: $(Q_m + Q_p$/total framework grains
% F: (P + K + gn)/total framework grains
% R: (Qv + Pv + Kv + Vg + Vs + Vp + Qs + Qc + Fs + Sm + Sc + U)/total framework grains
% U: U/total lithic fragments
% V: (Qv + Pv + Kv + Vg + Vs + Vp)/total lithic fragments
% S: (Qs + Qc + Fs + Sm + Sc)/total lithic fragments

Modified Gazzi-Dickinson Method

% Q: (Qm + Qp + Qgn + Qv + Qs + Qc)/total framework grains
% F: (P + K + gn + Pv + Kv + Fs + Fgn)/total framework grains
% L: (Vg + Vs + Vp + Sm + Sc + U)/total framework grains
% U: U/total lithic fragments
% V: (Vg + Vs + Vp)/total lithic fragments
% S: (Sm + Sm + Sc)/total lithic fragments
C/Q: (Qp + Qgn + Qv + Qs + Qc)/Q
P/F: (P + Pv + Ps)/F

Cerro Colorado No. 1   <u>TABLE 1</u>

Counted Parameters

Depth (ft)	Q_m	Q_p	P	K	gn	Q_v	P_v	K_v	V_g	V_t	V_p	Q_s	Q_c	F_s	S_c	S_m	U	M	HM	Opq	DC	Cmt	MP
955	91	22	12	19	11	0	0	0	0	0	0	0	10	0	0	0	32	0	0	0	3	15	85
1065	105	7	20	22	8	0	1	0	3	0	0	1	5	0	0	0	32	0	3	0	18	17	58
1136	108	11	9	22	9	0	0	0	0	0	0	0	7	0	3	0	32	0	1	0	6	8	84
1256	94	18	11	27	7	0	1	0	0	0	3	0	7	0	0	1	41	1	0	0	4	14	71
1325	93	5	10	21	7	0	0	0	0	0	0	0	3	0	0	0	43	1	0	0	34	17	66
1375	94	10	19	24	7	1	0	1	0	0	14	0	14	0	0	9	16	1	0	0	34	6	50
1466	71	7	20	22	4	0	9	3	0	0	73	0	9	0	0	0	24	1	1	0	22	20	14
1495	65	12	13	15	0	1	0	0	0	0	22	0	13	0	0	1	9	2	0	0	96	28	23
1516	1	0	0	0	0	0	7	14	0	0	234	0	0	0	0	0	0	5	0	0	0	0	39
1556	0	0	1	0	0	0	10	1	0	0	94	0	0	3	0	0	1	3	0	0	156	0	31
1575	0	0	0	0	0	0	15	1	0	0	238	0	0	0	0	0	0	3	0	0	0	0	43
1592	0	0	0	0	0	0	9	11	0	0	250	0	0	0	0	0	0	5	0	0	0	0	25
1605	0	0	0	0	0	0	5	5	0	0	244	0	0	0	0	0	0	3	0	0	0	0	43
1626	0	0	0	0	0	0	26	8	0	0	229	0	0	0	0	0	0	3	1	0	0	0	33
1635	0	0	0	0	0	0	18	5	0	0	245	0	0	0	0	16	0	5	0	0	0	0	11

Recalculated Parameters

Depth (ft)	Standard Method						Modified Gazzi-Dickinson Method							
	% Q	% F	% R	% U	% V	% S	%Q	%F	%L	%U	%V	%S	C/Q	P/F
955	57.36	21.32	21.32	76.19	0	23.81	65.48	18.78	15.74	100	0	0	0.29	0.32
1065	54.9	24.51	20.59	76.19	9.52	14.29	59.9	22.77	17.33	91.43	8.57	0	0.13	0.46
1136	59.2	19.9	20.9	76.19	0	23.81	64.18	18.41	17.41	91.43	0	8.57	0.16	0.24
1256	53.33	21.43	25.24	77.36	7.55	15.09	59.52	19.05	21.43	91.11	6.67	2.22	0.25	0.3
1325	53.85	20.88	25.27	93.48	0	6.52	57.69	18.68	23.63	100	0	0	0.11	0.29
1375	49.76	23.92	26.32	29.09	29.09	41.82	57.89	23.44	18.66	41.03	35.9	23.08	0.22	0.39
1466	32.23	19.01	48.76	20.34	72.03	7.63	35.95	23.97	40.08	24.74	75.26	0	0.18	0.5
1495	50.99	18.54	30.46	19.57	50	30.43	60.26	18.54	21.19	28.13	68.75	3.13	0.29	0.46
1516	0.39	0	99.61	0	100	0	0.39	8.2	91.41	0	100	0	0	0.33
1556	0	0.91	99.09	0.92	96.33	2.75	-	-	-	-	-	-	-	-
1575	0	0	100	0	100	0	-	-	-	-	-	-	-	-
1592	0	0	100	0	100	0	-	-	-	-	-	-	-	-
1605	0	0	100	0	100	0	-	-	-	-	-	-	-	-
1626	0	0	100	0	100	0	-	-	-	-	-	-	-	-
1635	0	0	100	0	94.37	5.63	-	-	-	-	-	-	-	-
mean	45.78	18.94	61.17	52.15	76.42	17.18	51.25	19.09	22.6	70.98	49.19	9.25	0.21	0.37
s.d.	18.73	7.05	37.99	34.11	37.41	12.6	20.92	4.69	9.05	33.38	38.15	9.64	0.07	0.09

Charles Wells 5   <u>TABLE 1, cont</u>

Counted Parameters

Depth (ft)	Qm	Qp	P	K	gn	Q$_v$	P$_v$	K$_v$	V$_g$	V$_s$	V$_p$	Q$_s$	Q$_c$	F$_s$	S$_c$	S$_m$	U	M	HM	Opq	DC	Cmt	MP
1677	67	5	63	50	1	0	0	0	1	1	0	0	1	0	3	0	13	7	12	7	0	18	51
1789.8	66	13	29	27	21	0	0	0	8	1	1	0	4	0	2	0	4	2	5	2	1	96	18
1804	5	6	38	29	14	0	4	0	27	1	0	0	0	0	2	1	10	4	2	1	0	2	84
1818.2	73	6	41	37	11	0	0	0	7	0	0	0	3	0	0	1	6	4	7	5	13	34	52
1851.4	72	7	49	39	6	0	0	0	11	1	1	0	9	0	0	4	7	0	10	4	6	9	65
2318.2	59	6	35	28	12	0	5	1	45	2	0	1	2	0	6	1	4	2	6	4	10	10	61
2330	80	7	31	22	17	0	1	0	27	3	1	0	4	0	0	3	2	1	2	1	8	31	59
2452.1	103	4	25	36	3	0	0	0	0	0	0	0	6	1	5	1	15	3	7	3	11	9	68
2510.3	47	9	17	16	27	0	0	0	16	4	3	0	1	0	0	1	2	5	0	2	56	71	23
2519.9	83	13	19	25	11	0	0	0	13	8	0	0	10	0	1	3	10	0	4	3	4	71	22
2992	76	12	23	17	24	0	3	1	40	5	2	0	2	0	0	1	0	2	7	3	4	50	28
3123.1	69	3	59	34	8	0	2	0	16	1	0	0	3	0	0	0	6	3	8	6	13	47	22
3162.1	82	8	37	17	9	0	1	0	25	0	0	0	4	0	0	0	3	5	1	7	17	72	12
3214.1	74	1	51	40	3	0	0	0	7	1	0	0	4	0	0	0	5	4	7	8	31	51	13

Recalculated Parameters

	Standard Method							Modified Gazzi-Dickinson Method							
Depth (ft)	% Q	% F	% R	% U	% V	% S		% Q	% F	% L	% U	% V	% S	C/Q	P/F
1677	35.12	55.61	9.27	68.42	10.53	21.05		35.44	55.83	8.74	72.22	11.11	16.67	0.08	0.56
1789.8	44.89	43.75	11.36	20	50	30		52.84	38.07	9.09	25	62.5	12.5	0.29	0.43
1804	39.13	39.13	21.74	22.22	71.11	6.67		43.4	36.71	19.81	24.39	68.29	7.32	0.17	0.55
1818.2	42.7	48.11	9.19	35.29	41.18	23.53		45.41	47.03	7.57	42.86	50	7.14	0.13	0.47
1851.4	38.35	45.63	16.02	21.21	39.39	39.39		42.72	45.63	11.65	29.17	54.17	16.67	0.18	0.52
2318.2	31.4	36.23	32.37	5.97	79.1	14.93		33.65	37.98	28.37	6.78	79.66	13.56	0.14	0.51
2330	43.94	35.35	20.71	4.88	78.05	17.07		50	31.82	18.18	5.56	86.11	8.33	0.19	0.51
2452.1	53.77	32.16	14.07	53.57	0	46.43		57.5	32	10.5	71.43	0	28.57	0.1	0.39
2510.3	39.16	41.96	18.88	7.41	85.19	7.41		49.31	31.94	18.75	7.41	88.89	3.7	0.34	0.37
2519.9	48.98	28.06	22.96	22.22	46.67	31.11		56.12	26.02	17.86	28.57	60	11.43	0.25	0.37
2992.1	42.72	31.07	26.21	0	94.44	5.56		50.49	26.21	23.3	0	97.92	2.08	0.27	0.48
3123.1	35.82	50.25	13.93	21.43	67.86	10.71		38.31	50.25	11.44	26.09	73.91	0	0.1	0.6
3162.1	48.39	33.87	17.74	9.09	78.79	12.12		52.15	32.8	15.05	10.71	89.29	0	0.15	0.62
3214.1	40.32	50.54	9.14	29.41	47.06	23.53		43.01	50	6.99	38.46	61.54	0	0.08	0.55
mean	41.76	40.84	17.4	24.7	60.72	20.68		46.46	38.73	14.81	29.9	67.95	11.63	0.18	0.5
s.d.	6.02	8.43	6.95	18.76	23.66	12.54		7.41	9.47	6.45	22.04	22.68	7.39	0.08	0.08

Charles Wells 6   TABLE 1, cont

Counted Parameters

Depth (ft)	Qm	Qp	P	K	gn	Q_v	P_v	K_v	V_g	V_s	V_p	Q_s	Q_c	F_s	S_c	S_m	U	M	HM	Opq	DC	Cmt	MP
2012	38	6	17	7	80	0	3	2	47	22	4	1	2	2	1	3	4	4	10	0	4	31	12
2037	54	8	29	23	12	0	2	0	22	0	3	0	2	0	0	4	34	2	1	1	18	11	74
2195	67	16	33	21	13	0		0	19	2	2	0	4	0	0	0	30	2	8	2	2	51	26
2350	73	3	30	17	13	0	0	1	46	6	4	0	2	0	4	2	11	2	2	4	1	40	39
2375	55	11	29	11	15	0	1	0	36	5	1	0	3	0	0	8	8	4	1	6	0	63	43
2520	46	8	19	20	15	0	2	1	44	3	8	0	5	0	2	13	10	4	2	2	4	64	28
3012	37	5	17	27	51	1	1	0	43	22	5	0	2	0	0	11	2	5	1	2	7	24	37
3042	37	3	14	27	17	0	7	0	83	10	12	0	2	0	0	7	5	3	8	11	7	13	34
3083	52	0	17	40	0	0	0	0	0	0	0	0	0	0	7	1	2	2	1	9	165	0	4
3095	88	2	18	29	3	0	0	0	1	0	0	0	3	0	6	0	8	1	3	4	131	0	3
3115	42	15	21	20	21	0	3	0	94	0	3	1	2	0	0	1	5	4	2	1	3	34	28
3195	65	2	47	46	6	0	1	0	14	0	0	0	2	0	7	0	14	4	7	12	1	20	52
3245	53	4	51	27	5	0	2	0	50	0	0	0	2	0	0	0	12	0	2	6	4	42	40

Recalculated Parameters

Depth (ft)	Standard Method							Modified Gazzi-Dickinson Method							
	% Q	% F	% R	% U	% V	% S		% Q	% F	% L	% U	% V	% S	C/Q	P/F
2012	18.41	43.51	38.08	4.4	85.71	9.89		32.64	33.47	33.89	4.94	90.12	4.94	0.51	0.25
2037	32.12	33.16	34.72	50.75	40.3	8.96		38.34	29.02	32.64	53.97	39.68	6.35	0.27	0.55
2195	39.71	32.06	28.23	50.85	42.37	6.78		44.02	30.62	25.36	56.6	43.4	0	0.27	0.55
2350	35.85	28.3	35.85	14.47	75	10.53		39.15	26.42	34.43	15.07	76.71	8.22	0.12	0.54
2375	36.07	30.05	33.88	12.9	69.35	17.74		43.72	24.59	31.69	13.79	72.41	13.79	0.31	0.67
2520	27.55	27.55	44.9	11.36	65.91	22.73		31.63	27.55	40.82	12.5	68.75	18.75	0.26	0.39
3012	18.75	42.41	38.84	2.3	82.76	14.94		25.45	37.5	37.05	2.41	84.34	13.25	0.35	0.21
3042	17.86	25.89	56.25	3.97	88.89	7.14		21.88	25.89	52.23	4.27	89.74	5.98	0.24	0.36
3083	43.7	47.9	8.4	20	0	80		43.7	47.9	8.4	20	0	80	0	0.3
3095	56.96	31.65	11.39	44.44	5.56	50		59.49	31.01	9.49	53.33	6.67	40	0.06	0.37
3115	25	27.19	47.81	4.59	91.74	3.67		31.14	23.68	45.18	4.85	94.17	0.97	0.41	0.44
3195	32.84	48.53	18.63	36.84	39.47	23.68		33.66	49.01	17.33	40	40	20	0.04	0.48
3245	27.67	40.29	32.04	18.18	78.79	3.03		30.81	41.92	27.27	7.41	92.59	0	0.13	0.64
mean	31.73	35.27	33	21.16	63.82	19.93		36.59	32.97	30.45	22.24	66.55	19.3	0.25	0.44
s.d.	11.17	8.14	13.77	18.19	26.34	21.91		9.76	8.59	12.94	20.88	27.87	22.78	0.14	0.14

SAF No. 1 $\qquad$ <u>TABLE 1, cont</u>

Counted Parameters

Depth (ft)	Qm	Qp	P	K	gn	Q_v	P_v	K_v	V_g	V_s	V_p	Q_s	Q_c	F_s	S_c	S_m	U	M	HM	Opq	DC	Cmt	MP
864	94	16	10	69	4	0	0	0	1	0	0	0	17	0	0	2	12	0	1	6	26	0	42
913	117	19	12	38	0	0	0	0	0	0	1	0	10	0	0	0	17	0	0	0	9	7	70
1440	85	10	7	37	0	0	0	0	0	0	0	0	12	0	0	0	32	0	0	0	0	54	63
1590	93	8	33	29	3	0	0	0	1	0	0	0	9	0	2	0	15	0	1	0	36	11	59
1785	103	20	5	28	6	0	0	0	4	0	0	0	22	0	0	0	22	0	0	0	1	0	89
2120	81	7	19	17	2	0	2	0	19	0	9	0	10	0	0	0	13	0	1	0	57	48	15
2203	76	14	5	49	0	0	0	0	5	0	0	0	4	0	0	0	16	0	0	6	0	111	14

Recalculated Parameters

	Standard Method							Modified Gazzi-Dickinson Method							
Depth (ft)	% Q	% F	% R	% U	% V	% S		% Q	% F	% L	% U	% V	% S	C/Q	P/F
864	48.89	36.89	14.22	37.5	3.13	59.38		56.89	36.44	6.67	80	6.67	13.33	0.27	0.12
913	63.55	23.36	13.08	60.71	3.57	35.71		67.91	23.26	8.84	89.47	10.53	0	0.2	0.24
1440	51.91	24.04	24.04	72.73	0	27.27		58.47	24.04	17.49	100	0	0	0.21	0.16
1590	52.33	33.68	13.99	55.56	3.7	40.74		58.55	32.12	9.33	83.33	5.56	11.11	0.18	0.53
1785	58.57	18.57	22.86	45.83	8.33	45.83		70.48	17.14	12.38	84.62	15.38	0	0.3	0.14
2120	49.16	21.23	29.61	24.53	56.6	18.87		54.75	22.35	22.91	31.71	68.29	0	0.17	0.53
2203	53.25	31.95	14.79	64	20	16		55.62	31.95	12.43	76.19	23.81	0	0.19	0.09
mean	53.95	27.1	18.94	51.55	15.89	34.83		60.38	26.76	12.86	77.9	21.71	12.22	0.22	0.26
s.d.	5.31	6.99	6.5	16.65	20.95	15.41		6.22	6.85	5.62	21.75	23.78	1.57	0.05	0.19

Table A-2. Visual estimate in phi units of grain size and sorting from sidewall core plugs. Mean calculated from relation (ø16% + ø50% + ø84%)/3; standard deviation calculated from relation (ø84% - ø16%)/2 (Folk, 1974).

WELL	DEPTH	84% is coarser than	50% is	16% is coarser than	calculated mean	mean equates to	observed mode	calculated std dev	std dev equates to	estimated sorting
CC-1	955	2.00	2.25	0.50	1.58	mL	mL	0.75	moderate	very well
CC-1	1028	3.00	2.25	1.50	2.25	fU	fU	0.75	moderate	very well
CC-1	1065	3.00	2.25	0.50	1.92	mL	fU	1.25	poor	poor
CC-1	1136	2.50	2.25	1.00	1.92	mL	fU	0.75	moderate	very well
CC-1	1256	2.50	2.25	1.00	1.92	mL	mL	0.75	moderate	well
CC-1	1325	3.00	3.25	2.00	2.75	fL	fL	0.50	well-mod	very well
CC-1	1375	2.50	2.25	0.50	1.75	mL	fU-mL	1.00	mod-poor	poor
CC-1	1466	3.00	2.75	2.00	2.58	fL	fL	0.50	well-mod	very well
CC-1	1495	pumice								
CW-5	1677	3.00	3.25	2.50	2.92	fL	vfU	0.25	very well	very well
CW-5	1789.8	3.00	2.25	0.50	1.92	mL	fU	1.25	poor	poor
CW-5	1804	2.50	1.75	0.00	1.42	mU	mL	1.25	poor	poor
CW-5	1818.2	3.00	2.75	1.00	2.25	fU	fL	1.00	mod-poor	moderate
CW-5	1851.4	2.50	2.75	1.00	2.08	fL	fL	0.75	mod	poor
CW-5	2318.2	3.00	1.75	0.00	1.58	mL	fU	1.50	poor	poor
CW-5	2330	3.00	2.25	0.50	1.92	mL	fU	1.25	poor	poor
CW-5	2452.1	3.00	3.25	2.00	2.75	fL	vfU	0.50	well-mod	very well
CW-5	2510.3	2.50	1.75	-1.00	1.08	mU	mL-mU	1.75	poor	poor
CW-5	2519.9	n/a								
CW-5	2558.2	3.00	2.75	1.50	2.42	fU	vfU	0.75	moderate	very well
CW-5	2952.1	3.00	3.75	2.50	3.08	vfU	vfL	0.25	very well	very well
CW-5	2992.1	2.00	1.75	-1.00	0.92	cL	fU-mL	1.50	poor	poor
CW-5	3079.1	mudrock								
CW-5	3123.1	3.00	3.25	1.50	2.58	fL	vfU	0.75	moderate	well
CW-5	3162.1	2.00	1.75	0.00	1.25	mU	fU-mL	1.00	mod-poor	poor
CW-5	3214.1	3.00	3.25	2.00	2.75	fL	vfU	0.50	well-mod	well

Table A-2. Visual estimate in phi units of grain size and sorting from sidewall core plugs. Mean calculated from relation (ø16% + ø50% + ø84%)/3; standard deviation calculated from relation (ø84% - ø16%)/2 (Folk, 1974).

WELL	DEPTH	84% is coarser than	50% is	16% is coarser than	calculated mean	mean equates to	observed mode	calculated std dev	std dev equates to	estimated sorting
CW-6	2012	2.00	0.75	-0.50	0.75	cL	cL	1.25	poor	poor
CW-6	2037	2.00	1.75	0.00	1.25	mU	mL	1.00	mod-poor	moderate
CW-6	2113	mudrock								
CW-6	2195	3.00	1.75	-0.50	1.42	mU	mL	1.75	poor	moderate
CW-6	2350	3.00	2.25	0.50	1.92	mL	mL	1.25	poor	moderate
CW-6	2375	3.00	1.75	0.00	1.58	mL	mU	1.50	poor	moderate
CW-6	2485	mudrock								
CW-6	2570	mudrock								
CW-6	2520	3.00	2.25	0.50	1.92	mL	mL	1.25	poor	poor
CW-6	2870	3.00	3.75	2.00	2.92	fL	vfL	0.50	well-mod	very well
CW-6	3012	3.00	1.75	-1.00	1.25	mU	vfU/mU	2.00	poor-v poor	poor
CW-6	3042	3.00	2.25	0.00	1.75	mL	mL	1.50	poor	poor
CW-6	3083	mudrock								
CW-6	3095	3.00	3.25	1.50	2.58	fL	vfU	0.75	moderate	very well
CW-6	3115	3.00	1.75	0.00	1.58	mL	vfU/mU	1.50	poor	poor
CW-6	3195	3.00	3.25	2.50	2.92	fL	vfU	0.25	very well	very well
CW-6	3245	2.00	2.25	1.00	1.75	mL	fU	0.50	well-mod	moderate
SAF-1	913	n/a								
SAF-1	1440	3.00	2.75	0.50	2.08	fU	fL	1.25	poor	well
SAF-1	1558	3.00	2.75	2.00	2.58	fL	fL	0.50	well-mod	very well
SAF-1	1590	3.00	2.25	0.50	1.92	mL	fU	1.25	poor	moderate
SAF-1	1785	2.50	1.75	0.50	1.58	mL	fU	1.00	mod-poor	moderate
SAF-1	2120	3.00	2.75	1.50	2.42	fU	vfL	0.75	moderate	poor
SAF-1	2203	3.00	2.25	0.50	1.92	mL	mL	1.25	poor	moderate

APPENDIX 6-B

Porosity Terms
Table B-1. Porosity distribution within Cerro Colorado 1
cores determined from 100 point counts per sample
Table B-2a. Host mineralogy of intragranular macroporosity and microporosity
Table B-2b. Host mineralogy of intragranular pore space: total of all wells

APPENDIX B
Definitions of Porosity Terms

Total macroporosity: the percentage of each thin-section, based on 300 point-counts, represented by macroporosity (relatively large, open pores impregnated with blue-dyed epoxy).

Intergranular macroporosity: the percentage of pore space, based on 100 point counts, occurring between framework grains that consists of residual primary porosity, oversized pores and through-going fractures.

> *Residual primary porosity*--that fraction of original porosity remaining after precipitation of authigenic minerals.

> *Oversized pores*--pore spaces that are unusually large with respect to surrounding pore space, implying dissolution of framework grains; no grain remnants or relict clay rims are present.

> *Through-going fracture*--epoxy-filled fractures that bisect two or more framework grains.

Intragranular macroporosity: the percentage of pore space, based on 100 point counts, occurring within framework grains that consists of framework grain dissolution and confined fractures.

> *Framework grain dissolution*--includes both pore space within a remnant, identifiable framework grain ("skeletal grain"), and pore space outlined by a remnant grain boundary or relict clay rim ("ghost grain").

> *Confined fracture*--epoxy-filled fracture that does not extend beyond an individual grain.

Intergranular microporosity: the percentage of pore space, based on 100 point counts, occurring between framework grains; diameters of micropores are on the order of several microns, and appear in thin-section as minute sponge-like areas of blue-dyed epoxy.

> *Clay*--microporosity interpreted as resulting from intergranular growths of authigenic clay.

> *Cement*--microporosity interpreted as resulting from intergranular growths of non-clay pore-filling minerals.

Intragranular microporosity: the percentage of pore space, based on 100 point counts, occurring within identifiable framework grains, that is interpreted as the result of framework alteration to a clay product.

Secondary porosity: the percentage of pore space, based on 100 point counts, consisting of the sum of oversized pores, framework grain dissolution, confined fractures and intragranular microporosity. Although intragranular microporosity is equated with the precipitation of secondary minerals (resulting in a solid-phase volume increase), it represents higher porosity relative to the framework grain it replaces, so it is included in this category. Through-going fractures are of uncertain origins, so they are excluded.

Minus-cement porosity: the percentage of each thin-section, based on 300 point-counts, consisting of the sum of intergranular cement (carbonate, zeolite and authigenic clay) and total macroporosity.

Table B-1. Porosity distribution within Cerro Colorado 1 cores determined from 100 point counts per sample.

Well Depth (ft)	INTERGRANULAR MACROPOROSITY				INTRAGRANULAR MACROPOROSITY			INTERGRANULAR MICROPOROSITY			INTRA-GRANULAR MICRO-POROSITY	SECONDARY POROSITY
	Primary	Oversize pore	Fracture through-going	Total	Frmwrk grain dissoln	Fracture confined	Total	Clay	Cement	Total	Total	Total
Cerro Colorado												
955	77	15	0	92	1	1	2	3	0	3	3	16
1065	57	2	0	59	10	0	10	11	0	11	20	12
1136	62	10	1	73	8	0	8	2	0	2	17	18
1256	56	13	0	69	10	1	11	0	0	0	20	23
1325	44	4	0	48	16	1	17	9	0	9	26	20
1375	47	4	0	51	16	3	19	11	0	11	19	20
1466	24	0	3	27	4	2	6	45	1	46	21	4
1495	24	0	8	32	8	1	9	40	0	40	19	8

Table B-1. Porosity distribution within Cerro Colorado 1 cores determined from 100 point counts per sample.

Well Depth (ft)	INTERGRANULAR MACROPOROSITY				INTRAGRANULAR MACROPOROSITY			INTERGRANULAR MICROPOROSITY			INTRA-GRANULAR MICRO-POROSITY	SECONDARY POROSITY
	Primary	Oversize pore	Fracture through-going	Total	Frmwrk grain dissoln	Fracture confined	Total	Clay	Cement	Total	Total	Total
Charles Wells 5												
1677	52	0	0	52	5	0	5	6	6	12	31	5
1789.8	19	2	0	21	4	7	11	59	0	59	9	6
1804	52	12	0	64	21	0	21	1	0	1	14	33
1818.2	39	1	1	41	4	0	4	34	2	36	18	5
1851.4	38	1	0	39	10	1	11	23	1	24	26	11
2318.2	38	5	0	43	19	4	23	10	3	13	21	24
2330	45	3	0	48	20	3	23	4	0	4	25	23
2452.1	36	2	1	39	14	0	14	19	0	19	28	16
2510.3	17	4	0	21	7	1	8	15	9	24	47	11
2519.9	43	7	0	50	2	3	5	7	22	29	16	9
2992.1	28	0	0	28	6	3	9	19	22	41	22	6
3123.1	14	0	0	14	8	5	13	29	0	29	44	8
3162.1	5	1	5	11	11	9	20	28	5	33	36	12
3214.1	8	0	2	10	2	2	4	53	0	53	33	2

Table B-1. Porosity distribution within Cerro Colorado 1 cores determined from 100 point counts per sample.

Well Depth (ft)	INTERGRANULAR MACROPOROSITY				INTRAGRANULAR MACROPOROSITY			INTERGRANULAR MICROPOROSITY			INTRA-GRANULAR MICRO-POROSITY	SECONDARY POROSITY
	Primary	Oversize pore	Fracture through-going	Total	Frmwrk grain dissoln	Fracture confined	Total	Clay	Cement	Total	Total	Total
CW 6												
2012	17	1	1	19	19	1	20	6	9	15	46	20
2037	41	9	0	50	27	1	28	6	0	6	16	36
2195	37	4	0	41	9	3	12	0	23	23	24	13
2350	36	0	0	36	14	4	18	1	8	9	37	14
2375	34	1	0	35	6	1	7	0	24	24	34	7
2520	16	0	0	16	7	2	9	0	35	35	40	7
3012	37	0	0	37	12	8	20	5	15	20	23	12
3042	27	6	0	33	19	5	24	0	2	2	41	25
3083	2	2	0	4	19	5	24	48	0	48	24	21
3095	11	1	0	12	22	4	26	42	0	42	20	23
3115	21	0	0	21	13	4	17	0	5	5	57	13
3195	43	3	0	46	11	0	11	14	0	14	29	14
3245	33	1	1	35	13	8	21	10	6	16	28	14

Table B-1. Porosity distribution within Cerro Colorado 1 cores determined from 100 point counts per sample.

Well Depth (ft)	INTERGRANULAR MACROPOROSITY				INTRAGRANULAR MACROPOROSITY			INTERGRANULAR MICROPOROSITY			INTRA-GRANULAR MICRO-POROSITY	SECONDARY POROSITY
	Primary	Oversize pore	Fracture through-going	Total	Frmwrk grain dissoln	Fracture confined	Total	Clay	Cement	Total	Total	Total
SAF 1												
864	59	0	0	59	4	15	19	10	0	10	12	4
913	70	6	0	76	5	4	9	8	0	8	7	11
1440	59	2	0	61	13	3	16	15	0	15	8	15
1590	33	3	0	36	16	2	18	29	1	30	16	19
1785	70	5	0	75	11	0	11	7	0	7	7	16
2120	16	1	1	18	22	2	24	40	4	44	14	23
2203	22	1	13	36	11	23	34	20	0	20	10	12

Table B-2a. Host mineralogy of intragranular macroporosity and microporosity. Skeletal framework grains are interpreted as resulting from dissolution processes, whereas shattered feldspar grains are interpreted as introduced by the coring process. Intragranular microporosity is interpreted as the product of framework grain alteration. Values are number of points counted out of 300 point counts per thin section.

Cerro Colorado 1

depth (ft)	skeletal framework grains					shattered feldspar	intragranular microporosity				
	qtz	plag	kspar	VRF	URF		qtz	plag	kspar	VRF	URF
955	0	0	1	0	0	0	0	0	0	0	0
1065	0	4	0	0	0	0	1	1	0	0	1
1136	0	2	2	0	2	0	2	1	4	0	2
1256	0	4	2	3	9	0	10	4	4	3	15
1325	2	4	0	0	19	0	8	4	1	0	25
1375	2	5	1	0	2	0	1	6	0	3	2
1466	0	11	1	2	0	0	2	5	0	48	0
1495	0	3	0	1	0	0	0	0	0	7	0
1516	0	0	0	0	0	14	1	4	5	73	0
1556	0	3	0	0	0	8	0	0	0	85	0
1575	0	3	0	0	0	10	0	3	0	68	0
1592	0	2	1	0	0	13	0	2	4	128	0
1605	0	1	0	0	0	5	0	0	0	142	0
1626	0	6	1	0	0	0	0	0	0	97	0
1635	0	6	1	0	0	0	0	0	0	96	0
sum	4	54	10	6	32	50	25	30	18	750	45
percent of category	3.77	50.94	9.43	5.66	30.19		2.88	3.46	2.07	86.41	5.18
category total	106					50	868				

Table B-2a continued

SAF 1

depth (ft)	skeletal framework grains					shattered feldspar	intragranular microporosity				
	qtz	plag	kspar	VRF	URF		qtz	plag	kspar	VRF	URF
864	1	2	1	0	0	7	0	0	0	0	1
913	0	3	2	0	1	7	0	0	0	0	2
1440	0	0	0	0	0	0	0	0	2	0	1
1590	0	7	5	1	0	0	2	2	0	1	0
1785	0	0	4	0	0	0	1	0	0	0	0
2120	0	0	0	10	0	0	0	0	1	13	0
2203	0	0	0	1	3	18	0	0	0	0	0
sum	1	12	12	12	4	32	3	2	3	14	4
percent of category	2.44	29.27	29.27	29.27	9.76		11.54	7.69	11.54	53.85	15.38
category total					41	32					26

Table B-2a continued

Charles Wells 6

depth (ft)	skeletal framework grains					shattered feldspar	intragranular microporosity				
	qtz	plag	kspar	VRF	URF		qtz	plag	kspar	VRF	URF
2012	1	5	0	5	2	0	0	0	0	21	0
2037	0	4	0	1	0	0	2	2	1	19	1
2195	1	3	1	4	0	0	1	0	1	13	2
2350	1	8	3	0	0	0	1	2	1	49	0
2375	0	6	0	6	0	0	0	0	0	28	1
2520	1	2	2	4	0	0	1	0	0	38	0
3012	0	1	0	2	0	0	0	2	0	27	0
3042	0	5	2	0	0	0	0	1	0	50	0
3083	0	2	2	0	0	0	0	0	0	0	0
3095	0	4	2	0	0	0	0	0	5	0	0
3115	0	8	1	0	0	0	1	1	1	60	0
3195	0	13	9	0	0	0	0	4	4	11	0
3245	0	7	3	4	0	0	2	1	0	30	0
sum	4	68	25	26	2	0	8	13	13	346	4
percent of category	3.2	54.4	20	20.8	1.6		2.08	3.39	3.39	90.1	.04
category total					125	0					384

Table B-2a continued

Charles Wells 5

depth (ft)	skeletal framework grains					shattered feldspar	intragranular microporosity				
	qtz	plag	kspar	VRF	URF		qtz	plag	kspar	VRF	URF
1677	1	4	11	0	0	0	0	0	0	0	0
1789.8	0	2	1	3	0	3	0		0	0	0
1804	0	6	6	2	0	3	0	0	0	3	0
1818.2	0	7	3	1	0	0	0	1	0	0	0
1851.4	0	3	6	3	0	0	0	0	0	3	0
2318.2	1	5	3	2	0	8	0	0	0	7	0
2330	0	3	3	2	0	0	0	0	0	2	0
2452.1	2	5	4	0	0	0	0	0	0	0	0
2510.3	0	3	2	5	0	0	0	0	0	8	0
2519.9	0	2	1	6	0	0	0	0	0	4	0
2992.1	3	9	4	5	0	7	1	1	1	16	0
3123.1	0	12	10	3	0	8	0	0	0	4	0
3162.1	1	9	1	2	0	2	0	0	0	.13	0
3214.1	0	6	8	1	0	0	0	0	0	3	0
sum	8	76	63	35	0	31	1	2	1	63	0
percent of category	4.4	41.76	34.62	19.23	0		1.49	2.99	1.49	94.03	0
category total					182	31					67

<u>Table B-2b.</u> Host mineralogy of intragranular pore space: total of all wells.

well	skeletal framework grains					shattered feldspar	intragranular microporosity				
	qtz	plag	kspar	VRF	URF		qtz	plag	kspar	VRF	URF
CC 1	4	54	10	6	32	50	25	30	18	750	45
CW 5	8	76	63	35	0	31	1	2	1	63	0
CW 6	4	68	25	26	2	0	8	13	13	346	4
SAF 1	0	10	11	11	1	7	3	2	3	14	3
sum	16	208	109	78	35	88	37	47	35	1173	52
category total					446	88					1344
percent of category	3.59	46.64	24.44	17.49	7.85	100	2.75	3.50	2.60	87.28	3.87

APPENDIX 6-C

Abundance and Distribution of Authigenic Mineral Cements

APPENDIX C

Abundance and distribution of authigenic mineral cements

Table C-1. Abundance and distribution of authigenic mineral cements (pore-filling mineral growths; Dickinson, 1970) determined from 300 point counts per sample. Samples are grouped by prevalent cement, defined as that cement occupying the highest volume of the pre-cement porosity. The percent of pre-cement porosity occupied by each cement is tabulated in the right-hand columns, and the number of points counted for each cement are tabulated in the left-hand columns. Samples with more than one cement in excess of an arbitrary 10% of pre-cement porosity are placed in a two-cement category. Point counts of intergranular and framework microporosity (center columns) are interpreted as dissolution and subsequent alteration of framework aluminosilicates to secondary clay minerals.

well	depth	zeolite	carbonate	inter-granular micro-porosity	framework micro-porosity	inter-granular macro-porosity	pre-cement porosity	%zeo	%clay	%CO$_3$	litho-facies
UNCEMENTED											
CW 5	1804	2	0	0	3	84	89	2.25	3.37	0.00	3
CW 5	2452.1	1	5	3	0	68	77	1.30	3.90	6.49	9
CW 6	3083	0	0	0	0	4	4	0.00	0.00	0.00	2
SAF 1	864	0	0	0	1	42	43	0.00	2.33	0.00	4
SAF 1	913	0	4	3	2	70	79	0.00	6.33	5.06	4
SAF 1	1785	0	0	0	1	89	90	0.00	1.11	0.00	4
CARBONATE											
CC 1	955	0	14	1	0	85	100	0.00	1.00	14.00	9
CW 5	1677	1	16	1	0	51	69	1.45	1.45	23.19	3
CW 5	1789.8	0	96	0	0	18	114	0.00	0.00	84.21	3
CW 5	1818.2	1	31	2	1	52	87	1.15	3.45	35.63	3
SAF 1	1590	0	10	1	5	59	75	0.00	8.00	13.33	4
SAF 1	2203	0	111	0	0	14	125	0.00	0.00	88.80	4

well	depth	zeolite	carbonate	inter-granular micro-porosity	framework micro-porosity	inter-granular macro-porosity	pre-cement porosity	%zeo	%clay	%CO$_3$	litho-facies

CLAY ALTERATION

well	depth	zeolite	carbonate	inter-granular micro-porosity	framework micro-porosity	inter-granular macro-porosity	pre-cement porosity	%zeo	%clay	%CO$_3$	litho-facies
CC 1	1136	0	0	8	9	84	101	0.00	16.83	0.00	9
CC 1	1256	0	0	14	35	71	120	0.00	40.83	0.00	9
CC 1	1325	0	1	16	38	66	121	0.00	44.63	0.83	9
CC 1	1375	0	0.1	6	15	50	71	0.00	29.54	0.14	9
CC 1	1466	0	0	19	55	14	88	0.00	84.09	0.00	4
CC 1	1495	0	0	28	7	23	58	0.00	60.34	0.00	4
CC 1	1516	0	0	0	73	39	112	0.00	65.18	0.00	4
CC 1	1556	0	0	0	85	31	116	0.00	73.28	0.00	4
CW 5	1851.4	1	1	7	3	65	77	1.30	12.99	1.30	3
CW 5	2318.2	6	1	3	7	61	78	7.69	12.82	1.28	9
CW 6	3095	0	0	0	5	3	8	0.00	62.50	0.00	2

ZEOLITE

well	depth	zeolite	carbonate	inter-granular micro-porosity	framework micro-porosity	inter-granular macro-porosity	pre-cement porosity	%zeo	%clay	%CO$_3$	litho-facies
CW 5	2330	24	5	2	2	59	92	26.09	4.35	5.43	9
CW 5	2519.9	66	1	4	4	22	97	68.04	8.25	1.03	9
SAF 1	1440	54	0	0	3	63	120	45.00	2.50	0.00	4

CLAY + CARBONATE

well	depth	zeolite	carbonate	inter-granular micro-porosity	framework micro-porosity	inter-granular macro-porosity	pre-cement porosity	%zeo	%clay	%CO$_3$	litho-facies
CC 1	1065	0	8	9	3	58	78	0.00	15.38	10.26	9
CW 5	3162.1	0	52	20	13	12	97	0.00	34.02	53.61	3
CW 5	3214.1	0	24	27	3	13	67	0.00	44.78	35.82	3
CW 6	2037	0.1	10	1	15	74	100	0.10	15.98	9.99	3
CW 6	3195	0	13	7	19	52	91	0.00	28.57	14.29	2
CW 6	3245	0	42	0	33	40	115	0.00	28.70	36.52	2
SAF 1	2120	0	39	9	14	15	77	0.00	29.87	50.65	4

well	depth	zeolite	carbonate	inter-granular micro-porosity	framework micro-porosity	inter-granular macro-porosity	pre-cement porosity	%zeo	%clay	%CO₃	litho-facies
					ZEOLITE + CLAY						
CW 5	2510.3	44	5	22	8	23	102	43.14	29.41	4.90	9
CW 5	2992.1	40	3	7	19	28	97	41.24	26.80	3.09	3
CW 5	3123.1	17	1	29	4	22	73	23.29	45.21	1.37	3
CW 6	2012	22	4	5	8	12	51	43.14	25.49	7.84	3
CW 6	2195	42	1	8	17	26	94	44.68	26.60	1.06	9
CW 6	2350	31	0	9	53	39	132	23.48	46.97	0.00	4
CW 6	2375	61	2	0	29	43	135	45.19	21.48	1.48	4
CW 6	2520	61	2	1	39	28	131	46.56	30.53	1.53	9
CW 6	3012	19	3	2	29	37	90	21.11	34.44	3.33	2
CW 6	3042	12	0	1	51	34	98	12.24	53.06	0.00	2
CW 6	3115	33	0	1	60	28	122	27.05	50.00	0.00	2

APPENDIX 6-D

Chemical Composition of Representative detrital feldspars from Charles Wells 5

APPENDIX D
Chemical composition of representative detrital feldspars from Charles Wells 5

Table D-1. Chemical composition of representative detrital feldspars from Charles Wells 5; results of analysis by electron microprobe methods against rhyolite glass standard. Elements are omitted from totals column if their concentration is less than the error.

Analysis No. 1, grain 1: Oligoclase feldspar $An_{27.2}$

	Na	Mg	Al	Si	K	Ba	Ca	Ti	Mn	Fe	O	Total
% element	5.552	0.014	12.652	27.878	0.998	0.054	4.010	0.009		0.209	46.832	98.208
error (+/-)	0.047	0.004	0.090	0.133	0.025	0.020	0.083	0.008		0.024		
weight % oxide	7.485	0.024	23.907	59.637	1.202	0.060	5.610	0.015		0.269		98.208
formula	0.660	0.002	1.282	2.713	0.070	0.001	0.273	0.001		0.010	8.000	5.011

Analysis No. 2, grain 1: Oligoclase feldspar $An_{27.5}$

	Na	Mg	Al	Si	K	Ba	Ca	Ti	Mn	Fe	O	Total
% element	5.578	0.012	12.578	28.142	1.030	0.059	4.083			0.213	47.105	98.800
error (+/-)	0.047	0.004	0.089	0.133	0.025	0.020	0.083			0.024		
weight % oxide	7.520	`0.020	23.767	60.201	1.240	0.066	5.713			0.274		98.800
formula	0.659	0.001	1.267	2.722	0.072	0.001	0.277			0.010	8.000	5.010

Analysis No. 3, grain 1: Oligoclase-andesine feldspar $An_{30.0}$

	Na	Mg	Al	Si	K	Ba	Ca	Ti	Mn	Fe	O	Total
% element	5.410	0.007	12.526	27.933	0.855	0.074	4.399			0.266	46.866	98.335
error (+/-)	0.046	0.004	0.089	0.133	0.023	0.020	0.086			0.025		
weight % oxide	7.293	0.011	23.669	59.753	1.030	0.083	6.155			0.342		
formula	0.643	0.001	1.268	2.716	0.060	0.001	0.300			0.013	8.000	5.001

Analysis No. 1, grain 2: Alkali feldspar 94.23% K

	Na	Mg	Al	Si	K	Ba	Ca	Ti	Mn	Fe	O	Total
% element	0.385	0.013	9.708	29.539	10.700	0.426		0.016		0.044	44.691	95.523
error (+/-)	0.014	0.003	0.069	0.132	0.075	0.025		0.008		0.020		
weight % oxide	0.519	0.022	18.344	63.190	12.889	0.476		0.026		0.057		95.523
formula	0.048	0.002	1.031	3.012	0.784	0.009		0.001		0.002	8.000	4.888

Analysis No. 2, grain 2: Alkali feldspar 96.63% K

	Na	Mg	Al	Si	K	Ba	Ca	Ti	As	Fe	O	Total
% element	0.248		9.611	29.632	12.205	0.444			0.018		44.946	97.104
error (+/-)	0.012		0.068	0.132	0.080	0.025			0.012			
weight % oxide	0.334		18.160	63.388	14.703	0.496			0.023			97.104
formula	0.031		1.014	3.004	0.889	0.009			0.001		8.000	4.948

Analysis No. 1, grain 3: Alkali feldspar 95.92% K

	Na	Mg	Al	Si	K	Ba	Ca	Cl	Mn	Fe	O	Total
% element	0.245		9.574	30.172	9.692	0.206		0.027			44.981	94.898
error (+/-)	0.012		0.068	0.133	0.072	0.023		0.011				
weight % oxide	0.331		18.090	64.545	11.675	0.230		0.027				94.898
formula	0.030		1.010	3.057	0.705	0.004		0.002			8.000	4.809

Analysis No. 2, grain 3: Alkali feldspar 86.63% K

	Na	Mg	Al	Si	K	Ba	Ca	Ti	Mn	Fe	O	Total
% element	0.956		9.693	30.252	10.567	0.278				0.096	45.640	97.483
error (+/-)	0.020		0.069	0.134	0.075	0.024				0.022		
weight % oxide	1.288		18.315	64.716	12.729	0.311				0.124		97.483
formula	0.117		1.008	3.020	0.758	0.006				0.005	8.000	4.913

Analysis No. 1, grain 4: Alkali feldspar 96.86% K

	Na	Mg	Al	Si	K	Ba	Ca	Ti	As	Fe	O	Total
% element	0.231		9.657	29.938	11.945	0.219			0.017	0.058	45.268	97.332
error (+/-)	0.012		0.069	0.132	0.079	0.023			0.012	0.021		
weight % oxide	0.311		18.247	64.044	14.389	0.244			0.022	0.075		97.332
formula	0.028		1.012	3.014	0.864	0.005			0.001	0.003	8.000	4.926

Analysis No. 1, grain 5: Oligoclase feldspar $An_{15.9}$ (fresh area)

	Na	Mg	Al	Si	K	Ba	Ca	Ti	Mn	Fe	O	Total
% element	6.546		11.606	30.766	0.057		2.162			0.057	48.541	99.735
error (+/-)	0.050		0.082	0.138	0.010		0.067			0.021		
weight % oxide	8.824		21.929	65.814	0.069		3.025			0.074		99.735
formula	0.751		1.134	2.888	0.004		0.142			0.003	8.000	4.922

Analysis No. 2, grain 5: Oligoclase feldspar $An_{11.5}$ (cloudy interior)

	Na	Mg	Al	Si	K	Ba	Ca	Ti	Mn	Fe	O	Total
% element	6.754	0.009	10.993	30.740	0.060		1.525		0.020	0.524	47.931	98.557
error (+/-)	0.051	0.004	0.078	0.138	0.010		0.060		0.016	0.031		
weight % oxide	9.105	0.015	20.772	65.759	0.072		2.134		0.026	0.674		98.557
formula	0.785	0.001	1.088	2.922	0.004		0.102		0.001	0.025	8.000	4.928

Analysis No. 1, grain 6: Groundmass of volcanic rock fragment

	Na	Mg	Al	Si	K	Ba	Ca	Ti	Cl	Fe	O	Total
% element	1.608	0.009	7.050	31.979	7.010	0.076	0.095	0.078	0.021	0.331	51.744	100.000
error (+/-)	0.026	0.004	0.050	0.134	0.061	0.020	0.054	0.009	0.010	0.026		
weight % oxide	2.168	0.015	13.321	68.410	8.444	0.085	0.133	0.130	0.021	0.426		93.151
formula	0.025	0.000	0.093	0.406	0.064	0.000	0.001	0.001	0.000	0.002	1.153	0.592

Analysis No. 2, grain 6: Groundmass of volcanic rock fragment

	Na	Mg	Al	Si	K	Ba	Ca	Ti	Cl	Fe	O	Total
% element	1.979	0.013	7.217	31.759	6.767	0.055	0.107	0.061	0.036	0.287	51.718	100.000
error (+/-)	0.029	0.04	0.052	0.134	0.060	0.019	0.054	0.009	0.011	0.025		
weight % oxide	2.668	0.022	13.637	67.939	8.152	0.061	0.150	0.103	0.036	0.369		93.136
formula	0.031	0.000	0.095	0.403	0.062	0.000	0.001	0.000	0.000	0.002	1.153	0.595

Table D-2. Chemical composition of representative clay samples from Charles Wells 5; results of analysis by electron microprobe methods against biotite standard. Mineral formulas are calculated on an anhydrous basis of eleven oxygen atoms. Elements are omitted from totals column if their concentration is less than the error.

Analysis No. 1: $(Na_{.44}K_{.22}Ca_{.12})(Al_{1.16}Fe_{.11}Mg_{.06})Si_{4.33}O_{11}$

	Na	Mg	Al	Si	K	Ba	Ca	Ti	Mn	Fe	O	Total
% element	1.767	.235	5.427	21.132	1.521		.839	.058		1.047	30.617	62.585
error (+/-)	.056	.044	.072	.123	.063		.059	.068		.120		
weight % oxide	2.381	.390	10.254	45.206	1.832		1.174			1.347		62.585
formula	.442	.056	1.156	4.325	.224		.120			.108	11.00	6.430

Analysis No. 2: $(Ca_{.10}K_{.08})(Al_{.90}Mg_{.54}Fe_{.44}Ti.03)Si_{4.23}O_{11}$

	Na	Mg	Al	Si	K	Ba	Ca	Ti	Mn	Fe	O	Total
% element	.045	1.299	2.398	11.740	.306		.385	.162		2.397	17.374	36.061
error (+/-)	.044	.047	.058	.094	.046		.048	.061		.149		
weight % oxide		2.153	4.531	25.115	.368		.539	.270		3.084		36.061
formula		.541	.900	4.234	.079		.097	.034		.435	11.00	6.321

Analysis No. 3: $(Ca_{.62}Na_{.57}K_{.06})(Al_{1.46}Mg_{.03}Fe_{.09})Si_{3.54}Al_{.46}O_{11}$

	Na	Mg	Al	Si	K	Ba	Ca	Ti	Mn	Fe	O	Total
% element	2.585	.138	10.234	19.752	.445		4.923	.130		.953	34.924	73.954
error (+/-)	.060	.046	.091	.125	.053		.096	.068		.124		
weight % oxide	3.485	.229	19.338	42.252	.536		6.889			1.226		73.954
formula	.567	.029	1.912	3.544	.057		.619			.086	11.00	6.813

Analysis No. 4: $(K_{.08}Ca_{.02})(Al_{.41}Mg_{.06}Fe_{.11}Ti.29)Si_{4.78}O_{11}$

	Na	Mg	Al	Si	K	Ba	Ca	Ti	Mn	Fe	O	Total
% element	.041	.399	3.004	36.306	.884		.218	3.762		1.606	47.537	93.717
error (+/-)	.049	.043	.064	.152	.059		.055	.119		.149		
weight % oxide		.661	5.677	77.667	1.065		.305	6.275		2.066		93.717
formula		.061	.412	4.785	.084		.020	.291		.106	11.00	5.760

Analysis No. 5: $(K_{.64}Na_{.56}Ca_{.09})(Al_{1.49}Fe_{.05})Si_{4.02}O_{11}$

	Na	Mg	Al	Si	K	Ba	Ca	Ti	Mn	Fe	O	Total
% element	2.325	.015	7.234	20.373	4.515		.641	.121		.461	31.765	67.315
error (+/-)	.061	.045	.080	.124	.089		.062	.068		.103		
weight % oxide	3.134		13.670	43.582	5.439		.897			.593		67.315
formula	.560		1.486	4.019	.640		.089			.046	11.00	6.839

Table D-3. Chemical compositions of representative zeolite samples from Charles Wells 5; results of analysis by electron microprobe methods against rhyolite glass standard.

Analysis No. 1: $(Ca_{.55}Mg_{.20}Na_{.07}K_{.04}Ba_{.02}Fe_{.01})Al_{1.98}Si_{7.10}O_{18}$

	Na	Mg	Al	Si	K	Ba	Ca	Ti	Mn	Fe	O	Total
% element	.269		9.429	29.178	12.808	.327		.029		.117	44.432	96.588
std dev	.012		.067	.131	.082	.024		.009		.022		
weight % oxide	.362		17.816	62.417	15.429	.366		.048		.150		96.588
formula	.076		2.265	6.733	2.123	.015		.004		.014	18.00	11.230

Ca + Sr + Ba/Na + K: 5.153
Si + Al: 9.081

Analysis No. 2: $(Ca_{.60}Mg_{.17}Na_{.08}K_{.04}Ba_{.02})Al_{2.09}Si_{7.01}O_{18}$

	Na	Mg	Al	Si	K	Ba	Ca	Ti	Mn	Fe	O	Total
% element	.251	.559	7.447	26.035	.179	.375	3.201				38.098	76.145
std dev	.012	.009	.053	.123	.013	.024	.076					
weight % oxide	.338	.928	14.072	55.694	.215	.419	4.478					76.145
formula	.083	.174	2.087	7.007	.035	.021	.604				18.00	10.009

Ca + Sr + Ba/Na + K: 5.297
Si + Al: 9.094

Analysis No. 3: $(Ca_{.54}Mg_{.17}K_{.03}Na_{.03}Ba_{.02})Al_{1.95}Si_{7.16}O_{18}$

	Na	Mg	Al	Si	K	Ba	Ca	Ti	Mn	Fe	O	Total
% element	.080	.574	7.417	28.275	.163	.396	3.018	.012		.021	40.513	80.490
std dev	.008	.009	.053	.128	.012	.024	.076	.008		.019		
weight % oxide	.108	.952	14.015	60.487	.196	.442	4.223	.021		.027		80.490
formula	.025	.168	1.954	7.156	.030	.020	.535	.002		.003	18.00	9.896

Ca + Sr + Ba/Na + K: 10.091

Si + Al: 9.110

Analysis No. 4: $(Ca_{.57}Mg_{.17}Na_{.06}K_{.04}Ba_{.03}Fe_{.01})Al_{2.05}Si_{7.05}O_{18}$

	Na	Mg	Al	Si	K	Ba	Ca	Ti	Mn	Fe	O	Total
% element	.192	.606	8.155	29.256	.214	.586	3.380	.012	.019	.057	42.539	85.015
std dev	.010	.009	.058	.131	.013	.026	.076	.008	.016	.020		
weight % oxide	.259	1.005	15.410	62.583	.257	.654	4.729	.020	.025	.073		85.015
formula	.057	.169	2.046	7.051	.037	.029	.571	.002	.002	.007	18.00	9.971

Ca + Sr + Ba/Na + K: 6.383

Si + Al: 9.097

Analysis No. 5: $(Ca_{.56}Mg_{.18}K_{.06}Na_{.05}Ba_{.02})Al_{2.04}Si7_{.07}O_{18}$

	Na	Mg	Al	Si	K	Ba	Ca	Ti	Mn	Fe	O	Total
% element	.150	.630	7.821	28.272	.307	.296	3.207				41.009	81.690
std dev	.010	.009	.056	.128	.015	.023	.075					
weight % oxide	.202	1.045	14.779	60.479	.369	.330	4.487					81.690
formula	.046	.182	2.036	7.068	.055	.015	.562				81.690	9.964

Ca + Sr + Ba/Na + K: 5.713

Si + Al: 9.104